Desarrollo de un sistema eficiente para generación de energía a través de dispositivos microfluídicos electroquímicos usando aerogeles tipo Pd-M

M.C. Alejandra Martínez Lázaro

2024

UNIVERSIDAD AUTONOMA DE QUERETARO
Facultad de Ingeniería

"Desarrollo de un sistema eficiente para generación de energía a través de dispositivos microfluídicos electroquímicos usando aerogeles tipo Pd-M"

TESIS

Que como parte de los requisitos para obtener el grado de

Doctora en Ingeniería

Presenta:

M.C. Alejandra Martínez Lázaro

Director:

Dra. Janet Ledesma García

Co-Director:

Dra. Ana Arenillas de la Puente

Querétaro, Qro. A 22 de Marzo del 2024

Desarrollo de un sistema eficiente para generación de energía a través de dispositivos microfluídicos electroquímicos usando aerogeles tipo Pd-M

por

Alejandra Martinez Lazaro

UNIVERSIDAD AUTONOMA DE QUERETARO

Facultad de Ingeniería

Maestría en Ciencias con terminación en Nanotecnología

“Desarrollo de un sistema eficiente para generación de energía a través de dispositivos microfluídicos electroquímicos usando aerogeles tipo Pd-M”

TESIS

Que como parte de los requisitos para obtener el grado de:

Doctor en Ingeniería

Presenta:

M.C. Alejandra Martínez Lázaro

Director:

Dra. Janet Ledesma García

Co-Director:

Dra. Ana Arenillas de la Puente

Dra. Janet Ledesma García

Presidente

Dra. Ana Arenillas de la Puente

Secretario

Dr. Carlos Guzmán Martínez

Vocal

Dra. Samantha Lizette Flores

Vocal

Luis Arturo Godínez Mora Tovar

Centro Universitario Querétaro, Qro.

22 de marzo del 2024

A Nachita …mi Ángel

Agradecimientos:

A CONAHCYT por brindarme el apoyo económico para llevar a cabo esta tesis doctoral.

A Janet y Gerardo por su apoyo incondicional estos últimos 6 años y por ser el pilar de mi trayectoria académica.

A Ana y a Samantha por su apoyo tan lejos de casa y por hacer de mis estadías en el INCAR amenas y de alto aprendizaje humano y académico.

Al equipo de LABMYN en quienes encontré unos amigos incondicionales.

A mi madre y a mi hermana, por que este logro es conjunto.

RESUMEN

El presente trabajo muestra una ruta de síntesis ultrarrápida usando microondas para la obtención de aerogeles metálicos, en la primera etapa del desarrollo de estos materiales se incorporaron metales de transición en la estructura atómica del Paladio, donde se obtuvieron aleaciones metálicas entre este y los metales Fe, Ni y Co. Los aerogeles híbridos Pd-M se utilizaron como catalizadores en celdas microfluídicas para distintas reacciones: Reacción de evolución de oxígeno (REO), reacción de reducción de oxígeno (RRO), Reacción de oxidación de urea (ROU) y reacción de oxidación de amonio (ROA). Como aplicación en sistemas electroquímicos de conversión de energía, se evaluó la actividad catalítica de los aerogeles Pd-M (M=Fe, Ni, Co) en celdas de combustible microfluídicas que utilizaban etanol y ácido fórmico como combustible, donde los aerogeles Pd-Ni y Pd-Co resultaron ser mayormente activos en el aprovechamiento de estos combustibles superando en 3 veces más a la actividad del Pd solo. La combinación del paladio con el metal de transición permitió reducir la dependencia del metal noble y aumentar el rendimiento electrocatalítico en las distintas reacciones donde se evaluaron, la mejora en la actividad catalítica se debió principalmente a un mayor porcentaje de dispersión de las especies Pd^0 y M^{2+} (Espectroscopia de fotoemisión de rayos X) y grandes áreas superficiales que permitieron al catalizador mejorar el transporte de moléculas.

Para enfocar la aplicación de los aerogeles hacia sistemas electroquímicos de producción de hidrogeno, se elaboraron aerogeles únicamente de metales de transición mediante la ruta de síntesis de los aerogeles Pd-M, esto para aprovechar las propiedades de los metales de transición para favorecer reacción de oxidación de urea, amonio y oxígeno. Estos aerogeles libres de metales preciosos mostraron tamaños de partículas de Angstroms donde la morfología de los materiales se puede definir como interatómica, de grandes áreas superficiales y especies dominantes Ni^{2+} y Fe^{2+} donde los enlaces entre metales Ni-Co y Fe-Ni mostraron se potenciadores de las reacciones analizadas.

El desarrollo y aplicación electroquímica de estos aerogeles metálicos M-M abren paso a una interesante aplicación de estos hacia potenciar celdas de combustibles a partir de metales preciosos y de transición, disminuyendo considerablemente la cantidad de catalizador en los electrodos y promoviendo las reacciones a mayores densidades de corriente en sistemas microfluidicos.

ABSTRACT

The present work shows an ultrafast synthesis route using microwaves to obtain metallic aerogels. In the first stage of the development of these materials, transition metals were incorporated into the atomic structure of Palladium, where metallic alloys were obtained between this noble metal and Fe, Ni and Co denominated as Pd-M aerogels. These hybrid aerogels were used as catalysts in microfluidic cells for different reactions: Oxygen evolution reaction (OER), oxygen reduction reaction (ORR), urea oxidation reaction (UOR) and reaction oxidation of ammonium (AOR). As an application in electrochemical energy conversion systems, the catalytic activity of Pd-M aerogels (M=Fe, Ni, Co) was evaluated in microfluidic fuel cells that used ethanol and formic acid as fuel, where Pd-Ni aerogels and Pd-Co turned out to be mostly active in the use of these fuels, exceeding the activity of Pd alone by 3 times. The combination of palladium with the transition metal allows to reduce the noble metal dependence and increase the electrocatalytic performance in the different reactions where they were evaluated. The improvement in the catalytic activity was mainly due to a higher percentage of dispersion of the Pd^0 and M^{2+} species. (X-ray photoemission spectroscopy) and large surface areas that allowed the catalyst to improve the transport of studied molecules.

To focus the application of aerogels towards electrochemical hydrogen production systems, aerogels were made only of transition metals through the synthesis route of Pd-M aerogels, this to take advantage of the properties of transition metals to favor the oxidation reaction of urea, ammonium and oxygen. These aerogels free of precious metals showed particle sizes of angstroms where the morphology of the materials can be defined as interatomic, with large surface areas and dominant species Ni^{2+} and Fe^{2+} where the bonds between Ni-Co and Fe-Ni metals showed enhancements of the reactions analyzed.

The development and electrochemical application of these M-M metallic aerogels open the way to an interesting application of these towards powering fuel cells from precious and transition metals, considerably reducing the amount of catalyst in the electrodes and promoting reactions at higher current densities in microfluidic systems.

PROLOGO

La presente tesis consta de 4 capítulos principales, los cuales explican de manera detallada como surge esta propuesta de investigación hasta su desarrollo: los aerogeles metálicos como catalizadores en celdas microfluídicas. En la primera parte se realiza un planteamiento a partir de la literatura a modo de defender la novedad en la aplicación de los aerogeles, seguido de un segundo capítulo donde se propone un método solgel y un secado rápido por liofilización para garantizar las características fisicoquímicas típicas de los aerogeles. En el tercer capítulo se defiende la actividad catalítica de los aerogeles híbridos Pd-M frente al aerogeles de Pd por sí solo y catalizadores comerciales en distintas reacciones en celdas microfluídicas, donde se aprecia que la incorporación en pequeñas proporciones del metal de transición potencializa el uso de combustibles como el etanol y el ácido fórmico, sin embargo, la mayor proporción de los metales de transición parece ser provechosa hacia otros procesos electroquímicos por que la última sección de esta tesis muestra aplicaciones de aerogeles libres de metales preciosos en celdas que generan y aprovechan el hidrogeno, dando una perspectiva verde de estos catalizadores. Finalmente se anexan otros trabajos de investigación relacionados otros con sistemas electroquímicos, donde se realizaron aportaciones valiosas en cuanto al desarrollo científico de los materiales aplicados

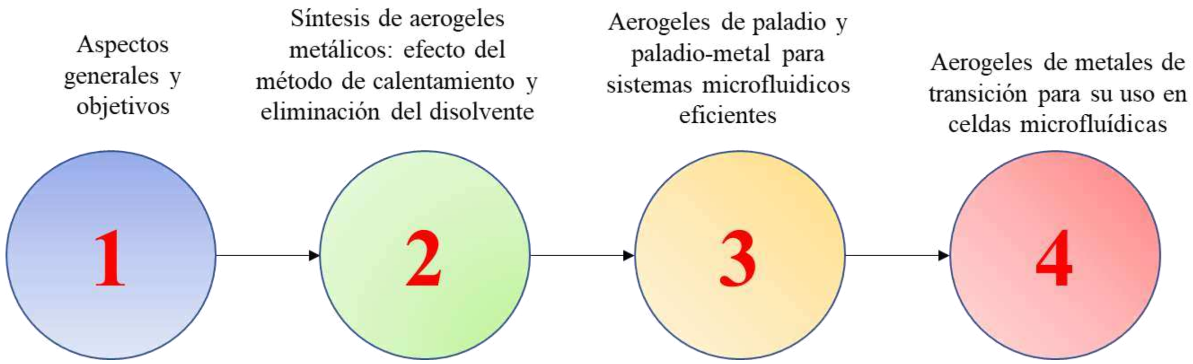

INDICE

INDICE

INDICE

ANEXOS

CAPÍTULO 1

ASPECTOS GENERALES Y OBJETIVOS

ANTECEDENTES

Desde su primera aparición en 2002, las celdas de combustible microfluídicas (MFC) han recibido una gran atención en las últimas dos décadas por su alta utilidad en la electrónica portátil(Moreno-zuria et al., 2017). En la tecnología de microceldas de combustible se utilizan microfluidos como electrolito lo que les da gran ventaja en comparación con las celdas convencionales ya que, a diferencia de estas, en las microceldas no es necesario utilizar una membrana de intercambio ya que la barrera entre catolito y anolito funcionan como una. Hasta la fecha, se han diseñado diferentes configuraciones de MFC (Fig.1.1), donde el tipo de flujo afecta directamente en la eficiencia de la celda.

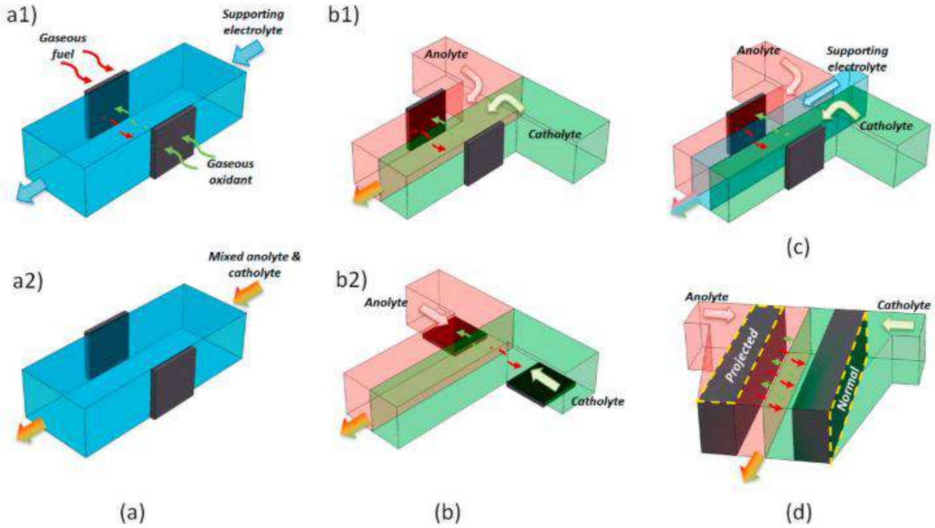

Fig. 1.1 Diferentes configuraciones para MFC: (a) Flujo simple: con reactante externo (a1) mezcla de reactantes (a2); (b) doble flujo: configuración co-flujo (b1) o contraflujo (b2); (c) triple flujo (d) flujo 3D a través de electrodos usado en un contraflujo (Wang et al., 2021).

También se han evaluado diferentes tipos de combustibles tales como especies de vanadio, hidrógeno, hidrocarburos, peróxido de hidrógeno, borohidruro y compuestos nitrogenados, cada uno de los cuales tiene sus ventajas e inconvenientes específicos (Wang et al., 2021). Para optimizar la potencia de salida y su utilización se han desarrollado continuamente catalizadores para diferentes combustibles(Eftekhari, 2017).

La tecnología de materiales nanoestructurados ha sido incorporada en la optimización de los electrodos de estos dispositivos (Eftekhari & Fang, 2017). Esto se debe a que ciertas características en la nanoescala son altamente significativas. Los materiales desarrollados para estos dispositivos están habitualmente basados en metales conductores, semiconductores o los materiales cerámicos (Zanella, 2012) y el tipo de catalizador utilizado afecta directamente a las reacciones involucradas y por lo tanto al desempeño de la celda.

La innovación de los nanomateriales en el campo de las celdas de combustible microfluídicas ha tenido un avance significativo donde destacan principalmente los metales nobles como Ru, Ir, Pt y Pd (Garrick et al.; Gonda et al.; Dinesh and Saraswathi; Dominguez-Quintero et al.), aunque de igual manera también algunos semiconductores como Fe, Ni, Co (Durano et al., 2017; Huo & Wei, 2009; Li et al., 2014; Ni et al., 2015; Ortiz-Ortega et al., 2014; H. Wu et al., 2018; Yan et al., 2010) han demostrados ser una opción competitiva. Sin embargo, por sus propiedades, su comportamiento y su resistencia a la corrosión, los metales nobles siguen aún dominando este tipo de aplicaciones catalíticas.

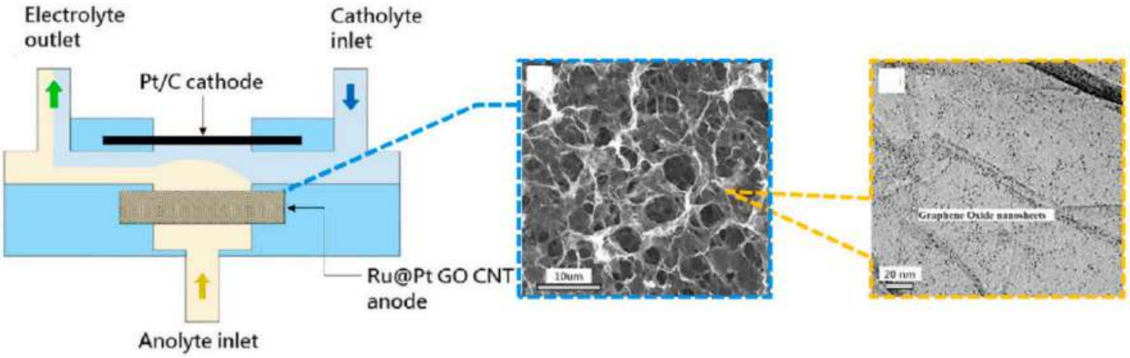

Fig. 1.2 MFC de flujo ortogonal con ánodo de flujo 3D basado en aerogel de Rt y Pt sobre grafeno (Kwok et al., 2018)

Los aerogeles nanoestructurados son una alternativa fiable para incorporarse en dispositivos microfluídicos ya que han tenido un gran éxito en aplicaciones electroquímicas (Heinrichs et al., 1997; Shi et al., 2018). Los aerogeles son una clase excepcional de materiales que son interesantes para varias aplicaciones de alto rendimiento gracias a sus extraordinarias propiedades físicas, tales como porosidad extremadamente alta, área superficial considerablemente mayor que otros sólidos tradicionales, y métodos de síntesis muy versátiles(Smirnova & Gurikov, 2018). Estos materiales presentan una gran variabilidad de formas ya que pueden obtenerse desde material en polvo, películas laminares, monolitos, cilindros, microesferas, discos o mediante el uso de técnicas de moldeo (Gu & Jana, 2017; Maleki, 2016; Vareda, Lamy-Mendes, & Duraes, 2018). Como ejemplos se han sintetizado nanocompuestos en aerogeles de SiO_2 (Heinrichs et al., 1997) y Fe_2O_3 (Huggins et al., 2010). Estos materiales han presentado buenos resultados en desionización capacitiva y han realzado la capacitancia electroquímica en supercapacitores (Z. Wu et al., 2023) y la oxidación de combustibles como el etanol (Abbas et al., 2017).

De forma similar y con la previa incorporación de surfactantes se han obtenido catalizadores de Pt soportados en aerogeles de carbono con alta actividad catalítica (Gonda et al., 2014) y se ha incorporado aerogeles a MFC como en el caso de Kwok et al. (Fig. 1.2).

Las aplicaciones emergentes más prometedoras para estos materiales son el almacenamiento de gases, tales como hidrógeno y metano, almacenamiento de la energía en supercondensadores de doble capa eléctrica, sensores, la desalinización mediante desionización capacitiva, su uso como soportes de catalizador en las pilas de combustible, baterías de ion-litio, entre otras (Heinrichs et al., 1997; Huggins et al., 2010; Sashkina et al., 2018; Zhang et al., 2018). Un área de oportunidad en el desarrollo de aerogeles son las aleaciones metálicas las cuales pueden resultar una alternativa interesante para su aplicación en celdas de combustible microfluídicas, ya que actualmente existen varias propuestas de mezclas metálicas como catalizadores en estos dispositivos, los aerogeles pueden ser un área de oportunidad al reducir las cantidades utilizadas en los electrodos, y mejorando significativamente el desempeño de las reacciones anódicas y catódicas debido a la alta disponibilidad de sitios activos. El análisis de la aplicación de aerogeles metálicos de distintas combinaciones de metales M-M, serán analizados en celdas microfluídicas electroquímicas como objetivo general de este trabajo utilizando calentamiento por microondas, el cual brindara ventajas tales como: mejora en la cinética de reacción el proceso de síntesis, ahorro de energía, calidad cristalina y aumento de sitios electroquímicamente activos.

JUSTIFICACIÓN

La necesidad de desarrollar tecnologías de producción de energía limpia, ha tenido un gran auge en los últimos años (Corbo et al., 2011). Diversas técnicas se han empleado para obtener energía verde, entra las cuales se encuentran los combustibles fósiles la eólica, la solar, hidrotérmica, hidrogeno, entre otras. El desarrollo de estas tecnologías depende en gran medida del dispositivo de procesamiento de energía, uno de los dispositivos de conversión de energía son las celdas de combustible, las cuales tienen aplicaciones a gran escala y en microescala. Uno de los dispositivos portátiles para generación de energía limpia es la celda de combustible microfluidica, cuyo desempeño depende en gran medida de los catalizadores utilizados en sus electrodos, además estas celdas brindan grandes ventajas y reducen costos de fabricación (Wang et al., 2021). Los materiales utilizados en los electrodos de estas celdas deben poseer ciertas características que permitan una alta eficiencia y larga durabilidad en los dispositivos. Los aerogeles metálicos constituyen un material idóneo para utilizarse en este campo debido a sus propiedades fisicoquímicas que han demostrado ser altamente competitivas en comparación con los actuales catalizadores nanoestructurados, fundamentalmente porque cuentan con mayor número y dispersión de centros activos que favorecen las reacciones electroquímicas (Maleki, 2018). Por lo tanto, se requiere que los materiales elaborados en el presente trabajo permitan la mejora del desempeño electroquímico de la celda, y minimicen la cantidad de metal precioso utilizado al mezclarse con un metal de transición para disminuir la dependencia de metales nobles además de aumentar la eficiencia y durabilidad de la celda de combustible.

DESCRIPCIÓN DEL PROBLEMA

El desarrollo de energías libres de combustibles fósiles ha dado paso a la creación de un sin número de dispositivos de conversión de energía química en energía eléctrica, como lo son las plantas de energía eólica, energía fotovoltaica y las celdas de combustible (Wang et al., 2018). Entre los dispositivos portátiles innovadores se encuentran las celdas de combustibles microfluídicas, las cuales son una alternativa altamente funcional en la conversión de energía por vía electroquímica (Eftekhari & Fang, 2017). Estos dispositivos son autosuficientes, sin embargo, su desempeño depende en gran parte de los catalizadores utilizados en los electrodos que componen el sistema de generación de energía. Los materiales más utilizados como catalizadores en estas celdas son principalmente de metales nobles tales como el Ir, Pt, Ru y Pd. A pesar de los esfuerzos por desarrollar catalizadores de metales no preciosos estos siguen dominando el área de catálisis debido a su alta estabilidad a la corrosión y alto desempeño electroquímico (Fan et al., 2018). Actualmente los catalizadores de metales de transición han demostrado un desempeño similar al de catalizadores basados en metales nobles, sin embargo, la resistencia a la corrosión de estos aún está por debajo de los metales como Pd, Pt, Au (Gralec & Lewera, 2016). Una alternativa para continuar utilizando metales nobles es el diseño de aerogeles de baja densidad, que por sus propiedades fisicoquímicas proporcionan los sitios activos para que ocurran las reacciones de oxido-reducción con bajas cantidades de catalizador. La combinación en un aerogel de metal abundante y un metal noble podría ser la solución hacia un proceso eficiente de generación de energía. Esta alternativa aún no ha sido investigada en celdas de combustible microfluídicas y de ser probada su eficacia resultaría en un avance significativo hacia el mejoramiento del desempeño de estos dispositivos.

Este proyecto busca mejorar el rendimiento de celdas de combustible microfluídicas a través de la combinación de un metal abundante en la tierra (Fe, Ni, Co), en la nanoestructura de un aerogel con un

metal noble dará como resultado una estructura mesoporosa con grandes áreas superficiales (+20 m^2 g^{-1}) las cuales aseguran los sitios activos con barreras energéticas adecuadas para ser electrocatalizador eficiente en procesos de generación de energía.

HIPÓTESIS

Los aerogeles y espinelas de combinaciones metálicas M-M (Pd, Co, Ni, Fe, Mn) pueden ser electrocatalizadores eficientes en dispositivos microfluídicos para procesos de conversión de energía, debido a que presentan sitios activos con potencial energético similar al que aportan los catalizadores comerciales basados en Pd/C y Pt/C.

OBJETIVO GENERAL

Evaluar el rendimiento en la generación y conversión de energía de celdas de combustible microfluídicas usando aerogeles nanoestructurados tipo M-M (M=Pd, Co, Ni, Fe, Mn).

OBJETIVOS ESPECÍFICOS

1. Sintetizar aerogeles M-M (M=Pd, Co, Ni, Fe) para la obtención de aerogeles nanoestructurados empleando la metodología sol-gel.
2. Caracterizar la composición química y estructural, morfología, y porosidad de los materiales nanoestructurados mediante diversas técnicas fisicoquímicas.

3. Caracterizar electroquímicamente los aerogeles nanoestructurados para determinar sus propiedades electrocatalíticas.
4. Evaluar la generación y conversión de energía de los aerogeles sintetizados en dispositivos microfluídicos.

Referencias

Abbas, S. A., Iqbal, M. I., Kim, S. H., & Jung, K. D. (2017). Catalytic Activity of Urchin-like Ni nanoparticles Prepared by Solvothermal Method for Hydrogen Evolution Reaction in Alkaline Solution. *Electrochimica Acta*, *227*, 382–390. https://doi.org/10.1016/j.electacta.2017.01.039

Corbo, P., Migliardini, F., & Veneri, O. (2011). Hydrogen Fuel Cells for Road Vehicles. In *Control*. Springer London. https://doi.org/10.1007/978-0-85729-136-3

Dinesh, B., & Saraswathi, R. (2016). Enhanced performance of Pt and Pt–Ru supported PEDOT–RGO nanocomposite towards methanol oxidation. *International Journal of Hydrogen Energy*, *41*(31), 13448–13458. https://doi.org/10.1016/j.ijhydene.2016.06.169

Domı́nguez-Quintero, O., Martı́nez, S., Henrı́quez, Y., D'Ornelas, L., Krentzien, H., & Osuna, J. (2003). Silica-supported palladium nanoparticles show remarkable hydrogenation catalytic activity. *Journal of Molecular Catalysis A: Chemical*, *197*(1–2), 185–191. https://doi.org/10.1016/S1381-1169(02)00583-6

Durano, M. M., Tamboli, A. H., & Kim, H. (2017). Cobalt oxide synthesized using urea precipitation method as catalyst for the hydrolysis of sodium borohydride. *Colloids and Surfaces A: Physicochemical and Engineering Aspects*, *520*, 355–360. https://doi.org/10.1016/j.colsurfa.2017.02.005

Eftekhari, A. (2017). Tuning the electrocatalysts for oxygen evolution reaction. *Materials Today Energy*, *5*, 37–57. https://doi.org/10.1016/j.mtener.2017.05.002

Eftekhari, A., & Fang, B. (2017). Electrochemical hydrogen storage: Opportunities for fuel storage, batteries, fuel cells, and supercapacitors. *International Journal of Hydrogen Energy*, *42*(40), 25143–25165. https://doi.org/10.1016/j.ijhydene.2017.08.103

Fan, H., Cheng, M., Wang, L., Song, Y., Cui, Y., & Wang, R. (2018). *Nano Energy Extraordinary electrocatalytic performance for formic acid oxidation by the synergistic effect of Pt and Au on carbon black*. *48*(March), 1–9.

Garrick, T. R., Diao, W., Tengco, J. M., Stach, E. A., Senanayake, S. D., Chen, D. A., Monnier, J. R., & Weidner, J. W. (2016). The Effect of the Surface Composition of Ru-Pt Bimetallic Catalysts for Methanol Oxidation. *Electrochimica Acta*, *195*, 106–111. https://doi.org/10.1016/j.electacta.2016.02.134

Gonda, M., Ohshima, M. A., Kurokawa, H., & Miura, H. (2014). Toluene hydrogenation over Pd and Pt catalysts as a model hydrogen storage process using low grade hydrogen containing catalyst inhibitors. *International Journal of Hydrogen Energy*, *39*(29), 16339–16346. https://doi.org/10.1016/j.ijhydene.2014.07.158

Gralec, B., & Lewera, A. (2016). *Applied Catalysis B : Environmental Catalytic activity of unsupported Pd-Pt nanoalloys with low Pt content towards formic acid oxidation*. *192*, 304–310.

Gu, S., & Jana, S. C. (2017). Open cell aerogel foams with hierarchical pore structures. *Polymer*, *125*, 1–9. https://doi.org/10.1016/j.polymer.2017.07.085

Heinrichs, B., Noville, F., & Pirard, J. P. (1997). Pd/SiO2-cogelled aerogel catalysts and impregnated aerogel and xerogel catalysts: Synthesis and characterization. *Journal of Catalysis*, *170*(2), 366–376. https://doi.org/10.1006/jcat.1997.1772

Huggins, F. E., Bali, S., Huffman, G. P., & Eyring, E. M. (2010). Iron-oxide aerogel and xerogel catalyst formulations: Characterization by 57Fe M??ssbauer and XAFS spectroscopies. *Spectrochimica Acta - Part A: Molecular and Biomolecular Spectroscopy*, *76*(1), 74–83. https://doi.org/10.1016/j.saa.2010.02.049

Huo, J., & Wei, M. (2009). Characterization and magnetic properties of nanocrystalline nickel ferrite synthesized by hydrothermal method. *Materials Letters*, *63*(13–14), 1183–1184. https://doi.org/10.1016/j.matlet.2009.02.024

Kwok Y, Wang Y, Tsang AC, L. D. (2018). Graphene-carbon nanotube composite aerogel with Ru@ Pt nanoparticle as a porous electrode for direct methanol microfluidic fuel cell. *Appl Energy*, *217*, 258–65.

Li, D., Sun, Y., Gao, P., Zhang, X., & Ge, H. (2014). Structural and magnetic properties of nickel ferrite nanoparticles synthesized via a template-assisted sol–gel method. *Ceramics International*, *40*(10), 16529–16534. https://doi.org/10.1016/j.ceramint.2014.08.006

Maleki, H. (2016). Recent advances in aerogels for environmental remediation applications: A review. *Chemical Engineering Journal*, *300*, 98–118. https://doi.org/10.1016/j.cej.2016.04.098

Maleki, H., & Hüsing, N. (2018). Applied Catalysis B : Environmental Current status , opportunities and challenges in catalytic and photocatalytic applications of aerogels : Environmental protection aspects. *“Applied Catalysis B, Environmental,” 221*, 530–555. https://doi.org/10.1016/j.apcatb.2017.08.012

Moreno-zuria, A., Ortiz-ortega, E., & Gurrola, M. P. (2017). *Evolution of microfluidic fuel stack design as an innovative alternative to energy production. 2*. https://doi.org/10.1016/j.ijhydene.2017.05.185

Ni, D., Lin, Z., Xiaoling, P., Xinqing, W., & Hongliang, G. (2015). Preparation and Characterization of Nickel-Zinc Ferrites by a Solvothermal Method. *Rare Metal Materials and Engineering*, *44*(9), 2126–2131. https://doi.org/10.1016/S1875-5372(16)30010-8

Ortiz-Ortega, E., Goulet, M. A., Lee, J. W., Guerra-Balcázar, M., Arjona, N., Kjeang, E., Ledesma-García, J., & Arriaga, L. G. (2014). A nanofluidic direct formic acid fuel cell with a combined flow-through and air-breathing electrode for high performance. *Lab on a Chip*, *14*(24), 4596–4598. https://doi.org/10.1039/c4lc01010h

Sashkina, K. A., Gurikov, P. A., Ayupov, A. B., Smirnova, I., & Parkhomchuk, E. V. (2018). Zeolite/silica aerogel composite monoliths and microspheres. *Microporous and Mesoporous Materials*, *263*(December 2017), 106–112. https://doi.org/10.1016/j.micromeso.2017.12.010

Shi, Q., Zhu, C., Tian, M., Su, D., Fu, M., Engelhard, M. H., Chowdhury, I., Feng, S., Du, D., & Lin, Y. (2018). Ultrafine Pd ensembles anchored-Au2Cu aerogels boost ethanol electrooxidation. *Nano Energy*, *53*(June), 206–212. https://doi.org/10.1016/j.nanoen.2018.08.047

Smirnova, I., & Gurikov, P. (2018). Aerogel production: Current status, research directions, and future opportunities. *Journal of Supercritical Fluids*, *134*(December 2017), 228–233. https://doi.org/10.1016/j.supflu.2017.12.037

Vareda, J. P., Lamy-Mendes, A., & Durães, L. (2018). A reconsideration on the definition of the term aerogel based on current drying trends. *Microporous and Mesoporous Materials*, *258*, 211–216. https://doi.org/10.1016/j.micromeso.2017.09.016

Wang, N., Zheng, H., Zhang, W., & Cao, R. (2018). Mononuclear first-row transition-metal complexes as molecular catalysts for water oxidation. *Chinese Journal of Catalysis*, *39*(2), 228–244. https://doi.org/10.1016/S1872-2067(17)63001-8

Wang, Y., Luo, S., Kwok, H. Y. H., Pan, W., Zhang, Y., Zhao, X., & Leung, D. Y. C. (2021). Microfluidic fuel cells with different types of fuels : A prospective review. *Renewable and Sustainable Energy Reviews*, *141*(February), 110806. https://doi.org/10.1016/j.rser.2021.110806

Wu, H., Xiao, W., Guan, C., Liu, X., Zang, W., Zhang, H., Ding, J., Feng, Y. P., Pennycook, S. J., & Wang, J. (2018). Hollow Mo-doped CoP nanoarrays for efficient overall water splitting. *Nano Energy*, *48*(January), 73–80. https://doi.org/10.1016/j.nanoen.2018.03.034

Wu, Z., Guo, C., Lu, Z., Yuan, C., Xu, Y., & Dai, L. (2023). A facile brushing method for constructing all-in-one high performance flexible supercapacitor with ordinary carbon materials. *Journal of Energy Storage*, *67*(December 2022), 107531. https://doi.org/10.1016/j.est.2023.107531

Yan, W., Jiang, W., Zhang, Q., Li, Y., & Wang, H. (2010). Structure and magnetic properties of nickel-zinc ferrite microspheres synthesized by solvothermal method. *Materials Science and Engineering B: Solid-State Materials for Advanced Technology*, *171*(1–3), 144–148. https://doi.org/10.1016/j.mseb.2010.03.088

Zanella, R. (2012). Metodologías para la síntesis de nanopartículas: controlando forma y tamaño. *Www.Mundonano.Unam.Mx*, *5*(1), 69–81. www.mundonano.unam.mx

Zhang, S., Feng, J., Feng, J., Jiang, Y., & Ding, F. (2018). Carbon aerogels by pyrolysis of TEMPO-oxidized cellulose. *Applied Surface Science*, *440*, 873–879. https://doi.org/10.1016/j.apsusc.2018.01.252

CAPÍTULO 2

SÍNTESIS DE AEROGELES METÁLICOS: EFECTO DEL MÉTODO DE CALENTAMIENTO Y ELIMINACIÓN DEL DISOLVENTE

2.1 METODOLOGÍA SOL-GEL

La manipulación de las condiciones de síntesis permite el control racional del tamaño y la forma de las partículas y provee los medios para adaptar las propiedades de los materiales sintéticosa una aplicación específica. Uno de los métodos más empleados hoy en día es el método sol-gel, el cual es un proceso de síntesis altamente utilizado en la elaboración de nanomateriales (Du et al., 2019) debido a que tiene varias ventajas sobre otros métodos como son: su potencial para producir compuestos de alta pureza, su capacidad para reducir las temperaturas de síntesis y su potencial para controlar el tamaño de nanopartículas (Zanella, 2012). Para entender la forma en que funciona este método de síntesis, es necesario conocer el proceso que tiene lugar y sus distintas etapas. Para ello primeramente es necesario analizar los "soles" como un factor independiente, estos son dispersiones de partículas coloidales en un líquido con diámetros entre 1 y 100 nm, aunque este rango puede variar con el cambio de las condiciones del sistema como presión, temperatura, viscosidad del solvente, entre otras. Una vez que el "sol" es formado, las partículas sólidas empiezan a formar agregados los cuales se hidrolizan y polimerizan por condensación, formando retículos en donde el solvente queda encapsulado, generando un medio viscoso conocido como "gel", el cual se caracteriza por ser una red polimérica interconectada, las cuales tienen en promedio longitudes más grandes que un micrómetro (Du et al., 2019; Titirici et al., 2006). Estos geles pueden adquirir diferentes estructuras según el tratamiento posterior a la formación del sol, los tratamientos utilizados para la formación de los geles incluyen utilizarlos para recubrimientos, hilado y la formación de sólidos pulverulentos o en forma de monolito.

Estos tratamientos les dan a los geles estructuras únicas correspondientes a su tratamiento previo, lo que hace al método sol-

gel un método muy versátil para realizar el diseño del material sintético. Finalmente, los geles son sometidos a procesos de eliminación del solvente para obtener el producto final.

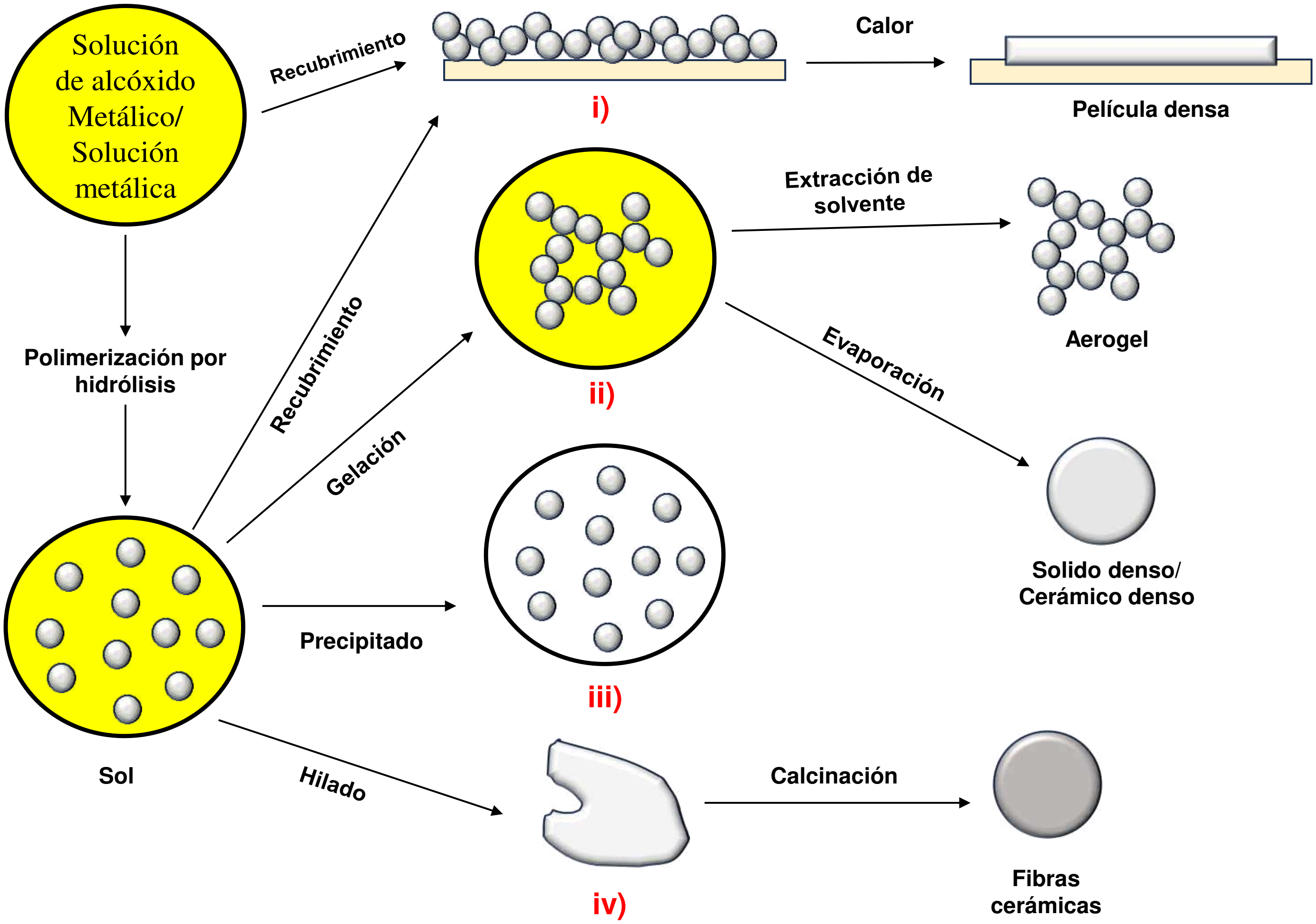

Fig. 2.1 Estructuración del método sol-gel.

Actualmente los geles pueden ser clasificados en cuatro categorías: i) estructuras laminares ordenadas; ii) redes poliméricas-metálicas covalentes completamente desordenadas; iii) redes poliméricas formadas a través de agregación física, predominantemente desordenadas y iv) estructuras desordenadas (ver Fig 2.1). La presente Tesis Doctoral se dedicó a obtener geles de naturaleza metálica que se sometieron a un proceso de gelación y extracción de solvente como se muestra en la Figura 2.1 siguiendo la ruta ii). A continuación se describen específicamente los procesos que se llevaron a cabo durante la obtención de estos aerogeles.

2.1.1. Soluciones precursoras

En trabajos realizados en la literatura de nanomateriales metálicos se usan comúnmente sales precursoras que contienen los metales que conformaran la celda unidad de los productos finales. En el caso de los aerogeles de Pd se utilizó $PdCl_2$ debió a su fácil disociación y una reacción de reducción in situ, la cual es una de las estrategias más comúnmente encontradas en la literatura para la preparación de aerogeles de metales nobles (Henning et al., 2017; Moussaoui et al., 2017). Esta ruta es esencialmente una síntesis de un solo paso que acorta y simplifica significativamente la obtención de aerogeles metálicos a partir de sales que contiene cloro como el $PdCl_2$. Así, los aerogeles se sintetizan mezclando la sal metálica con un agente reductor fuerte, típicamente $NaBH_4$, $LiAlH_4$, hidracina, citrato de sodio, ácido tánico o, en nuestro caso, de ácido glioxílico (combinado con una base). Este último ha sido seleccionado debido a su fácil manipulación y efectividad en la reacción de reducción al combinarse con carbonato de sodio como base. Los dos reactivos conducen a la reducción de la sal precursora a Pd^{2+} a Pd^0 a una temperatura en torno a 65 °C, una temperatura relativamente baja, y un tiempo de reacción de 2 horas.

La reacción que tiene lugar, comienza con la desproporción del ácido glioxílico en un medio básico produciendo ácido oxálico:

$$2\ OCHCOOH + H_2O \rightarrow HOCH_2COOH + HOOC\text{–}COOH \qquad \text{(Ec 2.1)}$$

2.1.2. Precipitación

Un precipitado es el sólido que se produce en una disolución por efecto de una reacción y que se deposita por efecto de la gravedad. En este caso ocurre debido a la reducción del cloruro de paladio, donde las partículas metálicas se agrupan y comienzan a formar una estructura de gel. Para que esto ocurra, el ácido oxálico formado en la reacción R1 reacciona con el $PdCl_2$ produciendo oxalato de paladio, cloruro de sodio y acido carbónico según la reacción:

$$HOOC\text{–}COOH + PdCl_2 + Na_2CO_3 \rightarrow Pd\ (COO)_2 + 2\ NaCl + H_2CO_3 \qquad \text{(Ec. 2.2)}$$

En estas condiciones, las nanopartículas de Pd en estado sol tienden a interaccionar hasta que la estabilidad de la solución se ve comprometida y pasa a un estado de gel. En ese momento de la reacción, el sistema pierde fluidez y la viscosidad se hace muy grande. Finalmente, el paladio se reduce completamente a paladio metálico, hasta que todo el Pd presente en la solución se agrupa, formando dos fases en la solución: una liquida y otra sólida que precipita. Esta reacción se muestra a continuación:

$$Pd\ (COO)_2 + OCHCOOH + 2\ OH^- \rightarrow Pd + 2\ C_2O_4^{2-} + H_2O + 2\ H^+ \qquad \text{(Ec. 2.3)}$$

2.1.3. Entrecruzamiento

Esta etapa de entrecruzamiento es llamada de este modo por ser la etapa donde las nanopartículas interaccionan entre sí y se forman enlaces entre ellas (Bi et al., 2015).

Las partículas no se disuelven en el disolvente, sino que se producen entrecruzamientos que refuerzan la estructura del material final. El tiempo de entrecruzamiento puede variar mucho dependiendo de las variables del proceso (Guo et al., 2020; Sashkina et al., 2018).

El hidrogel obtenido, se lava finalmente varias veces. Utilizando agua desionizada intercambiando cuidadosamente el sobrenadante para garantizar la integridad del hidrogel formado, pero minimizando la presencia de impurezas (sales remanentes y materia orgánica). materia). Finalmente, el disolvente remanente se elimina para obtener el producto sólido.

2.2. INFLUENCIA DEL MÉTODO DE CALENTAMIENTO

En los procesos de obtención de nanomateriales normalmente se emplean métodos de calentamiento convencionales que inducen el calor por convención y conducción.

2.2.1 Tipos de calentamiento

El calentamiento por convección es el tipo de calentamiento más utilizado en la literatura, y cuya fuente de emisión suele ser un horno convencional o estufa. Este tipo de transferencia de calor ocurre desde una partícula a otra, de un lugar a otro, por el movimiento de fluidos, en este caso la solución precursora con los reactivos iniciales. Por lo que se asume que en este caso el calor se transmite desde el exterior hacia el interior del recipiente que contiene la mezcla de reacción (Samir De et al., 2022), produciendose gradientes de temperatura.

A diferencia de este tipo de calentamiento la radiación microondas calienta al mismo tiempo todo el volumen de la solución precursora, minimizando los gradientes de temperatura. En esta Tesis Doctoral, se comparó la sintesis de aerogeles mediante calentamiento convencional y microondas, para evaluar el efecto de cada uno de ellos en el material final obtenido.

2.2.2 Efecto de la radiación microondas

La radiación microondas es un tipo de radiación electromagnética. En el espectro electromagnético, las microondas se encuentran entre la radiación infrarroja y las ondas de radio, por lo que no son una radiación ionizante. Las microondas interaccionar con ciertas ciertas sustancias, fundamentalmente compuestos polares, provocando calentamiento al hacer vibrar sus átomos debido al campo electromagnético.

Al aplicar radiación de microondas la solución se calienta uniformemente ya que los distintos compuestos presentes en la mezcla precursora (agua y reactivos) absorven microondas, lo cual implica la vibración y calentamiento de todos ellos a la vez. Se trata, por lo tanto, de un calentamiento volumétrico.

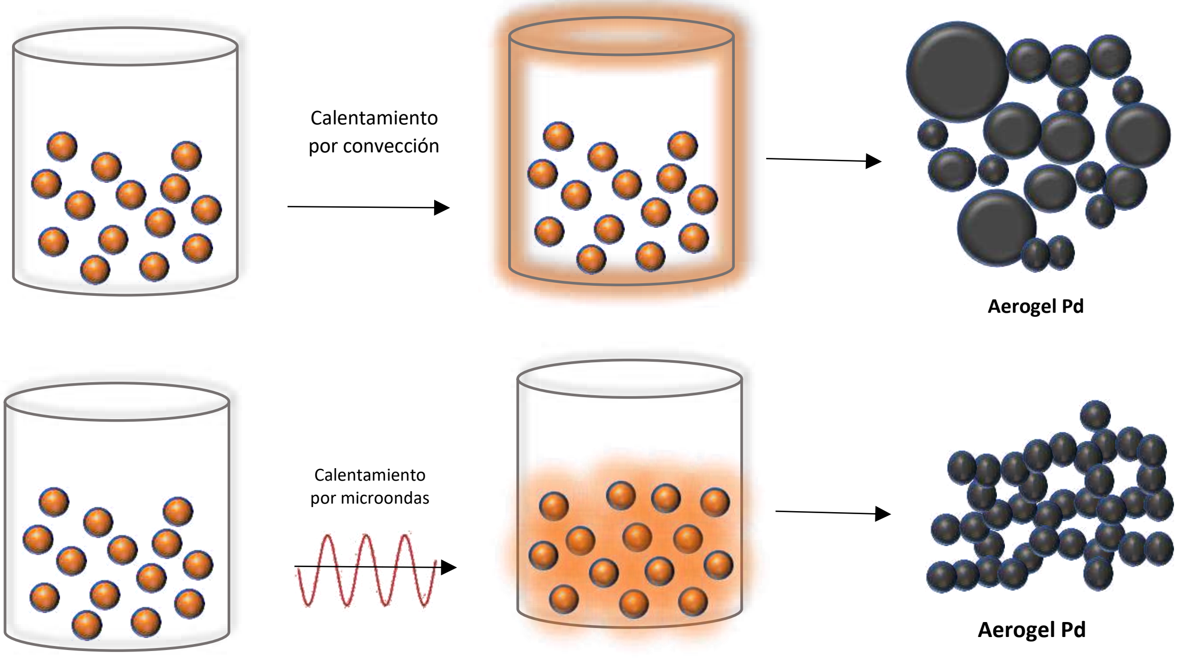

Fig. 2.2 Efecto del tipo de calentamiento sobre la formación de aerogeles metálicos.

Este tipo de calentamiento tiene tambien influencia en las reacciones que tienen lugar, provocando diferencias en los materiales formados.

La síntesis asistida con microondas provocó un efecto en el tamaño de las nanopartículas formadas, ya que el calentamiento es más homogéneo, formándose nanopartículas de menor tamaño y más homogéneas en comparación al calentamiento por convección. Otras propiedades fisicoquímicas tambíen se vieron influenciadas, como un favorecimiento del estado Pd^0 y un área superficial mayor en comparación con el calentamiento convencional.

2.3. INFLUENCIA DEL MÉTODO DE SECADO

2.3.1. Tipos de secado

El proceso de secado consiste en la eliminación del solvente o medio de reacción utilizado, tras finalizar las reacciones de síntesis. Existen distintas alternativas para el secado de un gel: secado en condiciones supercríticas, secado en condiciones criogénicas y secado por simple evaporación. Estos métodos de secado se han empleado en la obtención de nanopartículas como peroskitas, espinelas, óxidos metálicos y aleaciones (Chen et al., 2015; Qiao & Swihart, 2017; Roh et al., 2023). A pesar de ser el método de secado más económico, el secado por evaporación del disolvente es el más agresivo, ya que el paso de líquido a gas genera unas tensiones superficiales en la estructura porosa que puede provocar cierto colapso de la estructura. El secado supercrítico es una opción que evita esta interfase líquido/vapor, y por lo tanto evita las tensiones superficiales, ya que la eliminación del disolvente se realiza en condiciones supercríticas (Wen et al., 2016).

Sin embargo, este tipo de secado es muy lento y costoso, puesto que es necesario trabajar a altas presiones y temperaturas para alcanzar el punto crítico del disolvente. Una vez que el disolvente se encuentra en condiciones supercríticas, la presion y temperatura se decrece de forma controlada y lenta para poder eliminar el solvente como gas. En la obtención de aerogeles es común que se utilice este tipo de secado (Gu & Jana, 2017; Wen et al., 2016).

2.3.2. Efecto del proceso de liofilización

A pesar de que el método de secado por fluidos supercríticos es eficiente en la obtención de aerogeles, resulta un método complicado y altamente costoso. Para el secado de las muestras en esta Tesis Doctoral, se propuso el proceso de liofilización en el que el producto se enfría con N_2 líquido y una vez congelado, se reduce la presión y se aumenta la temperatura de forma controlada (Figura 2.3), de manera que el disolvente sublima, evitando la interfase líquido/vapor y por lo tanto evitando las tensiones superficiales que pueden comprometer la estructura del aerogel.

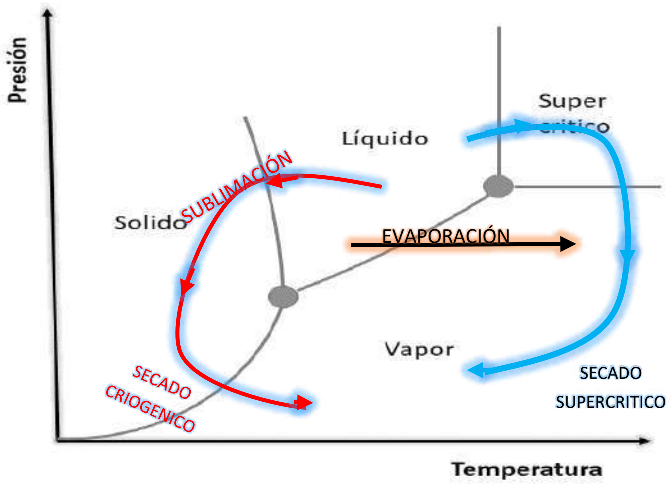

Fig. 2.3 Diagrama de fases de un fluido y esquematización de los tres tipos de secado posibles en la síntesis de aerogeles.

Esta forma de secado se conoce también como secado en frio y los aerogeles obtenidos por este método también pueden adquirir el nombre de aerogeles fríos o criogeles (Suenaga & Osada, 2019).

Publicación Científica y Patente de Invención

A continuación se incluye un articulo científico que recoge el trabajo realizado en esta Tesis Doctoral en relación con la síntesis en un solo paso de aerogeles de paladio. Se evaluaron distintos tipos de secado, e incluso se evaluó el efecto de la radiacion microondas en las distintas etapas de la sintesis. Se encontró que el calentamiento con microndas produce cambios fisicoquímicos en el aerogel de paladio que resultaron muy efectivos para su actividad electrocatalítica, especialmente en la electrooxidación de ácido fórmico.

La relevancia de los resulados obtenidos dio lugar a la solicitud de una Patente de Invención del procedimiento de síntesis, que también se incluye en esta memoria de Tesis Doctoral.

⑲ OFICINA ESPAÑOLA DE
PATENTES Y MARCAS

ESPAÑA

⑪ Número de publicación: **2 931 215**

㉑ Número de solicitud: 202130563

(51) Int. CI.:

B01J 23/38 (2006.01)

⑫ SOLICITUD DE PATENTE A1

㉒ Fecha de presentación:

17.06.2021

㊸ Fecha de publicación de la solicitud:

27.12.2022

(71) Solicitantes:

CONSEJO SUPERIOR DE INVESTIGACIONES
CIENTÍFICAS (CSIC) (50.0%)
C/ Serrano, nº 117
28006 Madrid (Madrid) ES y
UNIVERSIDAD AUTÓNOMA DE QUERÉTARO
(50.0%)

(72) Inventor/es:

ARENILLAS DE LA PUENTE, Ana;
MONTES MORÁN, Miguel Ángel;
RAMÍREZ MONTOYA, Luis Adrián;
MARTÍNEZ LÁZARO, Alejandra;
ARRIAGA HURTADO, Luis Gerardo y
LEDESMA GARCÍA, Janet

(74) Agente/Representante:

PONS ARIÑO, Ángel

(54) Título: **Procedimiento para la obtención de aerogeles metálicos, aerogeles así obtenidos y usos de los mismos**

(57) Resumen:

Procedimiento para la obtención de aeroqeles metálicos, aeroqeles así obtenidos y usos de los mismos.

La presente invención se refiere a un procedimiento para la preparación de un aerogel metálico basado en: a) la reducción de las sales metálicas para la formación de nanopartículas, b) seguida por el ensamblaje de las nanopartículas en redes tridimensionales para la obtención del hidrogel (gelación) y c) finalmente el secado del hidrogel para obtener el aerogel final, utilizándose un calentamiento por microondas durante las etapas de reducción y gelación. La invención también se refiere al aerogel obtenido por este procedimiento, así como al uso del mismo como electrocatalizador.

materials

MDPI

Article

Facile Synthesis of Unsupported Pd Aerogel for High Performance Formic Acid Microfluidic Fuel Cell

Alejandra Martínez-Lázaro [1], Luis A. Ramírez-Montoya [2], Janet Ledesma-García [1], Miguel A. Montes-Morán [3], Mayra P. Gurrola [4], J. Angel Menéndez [3], Ana Arenillas [3,*] and Luis G. Arriaga [5,*]

[1] División de Investigación y Posgrado, Facultad de Ingeniería, Universidad Autónoma de Querétaro, Santiago de Queretaro 76010, Mexico; AleeM.Lazaro@live.com (A.M.-L.); janet.ledesma@uaq.mx (J.L.-G.)

[2] Laboratory for Research on Advanced Processes for Water Treatment, Engineering Institute, Universidad Nacional Autónoma de México (UNAM), Blvd. Juriquilla 3001, Santiago de Queretaro 76230, Mexico; lar-75@hotmail.com

[3] Instituto de Ciencia y Tecnología del Carbono, INCAR-CSIC. Francisco Pintado Fe, 33011 Oviedo 26., Spain; miguel@incar.csic.es (M.A.M.-M.); angelmd@incar.csic.es (J.A.M.)

[4] CONACYT-Tecnológico Nacional de México/Instituto Tecnológico de Chetumal. Av. Insurgentes 330, David Gustavo Gutiérrez, Chetumal 77013, Mexico; mayra.pg@chetumal.tecnm.mx

[5] Centro de Investigación y Desarrollo Tecnológico en Electroquímica, Santiago de Queretaro 76703, Mexico

* Correspondence: aapuente@incar.csic.es (A.A.); larriaga@cideteq.mx (L.G.A.)

Abstract: In this work, unsupported Pd aerogel catalysts were synthesized for the very first time by using microwaves as a heating source followed by a lyophilization drying process and used towards formic acid electro-oxidation in a microfluidic fuel cell. Aerogels were also made by heating in a conventional oven to evaluate the microwave effect during the synthesis process of the unsupported Pd aerogels. The performance of the catalysts obtained by means of microwave heating favored the formic acid electro-oxidation with H_2SO_4 as the electrolyte. The aerogels' performance as anodic catalysts was carried out in a microfluidic fuel cell, giving power densities of up to 14 mW cm^{-2} when using mass loads of only 0.1 mg on a 0.019 cm^2 electrode surface. The power densities of the aerogels obtained by microwave heating gave a performance superior to the resultant aerogel prepared using conventional heating and even better than a commercial Pd/C catalyst.

Keywords: unsupported aerogel; microwave heating; microfluidic fuel cell; electro-oxidation

check for updates

Citation: Martínez-Lázaro, A.; Ramírez-Montoya, L.A.; Ledesma-García, J.; Montes-Morán, M.A.; Gurrola, M.P.; Menéndez, J.A.; Arenillas, A.; Arriaga, L.G. Facile Synthesis of Unsupported Pd Aerogel for High Performance Formic Acid Microfluidic Fuel Cell. *Materials* **2022**, *15*, 1422. https://doi.org/10.3390/ma15041422

Academic Editor: Alessandro Dell'Era

Received: 6 January 2022
Accepted: 10 February 2022
Published: 15 February 2022

1. Introduction

Noble metals have been widely used as electrocatalysts for energy conversion devices, including fuel cells, water electrolysis, and metal–air batteries [1]. Fuel cells supply energy in a similar way as batteries, although they do not require charging and operate as long as fuel is provided [2,3]. Fuel cells fed with formic acid supply electricity and heat, based on the electrochemical oxidation of fuels in the anode and the reduction of oxygen in the cathode, where H_2 is formed [4,5]. Pd nanostructures have been used specially in direct formic acid fuel cells that are considered green energy sources for portable electronics and hybrid vehicles due to their high open-circuit voltage, safety and reliability, and low fuel crossover effect, including Pd nanoparticles supported on graphene [6], since nanostructures have simple morphology [7] until hybrid variation of Pd–Cu [8] and Pd–Co [9]. Although these supported materials have great performance towards formic acid oxidation (FAO), the carbonaceous support is still a problem when working with devices that work at high voltages.

Conventional formic acid fuel cells usually employ a physical barrier for the separation of electrodes, which presents many limitations such as membrane fouling and clogging [10]. Therefore, fuel cells working with microfluids would take advantage of laminar flow as a fluid separator and avoid the use of membranes and their drawbacks [11]. Microfluidic fuel cells have the advantage of being portable and of carrying out small-scale processes offering high efficiency of energy conversion. The development of this type of device allows to incorporate the electro-oxidation of formic acid for diverse technological applications on a small scale [12]. On the other hand, miniaturizing the cell may reduce fabrication costs. A study has recently presented a novel microfluidic fuel cell (MFC) that incorporates the innovation of using a laminar flow instead of the conventional solid membrane to separate the fuel and oxidant [13]. Hence, the membrane-related issues are eliminated in this new MFC, which also offers savings in the manufacturing costs. However, it is still necessary to develop effective materials for these types of devices.

The use of catalysts for generating hydrogen from formic acid could minimize the dependence on lithium batteries in a large number of mobile devices [7]. Formic acid can be decomposed catalytically according to the following reactions:

$$HCOOH_{(l)} \rightarrow H_{2\,(g)} + CO_{2\,(g)} \tag{1}$$

$$HCOOH_{(l)} \rightarrow H_2O_{(l)} + CO_{(g)} \tag{2}$$

Noble metals have been extensively studied as catalysts due to their high efficiency, non-toxicity, and stability. Particularly, Pd is widely used in anodes for FAO [9,10]. The synergistic effect of the metallic phase and oxyphilic properties of the Pd surface provides active sites for adsorption and dissociation of formic acid besides providing promoters of oxygen-containing species at low potentials [14,15]. There are a great number of Pd-based catalysts in the bibliography for acid formic oxidation, however, improving their activity is still a requirement in order to be implemented in fuel cells.

Mesoporous materials with low density and a greater number of active sites such as aerogels would allow the use of less mass of the catalyst and, at the same time, to provide a high catalytic activity [12–14]. Noble metal aerogels have approximately 90% air and very low contents of the active metal which reduces the cost of the catalysts [15,16]. These materials are commonly obtained by a sol-gel process and supercritical drying [16,17], however, other techniques such as lyophilization allow promising aerogel qualities [18]. Lyophilization, like supercritical drying, shows high efficiency in the formation of metallic aerogels [19–21]; this has been demonstrated in works such as Cu(II) cryogels [22] and Pd/CeO_2-ZrO_2 alloy aerogels that have been used in the reduction of CO [23] poly(3-sulfopropylmethacrylate) (p(SPM)) cold gels for H_2 production and mostly organic aerogels as supports for other catalytic materials [24–26].

The aerogel synthesis in this work was implemented under microwave radiation. This heating technology allowed, not only the saving of processing time that is usually associated with this type of heating but also to obtain materials with homogeneous and controlled low particles. This fact is quite advantageous, as the particles are usually obtained with more heterogeneous and big particle sizes when the materials are prepared under long conventional heating. The microwave heating allows heating of the bulk precursor solution without gradients, which favors a very good dispersion of nucleation points for the reaction occurring and therefore a better control of the final particle size. Furthermore, the use of microwaves may also influence some chemical reactions and the final products may present some chemical differences in comparison with the ones obtained by conventional heating. In this work, the use of microwave heating provides many benefits such as facile synthesis of homogeneous and low particle size synthesis of Pd aerogels, with high activity towards the oxidation of formic acid in an MFC due to their unique physicochemical characteristics.

2. Experimental

2.1. Pd Aerogels Chemical Synthesis

The synthesis of Pd aerogels was carried out by adding 10 mL of a 2 mg/mL solution of $PdCl_2$ (99%, Sigma-Aldrich ReagentPlus®, anhydrous powder, St. Louis, MO, USA) in deionized water into a solution of 240 mg of sodium carbonate (≥99.5%, J.T. Baker®) and 40 mg of glyoxylic acid monohydrate (98% Sigma-Aldrich) (ratio 6:1) in 40 mL of deionized water at 67.5 °C (Figure 1) for two hours in all cases. Two different devices were used as a heating source for this initial step of the reaction: conventional heating in a lab oven (CON) and microwave heating (MW). In the case of microwave heating, the reaction temperature was controlled by a thermocouple introduced in the precursor mixture and connected to a proportional–integral–derivative (PID) temperature controller installed in the microwave oven.

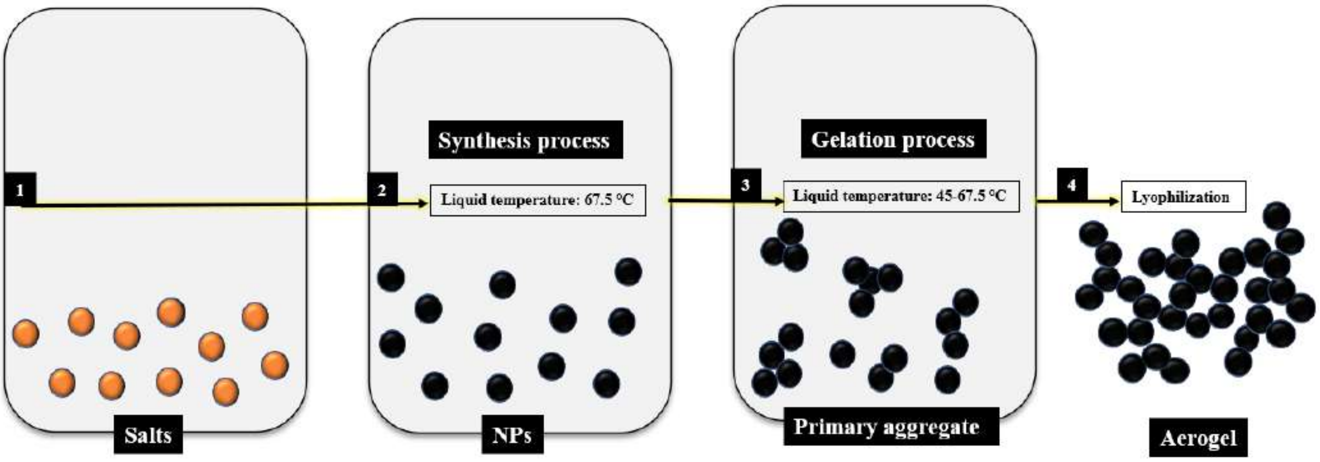

Figure 1. Procedure for obtaining aerogels using the sol-gel methodology in this work.

Once the first reactions took place, the reduction reaction and gelation process were also carried out by heating the mixture either by conventional heating (CON) or microwave heating (MW) under different operating conditions (i.e., 45 °C or 67 °C and 7 h or 24 h), as described in Table 1. After the gelation process, hydrogels were washed several times using deionized water and ethanol to remove the organic residues in the aqueous solution. Before submitting the clean samples to the lyophilization process, they were frozen with Liquid N_2, with a volume of 3 mL of deionized water and finally they were dried in a lyophilizer (LYO). A conventional drying in a lab oven (CON) was also performed for comparative proposes.

Table 1. Synthesis procedures and operating conditions to obtain the aerogels of this work.

Sample	Synthesis at 67.5 °C for 2 h	Heating Reduction Device	Reduction Conditions	Drying Device
PdA-CC	CON	CON	24 h/45 °C	LYO
PdA-MC	MW	CON	24 h/45 °C	LYO
PdA-MM	MW	MW	7 h/45 °C	LYO
PdA-MMT	MW	MW	7 h/67 °C	LYO
PdA-CON	CON	CON	24 h/45 °C	CON

2.2. Physicochemical Characterization

The morphology of the Pd aerogels was characterized using a JEOL JEM-2100F high-resolution transmission electron microscope (HR-TEM) with spherical aberration correction and a scanning electron microscope (SEM, Quanta FEG 650 microscopes from FEI). The crystal structures were measured by X-ray diffraction (XRD; D8-advance diffractometer Bruker) equipped with a CuKα X-ray source ($\lambda = 0.1541$ nm, 40 kV, 40 mA), using a step size of 0.02° 2θ and a scan step time of 5 s. The specific surface area and the pore size distribution were determined by nitrogen adsorption–desorption isotherms at −196 °C (Micromeritics ASAP 2020), after an overnight outgassing at 120 °C. The electronic structure of elements was measured by X-ray photoelectron spectroscopy (XPS; K-Alpha+ spectrometer equipped with the Avantage Data System from Thermo Scientific^{TM}, Waltham, MA, USA).

2.3. Electrochemical Measurements

2.3.1. Electrocatalytic Activity in Half-Cell Configuration

The electrochemical evaluation of the Pd aerogels was carried out in a Biologic VMP3 Potentiostat/Galvanostat using a conventional three-electrode electrochemical cell in acid media at a scan rate of 20 mV s^{-1}. A glass-carbon electrode (3 mm) was used as the working electrode, Hg/Hg_2SO_4 electrode as the reference electrode, and Pt wire as the counter electrode. The electrocatalyst ink was prepared using each aerogel sample in a mixture of 500 µL of deionized water and 50 µL of Nafion® (5%) per milligram of catalyst. The ink was sonicated for one hour and then 5 µL were deposited over the electrode surface. A similar ink was prepared using commercial Pd/C (20%, Sigma Aldrich, St. Louis, MI, USA) as catalyst and it was used for comparison. The electrolyte was bubbled with N_2 for 30 min before the electrochemical measurement.

The electrochemical profile for each sample was obtained in cyclic voltammetry (CV) experiments in 0.5 M H_2SO_4 within a potential range of 0–1.4 V vs. RHE, where the faradaic processes were visible in a current (i.e., J) that was tested by mg of catalyst.

2.3.2. FAO Performance

The electrocatalytic activity of the Pd aerogels towards FAO were tested by cyclic voltammetry (CV) in a 0.5 M of HCOOH in 0.5 M H_2SO_4 electrolyte. As for the electrocatalytic activity in the half-cell configuration, at potential range between 0 and 1.4 V vs. RHE was explored. The results were also compared with the FAO electrocatalytic activity of a commercial reference (Pd/C 20%, Sigma Aldrich).

2.3.3. Stability Performance

The stability performance was carried out by a chronoamperometry (CA) technique at 0.3 V vs. RHE for 24 h at nitrogen atmosphere.

2.3.4. Evaluation of the Microfluidic Fuel Cell System

The description of the MFC used for these experiments has been previously reported [27]. Both the anode and cathode were Pd aerogel samples deposited on Toray carbon paper-060 (TCP) with a transversal area of 0.02 cm^2. The electrocatalyst loading was 0.1 mg for both electrodes. Linear sweep voltammetry (LSV) was performed by injecting 0.5 M HCOOH with H_2SO_4 as the electrolyte in the anode with the evaluated catalyst; and 0.5 M H_2SO_4 in the cathode with commercial Pt/C as previous studies reported its best performance [19]. A flow rate of 200 µL min^{-1} was used in the test, i.e., Figure 2.

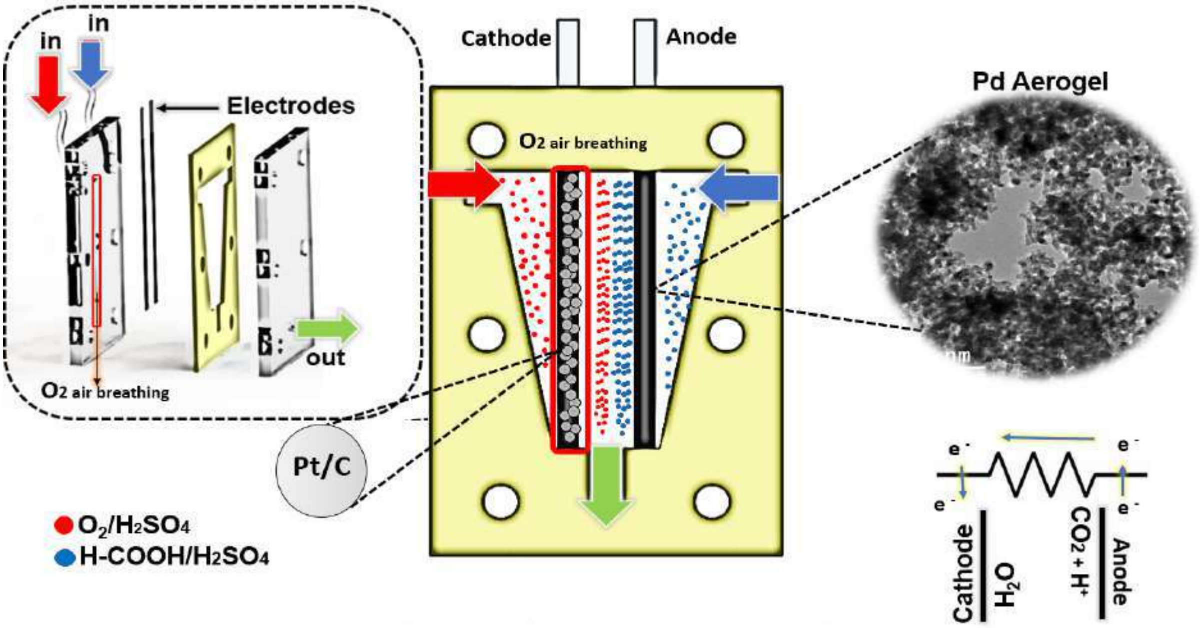

Figure 2. Microfluidic system for formic acid electro-oxidation.

3. Results and Discussion

3.1. Physicochemical Characterization

The route selected in this paper, i.e., in situ reduction and subsequent fusion, is one of the two common strategies found in the literature for the preparation of Pd aerogels [28–31]. This route is essentially a one-pot synthesis that significantly shortens and simplifies the metal nanoparticles aerogels. The aerogels are thus synthetized by mixing noble metal salts ($PdCl_2$ in our case) with a strong reducing agent, typically $NaBH_4$, $LiAlH_4$, hydrazine, sodium citrate, tannic acid or, in our case, glyoxylic acid monohydrate (combined with a base). The two reactants lead to the Pd^{2+} to Pd^0 reduction at moderate temperatures, typically around 60 °C. Under these conditions, the metal nanoparticles in the sol state tend to aggregate until the stability of the solution is compromised and turned into a gel state (Figure 1). The hydrogel obtained after the Pd aggregation is finally washed several times using deionized water by carefully exchanging the supernatant to ensure the integrity of the formed hydrogel but minimizing the presence of impurities (remnant salts and organic matter) and dried either using supercritical CO_2 extraction or, in our case, lyophilization.

Glyoxylic acid monohydrate (combined with a base) is a popular reducing agent in the electroless copper plating [32], and it has been used before in the synthesis of metal aerogels [31]. Although the mechanism of the Pd reduction is not fully understood, it is plausible that the contribution of the glyoxylic acid is twofold according to the following equations. First, the disproportionation of the glyoxylic acid in a basic medium occurs:

$$2OCHCOOH + H_2O \rightarrow HOCH_2COOH + HOOC\text{-}COOH \tag{3}$$

The oxalic acid would then react with the $PdCl_2$:

$$HOOC\text{-}COOH + PdCl_2 + Na_2CO_3 \rightarrow Pd(COO)_2 + 2NaCl + H_2CO_3 \tag{4}$$

Finally, the palladium oxalate would be reduced by the glyoxylic acid [32]:

$$Pd(COO)_2 + OCHCOOH + 2OH^- \rightarrow Pd + 2C_2O_4{}^{2-} + H_2O + 2H^+ \tag{5}$$

In this work, the yield of the Pd aerogel synthesis was 67%.

The XPS analysis was performed to evaluate the composition and electronic structure of the four Pd aerogels obtained. Figure 3 displays their core-level binding energy Pd 3d5/2 (336.8–337.0 eV) and Pd 3d3/2 (340.0–341.0 eV) XP spectra [21,33]. For all samples, each peak can be deconvoluted into two contributions: 335.0 and 340.2 eV for metallic Pd; and 337.0 and 342.4 eV for Pd^{2+} [34]. XPS data revealed that Pd^0 is the main species on the Pd aerogels surface for PdA-MMT. The high-resolution Pd XPS profiles of samples PdA-CC and PdA-MM are very similar pointing out that the microwave heating produces an analogous reduction process but with a remarkable saving of time (i.e., 7 h vs. 24 h, see Table 1). In addition, it can be also observed that the Pd metallic phase on PdA-MMT aerogel is higher than that on the other samples. This analysis shows that the ratio between Pd^0 and Pd^{2+} favors Pd^0 when the aerogels were prepared by microwave heating, and this would probably be one of the main reasons for high stability and performance of that catalyst, as it will be shown below. Therefore, increasing the temperature from 45 °C to 67 °C during the reduction stage would be preferred because it brings about a greater quantity of metallic Pd^0.

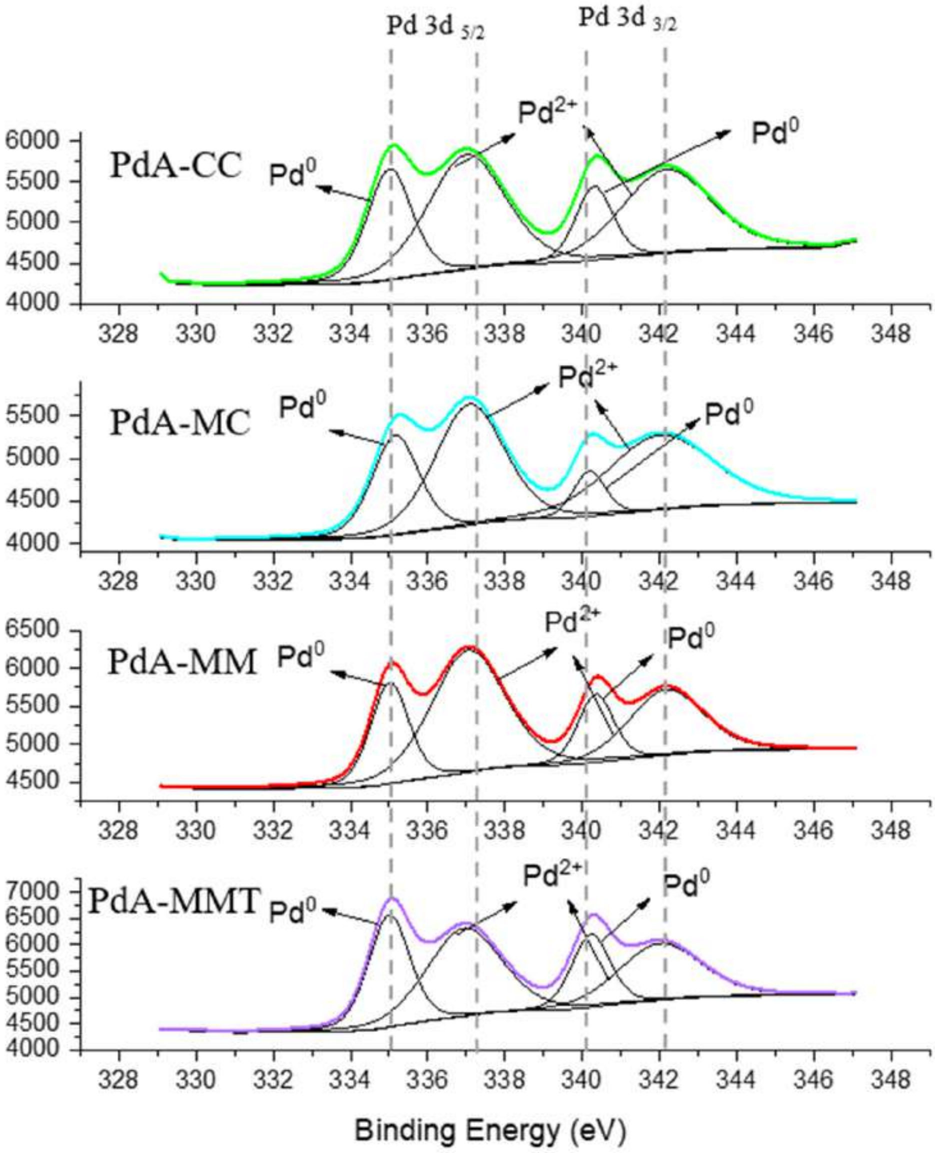

Figure 3. XPS of the Pd aerogels obtained.

Powder X-ray diffraction (XRD) measurements were performed to evaluate the crystallinity of Pd aerogels samples. Figure 4 illustrates the XRD patterns of the synthesized catalysts. In all XRD patterns, two major diffraction peaks appear at about 40.1° 2θ and 46.6° 2θ, which are ascribed to the (111) and (200) reflection planes of metallic Pd, respectively [35]. These peaks agree with a face-centered cubic crystal structure of Pd (JCPDS# 46-1043) [36]. In addition, the crystallite size was calculated using the Scherrer equation:

$$d_{111} = \frac{K\lambda}{\beta_{111} \cos\theta}$$

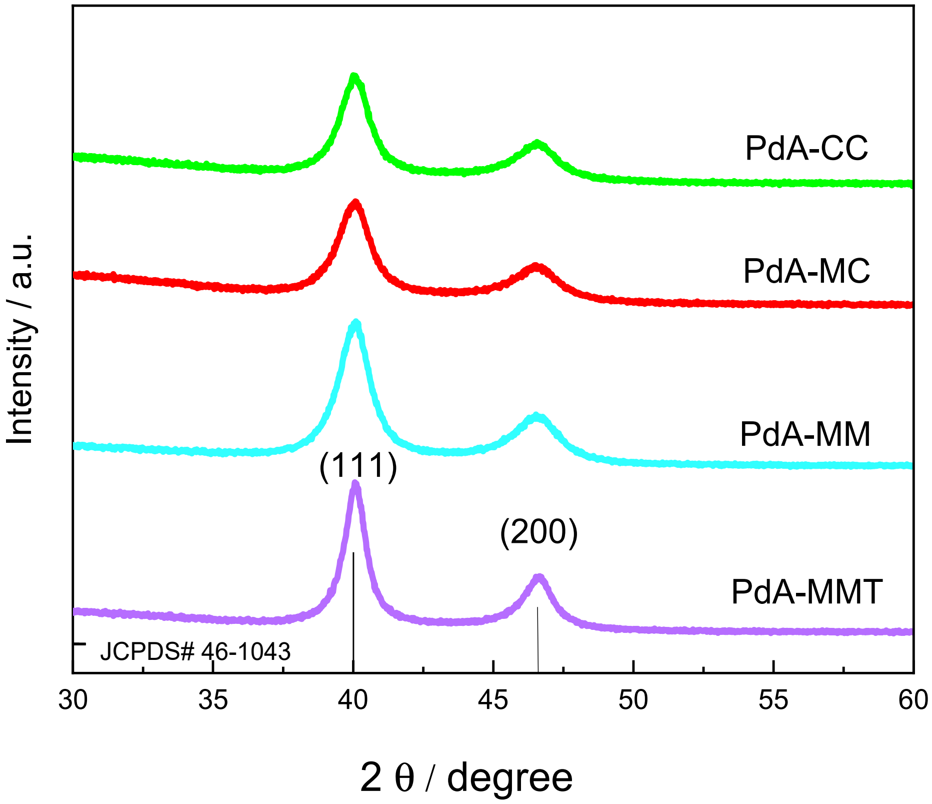

Figure 4. XRD of Pd aerogels samples.

The crystallite sizes for the PdA-CC, PdA-MC, PdA-MM, and PdA-MMT samples were 10.3, 7.2, 6.9, and 7.6 nm, respectively.

The use of microwaves reduces the size of the Pd crystallites, the minimum size being obtained when microwave was used as the heating method in the two stages of the synthesis. The size of the crystal is significantly smaller when using microwaves as a heating method because this heating process is volumetric and heat gradients are minimized. Thus, the reaction occurs uniformly in the precursor mixture. This means that under microwave heating, there are multiple crystallization spots in the precursor solution, whereas in conventional heating, the temperature gradient produces less crystallization spots that grow to form larger particles.

The morphologies of the Pd aerogels were characterized by SEM and the images are presented in Figure 5c–f.

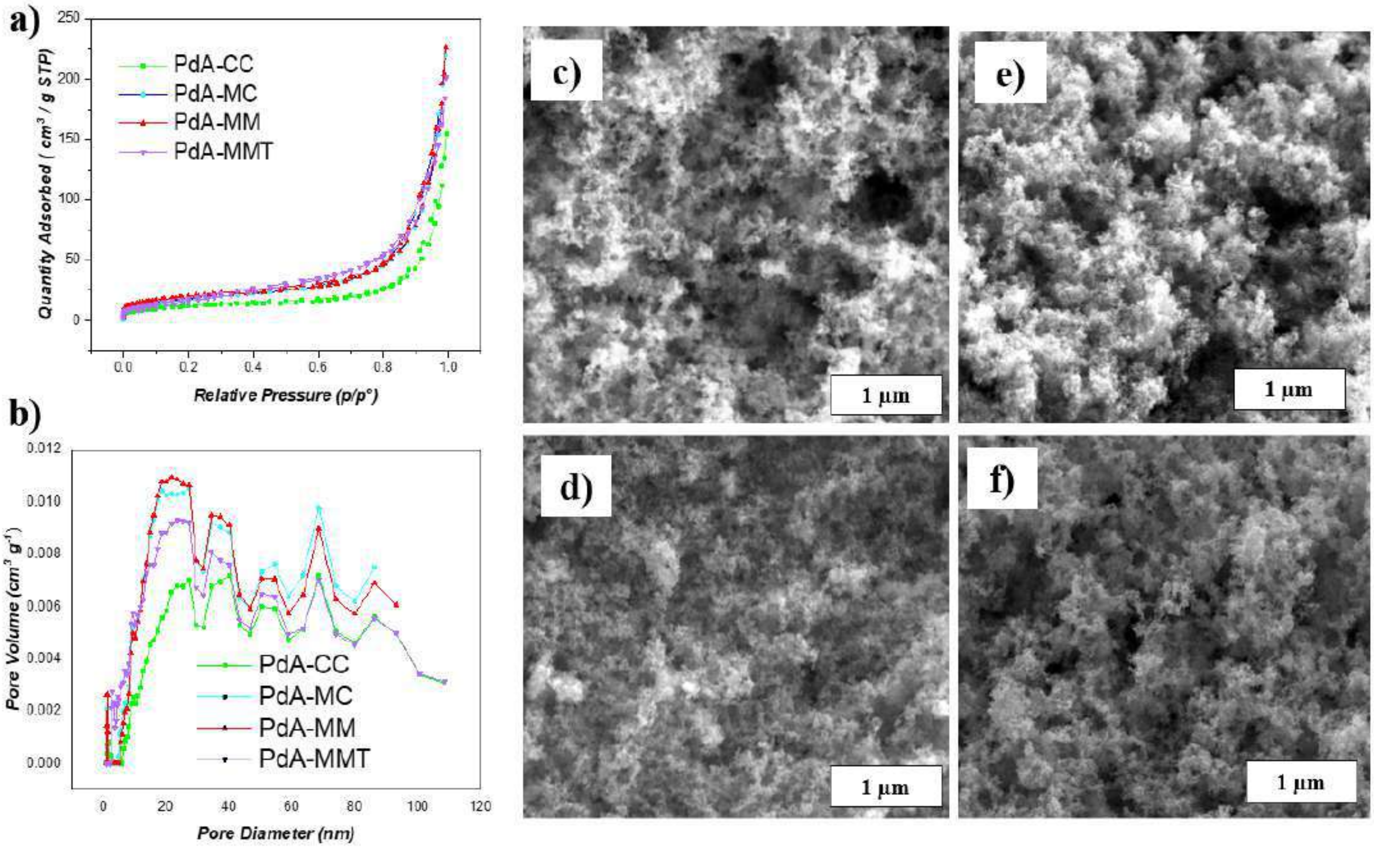

Figure 5. Physicochemical analysis. BET analysis of Pd aerogels: (**a**) N_2 adsorption isotherms; and (**b**) pore size distribution. SEM of Pd aerogels: (**c**) PdA-CC; (**d**) PdA-MC; (**e**) PdA-MM; and (**f**) PdA-MMT.

The aerogels obtained present a three-dimensional porous network anchored with nanochains which are extremely thin and make the material look like a sponge with a wide pore size distribution in the range of mesopores and macropores, i.e., Figure 5a,b.

All samples present a similar morphology, although sample PdA-MM (i.e., Figure 5c) seems to present the most open 3D structure. Slight differences in morphology between the different metallic Pd aerogels are attributed, again, to the heating technology applied in their synthesis. Thus, a finer distribution of particles appears in the material synthesized and reduced by microwave heating. This can be explained in Figure 6f where it is observed that the distribution of heat within the solution, by the radiation of microwaves, allows the reaction to occur homogeneously. Instead, larger particles are formed by conventional heating due to the fact that the heat distribution begins at the edges and causes the reaction to occur in an inhomogeneous way, resulting in larger particles that decrease the BET surface area in the aerogels.

TEM images at different magnifications show chains of particles surrounding pores of different sizes. The spherical nanoparticles in those chain structures present different lengths depending on the treatment performed during the synthesis of the aerogels. Particle diameters of up to 30 nm for the aerogels were synthesized in the conventional oven, i.e., Figure 6c, whereas particles less than 9 nm in diameter are characteristic of samples synthesized in MW (Figure 6d–f). To understand the effect of heating on the particle size, the normal distribution of the widths was analyzed, the trend of the means for each sample analyzed is observed in the histograms, being 15.3 nm for PdA-CC, 6.2 nm for PdA-MC, and 5 nm for PdA-MM and Pd-MMT. Therefore, a smaller particle size is attributed to the effect of microwave heating.

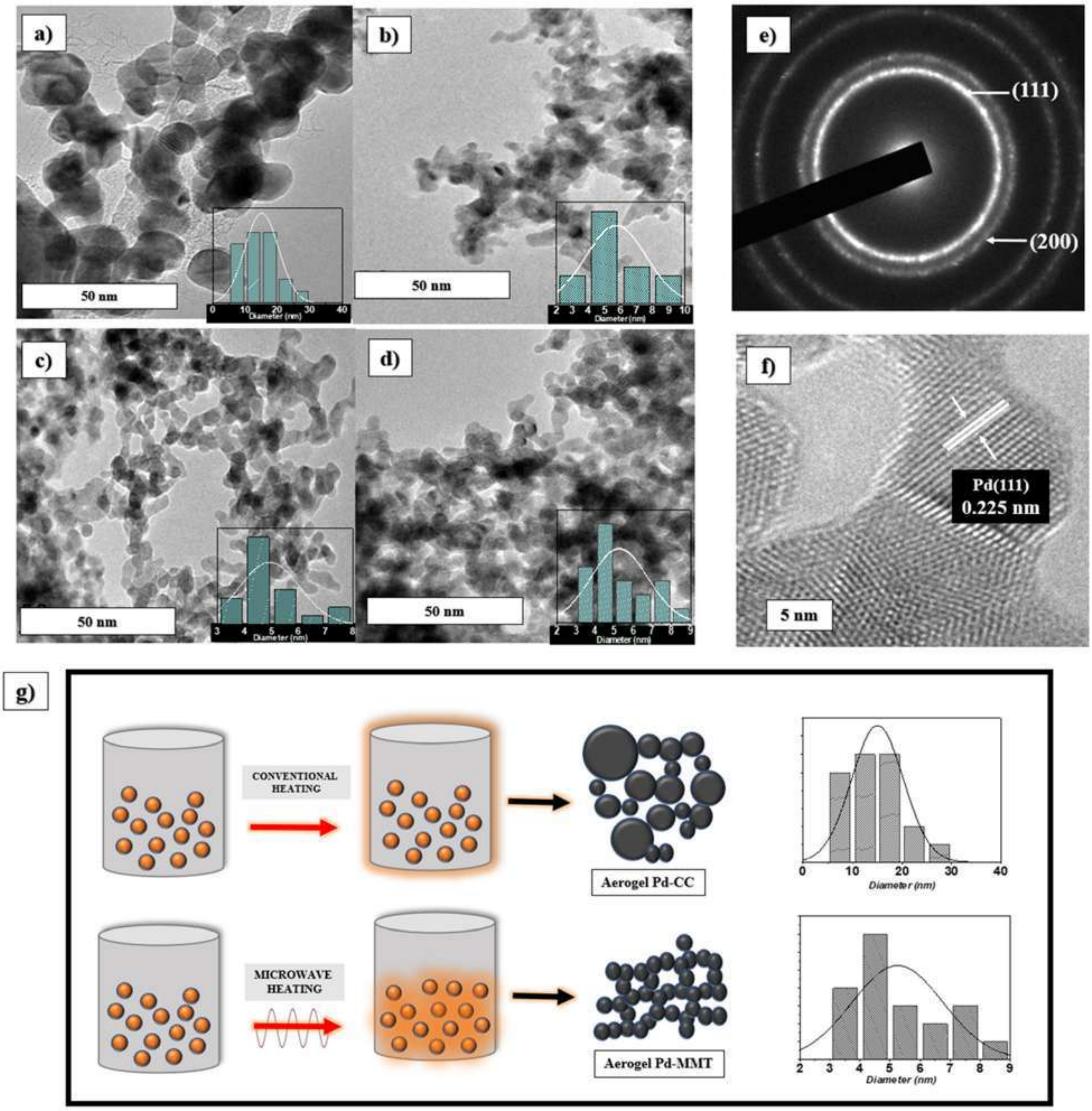

Figure 6. TEM micrographs of Pd aerogels. (**a**) PdA-CC, (**b**) PdA-MC, (**c**) PdA-MM, (**d**) PdA-MMT, (**e**,**f**) crystallographic patterns observed in PdA-MMT aerogel, and (**g**) heating effect on the particle size of Pd-CC and Pd-MMT aerogels.

According to the different structures observed by SEM and TEM, different porosity and therefore availability of reactive surface area of the aerogels studied was expected, which could be relevant for their further use in electrochemistry. Porous properties of samples were investigated by nitrogen adsorption–desorption isotherm at −196 °C (see Figure 5a). The isotherms of the aerogels are of type II according to the IUPAC classification, which are characteristic of meso–macroporous materials [36] according to the low volume of adsorption at low relative pressures, the sharp increase in the adsorption at high relative pressures, and the absence of a hysteresis loop. Furthermore, the pore size distribution reveals a high volume of mesopores (i.e., 2–50 nm) and macropores (i.e., >50 nm) as can be seen in Figure 5b. The surface area of the samples was determined using the BET equation, giving relatively low values due to the lack of microporosity (i.e., pores < 2 nm) in these samples: 45, 65, 75, and 77 m^2g^{-1} for PdA-CC, PdA-MC, PdA-MM, and PdA-MMT, respectively. Nevertheless, a trend to increase the BET surface area is observed if microwave heating is used in the different steps during the synthesis.

3.2. Electrocatalytic Performances

The electrocatalytic activity for aerogels samples were evaluated using cyclic voltammetry (CV). First, electrochemical profiles were obtained in a 0.5 M H_2SO_4 aqueous solution at ambient conditions with a sweep rate of 20 mVs^{-1} (Figure 7a). The peaks detected are attributed to (i) the hydrogen desorption in the 0.1–0.25 V range, (ii) hydrogen adsorption at 0.23 V, (iii) reduction of Pd (II) oxide at 0.65–0.75 V, and (iv) formation of Pd (II) oxide at 1–1.2 V. All these phenomena are present in the cyclic voltammograms of all Pd aerogels. However, the use of microwave radiation during any of the synthesis steps clearly improves the electrochemical activity of the materials.

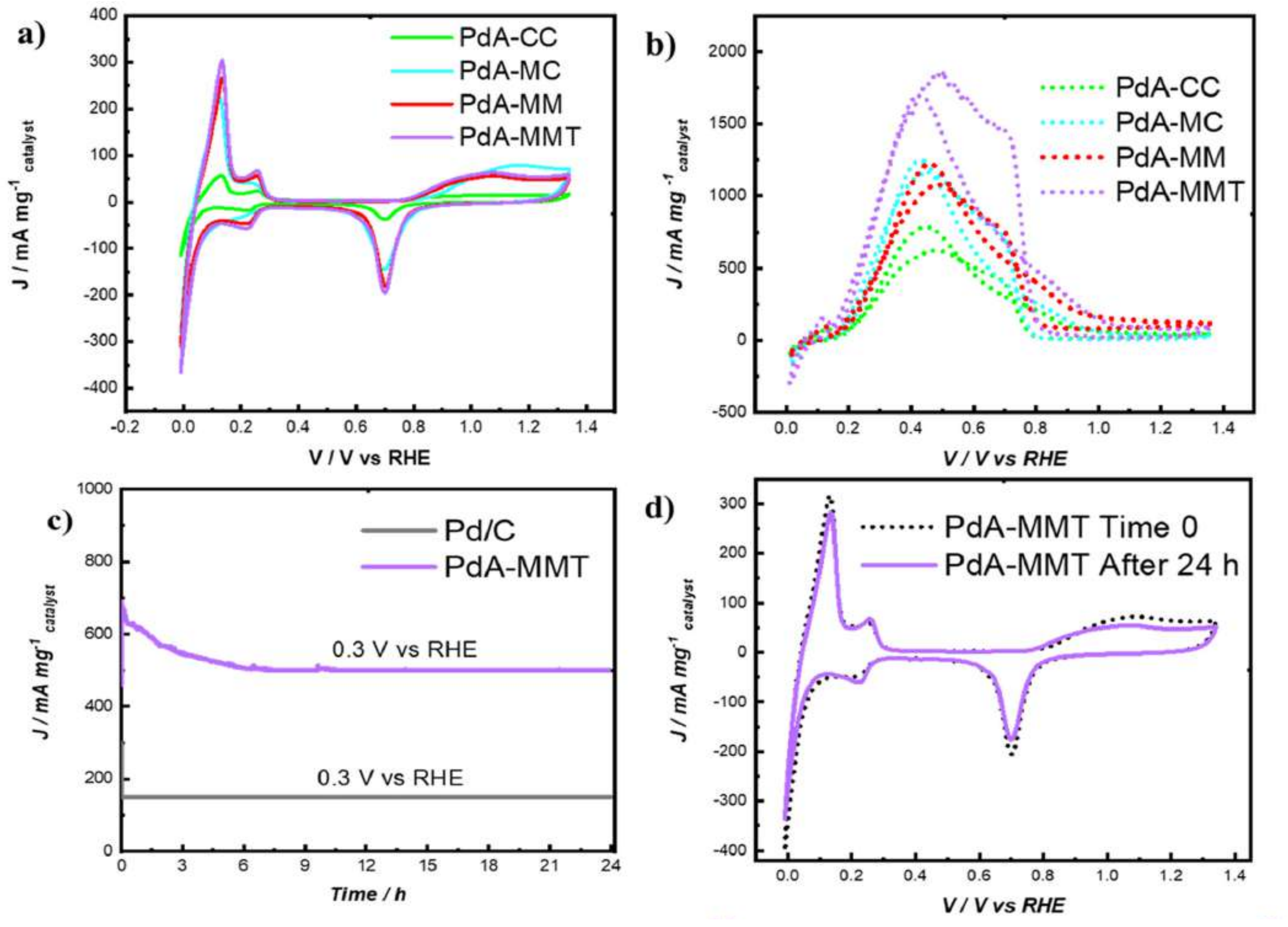

Figure 7. *Cont.*

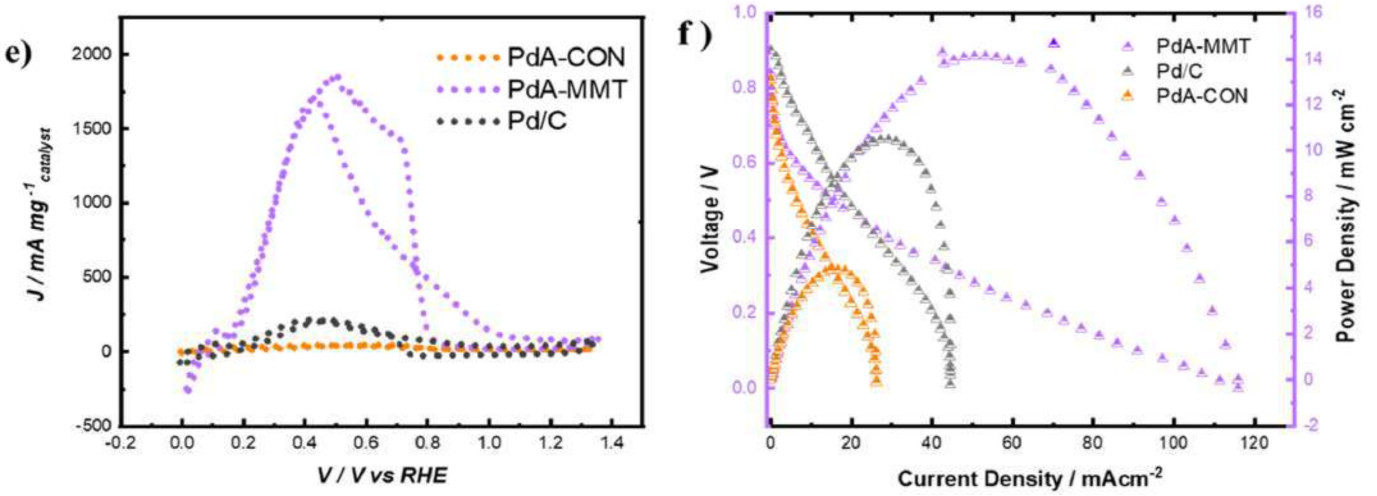

Figure 7. Electrochemical performance. (**a**) Pd aerogels profiles in 0.5 M H_2SO_4; (**b**) comparison between the aerogels in FAO; (**c**) stability performance on Pd-MMT vs. Pd/C; (**d**) PdA-MMT CV before and after the CA for 24 h; (**e**) FAO performance between PdA-CON, PdA-MMT, and Pd/C; and (**f**) MFC performance for the best aerogels obtained (PdA-MMT), a commercial catalyst (Pd/C) and an in-lab catalyst obtained by conventional procedure (PdA-CON).

To quantify this improvement, the electrochemical active surface area (*ECSA*) was evaluated on the electrode surface of each catalyst. The values of *ECSA* for the samples studied in this work were estimated from the cyclic voltammograms (i.e., Figure 7a) by using the reduction charge of Pd (II) oxide according to the following Equation (2):

$$ECSA = \frac{Q_m}{m_{Pd} ed_m}$$

where, Q_m denotes coulombic charge (Q per μCcm^{-2}) for the reduction of Pd (II) oxide achieved by integrating the charges related to the reduction of Pd (II) oxide for the different samples; m_{Pd} is the mass amount of Pd loaded (g cm^{-2}) on the GC electrode surface and ed_m is a constant (424 μC cm^{-2}), which corresponds to the reduction of a Pd (II) oxide monolayer [37].

The *ECSA* values of the Pd aerogels samples depicted in Figure 7a are shown in Table 2. *ECSA* values for PdA-CON and the commercial Pd/C catalyst are also included for comparative purposes. As expected from the cyclic voltammograms, there is a great increase in the electrochemical active surface area for the samples prepared using MW. The lower particle size detected by TEM, the lower size of the crystals detected by XRD, and the higher content of the Pd^0 evaluated by XPS, in samples obtained using microwave heating show clearly that this process has a huge impact on the electrochemical performance of the resulting Pd aerogels. In other words, by means of microwave heating instead of conventional heating for the synthesis of Pd aerogels, the innovation presented in this work, not only the is the processing time reduced but also the electrochemical behavior of these materials is notably enhanced.

Table 2. Electrochemical active surface area (*ECSA*) values for the samples studied.

Sample	***ECSA* (m^2/g)**
PdA-CON	1.3
PdA-CC	22.1
PdA_MC	22.1
PdA-MM	22.8
PdA-MMT	28.5
Pd/C	16

This is further corroborated when performing the CV experiments in an electrolyte containing formic acid (i.e., Figure 7b). The evaluation of FAO was carried out in the same range of potential as the CV tests (0.0–1.4 V vs. RHE, see Figure 7a). Comparison of the electrochemical profiles with FAO curves recorded by GC electrodes clearly demonstrated that Pd aerogels offered strong peaks for the electro-oxidation at room temperature conditions [38]. The maximum current values during FAO occur at 0.4 V vs. RHE. Again, the effect of using microwave heating for the synthesis of the Pd aerogels clearly increases their activity in the electro-oxidation of formic acid. Thus, a maximum mass current (J) of 1750 mA mg^{-1} was for the PdA-MMT sample; in the case of PdA-MM and PdA-MC materials, values of 1200 and 1190 mA mg^{-1} were respectively obtained, being the lowest performance for a PdA-CC sample with 700 mA mg^{-1}. On the other hand, it seems clear that increasing the temperature of the reduction step from 45 °C to 67 °C makes a difference in the formic acid oxidation activity (see Figure 7b).

As for the formic acid electro-oxidation mechanism with these Pd aerogels, the reaction occurs following two parallel paths, one giving rise to CO_2 at reasonably low overpotentials through the so-called active intermediate and a chemical dehydration step leading to adsorbed CO, which will be oxidized to CO_2 at higher potentials [39]. The peaks between 0.2 and 0.6 V for all Pd catalysts (Figure 7d) represent a direct pathway ($HCOOH \rightarrow COOHads/HCOOads + H^+ + e^- \rightarrow CO_2 + 2H^+ + 2e^-$), while the peaks ranging from 0.7 to 0.9 V represent an indirect pathway ($HCOOH \rightarrow COads + H_2O \rightarrow CO_2 + 2H^+ + 2e^-$) [40]. Since the maximum electrochemical activity of all Pd aerogels studied was measured at ca. 0.4 V, the direct pathway is clearly favored in this case.

The best sample, PdA-MMT, obtained in this work was also compared with the Pd/C commercial catalyst (20 wt%) and PdA-CON in order to show the benefits of using the novel synthesis presented in this work (i.e., microwave heating during the synthesis and lyophilization as the drying procedure). To analyze the catalytic activity of PdA-MMT versus Pd/C, the maximum current intensity shown in Figure 7e should be compared. It can be seen that a current density near to 1900 mA mg^{-1} was observed for the aerogel against almost 300 mA mg^{-1} for Pd/C. Whilst in the case of the behavior of the PdA-MMT vs. the PdA-CON sample, a significant increase in electrochemical activity was detected for the PdA-MMT sample (see Figure 7e).

In order to characterize not only the activity but also the stability of the PdA-MMT sample, a test was carried out for 24 h on this sample and the commercial catalyst Pd/C (Figure 7c,d). The results reveal that the great activity of the sample obtained in this work (PdA-MMT) is totally maintained and stable with time.

3.3. Microfluidic Fuel Cell Performance

A microfluidic fuel cell was used for testing samples to verify their activity under real operating conditions, using 0.5 M formic acid with 0.5 M H_2SO_4 as the electrolyte for the anodic reaction. Three materials have been tested, namely, PdA-MMT, PdA-CON, and the commercial Pd/C catalysts used as reference materials. Linear sweep voltammetry is a specific electrochemical protocol to discriminate the catalytic activity of the anode materials. The microcell works by pumping 200 μL min^{-1} of the electrolyte fuel (0.5 M HCOOH in 0.5 M H_2SO_4) into the anode, and 200 μL min^{-1} of only 0.5 M H_2SO_4 into the Pt/C cathode. Both electrodes were normalized to a mass charge of 0.1 mg of each material over an area of 0.019 cm^2. The polarization curves were obtained for stable open circuit voltage (OCV) and values registered for the PdA-MMT, Pd/C, and PdA-CON samples were 0.88, 0.9, and 0.84 V, respectively. The power density obtained in Figure 7f shows favorable results for the aerogel obtained by MW heating. Small bubbles could be detected on the anode during the experiment, corresponding to the generation of hydrogen. The mass current of the PdA-MMT aerogel is almost three times higher than the commercial Pd/C catalyst (i.e., Figure 7e), corroborating, again, the superior performance of the aerogels obtained by using microwave heating during the synthesis. The superior catalytic activity of PdA-MMT may be attributed to the most active Pd surface. The use of microwave heating during the synthesis of the aerogels leads not only to a better morphology of the aerogels but also to a higher content of metallic Pd^0. Previous studies reveal that Pd^{2+} species are catalytically inactive for FAO [41]. Therefore, the use of microwave heating has a determinant influence on the production of effective Pd aerogel catalysts.

Table 3 shows the performance of other microfluidic devices from the bibliography in comparison with the one used in this work with the Pd catalyst obtained by the innovative method presented. It may be observed that the configuration used in this work using PdA-MMT as anodic material allows to obtain extremely higher yield per mass of catalyst in terms of density power.

Table 3. Anodic catalyst comparison.

Anodic Catalyst	Formic Acid Concentration	Mass Loading/mg cm^{-2}	OCV/V	J/mA cm^{-2}	W Max/mW cm^2	Reference
Pd/C	0.5 M	0.7	0.9	7.4	2.9	[42]
Pd/C	0.5 M	0.1	0.9	43	10.5	This work
Pd/MWCNT	0.5 M	1.3	0.9	9.1	2.3	[43]
Pd50Co50/MWCNT	0.5 M	1.2	0.9	5.9	1.75	[38]
PdA-MMT	0.5 M	0.1	0.88	118.3	14	This work
Pd/graphene	0.5 M	2	0.7	30	15.2	[26]
Pt/CN$_x$	0.5 M	1	1.1	9.79	3.43	[44]
Pt-Ru	3 M	3	0.47	1.2	12.5	[45]
Au-Pt	1 M	-	1.2	28	12	[46]
Pd	0.5 M	10	0.95	125	26	[47]
Pt	0.5 M	-	1.1	8	2.2	[48]

4. Conclusions

The use of microwave heating during the synthesis, followed by lyophilization as the drying step, renders Pd aerogels with a particle size smaller than 5 nm in anchored chains. Furthermore, Pd^0 species are generated in a greater proportion when microwave heating is used during the synthesis. These facts demonstrate that the sample obtained by microwave heating presents a much higher electrochemical active surface area, thus favoring the formic acid electro-oxidation reaction. The PdA-MMT sample showed a three-times superior performance in a microfluidic fuel cell than a commercial Pd/C catalyst, reaching current densities of up to 118.3 mA cm^{-2}.

This result shows that the innovative synthesis route presented in this work, using microwave heating for the synthesis process, leads to the production of very competitive aerogels to be used as electrocatalysts.

Author Contributions: Conceptualization, L.G.A. and J.L.-G.; methodology, A.A. and L.A.R.-M.; formal analysis, A.M.-L.; resources, L.G.A., J.A.M. and A.A.; writing—original draft preparation, A.M.-L. and L.A.R.-M.; writing—review and editing, L.G.A., M.A.M.-M.; J.L.-G., M.P.G. and A.A.; supervision, L.G.A. and A.A. All authors have read and agreed to the published version of the manuscript.

Funding: Mexican Council for Science and Technology (CONACYT) through project Ciencia de Frontera Grant no. 845132 and estancia Sabatica Conacyt 2021-2. Grant PID2020-113001RB-I00 funded by MCIN/AEI/ 10.13039/501100011033 and by the European Union NextGenerationEU/PRTR; Grant PCI2020-112039 funded by MCIN/AEI/ 10.13039/501100011033 and by the European Union NextGenerationEU/PRTR.

Conflicts of Interest: The authors declare no conflict of interest.

References

1. Zhang, B.; Ren, L.; Xu, Z.; Cheng, N.; Lai, W.; Zhang, L.; Hao, W.; Chu, S.; Wang, Y.; Du, Y.; et al. Atomic Structural Evolution of Single-Layer Pt Clusters as Efficient Electrocatalysts. *Small* **2021**, *1–8*, 2100732. [CrossRef]
2. Hidayah, N.; Irwan, M. Three-dimensional CFD modeling of a direct formic acid fuel cell. *Int. J. Hydrogen Energy* **2019**, *44*, 30627–30635.

3. Fan, H.; Cheng, M.; Wang, L.; Song, Y.; Cui, Y.; Wang, R. Extraordinary electrocatalytic performance for formic acid oxidation by the synergistic effect of Pt and Au on carbon black. *Nano Energy* **2018**, *48*, 1–9. [CrossRef]
4. Ying, L.; Ouyang, Y.; Wang, S.; Gong, Y.; Jiang, M. Ultrafast synthesis of uniform 4–5 atoms-thin layered tremella-like Pd nanostructure with extremely large electrochemically active surface area for formic acid oxidation. *J. Power Sources* **2020**, *447*, 227248.
5. Choi, M.; Ahn, C.; Lee, H.; Kwan, J.; Oh, S.; Hwang, W.; Yang, S.; Kim, J.; Kim, O.; Choi, I. Bi-modified Pt supported on carbon black as electro-oxidation catalyst for 300 W formic acid fuel cell stack. *Appl. Catal. B Environ.* **2019**, *253*, 187–195. [CrossRef]
6. Yang, Q.; Lin, H.; Wang, X.; Ying, L.; Jing, M.; Yuan, W. Dynamically self-assembled adenine-mediated synthesis of pristine graphene-supported clean Pd nanoparticles with superior electrocatalytic performance toward formic acid oxidation. *J. Colloid Interface Sci.* **2022**, *613*, 515–523. [CrossRef]
7. Wang, H.; Chen, H.; Wang, H.Q.; Ou, C.R.; Li, R.; Liu, H.B. Synthesis of ultrafine low loading Pd–Cu alloy catalysts supported on graphene with excellent electrocatalytic performance for formic acid oxidation. *Int. J. Hydrogen Energy* **2020**, *45*, 10735–10744. [CrossRef]
8. Douk, A.S.; Saravani, H.; Noroozifar, M. A fast method to prepare Pd-Co nanostructures decorated on graphene as excellent electrocatalyst toward formic acid oxidation. *J. Colloid Interface Sci.* **2018**, *739*, 882–891.
9. Hu, S.; Che, F.; Khorasani, B.; Jeon, M.; Won, C. Improving the electrochemical oxidation of formic acid by tuning the electronic properties of Pd-based bimetallic nanoparticles. *Appl. Catal. B Environ.* **2019**, *254*, 685–692. [CrossRef]
10. Kwon, T.; Choi, K.; Han, J. Separation of Ultra-High-Density Cell Suspension via Elasto-Inertial Microfluidics. *Small* **2021**, *17*, 2101880. [CrossRef]
11. Hao, R.; Yu, Z.; Du, J.; Hu, S.; Yuan, C.; Guo, H.; Zhang, Y.; Yang, H. A High-Throughput Nanofluidic Device for Exosome Nanoporation to Develop Cargo Delivery Vehicles. *Small* **2021**, *12*, 2102150. [CrossRef] [PubMed]
12. Moreno-zuria, A.; Ortiz-ortega, E.; Gurrola, M.P. Evolution of microfluidic fuel stack design as an innovative alternative to energy production. *Int. J. Hydrogen Energy* **2017**, *42*, 27929–27939. [CrossRef]
13. Ouyang, T.; Chen, J.; Huang, G.; Lu, J.; Mo, C.; Chen, N. A novel two-phase model for predicting the bubble formation and performance in microfluidic fuel cells. *J. Power Sources* **2020**, *457*, 228018. [CrossRef]
14. Gharib, A.; Arab, A. Electrodeposited Pd, Pdsingle bondCd, and Pdsingle bondBi nanostructures: Preparation, characterization, corrosion behavior, and their electrocatalytic activities for formic acid oxidation. *J. Electroanal. Chem.* **2020**, *866*, 114166. [CrossRef]
15. Bao, Y.; Liu, H.; Liu, Z.; Wang, F.; Feng, L. Pd/FeP catalyst engineering via thermal annealing for improved formic acid electrochemical oxidation. *Appl. Catal. B Environ.* **2020**, *274*, 119106. [CrossRef]
16. Rupa, P.; Harivignesh, R.; Sung, Y.; Kalai, R. Polyol assisted formaldehyde reduction of bi-metallic Pt-Pd supported agro-waste derived carbon spheres as an efficient electrocatalyst for formic acid and ethylene glycol oxidation. *J. Colloid Interface Sci.* **2020**, *561*, 358–371. [CrossRef]
17. Bi, Y.; Liu, M.; Ren, H.; Shi, X.; He, S.; Zhang, Y.; Zhang, L. Investigation on gelation process and microstructure for copper-based aerogel prepared via sol–gel method. *J. Non-Cryst. Solids* **2015**, *425*, 195–198. [CrossRef]
18. Suenaga, S.; Osada, M. Preparation of β-chitin nanofiber aerogels by lyophilization. *Int. J. Biol. Macromol.* **2019**, *126*, 1145–1149. [CrossRef]
19. Herrmann, A.K.; Formanek, P.; Borchardt, L.; Klose, M.; Giebeler, L.; Eckert, J.; Kaskel, S.; Gaponik, N.; Eychmüller, A. Multimetallic Aerogels by Template-Free Self-Assembly of Au, Ag, Pt, and Pd Nanoparticles. *Chem. Mater.* **2014**, *26*, 1074–1083. [CrossRef]
20. Wang, H.; Fang, Q.; Gu, W.; Du, D.; Lin, Y.; Zhu, C. Noble Metal Aerogels. *ACS Appl. Mater. Interfaces* **2020**, *12*, 52234–52250. [CrossRef]
21. Du, R.; Fan, X.; Jin, X.J. Emerging Noble Metal Aerogels: State of the Art and a Look Forward. *Matter* **2019**, *1*, 39–56. [CrossRef]
22. Erdem, A.; Ngwabebhoh, F.A.; Yildiz, U. Novel macroporous cryogels with enhanced adsorption capability for the removal of Cu(II) ions from aqueous phase: Modelling, kinetics and recovery studies. *J. Environ. Chem. Eng.* **2017**, *5*, 1269–1280. [CrossRef]
23. Osaki, T. Factors controlling catalytic CO oxidation activity on Pd/CeO2-ZrO2-Al2O3 cryogels. *Mater. Res. Bull.* **2019**, *118*, 110498. [CrossRef]
24. Yildiz, S.; Aktas, N.; Sahiner, N. Metal nanoparticle-embedded super porous poly(3-sulfopropyl methacrylate) cryogel for H2 production from chemical hydride hydrolysis. *Int. J. Hydrogen Energy* **2014**, *39*, 14690–14700. [CrossRef]
25. Baimenov, A.; Berillo, A.D.; Poulopoulos, G. A review of cryogels synthesis, characterization and applications on the removal of heavy metals from aqueous solutions. *Adv. Coll. Int. Sci.* **2020**, *276*, 102088. [CrossRef]
26. Li, D.; Xu, H.; Zhang, L.; Leung, D.Y.; Vilela, F.; Wang, H. Boosting the performance of formic acid microfluidic fuel cell: Oxygen annealing enhanced Pd@graphene electrocatalyst. *Int. J. Hydrogen Energy* **2016**, *41*, 10249–10254. [CrossRef]
27. Ortiz-Ortega, E.; Goulet, M.A.; Lee, J.W.; Guerra-Balcázar, M.; Arjona, N.; Kjeang, E.; Ledesma-García, J.; Arriaga, L.G. A nanofluidic direct formic acid fuel cell with a combined flow-through and air-breathing electrode for high performance. *Lab Chip* **2014**, *14*, 4596–4598. [CrossRef] [PubMed]
28. Zhu, C.; Du, D.; Eychmüller, A.; Lin, Y. Engineering Ordered and Nonordered Porous Noble Metal Nanostructures: Synthesis, Assembly, and Their Applications in Electrochemistry. *Chem. Rev.* **2015**, *115*, 8896–8943. [CrossRef]
29. Liu, W.; Herrmann, A.K.; Geiger, D.; Borchardt, L.; Simon, F.; Kaskel, S.; Gaponik, N.; Eychmüller, A. High-performance electrocatalysis on palladium aerogels. *Angew. Chem. Int. Ed. Engl.* **2012**, *51*, 5743–5747. [CrossRef]

30. Zhu, C.; Shi, Q.; Fu, S.; Song, J.; Xia, H.; Du, D.; Lin, Y. Efficient Synthesis of MCu (M = Pd, Pt, and Au) Aerogels with Accelerated Gelation Kinetics and their High Electrocatalytic Activity. *Adv. Mater.* **2016**, *28*, 8779–8783. [CrossRef]
31. Douk, A.S.; Saravani, H.; Abad, M.Z.Y.; Noroozifar, M. Three-Dimensional Engineering of Nanoparticles To Fabricate a Pd–Au Aerogel as an Advanced Supportless Electrocatalyst for Low-Temperature Direct Ethanol Fuel Cells. *ACS Appl. Energy Mater.* **2020**, *3*, 7527–7534. [CrossRef]
32. Honma1, H.; Kobayashi, T.J. Electroless Copper Deposition Process Using Glyoxylic Acid as a Reducing Agent. *Electrochem. Soc.* **1994**, *141*, 730. [CrossRef]
33. Maleki, H.; Hüsing, N. Current status, opportunities and challenges in catalytic and photocatalytic applications of aerogels: Environmental protection aspects. *Appl. Catal. B Environ.* **2018**, *221*, 530–555. [CrossRef]
34. Liu, X.; Bu, Y.; Cheng, T.; Gao, W.; Jiang, Q. Flower-like carbon supported Pd–Ni bimetal nanoparticles catalyst for formic acid electrooxidation. *Electrochim. Act.* **2019**, *324*, 134816. [CrossRef]
35. Caglar, A.; Selim, M. Effective carbon nanotube supported metal (M = Au, Ag, Co, Mn, Ni, V, Zn) core Pd shell bimetallic anode catalysts for formic acid fuel cells. *Renew. Energy* **2020**, *150*, 78–90. [CrossRef]
36. Doustkhah, E.; Mohtasham, H.; Farajzadeh, M.; Rostamnia, S.; Wang, Y.; Arandiyan, H. Organosiloxane tunability in mesoporous organosilica and punctuated Pd nanoparticles growth; theory and experiment. *Microporous Mesoporous Mater.* **2020**, *293*, 109832. [CrossRef]
37. Gao, N.; Ma, R.; Wang, X.; Jin, Z. Activating the Pd-Based catalysts via tailoring reaction interface towards formic acid dehydrogenation. *Int. J. Hydrogen Energy* **2020**, *45*, 17575–17582. [CrossRef]
38. Saravani, H.; Farsadrooh, M.; Share, M. Two-dimensional engineering of Pd nanosheets as advanced electrocatalysts toward formic acid oxidation. *Int. J. Hydrogen Energy* **2020**, *45*, 21232–21240. [CrossRef]
39. Herrero, E.; Feliu, J.M. Understanding formic acid oxidation mechanism on platinum single crystal electrodes. *Curr. Opin. Electrochem.* **2018**, *9*, 145–150. [CrossRef]
40. Douk, A.S.; Saravani, H.; Noroozifar, M. Three-dimensional assembly of building blocks for the fabrication of Pd aerogel as a high performance electrocatalyst toward ethanol oxidation. *Electrochim. Act.* **2018**, *275*, 182–191. [CrossRef]
41. Yang, L.; Wang, X.; Liu, D.; Cui, G.; Dou, B.; Wang, J. Efficient anchoring of nanoscale Pd on three-dimensional carbon hybrid as highly active and stable catalyst for electro-oxidation of formic acid. *Appl. Catal. B Environ.* **2020**, *263*, 118304. [CrossRef]
42. Morales-Acosta, D.; G, H.R.; Godinez, L.A.; Arriaga, L.G. Performance increase of microfluidic formic acid fuel cell using Pd/MWCNTs as catalyst. *J. Power Sources* **2010**, *195*, 1862–1865. [CrossRef]
43. Morales-Acosta, D.; Morales-Acosta, M.D.; Godinez, L.A.; Álvarez-Contreras, L.; Duron-Torres, S.M.; Ledesma-García, J.; Arriaga, L.G. PdCo supported on multiwalled carbon nanotubes as an anode catalyst in a microfluidic formic acid fuel cell. *J. Power Sources* **2011**, *196*, 9270–9275. [CrossRef]
44. Jindal, A.; Basu, S.; Chauhan, N.; Ukai, T.; Kumar, D.; Samudhyatha, K.T. Application of electrospun CNx nanofibers as cathode in microfluidic fuel cell. *J. Power Sources* **2017**, *342*, 165–174. [CrossRef]
45. Zhang, H.; Xuan, J.; Leung, D.; Wang, H.; Xu, H.; Zhang, L. Advanced gas-emission anode design for microfluidic fuel cell eliminating bubble accumulation. *J. Micromech. Microeng.* **2017**, *27*, 105016. [CrossRef]
46. Park, H.; Lee, K.; Sung, H.J. Performance of H-shaped membraneless micro fuel cells. *J. Power Sources* **2013**, *226*, 266–271. [CrossRef]
47. Brushett, F.; Jayashree, R.; Zhou, W.; Kenis, P. Investigation of fuel and media flexible laminar flow-based fuel cells. *Electrochim. Act.* **2009**, *54*, 7099–7105. [CrossRef]
48. Choban, E.; Markoski, L.; Wieckowski, A.; Kenis, P. Microfluidic fuel cell based on laminar flow. *J. Power Sources* **2004**, *128*, 54–60. [CrossRef]

Conclusiones

En esta Tesis Doctoral se ha mostrado por primera vez que es posible obtener aerogeles de paladio en un solo paso mediante un método de calentamiento por microondas, y que éste influye notablemente en la síntesis sol-gel de aerogeles de Pd, disminuyendo el tamaño de partícula y de cristal, aumentando el área superficial e incrementando la cantidad de Pd^0 respecto al Pd^{2+} y siendo la cantidad del primero la principal causa de un excelente desempeño hacia la oxidación de acido fórmico en un dispositivo microfluídico. Este excelente comportamiento permiten utilizar bajas cantidades de catalizador en los electrodos, para un mismo desempeño, justificando asi el uso del metal noble.

Referencias

Bi, Y., Liu, M., Ren, H., Shi, X., He, S., Zhang, Y., & Zhang, L. (2015). Investigation on gelation process and microstructure for copper-based aerogel prepared via sol-gel method. *Journal of Non-Crystalline Solids*, *425*, 195–198. https://doi.org/10.1016/j.jnoncrysol.2015.06.021

Chen, P., Xu, K., Fang, Z., Tong, Y., Wu, J., Lu, X., Peng, X., Ding, H., Wu, C., & Xie, Y. (2015). Metallic Co 4 N Porous Nanowire Arrays Activated by Surface Oxidation as Electrocatalysts for the Oxygen Evolution Reaction . *Angewandte Chemie*, *127*(49), 14923–14927. https://doi.org/10.1002/ange.201506480

Du, R., Fan, X., Jin, X., Hübner, R., Hu, Y., & Eychmüller, A. (2019). Emerging Noble Metal Aerogels: State of the Art and a Look Forward. *Matter*, *1*(1), 39–56. https://doi.org/10.1016/j.matt.2019.05.006

Gu, S., & Jana, S. C. (2017). Open cell aerogel foams with hierarchical pore structures. *Polymer*, *125*, 1–9. https://doi.org/10.1016/j.polymer.2017.07.085

Guo, R., Dang, L., Liu, Z., & Lei, Z. (2020). Incorporation of electroactive NiCo2S4 and Fe2O3 into graphene aerogel for high-energy asymmetric supercapacitor. *Colloids and Surfaces A: Physicochemical and Engineering Aspects*, *602*(May), 125110. https://doi.org/10.1016/j.colsurfa.2020.125110

Henning, S., Ishikawa, H., Kühn, L., Herranz, J., Müller, E., Eychmüller, A., & Schmidt, T. J. (2017). Unsupported Pt-Ni Aerogels with Enhanced High Current Performance and Durability in Fuel Cell Cathodes. *Angewandte Chemie - International Edition*, *56*(36), 10707–10710. https://doi.org/10.1002/anie.201704253

Mart, A., Ram, L. A., Ledesma-garc, J., Montes-mor, M. A., Gurrola, M. P., Men, J. A., Arenillas, A., & Arriaga, L. G. (2022). *Facile Synthesis of Unsupported Pd Aerogel for High Performance Formic Acid Microfluidic Fuel Cell*.

Moussaoui, R., Elghniji, K., ben Mosbah, M., Elaloui, E., & Moussaoui, Y. (2017). Sol–gel synthesis of highly TiO2aerogel photocatalyst via high temperature supercritical drying. *Journal of Saudi Chemical Society*, *21*(6), 751–760. https://doi.org/10.1016/j.jscs.2017.04.001

Qiao, L., & Swihart, M. T. (2017). *Solution-phase synthesis of transition metal oxide nanocrystals : Morphologies , formulae , and mechanisms*. *244*, 199–266.

Roh, H., Lim, C., Kim, D., Park, T., & Yong, K. (2023). Hierarchically nanostructured Ni(Mo,Co)-WOx electrocatalysts for highly efficient urea electrolysis. *Applied Surface Science*, *610*(November 2022), 155520. https://doi.org/10.1016/j.apsusc.2022.155520

Samir De, B., Cunningham, J., Khare, N., Luo, J. L., Elias, A., & Basu, S. (2022). Hydrogen generation and utilization in a two-phase flow membraneless microfluidic electrolyzer-fuel cell tandem operation for micropower application. *Applied Energy*, *305*(September 2021), 117945. https://doi.org/10.1016/j.apenergy.2021.117945

Sashkina, K. A., Gurikov, P. A., Ayupov, A. B., Smirnova, I., & Parkhomchuk, E. V. (2018). Zeolite/silica aerogel composite monoliths and microspheres. *Microporous and Mesoporous Materials*, *263*(December 2017), 106–112. https://doi.org/10.1016/j.micromeso.2017.12.010

Suenaga, S., & Osada, M. (2019). Preparation of β-chitin nanofiber aerogels by lyophilization. In *International Journal of Biological Macromolecules* (Vol. 126, pp. 1145–1149). https://doi.org/10.1016/j.ijbiomac.2019.01.006

Titirici, M. M., Antonietti, M., & Thomas, A. (2006). A generalized synthesis of metal oxide hollow spheres using a hydrothermal approach. *Chemistry of Materials*, *18*(16), 3808–3812. https://doi.org/10.1021/cm052768u

Wen, D., Liu, W., Haubold, D., Zhu, C., Oschatz, M., Holzschuh, M., Wolf, A., Simon, F., Kaskel, S., & Eychmüller, A. (2016). Gold Aerogels: Three-Dimensional Assembly of Nanoparticles and Their Use as Electrocatalytic Interfaces. *ACS Nano*, *10*(2), 2559–2567. https://doi.org/10.1021/acsnano.5b07505

Zanella, R. (2012). Metodologías para la síntesis de nanopartículas: controlando forma y tamaño. *Www.Mundonano.Unam.Mx*, *5*(1), 69–81. www.mundonano.unam.mx

CAPÍTULO 3

AEROGELES DE PALADIO Y PALADIO-METAL PARA SISTEMAS MICROFLUIDICOS EFICIENTES

3.1 ELECTROCATALIZADORES DE PALADIO PARA LA ELECTROOXIDACION DE ETANOL

En la actualidad la producción de energía se ha enfocado fuertemente al uso de biocombustibles con el fin de satisfacer las altas exigencias y requisitos de sostenibilidad actuales, evitando asi los combustibles fósiles (Corbo et al., 2011). Uno de los biocombustibles que surge como una alternativa eficiente es el etanol, el cual puede aprovecharse en un sistema electroquímico para generar energía a partir del siguiente mecanismo (Yazdan-abad et al., 2019):

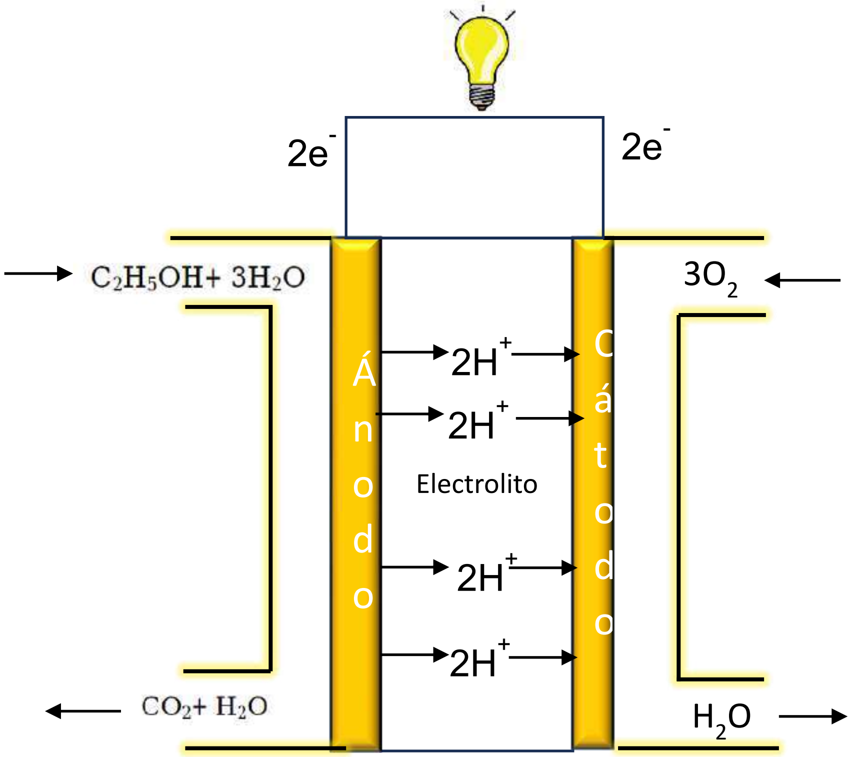

Fig. 3.1 Esquema de funcionamiento de una celda electroquímica de etanol

En el ánodo el etanol es oxidado a un potencial teórico de 0.084 V vs ERH (electrodo reversible de hidrogeno):

$$C_2H_3OH + 3H_2O \rightarrow 2CO_2 + 12e^- + 12H^+ \qquad \text{(Ec. 3.1)}$$

En el cátodo, en el cual el oxígeno es reducido para formar agua a un potencial estándar de 1.229 V vs ERH:

$$3O_2 + 12\,H^+ + 12e^- \rightarrow 6H_2O \qquad \text{(Ec. 3.2)}$$

De lo anterior podemos considerar ambos potenciales para calcular un potencial de circuito abierto teórico de 1.145 V vs ERH.

3.1.1. Selectividad del paladio hacia la electrooxidación de etanol

Para llevar a cabo la oxidación de etanol por via electroquímica se han empleado catalizadores de metales nobles como el Pd, ya que tiene excelentes propiedades relacionadas principalmente con la actividad y la estabilidad, tales como: evitar el desprendimiento de partículas; minimizar la pérdida de contacto eléctrico y brindar mayor durabilidad debido a su baja susceptibilidad a la degradación (Abbas et al., 2017; Douk & Saravani, 2020). Las reacciones que tienen lugar e involucran al paladio en presencia del etanol son las siguientes:

$\text{Pd} + \text{OH}^- \rightarrow \text{Pd-OH}_{ads} + e^-$ (Ec. 3.3)

$\text{Pd-CH}_3\text{CH}_2\text{OH} \rightarrow \text{Pd -(CH}_3\text{CH}_2\text{OH)}_{ads}$ (Ec. 3.4)

$\text{Pd-(CH}_3\text{CH}_2\text{OH)}_{ads} + 3\text{OH}^- \rightarrow \text{Pd-(CH}_3\text{CO)}_{ads} + 3\text{H}_2\text{O} + 3e^-$ (Ec. 3.5)

$\text{Pd-(CH}_3\text{CO)}_{ads} + \text{Pd-OH}_{ads} + \text{OH}^- \rightarrow \text{CH}_3\text{COO}^- + 2\text{Pd} + \text{H}_2\text{O}$ (Ec. 3.6)

En la reacción 6 se puede observar que el Pd-OH formado beneficia la reacción de oxidación del combustible evitando intermediarios, pasando nuevamente a Pd y quedando disponible para oxidar nuevamente el combustible (Douk et al., 2018).

En algunas reacciones electroquímicas los metales nobles resultan altamente efectivos, como lo es el caso de la reacción de oxidación de etanol. La excelente actividad electrocatalítica de los metales nobles como el Pd hacia esta reacción hace que no se dude de su capacidad y se utilicen comúnmente como electrocatalizadores en dispositivos comerciales. Sin embargo, se trata de un mateiral muy costoso y poco abundante (Morales-Acosta et al., 2010). Es principalmente por este problema por el que en esta Tesis Doctoral se ha propuesto reducir el uso de metales nobles mediante la combinación con metales de transición, mucho mas abundantes y de bajo costo.

3.2. EFECTO DE LA INCORPORACIÓN DE METALES DE TRANSICIÓN EN AEROGELES DE PALADIO PARA LA ELECTROOOXIDACIÓN DE ETANOL

Los metales de transición (MT) son excelentes transportadores de oxigeno y es por ello que podrían beneficiar la oxidación de etanol, ya que el OH- presente en la solución llegaría a la superficie del electrodo rápidamente. Esto combinado con la selectividad del Pd hacia grupos CH_3CO (R5), generados en esta reacción, y que son adsorbidos en la superficie de los catalizadores de Pd, produce que la combinación Pd-MT acelere considerablemente la reacción de evolución de oxígeno (Douk & Saravani, 2022), propiciando la formación de acido acético y agua (R6). Por lo tanto, el proceso anterior puede describirse de la siguiente forma:

$$\text{Pd-}(CH_3CO)_{ads} + \text{Pd(M)-}OH_{ads} + OH^- \rightarrow CH_3COO^- + 2\text{Pd(M)} + H_2O \qquad \text{(Ec. 3.7)}$$

En la presente Tesis Doctoral se evaluaron distintas concentraciones de los metales Ni, Fe y Co en combinación con el Pd, para evaluar la influencia de los metales de transición hacia la oxidación de etanol y relacionar su actividad con las propiedades fisicoquímicas de cada aerogel.

Publicacion cientifica

En el articulo científico que se incluye a continuación (revista Materials Today Nano, situalda en el Q1 de Materiales) se muestran los principales resultados de la evaluación de las combinaciones de Pd-(Metal de Transición) hacia la reacción de oxidación de etanol. Los mejores resultados se presentaron en las muestras que contenían una menor cantidad del metal de transición, como podría esperarse. Sin embargo, las combinaciones entre metales de transición y el paladio superaron al Pd por si solo debido a un efecto sinérgico. Esto resulat muy relevante ya que se minimiza la utilización del metal noble a la vez que se mejoran las prestaciones electroquímicas del catalizador.

Materials Today Nano 22 (2023) 100308

Contents lists available at ScienceDirect

Materials Today Nano

journal homepage: https://www.evise.com/profile/#/MTNANO/login

Novel and high electrocatalytic activity aerogel Pd-TM (TM=Co, Ni, Fe)

A. Martínez-Lázaro [a, e], M.H. Rodriguez-Barajas [a, e], N. Rey-Raap [b], F.I. Espinosa [c], L. Álvarez-Contreras [d], J. Ledesma-García [a], A. Arenillas [b, **], L.G. Arriaga [c, *]

[a] División de Investigación y Posgrado, Facultad de Ingeniería, Universidad Autónoma de Querétaro, 76010, Santiago de Querétaro, Mexico
[b] Instituto de Ciencia y Tecnología del Carbono, INCAR-CSIC, Francisco Pintado Fe, 26. 33011 Oviedo, Spain
[c] Centro de Investigación y Desarrollo Tecnológico en Electroquímica, 76703, Santiago de Querétaro, Mexico
[d] Centro de Investigación en Materiales Avanzados S. C., 31136, Complejo Industrial Chihuahua, Chihuahua, Mexico

A R T I C L E I N F O

Article history:
Received 3 November 2022
Received in revised form
10 January 2023
Accepted 15 January 2023
Available online 21 January 2023

Keywords:
Aerogels
Unsupported electrocatalysts
Ultrafast synthesis
Non-noble electrocatalyst
Ethanol oxidation reaction

A B S T R A C T

In the present research work, unsupported Pd-TM aerogel catalysts are prepared by an ultrafast synthesis by means of a combination of microwave heating and lyophilization. These novel aerogels are synthesized to explore the effect of transition metals on a Pd aerogel matrix in order to reduce the dependence on noble metals and increase its electrocatalytic properties for different electrochemical reactions. Physicochemical characterization of Pd-TM aerogels reveals a successful combination of high specific surface area, electrochemical surface area, and specific oxidation states. The combination of these properties in Pd-TM aerogels enhances the electrocatalytic activity towards ethanol electrooxidation compared to bare Pd aerogels. Among all the Pd-TM, PdNi aerogel presents the highest current per unit mass with 117 mA/mg, being a clear improvement compared to the Pd aerogel (48 mA/mg).

1. Introduction

There is a constantly increasing interest in improving electrochemical devices for the production of energy in order to satisfy its currently high demand and sustainability requirements. However, these devices traditionally employ noble metals catalysts [1–4], since they have excellent properties mainly related to activity and stability, such as (i) avoiding detachment of particles, (ii) minimizing loss of electrical contact, and (iii) improved durability due to their less susceptible to degradation [5]. In the search for innovative catalysts, noble metals have been usually incorporated into different materials that act as supports and facilitate the availability of these active sites. Furthermore, even more recently, some innovative materials are being developed to provide physicochemical properties, such as porosity and high surface area, to the noble metal catalyst themselves in order to improve their performance avoiding the use of supports [6,7]. Among these new materials the use of noble metals for the manufacture of aerogels has been of great interest in recent years, however, most of the metallic aerogels investigated recently are made with an organic compound and noble metals, such as Pt [8–10], Au [11,12], Pd [13–16], Ag [17,18] and their combinations [7,19–23], as well as aerogels of metal oxides and noble metals [16,24,25]. These unique materials have been applied as efficient electrocatalysts for the electrooxidation of organic fuels such as ethanol, formic acid, and oxygen. These materials are highly novel due to their unique morphology of assembled nanoparticles; recent work shows that assembling sheets considerably improves the catalytic activity of aerogels towards oxidation reactions [49–52].

The synthesis methods of aerogels have changed over the years [6,13], although literature shows that slight modifications of the synthesis steps will be traduced in notable differences in their final properties [26]. In 1846, J.J. Ebelmen, synthesized the first silica aerogel using the sol-gel method [27]. This methodology involves a gelation process, where a solution loses its fluidity and takes the appearance of an elastic solid, followed by curing and drying steps. The drying step is usually performed under supercritical conditions (i.e. temperatures higher than 300 °C and up to 219 atm) [28]. However, other drying methods have been proposed in the last decades, such as lyophilization, which avoids such as extreme operating conditions [7,29].

---

* Corresponding author.
** Corresponding author.
E-mail addresses: aapuente@incar.csic.es (A. Arenillas), larriaga@cideteq.mx (L.G. Arriaga).
[e] A. Martinez-Lázaro and M. H. Rodriguez-Barajas contributed equally to the work.

https://doi.org/10.1016/j.mtnano.2023.100308
2588-8420/© 2023 Elsevier Ltd. All rights reserved.

Microwave heating can be used for chemical synthesis as a heating source besides to favour interactions between reactants [30,31]. Their dipolar polarization and conduction of ions in liquid solutions cause the collision of ions and molecules to produce uniform heating in the precursor mixture, promoting the reactions. This technology is very effective as the energy is transferred directly to the reactants, minimizing gradients and energy losses. As a consequence, synthesis time is considerably reduced. Hence has been previously used for sol-gel synthesis of carbon [32,33] and silica gels [34,35]. Moreover, Martínez-Lázaro et al. used microwave heating to produce Pd aerogels with high yield by using a rapid and controlled synthesis process [29].

Pd has been successfully used as electrocatalyst due to its high speed of electron transfer [21,36,37], and is considered a replacement for Pt as electrocatalyst in the ethanol oxidation reaction due to the higher density current in alkaline media [13,19–21,38]. On the other hand, there is an increasing interest in developing new and efficient electrocatalysts but avoiding the use of noble metals due to their high cost and low availability [46–48]. Therefore, in this work, Pd was partially substituted by transition metals (TM). Specifically Fe, Co, and Ni were combined with Pd to produce a cost- and electrocatalytic-effective metallic aerogel by means of microwave heating. The innovative procedure and final aerogels obtained are presented as an interesting step forward in the development of innovative and efficient electrocatalysts for energy generation devices.

2. Experimental procedures

2.1. Chemical reagents

$PdCl_2$ (99%, Sigma-Aldrich ReagenPlus®, anhydrous powder, St Louis, MO, USA), $CoCl_2 * 6H_2O$ (98%, Sigma-Aldrich ®, ACS reagent, St Louis, MO, USA), $NiCl_2 * 6H_2O$ (99.9%, Sigma-Aldrich®, St Louis, MO, USA), $FeCl_2$ (98%, Sigma-Aldrich ®, St Louis, MO, USA), Na_2CO_3 anhydrous (99.5%, JT. Baker R®), Glyoxilic acid (98% Sigma-Aldrich). Water was provided with the UPT-IV-10L system (18.3 MΩ cm).

2.2. Microwave-assisted synthesis of aerogels

The synthesis procedure is based on previous work on Pd-aerogels [29] with some modifications. Aerogels [Pd:TM] were prepared in proportion [4:1] for each metal salt (Co, Fe, Ni). The concentration of the precursor salt solution mixture was 2 mg/ml20 ml of the mixture was taken to react with sodium carbonate and glyoxylic acid monohydrate solution (ratio 6:1) [14] in deionized water. The heating source consisted in a microwave heating (MW) at 67 °C controlled by introducing a thermocouple into the precursor mixture. All process was carried out during 7 h: the first 2 h takes place the formation of the colloids and the last 5 h the gelation and crosslinking processes are carried out. Subsequently, the samples were cooled to room temperature for washing before drying.

The drying process was performed with a residual volume of deionized water. The mixture was then frozen with liquid N_2 and the solvent eliminated by lyophilization (HyperCOOL, model: HC3110) at −110 °C for 24 h. A scheme of the whole synthesis process is presented in Fig. 1.

2.3. Physicochemical characterization

The morphology of Pd-TM aerogels was characterized using a scanning electron microscope (SEM, Quanta FEG 650 microscopes from FEI). The crystal structures were evaluated by X-ray diffraction (XRD; D8-advance diffractometer Bruker) equipped with CuKα X-ray source (λ = 0.1541 nm, 40 kV, 40 mA) using a step size of 0.02° 2Θ and a scan step time of 5 s. The calculation of the lattice constant (d_{hkl}) was made from the following expressions:

$$d_{spacing} = \frac{\lambda}{2 \sin \theta} \tag{1}$$

$$d_{hkl} = d_{spacing} \sqrt{h^2 + k^2 + l^2} \tag{2}$$

where $d_{spacing}$ is the interplanar spacing and h, k and l the miller index. The position of the 2Θ peaks and the width at the half height of the peak $(\beta_{hkl})_{\text{sample}}$ were also determined. The instrumental correction was carried out with a standard pattern and the error of the instrument and β_{Total} was adjusted using the following expression:

$$\beta_{Total} = \beta_{Experimental} + \beta_{sample} \tag{3}$$

where $\beta_{Experimental}$ is the error of the instrument and β_{sample} the sample values. From the data collected in the XRD, the crystallite size and the microstrain of the crystal lattice were determined. First, the crystallite size (D_{111}) was calculated using the Scherrer equation:

$$D_{111} = \frac{K\lambda}{\beta_{111} \cos \Theta} \tag{4}$$

where K is Scherrer constant corresponding to cubic symmetry, and (β_{111}) is the line broadening of width at half maximum.

The specific surface area was estimated by nitrogen adsorption-desorption isotherms at −196 °C (Micromeritics ASAP 2020), after outgassing the samples overnight at 120 °C. The chemical surface composition and the oxidation state of elements were measured by X-ray photoelectron spectroscopy (XPS, Analyzer Phoibos 100, SPECS, Germany). A monochromatic AlKα X-ray source operating at 14 kV was employed to perform the analysis.

2.4. Electrochemical measurements

2.4.1. Electrocatalytic activity in half-cell configuration

The electrochemical evaluation of the Pd-TM aerogels was carried out in a conventional three-electrode cell in alkaline media at 50 mV/s scan rate. A glassy carbon electrode (3 mm of diameter), an Ag/AgCl electrode, and a Pt wire were used as working, reference and counter electrodes, respectively. The electrocatalyst ink was prepared using each sample in a mixture of deionized water (500 μL) and Nafion® (5%, 50 μL) per milligram of aerogel.

The ink was sonicated during 15 min and then 10 μL were deposited over the working electrode surface. The electrolyte was bubbled with N_2 for 40 min before the electrochemical measurements. For each sample, the electrochemical profile was obtained by cyclic voltammetry (CV) experiments in 0.5 M KOH within a potential range of −0.25 to 1.6 V vs RHE. The electrochemical active surface area (ECSA) of each aerogel was estimated from the cyclic voltammograms by using the reduction charge of Pd (II) oxide according to the following equation:

$$ECSA = \frac{Q_m}{m_{Pd} e d_m} \tag{5}$$

where, Q_m denotes coulombic charge (Q per μC cm^{-2}) for the reduction of Pd (II) oxide achieved by integrating the charges related to the reduction of Pd (II) oxide for the different samples; *mPd* is the mass amount of Pd loaded (g cm^{-2}) on the glassy carbon

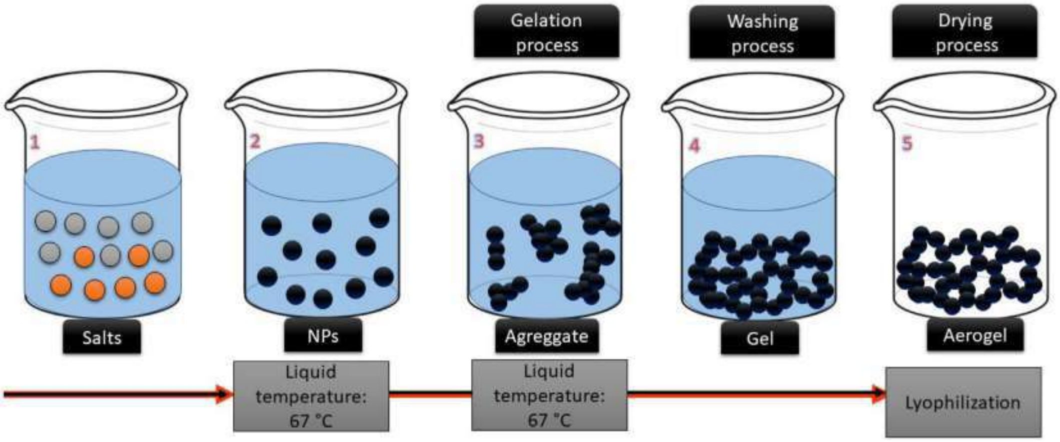

Fig. 1. Pd-TM aerogel synthesis.

electrode surface and ed_m is a constant (424 μC/cm), which corresponds to the reduction of a Pd (II) oxide monolayer.

2.4.2. *Ethanol electrooxidation performance*

The electrocatalytic activity of the Pd-TM aerogels towards the electrooxidation of ethanol was tested by cyclic voltammetry (CV) in 0.5 M KOH + 0.5 M ethanol solution within a potential range between −0.25 and 1.6 V vs. RHE. This solution was bubbled with N_2 for 40 min before each electrochemical measurement.

2.4.3. *Electrochemical stability*

The stability performance was carried out by chronoamperometry in the three-electrode system at 0.6 V *vs.* RHE for 90 h in 0.5 M KOH +0.5 M ethanol as electrolyte.

3. Results and discussion

3.1. *Physicochemical characterization*

XRD spectra of the synthesized aerogels are shown in Fig. 2a. In the XRD pattern of the Pd and Pd-TM aerogels were observed four major diffraction peaks appear at the 2Θ values. The peak with the highest intensity was used for the calculation of crystallite size. For Pd aerogel, the peaks were 40.1°, 46.6°, 68.1° and 82.1° which are ascribed to the (111), (200), (220) and (311) reflection planes of Pd (JCPDS #46–1043), respectively. These peaks are according with a face-centered cubic (FCC) crystal structure. Despite the resulting aerogels revealed characteristic peaks of Pd, a shift in the position of the Pd-peaks was observed for Pd-TM aerogels. These show a change to the left suggesting the presence of alloys. The PdCo aerogel presents the peaks in 2Θ were 40.1°, 46.2° 68.1° and 81.8°, comparing with the reference JCPDS #65–6075 corresponding to PdCo, which has a peak with high intensity in 2Θ with the value of 41.7° corresponding to reflection plane (111), being further away from the one obtained and coinciding even more with the JCPDS #46–1043 of Pd [39]. In the case of PdNi aerogel, peaks were located at 39.9°, 46.6°, 67.9° and 81.9, presenting a more significant displacement compared to the JCPDS #46–1043 of Pd, JCPDS #72–9071 corresponding to PdNi [40] with peaks in 40.2°, 47°, 68.8°, 82.9° and 87.3° which do not correspond to those obtained, again indicating more excellent proximity to the JCPDS of the Pd. Finally, PdFe aerogel with peaks in 35.5°, 40.1°, 46.9°, 57.1°, 62.9°, 68°, 81.9° and 86.6, presenting again the trend observed with the previously mentioned aerogels where a shift to the left is shown. Although the closeness of the peaks is observed, corresponding to the JCPDS of the Pd, it is taken into account presents peaks at 35.5° and 86.6° that correspond to reflection planes of FeO(OH) (JCPDS #74–3080) [41].

The $d_{spacing}$ for Pd, PdCo, PdNi and PdFe aerogels calculated at (111), (200), (220) and (311) were 2.24 Å, 1.95 Å, 1.37 Å and 1.17 Å, respectively. These values were employed to calculate the lattice constants (d_{hkl}) and evaluate if the addition of TM to the Pd structure makes any difference. Thus, the calculated d_{111} values were 3.89, 3.90, 3.89 and 3.88 for Pd, PdCo, PdNi and PdFe, respectively (the error is ≤ 0.3 of the standard JCPDS #46–1043 with a value of 3.89).

The crystallite sizes obtained using the 2Θ value of 40.1°, with the Scherrer equation (Eq. (4)) were 9.46, 3.70, 3.96 and 11.04 nm for Pd, PdCo, PdNi and PdFe, respectively. There is a great difference between materials, detecting a notable decrease of crystallite size for PdCo and PdNi aerogels and a slight increase for PdFe aerogel compared to that obtained for Pd aerogel.

Calculation of microstrain (ε) with XRD data was also performed to evaluate if it was the cause of the broadening of the peaks, indicating dislocations within the crystal structure. For this evaluation the following equation was used:

$$\varepsilon = \frac{\beta_{Total}}{4\tan\theta} \tag{6}$$

The data obtained could indicate a decrease in microstrain as the angle increases and the crystallite size should be consistent in a range of two theta values. However, the microstrain values obtained do not show a decreasing trend and the crystallite size decreases as the angle increases. This result clearly indicates that the crystallite size also contributes to peak broadening. Therefore, the Williamson Hall method (W–H) was employed using the following expression:

$$\beta_{Total}\cos\theta_{hkl} = \varepsilon(4\,sen\,\theta_{hkl}) + \frac{K\lambda}{D} \tag{7}$$

The first four reflections (111), (200), (220) and (311) were used to construct the plot of $4\mathrm{sen}\Theta_{hkl}$ vs $\beta_{Total}\cos\Theta_{hkl}$. The crystallite size and the microstrain are obtained from the intercept and slope of the fitted line, respectively. The values obtained for crystallite size were 5.5 nm and 2.53 nm for PdNi and PdFe (Fig. 2b). According to the results, an increasing trend is observed, implying the presence of defects (i.e. distortions, dislocations, faulting and relaxation of the grain surface). In addition, the fitting line does not cross the ordinate axe through the origin, indicating a significant size effect.

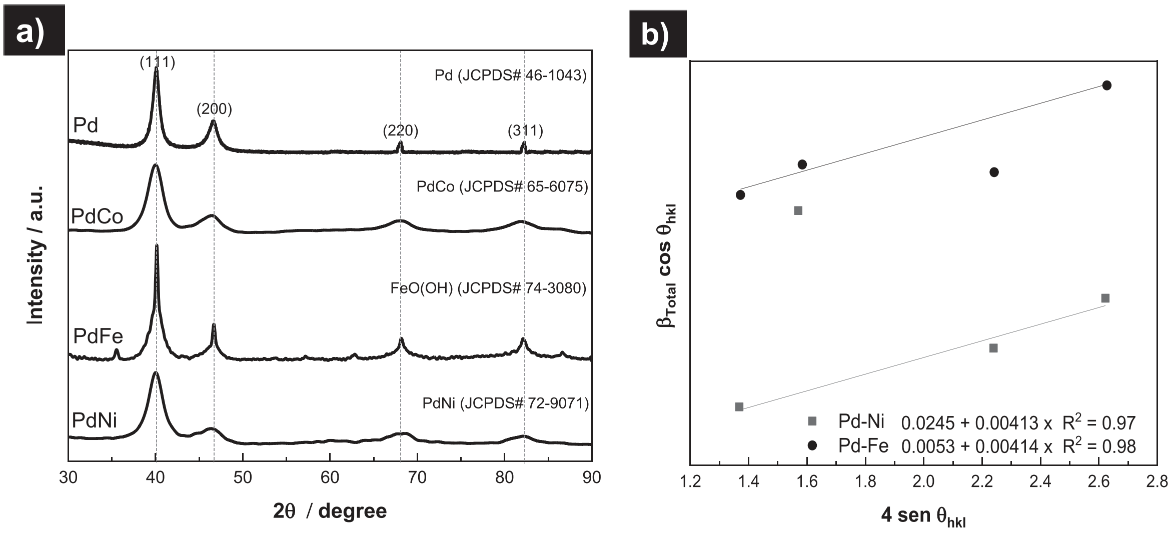

Fig. 2. a) XRD of Pd and Pd-TM (Ni, Fe, Co). b) W–H plot of PdNi and PdFe aerogels.

The microstrain obtained in both samples is very close, as shown by the slope of the adjustment. For PdNi a linear adjustment was obtained without taking into account the point that is too deviated (1.6, 0.041). In the case of PdCo, the W–H method was not able to be applied, since the values of 4 *sen* θ_{hkl} do not vary with $\beta_{Total}\cos\Theta_{hkl}$. This is due to the fact that the stress in the crystal lattice since the strain is not related to the broadening of the diffraction peaks. In the case of PdNi and PdFe assuming that the broadening of the peaks is due to the contribution of microstrain.

The specific surface area of the Pd-TM aerogels was determined by the Brunauer-Emmett-Teller (BET) method applied to the nitrogen adsorption-desorption isotherms (Fig. 3) yielding values of 77, 66, 47 and 4 m^2/g for Pd, PdCo, PdNi, and PdFe respectively. This indicates the presence of certain microporosity in these samples, especially for Pd, PdCo and PdNi aerogels. The helium densities of these samples are 1.4, 1.2 and 2.5 g/cm^3 for PdCo, PdNi and PdFe, respectively. These values indicate a clear difference in the total porosity of the samples, being the Pd–Ni the sample less dense, and therefore, with higher total porosity. By applying 2D-NLDFT to the adsorption isotherms, a pore size distribution is obtained (Fig. 3b). Although it cannot be provided a mean pore size for each aerogel obtained due to the wide pore size distribution, it can be said that there is a clear trend to increase in the pore size from PdFe, PdNi, to PdCo. The lowest helium density of PdNi aerogel probably indicates the presence of macroporosity in higher extent than in PdCo and for sure in much higher extent than PdFe. This latter aerogel is the less porous of the series.

BET surface areas of Pd aerogels should be in the range of 32–162 m^2/g, the density in the range of 0.10–12 g/cm^3 and the pore size <50 nm according to the bibliography [6,19,20]. In fact, the surface area of the Pd aerogel is referenced as 50 m^2/g and the pore size of about 11 nm [20]. Comparing these values with the values obtained in this work, except in the case of PdFe aerogel, in general, the porous properties are preserved. This is a very relevant feature because is a key factor for promoting mass transport through the 3D porous network.

Further, the morphology of the aerogels was characterized by Field Emission Scanning Electron Microscopy (FESEM) and High Resolution Transmission Electron Microscopy (HRTEM). The micrographs are presented in Fig. 4.

The aerogels present a foam-like morphology, with a 3-dimensional open porous network. The FESEM images show a

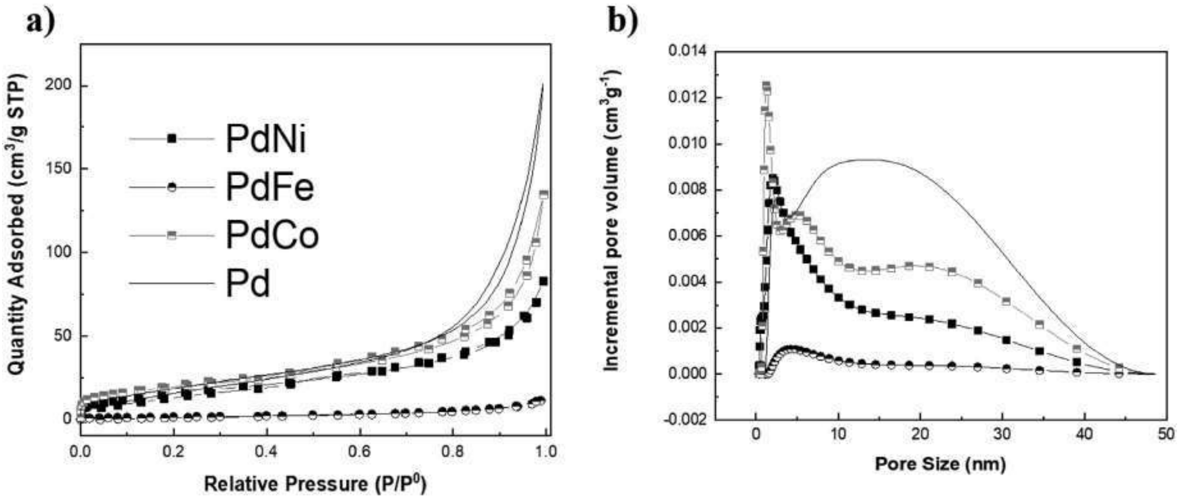

Fig. 3. a) N_2 adsorption-desorption isotherms for the synthesized Pd-TM aerogel samples b) Pore size distribution in the samples studied according to 2D-NLDFT model.

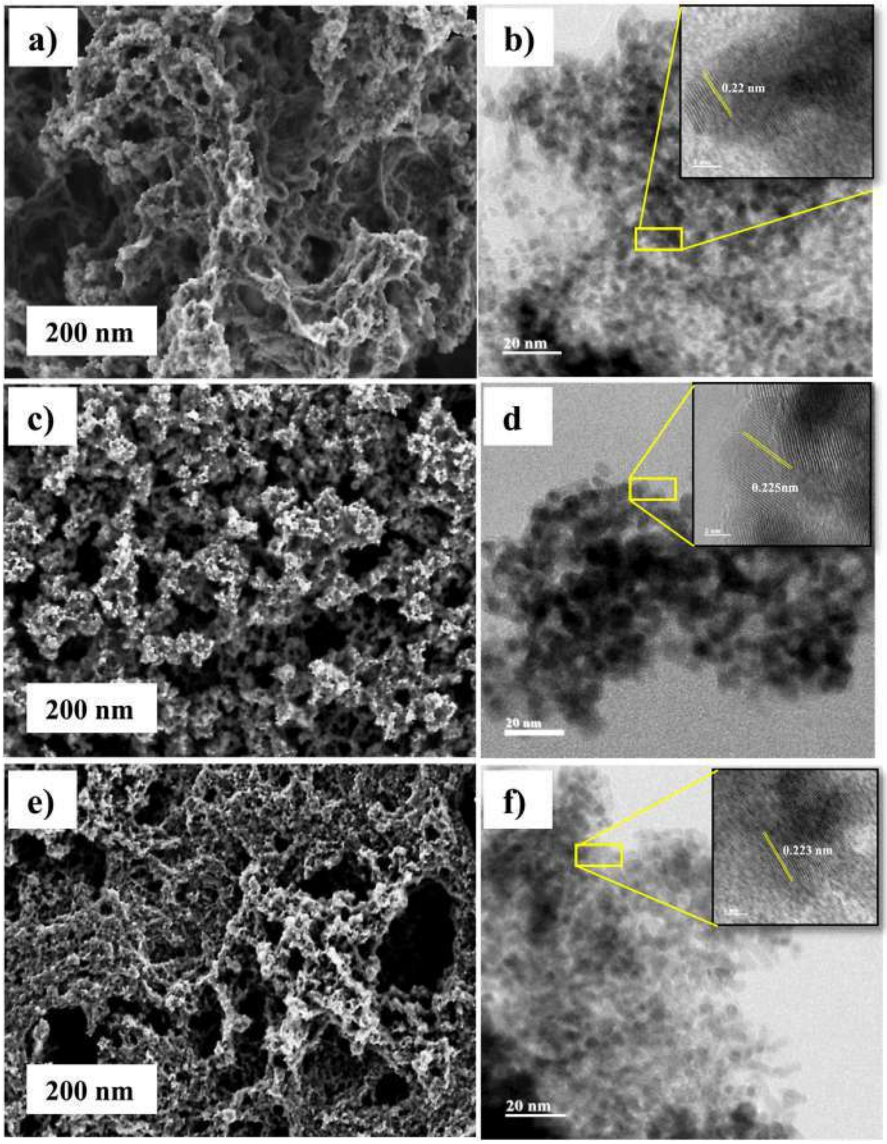

Fig. 4. FESEM (a, b, c) and HRTEM (d, e, f) images of the synthesized aerogels: a and d correspond to PdCo; b and e are PdNi aerogel and c and f correspond to PdFe aerogel.

more open porosity structure in the case of PdCo (Fig. 4a), and a more fused and less porous structure in the case of the PdFe aerogel (Fig. 4c). The aerogel PdNi (Fig. 4b) presents an intermediated porous morphology. These observations are in agreement with the results previously discussed from helium density and N_2 adsorption-desorption isotherms. HR-TEM analysis reveals an interconnected distribution of particles in all samples obtained (Fig. 4 d-f). Images at different magnifications show chains of particles defining pores of different sizes between them, typically characteristic for aerogels. PdCo aerogel shows particle sizes between 2 and 4 nm, similar to the sample PdFe (between 1 and 3 nm). It seems that Co and Fe metal transition incorporation allows obtaining smaller sizes than that obtained for PdNi particles (5–8 nm). At higher magnification, it can be seen that the interplanar distances are slightly higher for PdNi aerogel (0.225 nm), which can be attributed to the presence of alloy between the two metals used in the synthesis. The interplanar distance for Pd–Co and PdFe is 0.22 and 0.223 nm respectively.

By means of X-ray photoelectronic spectroscopy (XPS), the analysis of the Pd–Ni, Pd–Fe, and PdCo aerogels was carried out to know their chemical composition and the oxidation state (see Fig. 5). The general spectrum of the samples (Fig. 5a) indicates the presence of C, Pd, Co, O, Fe, and Ni, as expected. The spectra of Pd 3d are shown in Fig. 5b, where a comparison is made of the oxidation states present in Pd–Fe, Pd–Ni, and Pd–Co samples. Each spectrum was deconvoluted into the orbitals Pd $3d^{5/2}$ and Pd $3d^{3/2}$, which peaks are centered at 335.1 eV and 342.2 eV corresponding to Pd^{2+}, 336.2 eV and 342.5 corresponding to Pd^{4+} while those located in 335.1 eV and 340.7 eV refer to Pd^0 [22,39,40]. A higher concentration of Pd^{2+} is observed in the Pd–Fe and Pd–Ni samples, meanwhile, Pd^{4+} is present in a higher concentration in the Pd–Fe and Pd–Co samples. The high-resolution scan of Fe 2p is presented in Fig. 5e. The spectra of Fe $2p^{3/2}$ and Fe $2p^{1/2}$ were deconvoluted, giving the peaks 709.8 eV and 724.09 eV that refer to Fe^0, signals in 712.5 eV and 724.2 eV that corresponds to Fe^{2+} and those located in 715.0 eV and 732.5 eV attributed to Fe^{3+}. These results suggest the presence of the Fe_2O_4 structure as already reported in the literature [41]. The quantitative evaluation of each peak was also made from the XPS results by dividing the area of the peak, which was calculated from the cross-sections and the mean depth of the exhaust

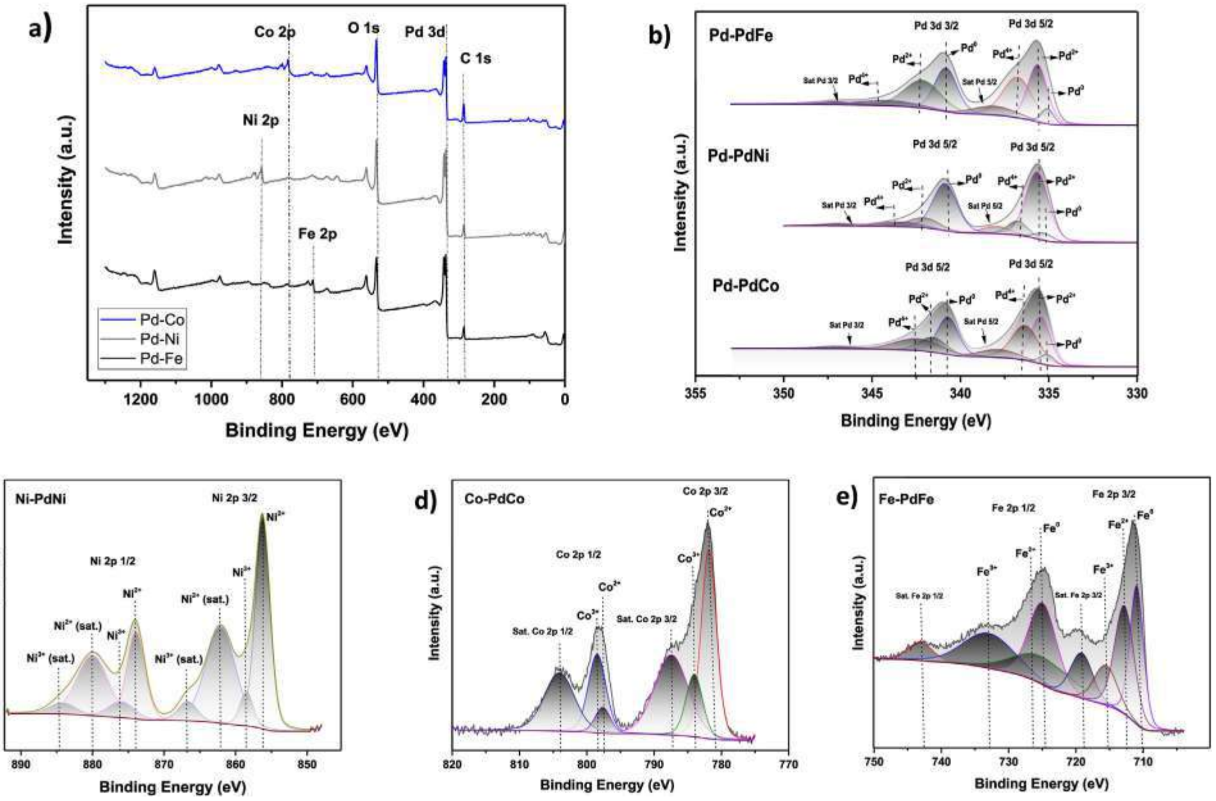

Fig. 5. a) High-resolution XPS general spectra for PdFe, PdNi and PdCo aerogels; b) high-resolution spectrum in the Pd 3d region for PdFe, PdNi and PdCo aerogels; c) high-resolution spectrum in the Ni 2p region for PdNi aerogel; d) high-resolution spectrum in the Co 2p region for PdCo aerogel; and e) high-resolution spectrum in the Fe 2p region in PdFe aerogel.

electrons [42]. XPS data were interpreted using the Avantage Thermo software, with angular resolution (ARXPS) and the adjustment of the peaks by the Analyzer software. $Fe_{0.94}$ $Pd_{0.1}$ was the molar proportion obtained for the PdFe aerogel. Furthermore, the chemical composition was also determined by calculating the percentage of the relative weight of the sample. PdFe aerogel presents a higher percentage of Pd^{2+} (41.8%) in comparison with Pd^{4+} (11.7%), the percentage of the iron species in its metallic state (Fe^0) is 40.2%, while the percentage of the oxidized species Fe^{2+} and Fe^{3+} is 38.5% and11.9%, respectively. These results suggest that PdFe aerogels can be oxidized, resulting in the oxidation of Fe^0 to Fe^{3+}. However, the oxidation is not complete, as can be seen in Fig. 5e, which is consistent with the results of XRD. The spectrum of Ni 2p is observed in Fig. 5c, having deconvolution orbitals in Ni $2p^{3/2}$ and Ni $2p^{1/2}$, with the peaks of 855.1 eV and 872.5 eV corresponding to Ni^{2+}, while those located at 856.6 eV and 874.0 eV refer to Ni^{3+} [43,44]. The molar proportion obtained for PdNi aerogel is $Ni_{0.64}Pd_{0.1}$. From the calculation of the percentage of the relative weight of the sample, it can be inferred that PdNi presents a higher percentage of Ni^{2+} (45.8%) than Ni^{3+} (28.7%).

The high-resolution scanning of Co 2p is presented in Fig. 5d. The spectra of Co $2p^{3/2}$ and Co $2p^{1/2}$ were deconvoluted, giving the peaks 784.9 eV and 797.2 that correspond to Co^{2+} and those located in 780.2 eV and 796.72 referred to Co^{3+}, which correspond to the Co_3O_4 structure [45]. The presence of the PdCo alloy on the surface can be appreciated, having the two spectra in their oxidation state. The quantitative evaluation of each peak was obtained by dividing the area of the peak, which was calculated from the cross-sections, and the mean depth of the escape electrons. The molar proportion for PdCo aerogels was $Pd_{0.1}Co_{0.72}$. In addition, the percentage of the relative weight of the sample indicates that there is a higher percentage of Pd^0 (40.3%) than the oxidized species Pd^{2+} (10.5%) and a higher proportion of the oxidized species Co^{2+} (38.5%) in comparison to Co^3 (18.6%). This shows that PdCo aerogels can be oxidized, resulting in a larger proportion of Co^{2+} than Co^{3+}, which is consistent with the results of XRD.

The elemental composition, the oxidation states, and the relationship between their concentrations evaluated by the XPS analysis will be related to the following electrochemical analysis.

3.2. Electrochemical performance

Aerogels were evaluated by cyclic voltammetry (CV) to determine their electrocatalytic activity for ethanol oxidation reaction (EOR) in a potential range between −0.25 and 1.6 V vs RHE. Electrochemical profiles were obtained in 0.5 M KOH as electrolyte at ambient conditions at 50 mV/s scan rate (Fig. 6a). A Pd aerogel sample obtained by the same synthesis method was also characterized for comparative purposes. The experimental CVs show the peaks attributed to Pd activity: (i) the hydrogen desorption in the range 0.1–0.2 V vs RHE, (ii) hydrogen adsorption at 0.3 V vs RHE, (iii) reduction of Pd (II) oxide from 0.55 to 0.8 V vs RHE and (iv) formation of Pd (II) oxide at 1–1.4 V vs RHE. All these phenomena are present in the cyclic voltammograms of all Pd aerogels. However, samples containing transition metals show peaks that are attributed to the oxidation and reduction of each metal species (i.e. Co, Ni and Fe). The redox processes of the noble metal species can be observed at different potentials (Fig. 6a), for PdNi at 1.2 V vs RHE, marked with the legend 3 [Ni]; for PdCo oxidation and reduction processes are observed between 1.1 and 1.3 V vs RHE, which can be seen with the legend 2 [Co]; while Fe redox processes occur between 0.3 and 0.6 V vs RHE, which are labeled 1 [Fe] and 1 [Fe]'.

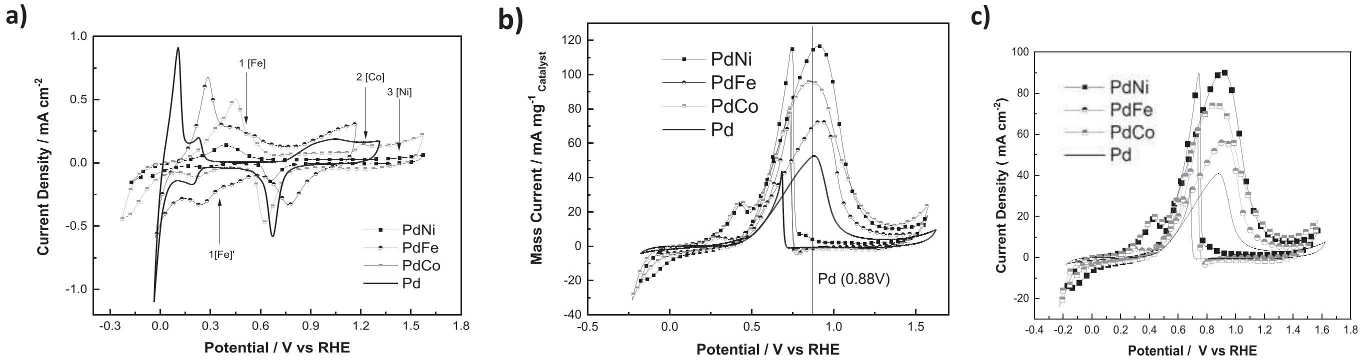

Fig. 6. a) CVs for PdNi, PdFe, PdCo, and Pd aerogels in 0.5 M KOH. b-c) EOR activity for PdNi, PdFe, PdCo, and Pd aerogel samples 0.5 M EtOH +0.5 M KOH at 50 mV/s scan rate.

ECSA values obtained were 3.2, 5.7, 9.4 and 26.5 m^2/g for Pd, PdNi, PdFe, and PdCo respectively. The Pd-TM aerogels show a significant improvement in the electrochemical performance in comparison to bare Pd and using low loading of noble metals. The ECSA values obtained in the PdTM improve the diffusion of the reagents, in this case, ethanol, through the electrode. In addition, XRD analysis shows that the formation of crystals between Pd and transition metals is clearly an advantage for electron transfer in comparison to bare Pd.

In order to compare the electrochemical performance of the Pd-TM electrocatalysts, the aerogels were evaluated for the ethanol oxidation reaction (EOR). It was performed by CV experiments in an electrolyte containing 0.5 M C_2H_6O + 0.5 M KOH. EOR was carried out in the same range of potential than the CV tests (i.e., from −0.25 to 1.6 V vs RHE). The electrochemical profiles for EOR demonstrated that Pd-TM aerogels show high performance at room temperature in the range of 0.7–1.1 V vs RHE, Fig. 6b.

It is observed that the current activity of the Pd-TM aerogels is improved, in comparison to bare Pd aerogel with a value of 48 mA/mg, following the trend PdNi > PdCo > PdFe, with 117, 96.1, and 73.35 mA/mg, respectively. PdNi aerogel shows the best electroactivity towards EOR (117 mA/mg). However, the thermodynamic reaction potential is slightly favored by the PdCo aerogel, whose highest peak current can be observed at (0.86 V vs. RHE, while thePdNi peak appears at 0.91 V vs. RHE. Since the difference in reaction potential towards the OER is very small, it can be assumed that the best catalyst is PdNi. These two values are close to the potential obtained with the Pd bare aerogel (i.e. 0.88 V vs RHE). In the case of the PdFe aerogel, this sample shows its maximum peak at 0.93 V vs RHE. The suggested mechanism for C_2H_5OH in an alkaline environment on electrode surfaces with Pd-TM aerogels is the next:

$$Pd + OH^- \rightarrow Pd\text{-}OH_{ads} + e^- \qquad (8)$$

$$Pd{-}CH_3CH_2OH \rightarrow Pd(TM)\text{-}(CH_3CH_2OH)_{ads} \qquad (9)$$

$$Pd\text{-}(CH_3CH_2OH)_{ads} + 3OH^- \rightarrow Pd\text{-}(CH_3CO)_{ads} + 3H_2O + 3e^- \qquad (10)$$

$$Pd\text{-}(CH_3CO)_{ads} + Pd\text{-}OH_{ads} + OH^- \rightarrow CH_3COO^- + 2Pd + H_2O \qquad (11)$$

Ethanol oxidation mechanism with these Pd-TM aerogels occurs in two pairs of reactions (Eqs. (8)–(11)) [51–53]. In the first two steps, the OH^- present in the solution reach the surface of the electrode and it absorbs OH^- efficiently since the transition metals accelerate this process [58]. On the other hand, the CH_3CO (Eq. (3)) generated in this reaction are adsorbed on the surface of Pd catalysts, this combination between Pd-TM considerably accelerates the EOR (Fig. 6b). In addition, the combination of the reaction of Pd-TM with hydroxyl groups and the CH_3CO adsorbed on the catalyst surface are the rate-determining step of the EOR (Eq. (4)). The transition metals (Ni, Fe, Co) provide an opportunity to improve the adsorption of OH_{ads} onto the surface of the catalyst and thus activate the catalyst surface and finally help to enhance the ethanol oxidation process [59]. On the other hand, the C–C bond in the C_2H_5OH molecule is very difficult to break, despite the fact that Pd-TM aerogels work efficiently, the interaction between C_2H_5OH and the catalyst ends up generating subproducts. Pd-TM catalysts promote the oxidation of the fuel following the trend: Co > Ni > Fe. These aerogels are highly active catalysts for EOR, and their performance is shown in Fig. 6b, where peaks between 0.7 and 1.1 V vs RHE for all aerogels represent the EOR reaction and CO_2 formation, and CO_2 desorption is observed in the potential range between 0.55 and 0.68 V vs RHE [38,53,54]. Comparison of ECSA, potential peak value and current density for EOR for obtained catalysts in this work with electrodes already reported is shown in Table 1. The results demonstrated that the electrocatalysts applied in this study have relative advantages, in terms of the potential value and current density.

Table 1
Performance comparison of similar electrocatalysts toward EOR.

Catalyst	Electrolyte	Scan rate (mVs^{-1})	ECSA (m^2/g)	Current $mAcm^{-2}$	Peak Potential	References
PdNi aerogel	0.5 M KOH + 0.5 M Ethanol	50	5.7	90.3	0.91 V vs RHE	This work
PdFe aerogel	0.5 M KOH + 0.5 M Ethanol	50	9.4	56.5	0.93 v VS RHE	This work
PdCo aerogel	0.5 M KOH + 0.5 M Ethanol	50	26.5	74.5	0.86 V vs RHE	This work
Pd aerogel	0.5 M KOH + 0.5 M Ethanol	50	3.2	40	0.88 v VS RHE	This work
Pt–Bi@CA (50:50)	1 M KOH + 0.1 M Ethanol	50	95.2	64.3	−0.23 Vvs Hg/HgO	[55]
Pd-WO_3/C (2,90:1)	1.0 M KOH + 1.0 M Ethanol	50	–	40	−0.1 v VS Hg/HgO	[56]
Pd@PANI-PDPA	0.5 M KOH + 1 M Ethanol	50	0.026	0.65	–	[57]
Pd–Ni–Fe/Vulcan	(0.2 KOH + 1.0 M Ethanol)	50	8.14	3.3	0.3 V vs Hg/HgO	[58]

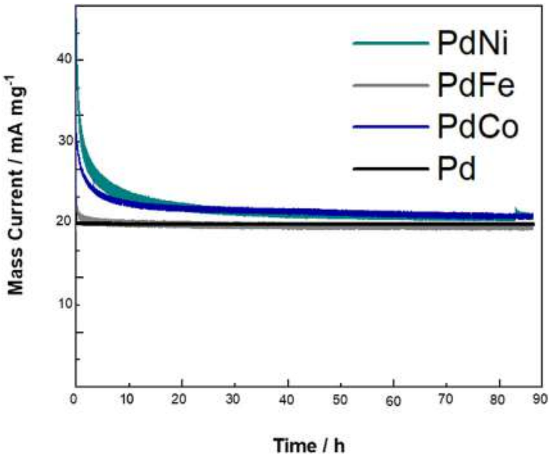

Fig. 7. Stability performance for PdNi, PdFe, PdCo, and Pd aerogels measured at 0.6 V vs RHE in 0.5 M KOH.

The maximum electrochemical activity value among all Pd-TM aerogels evaluated was detected in the range from 0.5 to 1.0 V vs RHE. Therefore, the stability test was carried out at 0.6 V vs RHE. Chronoamperometry was performed for 90 h as shown in Fig. 7. Apparently, PdNi retains 25 mA mg^{-1} at 10 h, and is higher than the rest of the catalysts, except PdCo, which retains 23 mAmg^{-1} in the same time interval. These two catalysts show the highest antitoxic capacity of the intermediate products and the high electrochemical stability [56] due to their constant performance. Although the Pd and PdFe samples also turn out to be highly stable and resistant to the corrosion of the medium, the PdNi and PdCo samples are superior. The retention capacity of the samples can be attributed to the number of active sites and their BET surface area mainly [56–58]. At the end of the 90-h test, the PdNi and PdCo samples showed only a 10% decrease in their charge retention. Some analysis of the materials after these electrochemical tests reveals that the degradation of PdNi and PdCo aerogels are negligible (see Supplementary Material) showing that they are very stable and effective electrocatalysts.

4. Conclusions

Pd-TM aerogels were successfully synthesized using a quick and simple synthesis procedure based on microwave heating and freeze-drying. The nanostructured aerogels obtained present high specific surface areas and electrochemical surface areas, favoring the diffusion of reactants and their activity versus electrochemical reactions. On the other hand, the chemical characterization of these Pd-TM aerogels may suggest the formation of alloys, although the crystalline size and morphology are maintained.

These physicochemical properties are traduced in a notable improvement of the electrochemical behavior of these aerogels. In fact, in the ethanol oxidation reaction, the Pd-TM aerogels result in 117, 96.1, and 73.35 mA/mg for PdNi, PdCo and PdFe, respectively. These values are clearly higher than the 48 mA/mg corresponding to the bare Pd aerogel.

The incorporation of these transition metals clearly improves the ethanol oxidation reaction compared to Pd due to their excellent combination of physicochemical properties. This opens the possibility towards the development of highly active catalysts with a low loading of noble metals, reducing dependence and costs in electrochemical conversion energy systems as fuel cells and water electrolyzers.

Credit author statement

A.Martínez-Lázaro: Writing-original draft, Methodology.
M.H. Rodriguez-Barajas: Writing-original draft, Methodology.
N. Rey-Raap: Investigation process, visualization, supervision.
F.I. Espinosa: Data curation.
J. Ledesma-García: Resources, Project administration, supervision.
A. Arenillas: Supervision, Resources.
L.G. Arriaga: Writing –Review and editing, Project administration, supervision.

Declaration of competing interest

The authors declare the following financial interests/personal relationships which may be considered as potential competing interests: L. G. Arriaga reports financial support was provided by Mexican Council for Science and Technology.

Data availability

Data will be made available on request.

Acknowledgements

Authors thank to Consejo Nacional de Ciencia y Tecnología CONACYT (Mexico) for funding through the Ciencia de Frontera 2020–845132, 2019-39569 and LN-321116. Also to Ministerio de Ciencia e Innovacion (Spain), the European Union Next Generation EU/PRTR and Science, Technology and Innovation Plan 2018-2022 of the Principado de Asturias with the projects PCI2020-112039 MCIN/AEI-10.13039/501100011033, PID2020-113001RB-I00 MCIN/AEI-10.13039/501100011033 and IDI/2021/50921. N.R.-R is grateful to the Horizon-MSCA-2021-PF-01-01 call for financial support through the Metgel project 101059852. Finally, thanks to Anabel de la Cruz and Cesar Leyva for TEM-analysis.

References

[1] M.P. Marčeta Kaninski, et al., Catalytic activity of Pt-based intermetallics for the hydrogen production-Influence of ionic activator, Appl. Catal. Gen. 321 (2007) 93–99, https://doi.org/10.1016/j.apcata.2007.01.036.
[2] J. Ma, L. Wang, X. Mu, Y. Cao, Enhanced electrocatalytic activity of Pt nanoparticles supported on functionalized graphene for methanol oxidation and oxygen reduction, J. Colloid Interface Sci. 457 (2015) 102–107, https://doi.org/10.1016/j.jcis.2015.06.031.
[3] M.A. Montero, M.R. Gennero De Chialvo, A.C. Chialvo, Electrocatalytic activity of core-shell Au@Pt nanoparticles for the hydrogen oxidation reaction, Int. J. Hydrogen Energy 36 (2011) 3811–3816, https://doi.org/10.1016/j.ijhydene.2010.12.115.
[4] A.J. Armenta-González, et al., An improved ethanol microfluidic fuel cell based on a PdAg/MWCNT catalyst synthesized by the reverse micelles method, Fuel 167 (2016) 240–247, https://doi.org/10.1016/j.fuel.2015.11.057.
[5] C. Gao, X. Zhang, J. Zhan, B. Cai, Engineering of aerogel-based electrocatalysts for oxygen evolution reaction, Electrochem. Sci. Adv. (2021), https://doi.org/10.1002/elsa.202100113.
[6] W. Liu, et al., Noble metal aerogels-synthesis, characterization, and application as electrocatalysts, Acc. Chem. Res. 48 (2015) 154–162, https://doi.org/10.1021/ar500237c.
[7] R. Du, et al., Emerging noble metal aerogels: state of the art and a look forward, Matter 1 (2019) 39–56, https://doi.org/10.1016/j.matt.2019.05.006.
[8] Y. Liu, M. Wei, J. Qu, L. Mao, Carbon aerogels supported Pt nanoparticles as electrocatalysts for methanol oxidation in alkaline media, J. Chin. Chem. Soc. 61 (2014) 404–408, https://doi.org/10.1002/jccs.201300637.
[9] L. Zhao, et al., Hybrid of carbon-supported Pt nanoparticles and three dimensional graphene aerogel as high stable electrocatalyst for methanol electrooxidation, Electrochim. Acta 189 (2016) 175–183, https://doi.org/10.1016/j.electacta.2015.12.072.
[10] Y.H. Kwok, A.C.H. Tsang, Y. Wang, D.Y.C. Leung, Ultra-fine Pt nanoparticles on graphene aerogel as a porous electrode with high stability for microfluidic methanol fuel cell, J. Power Sources 349 (2017) 75–83, https://doi.org/10.1016/j.jpowsour.2017.03.030.
[11] Y. Tai, K. Tajiri, Preparation, thermal stability, and CO oxidation activity of highly loaded Au/titania-coated silica aerogel catalysts, Appl. Catal. Gen. 342 (2008) 113–118, https://doi.org/10.1016/j.apcata.2008.03.006.

[12] S. Keshipour, S.S. Mirmasoudi, Cross-linked chitosan aerogel modified with Au: synthesis, characterization and catalytic application, Carbohydr. Polym. 196 (2018) 494–500, https://doi.org/10.1016/j.carbpol.2018.05.068.

[13] J. Zhang, et al., Ethanol electrooxidation on highly active palladium/graphene oxide aerogel catalysts, Chem. Phys. 534 (2020), https://doi.org/10.1016/j.chemphys.2020.110753.

[14] A.S. Douk, H. Saravani, M. Farsadrooh, Three-dimensional inorganic polymer of Pd aerogel as a highly active support-less anode catalyst toward formic acid oxidation, Int. J. Hydrogen Energy 44 (2019) 18028–18037, https://doi.org/10.1016/j.ijhydene.2019.05.084.

[15] B.B. Sahoo, et al., Pd supported on 3D graphene aerogel as potential electrocatalyst for alkaline direct methanol fuel cells, Mater. Today: Proc. 41 (2021) 150–155, https://doi.org/10.1016/j.matpr.2020.08.446.

[16] Z. Zhao, et al., Thermally stable Pd/reduced graphene oxide aerogel catalysts for solvent-free oxidation of benzyl alcohol, Chem. Phys. Lett. 746 (2020), https://doi.org/10.1016/j.cplett.2020.137306.

[17] X. Zhao, et al., Constructing efficient polyimide(PI)/Ag aerogel photocatalyst by ethanol supercritical drying technique for hydrogen evolution, Appl. Surf. Sci. 502 (2020), https://doi.org/10.1016/j.apsusc.2019.144187.

[18] M. Liu, X. Liu, P. Wang, X. Zhang, N-doped three-dimensional graphene aerogel with a high loading of Ag particles as an efficient catalyst and antibacterial agent, Colloids Surf. A Physicochem. Eng. Asp. 626 (2021), https://doi.org/10.1016/j.colsurfa.2021.126886.

[19] M.T.X. Nguyen, et al., Pd coated one-dimensional Ag nanostructures: controllable architecture and their electrocatalytic performance for ethanol oxidation in alkaline media, Int. J. Hydrogen Energy 46 (2021) 3909–3921, https://doi.org/10.1016/j.ijhydene.2020.10.226.

[20] A. Shafaei Douk, H. Saravani, M. Noroozifar, Three-dimensional assembly of building blocks for the fabrication of Pd aerogel as a high performance electrocatalyst toward ethanol oxidation, Electrochim. Acta 275 (2018) 182–191, https://doi.org/10.1016/j.electacta.2018.04.073.

[21] Q. Shi, et al., Ultrafine Pd ensembles anchored-Au2Cu aerogels boost ethanol electrooxidation, Nano Energy 5 (2018) 206–212, https://doi.org/10.1016/j.nanoen.2018.08.047.

[22] Y. Bao, M. Zha, P. Sun, G. Hu, L. Feng, PdNi/N-doped graphene aerogel with over wide potential activity for formic acid electrooxidation, J. Energy Chem. (2021) 748–754, https://doi.org/10.1016/j.jechem.2020.12.007.

[23] C.H.A. Tsang, D.Y.C. Leung, Use of Pd-Pt loaded graphene aerogel on nickel foam in direct ethanol fuel cell, Solid State Sci. 75 (2018) 21–26, https://doi.org/10.1016/j.solidstatesciences.2017.11.005.

[24] B. Heinrichs, F. Noville, J.P. Pirard, Pd/SiO2-cogelled aerogel catalysts and impregnated aerogel and xerogel catalysts: synthesis and characterization, J. Catal. 170 (1997) 366–376, https://doi.org/10.1006/jcat.1997.1772.

[25] L. Chen, et al., Tailoring performance of Co–Pt/MgO–Al2O3 bimetallic aerogel catalyst for methane oxidative carbon dioxide reforming: effect of Pt/Co ratio, Int. J. Hydrogen Energy 44 (2019) 19878–19889, https://doi.org/10.1016/j.ijhydene.2019.05.201.

[26] D.Y. Li, Y.K. Sun, P.Z. Gao, X.L. Zhang, H.L. Ge, Structural and magnetic properties of nickel ferrite nanoparticles synthesized via a template-assisted sol-gel method, Ceram. Int. 40 (2014) 16529–16534, https://doi.org/10.1016/j.ceramint.2014.08.006.

[27] J.J. Ebelmen, Untersuchungen über die Verbindungen der Borsäure und Kieselsäure mit Aether, Liebigs Ann. Chem. 57 (1846) 319–355.

[28] H. Maleki, N. Hüsing, Current status, opportunities and challenges in catalytic and photocatalytic applications of aerogels: environmental protection aspects, Appl. Catal. B Environ. 221 (2018) 530–555, https://doi.org/10.1016/j.apcatb.2017.08.012.

[29] A. Martínez-Lázaro, et al., Facile synthesis of unsupported Pd aerogel for high performance formic acid microfluidic fuel cell, Materials 15 (2022) 1422, https://doi.org/10.3390/ma15041422.

[30] H. Zhao, et al., Ultrafast generation of nanostructured noble metal aerogels by a microwave method for electrocatalytic hydrogen evolution and ethanol oxidation, ACS Appl. Nano Mater. 4 (2021) 11221–11230, https://doi.org/10.1021/acsanm.1c02746.

[31] A.M. Schwenke, S. Hoeppener, U.S. Schubert, Synthesis and modification of carbon nanomaterials utilizing microwave heating, Adv. Mater. 27 (2015) 4113–4141, https://doi.org/10.1002/adma.201500472.

[32] N. Rey-Raap, J.A. Menendez, A. Arenillas, Simultaneous adjustment of the main chemical variables to fine-tune the porosity of carbon xerogels, Carbon 78 (2014) 490–499, https://doi.org/10.1016/j.carbon.2014.07.030.

[33] I.D. Alonso-Buenaposada, N. Rey-Raap, E.G. Calvo, J.A. Menéndez, A. Arenillas, Effect of methanol content in commercial formaldehyde solutions on the porosity of RF carbon xerogels, J. Non-Cryst. Solids 426 (2015) 13–18, https://doi.org/10.1016/j.jnoncrysol.2015.06.017.

[34] S.L. Flores-López, S.F. Villanueva, N. Rey-Raap, A. Arenillas, Hybrid RF-Si xerogels A cost-effective proposal for insulator materials, Materials 15 (2022) 265, https://doi.org/10.3390/ma15010265.

[35] S.L. Flores-López, M.A. Montes-Morán, A. Arenillas, Carbon/silica hybrid aerogels with controlled porosity by a quick one-pot synthesis, J. Non-Cryst. Solids 569 (2021), 120992, https://doi.org/10.1016/j.jnoncrysol.2021.120992.

[36] Z. Chen, et al., High-performance Pd nanocatalysts based on the novel N-doped Ti3C2 support for ethanol electrooxidation in alkaline media, Electrochim. Acta 390 (2021), https://doi.org/10.1016/j.electacta.2021.138902.

[37] M. Niu, et al., Synthesis of nanoporous CuO/TiO2/Pd-NiO composite catalysts by chemical dealloying and their performance for methanol and ethanol electro-oxidation, J. Power Sources 362 (2017) 10–19, https://doi.org/10.1016/j.jpowsour.2017.07.011.

[38] L. Wang, et al., In situ assembly of ultrafine AuPd nanowires as efficient electrocatalysts for ethanol electrooxidation, Int. J. Hydrogen Energy 46 (2020) 8549–8556, https://doi.org/10.1016/j.ijhydene.2020.12.040.

[39] X. Zhang, et al., Mesoporous KIT-6 supported Pd-MxOy (M = Ni, Co, Fe) catalysts with enhanced selectivity for p-chloronitrobenzene hydrogenation, Catal. Lett. 145 (2015) 784–793, https://doi.org/10.1007/s10562-015-1480-0.

[40] C. Zhu, et al., Kinetically controlled synthesis of PdNi bimetallic porous nanostructures with enhanced electrocatalytic activity, Small 11 (2015) 1430–1434, https://doi.org/10.1002/smll.201401432.

[41] J. Wan, Z. Liu, X. Yang, P. Cheng, C. Yan, Cyanogel-derived synthesis of porous pdfe nanohydrangeas as electrocatalysts for oxygen reduction reaction, Nanomaterials 11 (2021), https://doi.org/10.3390/nano11123382.

[42] T. Raj kumar, G. Gnana kumar, A. Manthiram, Biomass-Derived 3D carbon aerogel with carbon shell-confined binary metallic nanoparticles in CNTs as an efficient electrocatalyst for microfluidic direct ethylene glycol fuel cells, Adv. Energy Mater. 9 (2019) 1–12, https://doi.org/10.1002/aenm.201803238.

[43] R. Ma, et al., Nanoscale surface engineering of PdCo/Al2O3 catalyst via segregation for efficient purification of ethene feedstock, Chem. Eng. Sci. 210 (2019), 115216, https://doi.org/10.1016/j.ces.2019.115216.

[44] Munonde, et al., A green approach for enhancing the electrocatalytic activity and stability of NiFe2O4/CB nanospheres towards hydrogen production, Renew. Energy 154 (2020) 704–714, https://doi.org/10.1016/j.renene.2020.03.022.

[45] X. Ma, et al., Construction of dual Z-scheme NiO/NiFe2O4/Fe2O3 photocatalyst via incomplete solid state chemical combustion reactions for organic pollutant degradation with simultaneous hydrogen production, Int. J. Hydrogen Energy 46 (2021) 31659–31673, https://doi.org/10.1016/j.ijhydene.2021.07.076.

[46] Hua, et al., Hexamethylenetetramine-assisted hydrothermal synthesis of octahedral nickel ferrite oxide nanocrystallines with excellent supercapacitive performance, J. Mater. Sci. 53 (2018) 7621–7636, https://doi.org/10.1007/s10853-018-2052-7.

[47] J.W. Zhang, B. Zhang, X. Zhang, Enhanced catalytic activity of ternary NiCoPd nanocatalyst dispersed on carbon nanotubes toward methanol oxidation reaction in alkaline media, J. Solid State Electrochem. 21 (2017) 447–453, https://doi.org/10.1007/s10008-016-3331-3.

[48] M. Martínez-Gil, et al., Effect of annealing temperature on the thermal transformation to cobalt oxide of thin films obtained via chemical solution deposition, Mater. Sci. Semicond. Process. 107 (2020), https://doi.org/10.1016/j.mssp.2019.104825.

[49] A.S. Douk, et al., Is the Pd aerogel assembled by nanosheets as an advanced three- dimensional support-less electrocatalyst in renewable energy? ACS Appl Eng. Mater (2022) https://doi.org/10.1021/acsaenm.2c00019.

[50] M.Z. Yazdan-abad, et al., Shape engineering of palladium aerogels assembled by nanosheets to achieve a high performance electrocatalyst, Appl. Catal. B Environ. 250 (2019) 242–249, https://doi.org/10.1016/j.apcatb.2019.02.064.

[51] A.S. Douk, et al., Three-dimensional engineering of nanoparticles to fabricate a Pd – Au aerogel as an advanced supportless electrocatalyst for low- temperature direct ethanol fuel cells, ACS Appl. Energy Mater. 8 (2020) 7527–7534, https://doi.org/10.1021/acsaem.0c00928.

[52] A.S. Douk, et al., Porous 3D inorganic superstructure of Pd – Ir aerogel as advanced support-less anode electrocatalyst toward ethanol oxidation, ACS Omega 35 (2020) 22031–22038, https://doi.org/10.1021/acsomega.0c01661.

[53] B. Cai, et al., Nanostructuring noble metals as unsupported electrocatalysts for polymer electrolyte fuel cells, Adv. En. Mater. (2017), 1700548, https://doi.org/10.1002/aenm.201700548, 1–16.

[54] W. Hong, et al., Facile synthesis of highly active PdAu nanowire networks as self- supported electrocatalyst for ethanol electrooxidation, Appl. Mater. Inter. 12 (2014) 9481–9487, https://doi.org/10.1021/am501859k.

[55] X. Tang, et al., Pt-Bi on carbon aerogels as efficient electrocatalysts for ethanol oxidation reaction in alkaline medium, J. Alloys Compd. 25 (2022), 168398, https://doi.org/10.1016/j.jallcom.2022.168398.

[56] M. Wang, et al., Electronic coupling interaction between Pd and WO3 nanoparticles for accelerating electro-oxidation reaction toward ethanol, J. Alloys Compd. 927 (2022), 166922, https://doi.org/10.1016/j.jallcom.2022.166922.

[57] S. Lakshmi, et al., Remarkable electrocatalytic activity of Pd nanoparticles dispersed on polyaniline-polydiphenylamine copolymer nanocomposite for methanol and ethanol oxidation reaction, Synth. Met. 281 (2021), 116925, https://doi.org/10.1016/j.synthmet.2021.116925.

[58] A. Eshghi, et al., Pd-Ni and Pd-Ni-Fe nanoparticles anchored on MnO$_2$/Vulcan as efficient ethanol electro-oxidation anode catalysts, Int. J. Hydrogen Energy 44 (2019) 28194–28205, https://doi.org/10.1016/j.ijhydene.2019.08.236.

3.2.1. Optimización de aerogeles paladio-cobalto como electrocatalizadores en celdas microfluídicas

Las celdas microfluídicas han sido los dispositivos propuestos en esta Tesis Doctoral por su fácil uso y múltiples ventajas, tal y como se mencionan en el Capítulo 1. Una de las ventajas más notables es que permiten evitar el uso de membranas poliméricas convencionales ya que estos dispositivos se basan en la utilización de un flujo laminar, esto quiere decir que los microfluidos no se mezclan y permiten el intercambio de iones en la interfaz entre ellos.

En esta Tesis Doctoral, un aerogel de PdCo fue evaluado como catalizador anódico. Ya que este material tuvo un excelente desempeño hacia la reacción de oxidación de etanol (ROE), con un potencial de 0.88 V vs RHE, en la literatura se han desarrollado innumerables materiales innovadores para la ROE a partir de metales nobles como Pt, Ag, y Ru para ser utilizados en la reacción anódica en microceldas de etanol. Sin embargo, en esta Tesis Doctoral se ha demostrado que estos aerogeles híbridos PdCo pueden competir contra los mejores catalizadores reportados en distintos trabajos de investigación.

A pesar de que los metales nobles como le Pt y el Pd son excelentes catalizadores la sinergia entre el Pd y el Co permitió alcanzar altos valores de potencial de circuito abierto cercanos a 1.6V. Esto es debido a la diferencia de potenciales de reacción entre los electrolitos, al combinar un católico acido(H_2SO_4) con un anolito básico (KOH) (Eshghi et al., 2019; Wang et al., 2020). Además, se encontró una proporción optima de ambos metales para la reacción anódica en la celda microfluídica de etanol. El estado de Pd^0 presente en la muestra es el factor determinístico hacia un desempeño de la ROE.

Publicaciones Científicas

En los siguientes artículos científicos se exploran las principales características fisicoquímicas y electroquímicas de los aerogeles de PdCo. Se analizan distintas estequiometrias entre ambos metales para establecer las propiedades catalíticas optimas para obtener un aerogel bimetálico como catalizador anódico en celdas de combustible microfluídicas y la electrooxidación de etanol.

ACS APPLIED ENERGY MATERIALS

www.acsaem.org Article

Effective Synthesis Procedure Based on Microwave Heating of the PdCo Aerogel Electrocatalyst for Its Use in Microfluidic Devices

A. Martínez-Lázaro, A. P. Mendoza-Camargo, M. H. Rodriguez-Barajas, F. I. Espinosa-Lagunes, Y. Salazar-Lara, A. Herrera-Gomez, O. Cortazar-Martínez, N. Rey-Raap, J. Ledesma-García,* A. Arenillas,* and L. G. Arriaga

Cite This: https://doi.org/10.1021/acsaem.3c00173 Read Online

ACCESS | Metrics & More | Article Recommendations | Supporting Information

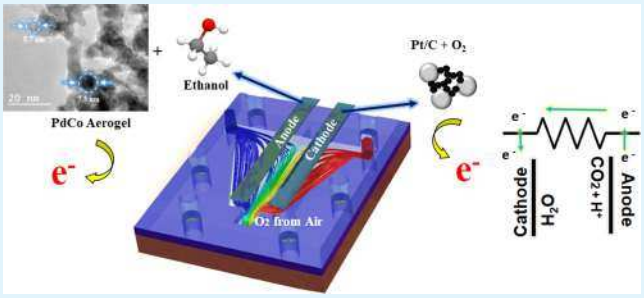

ABSTRACT: Unsupported PdCo aerogels were successfully synthesized by means of microwave heating. The use of this heating methodology provides some advantages compared to conventional heating in terms of saving synthesis time and improved physicochemical properties (i.e., greater surface area and mesoporosity). The combination of palladium with cobalt reduces the dependence of the noble metal and increases the electrocatalytic performance in the ethanol oxidation reaction due to a higher percentage of Pd^0 in the PdCo aerogel, confirmed using the X-ray photoelectron spectroscopy (XPS) technique. For the application in energy conversion electrochemical systems, the catalytic activity of aerogels was evaluated in a microfluidic fuel cell that uses ethanol as fuel, where the PdCo aerogel synthesized by microwave heating exhibited great performance with 330 mA cm^{-2} current density, tripling the value of the palladium-based aerogel.

KEYWORDS: *microwave heating, bimetallic aerogel, microfluidic fuel cell, high-surface electrocatalyst, ethanol oxidation reaction*

1. INTRODUCTION

In the last years, microfluidic fuel cells (MFCs) have shown significant advances due to their relevance and versatility in many microscale applications as portable devices.[1] MFCs avoid the use of conventional polymeric membranes since they are based on laminar flows with ion exchange at the interface between them.[2] Various fluids have been evaluated in a series of devices such as blood or sweat and some fuels such as hydrogen or hydrocarbons.[3] To date, different MFC configurations have been reported, where different factors affect the performance of the device, the main one being the catalyst used at both the anode and cathode. Hence, the continuous improvement of catalysts used for fuel cells and other electrochemical devices and systems is one of the current challenges to ensure the performance of these technologies.[4] Despite the fact that countless innovative materials have currently been developed for several fuel oxidation reactions, noble metal-based catalysts such as Pt, Ag, and Pd still play a predominant role because of their superior catalytic activity, resistance to corrosion, and high electrochemical stability. Therefore, these precious metals guarantee a good performance of MFCs. However, the scarcity and high cost continue to be an impediment for massive use in these devices. Aerogels have emerged as an interesting proposal to solve the excessive use of noble metals thanks to their high porosity and surface area.[5,6] Aerogels allow the use of very small amounts of the catalyst while maintaining their catalytic effectiveness.[7] The advantages of their morphology and ultralow density give aerogels a relevant role in nanotechnology and heterogeneous catalysis.[8,9] Several aerogels have been evaluated toward electrochemical oxidation reactions such as Pd,[10,11] bimetallic materials such as Ag or Cu,[7] noble metal aerogels supported on carbon-based materials,[12] and Pt aerogels.[7,8,13]

On the other hand, there are several investigations where the oxidation processes are carried out using different types of fuel as formic acid,[14−16] glycerol,[17] or ethanol.[18] The proposal toward improving aerogels as catalysts is functionalizing them with transition metals abundant in the earth such as Co, Ni, and Mn. The incorporation of transition metal atoms in the structure of a noble metal aerogel could be a great step toward the continuous improvement of this innovative material. The main advantage provided by the transition metals will be the increase of the catalytic activity and the low cost of the material due to their abundance in nature.[19] The optimal composition between noble and transition metals will benefit the catalytic

Received: January 23, 2023
Accepted: May 26, 2023

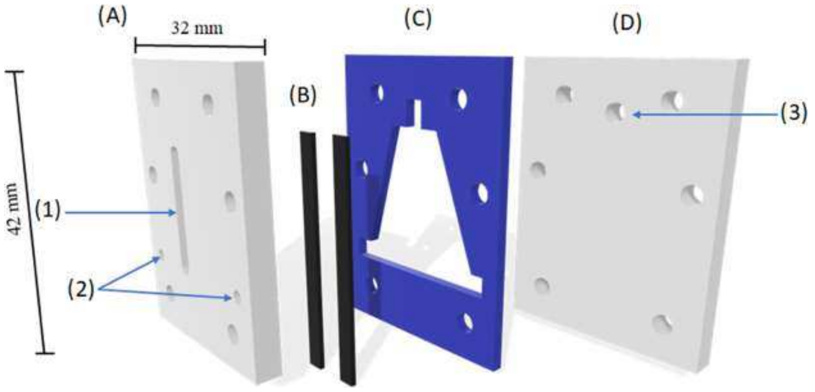

Figure 1. Microfluidic fuel cell (MFC)-type ″Y″ configuration. (A) Top cover, (B) carbon paper electrodes, (C) silastic gaskets, and (D) lower cover.

performance, chemical stability, and corrosion resistance, which are characteristics of noble metals.[20,21]

In this work, a bimetallic aerogel is synthesized by incorporation of a transition metal (cobalt) in the noble metal structure (palladium) by means of a novel process based on microwave heating. The effect of the heating technology (i.e., microwave vs conventional heating) is also analyzed in terms of physicochemical properties and electrocatalytic performance of the aerogel. As a practical application, the PdCo aerogel has also been evaluated in a microfluidic fuel cell that works with ethanol as fuel.

2. EXPERIMENTAL SECTION

2.1. Aerogel Synthesis. The synthesis of Pd−Co aerogels was carried out by adding 10 mL of $PdCl_2$ (2 mg/mL, 99% Sigma-Aldrich ReagentPlus) to a solution of sodium carbonate (≥99.5%, J. T. Baker) and glyoxylic acid monohydrate (98% Sigma-Aldrich) (ratio 6:1) in 40 mL of deionized DI water. The mixture was heated at 68 °C for 2 h for the nucleation reaction. The gelation process elapsed for 7 h at 45 °C. Two different PdCo samples were prepared: The first one, PdCo-MW, consisted of PdCo obtained by microwave heating (MW) in two steps (i.e., nucleation and gelation process). Meanwhile, the second material PdCo-OV was synthesized with the same procedure as the first one, except for using conventional heating in an oven (OV) for the same time (2 h at 68 °C for nucleation and 7 h at 45 °C for gelation). For control experiments, a palladium aerogel, Pd-MW, was obtained by microwave heating at the same conditions of PdCo-MW. Samples from the wet gels were washed several times with DI water and ethanol. Three samples were cooled to room temperature for washing before drying. The drying process was performed with a residual volume of 3 mL of DI water. The mixture was then frozen with liquid N_2, and the solvent was eliminated by lyophilization (HyperCOOL, model: HC3110) at −110 °C for 1 day (Figure S1).

2.2. Physicochemical Characterization. The crystal structures were characterized by X-ray diffraction (XRD; D8-advance diffractometer Bruker) equipped with a Cu Kα X-ray source (λ = 0.1541 nm, 40 kV, 40 mA,), using a step size of 0.02° 2θ and a scan step time of 5 s. The morphology of the aerogel samples was characterized using a JEOL JEM-2100F high-resolution transmission electron microscope (HR-TEM) with spherical aberration correction. The specific surface area and the pore size distribution were estimated by nitrogen adsorption−desorption isotherms at −196 °C (Micromeritics ASAP 2020), after overnight outgassing at 120 °C. The electronic structure of elements was measured by X-ray photoelectron spectroscopy (XPS; K-Alpha+ spectrometer equipped with the Avantage Data System from Thermo Scientific).

2.3. Ethanol Oxidation Reaction Evaluation. Electrochemical performance toward the ethanol oxidation reaction (EOR) for PdCo and Pd aerogels was carried out in a Biologic VMP3 potentiostat/galvanostat using a conventional three-electrode electrochemical cell in acid media at 20 mV s^{-1} scan rate. A glassy carbon electrode (3 mm diameter) was used as the working electrode, with a Ag/AgCl electrode and a Pt wire as reference and counter electrodes, respectively. The electrocatalyst ink was prepared using each aerogel sample in a mixture of DI water (500 μL) + Nafion (5%, 50 μL) per milligram of the catalyst. The ink was sonicated for 1 hour, and then, 10 μL was deposited over the electrode surface. The electrolyte was bubbled with N_2 for 30 minutes before the electrochemical measurements. Electrochemical profiles were obtained using the cyclic voltammetry technique (CV); all experiments were performed in 1 M KOH in the absence or presence of 0.5 M ethanol within a potential range between −0.1 and 1.8 V vs RHE, where the faradaic processes were visible in a mass current, normalized by mg of the catalyst.

2.4. Microfluidic Fuel Cell Configuration. The description of the microfluidic fuel cell (MFC) type "Y" configuration has been previously reported by our group.[22] Briefly, according to Figure 1, the top cover made of acrylic (A) had 19.5 mm height with a slot by air-breathing arrangement (1) and fluid injection area (2). (B) A pair of carbon paper electrodes (41 mm height and 3 mm width) is placed. (C) It corresponds to a Silastic membrane with a geometric adaptation that favors the formation of a microfluidic exchange zone. (D) It is a lower cover made with acrylic, which contains a groove to vent fluids (3). The air-breathing cathodic compartment was equipped with a commercial catalyst based on Pt/C (10 wt %, Alfa Aesar) and 0.5 M H_2SO_4 previously bubbled with O_2 for 30 minutes, as a catholyte. The flux rate was 200 μL min^{-1} in both MFC compartments. The linear sweep voltammetry (LSV) technique was used to obtain curves from open-circuit voltage (OCV) until 0 V to observe the mass current obtained. The chronoamperometric test was carried out at 1.1 V for 3 days in order to evaluate the catalyst stability.

3. RESULTS

3.1. Physicochemical Characterization. XRD patterns of the synthesized aerogels are shown in Figure 2. In addition, the crystallite size was calculated using the Scherrer equation

$$d_{111} = \frac{K\lambda}{\beta_{111}\cos\theta} \tag{1}$$

XRD patterns for PdCo-MW and Pd-MW aerogels were observed with four major diffraction peaks appearing at the 2Θ values. The peak with the highest intensity was taken for the calculation of crystallite size. In the Pd-MW aerogel, the peaks were 40.1, 46.5, 68.1, and 82.1°, which are ascribed to the (111), (200), (220), and (311) reflection planes of Pd (JCPDS #46-1043), respectively. These peaks agree with a face-centered cubic (FCC) crystal structure. The resulting aerogels revealed characteristic Pd peaks and a shift in position (111) to

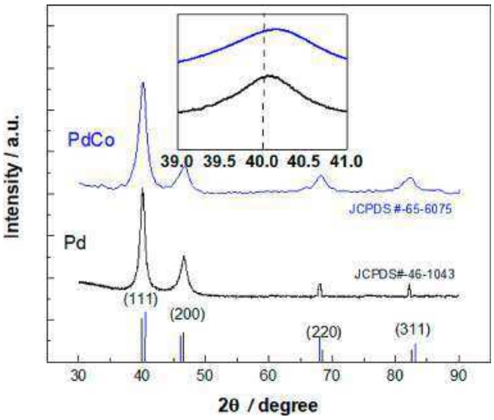

Figure 2. XRD patterns for PdCo-MW and Pd-MW samples.

the left, suggesting the presence of PdCo alloys as shown in Figure 2. The PdCo aerogel presents peaks in 2Θ, which were 40.4, 46.2, 68.1, and 81.8°, compared with the reference JCPDS #65-6075 corresponding to PdCo, which has a peak with high intensity in 2Θ with a value of 41.7° corresponding to the reflection plane (111), being further away from the one obtained and coinciding even more with the JCPDS #46-1043 of Pd.

The crystallite sizes obtained using the 2Θ values of 40.1 and 40.35° with the Scherrer equation (eq 1) were 9.46 and 3.70 nm for Pd-MW and PdCo-MW, respectively. There is a great difference between materials, detecting a notable decrease of crystallite size for PdCo-MW compared to that obtained for the Pd aerogel.

HR-TEM was performed to characterize the morphology and structure of the synthesized aerogels. The analysis reveals interconnected clusters at nanometric size, not independent nanoparticles, which are related to the typical structure seen in all sol−gel materials (Figure 3). TEM images at different magnifications show chains of particles defining pores of different sizes between them, typically a characteristic for aerogels. The sample PdCo-MW shows particle sizes between 5.7 and 7.5 nm, similar to those of the sample PdCo-OV (between 5.6 and 7 nm). It seems that transition metal incorporation allows obtaining smaller particles than the ones formed in Pd-MW, where particles up to 8 nm can be observed. These particle sizes are going to be important for the porosity and specific surface area developed in these aerogels, which in turn are relevant for the further superficial reactions that could take place in any application, as will be discussed later.

At higher magnification, it can be seen that the interplanar distances are wider for cobalt-containing catalysts, which can be attributed to the presence of the alloy between the two metals used in the synthesis.[23−25] The interplanar distance for Pd-MW is 0.22 nm, while the incorporation of transition metals increases this value to 0.24 and 0.255 for PdCo-OV and PdCo-MW, respectively. This may be interpreted as cobalt and palladium crystals coexisting in the chemical structure of the nanoparticles.[25−28] The slight differences between PdCo-MW and PdCo-OV could be attributed to different chemical compositions due to the different heating processes employed during the synthesis process.

In addition, the N_2 adsorption/desorption isotherms presented in Figure 4 clearly show that the materials present a mesoporous structure: (i) there is an increasing N_2 adsorption volume at intermediate relative pressures and (ii) there is a hysteresis loop in the desorption isotherm. This mesoporous structure can only be obtained if the materials are aerogels; otherwise, this structure would not be developed. Furthermore, in the case of nanoparticles, the N_2 adsorption isotherms usually exhibit a sharp increase in the adsorbed volume near the saturation point ($P/P_0 = 1$) due to interparticular condensation, but this is not the case as the adsorption is gradual with the relative pressure. Therefore, it is clearly demonstrated that the materials presented in this article are indeed bimetallic aerogels. The surface area of the samples was determined using the BET equation, obtaining values of 63, 58, and 50 $m^2 g^{-1}$ for PdCo-MW, PdCo-OV, and Pd-MW, respectively.

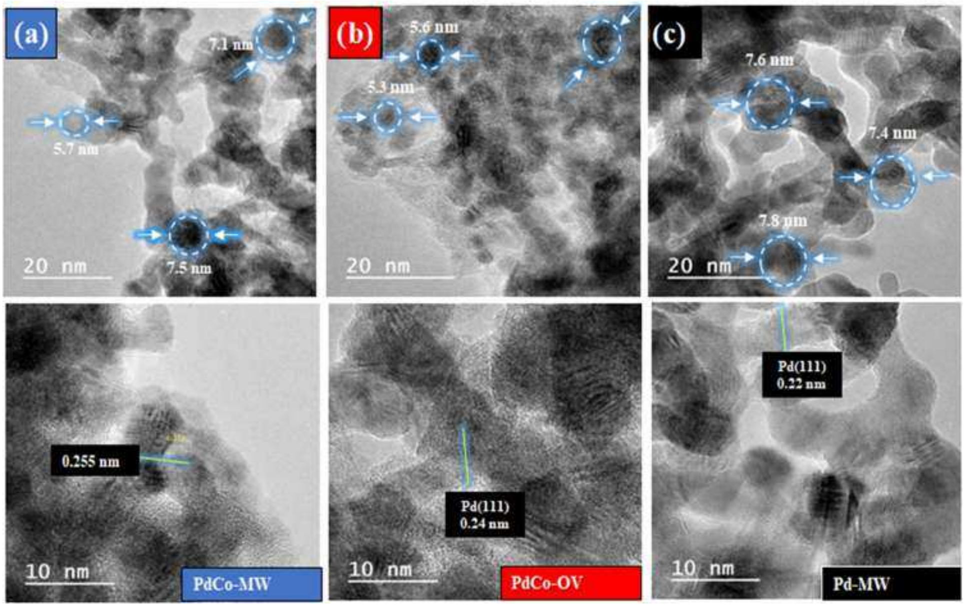

Figure 3. HR-TEM images of aerogel samples. (a) PdCo-MW; (b) PdCo-OV; and (c) Pd-MW.

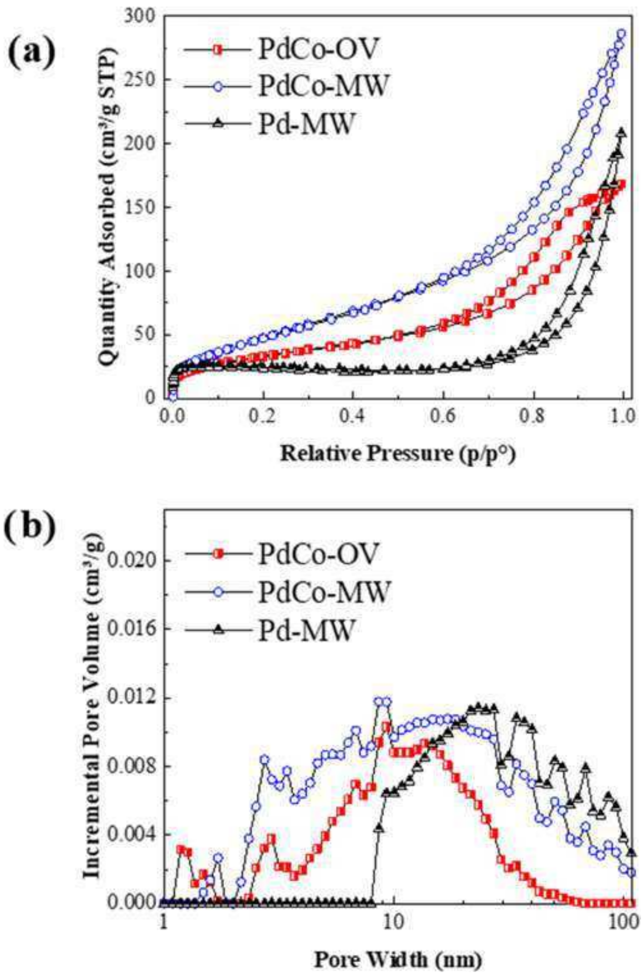

Figure 4. (a) BET analysis of aerogels. (b) Pore size distribution in aerogel samples.

Using the X-ray photoelectron spectroscopy (XPS) technique, the analysis of PdCo aerogels was performed in all samples to know the chemical composition and oxidation states (Figure 5). The broad spectrum of the sample, as shown in Figure 5a, indicates the presence of C, Pd, Co, and O peaks of impurities such as Na and Si, which are typical of the synthesis of the study material. The spectrum of Pd 2p is observed in Figure 5b, having binding energies for Pd 3d$_{3/2}$ and Pd 3d$_{5/2}$, corresponding to the peaks of 340.7 and 335.55 eV, respectively.

The deconvoluted spectrum shows the energy band values at peaks with 336.43 and 341.76 eV at Pd^{2+}. In contrast, those located at 335.15 and 340.5 eV refer to Pd^0, which is attributed to an oxidation state,[27−29] constituting the Pd/PdO. However, when comparing the synthesized aerogels, a higher concentration of Pd^{2+} is shown for the PdCo-OV sample than for the PdCo-MW sample, so the heating process of the PdCo-MW aerogel presents more stability by containing a higher concentration of Pd^0.

High-resolution Co 2p scanning is presented in Figure 5c, where the spectra of Co 2p exhibit two prominent peaks with binding energies of 780 and 796 eV corresponding to Co 2p$_{3/2}$ and Co 2p$_{1/2}$, respectively. The difference between the peaks of Co 2p is due to the splitting energy of the spin−orbit. The oxidation state of cobalt ions was determined from the high-resolution spectra of Co 2p by the Lorentzian−Gaussian adjustment method, where the adjusted peaks correspond to the binding energy values, giving the peaks of 780.5 and 795.4 eV corresponding to Co^{2+}, and those located at 782.2 and 797.7 eV refer to Co^{3+}, with a margin of error of the binding energies reported for the structure for Co$_3$O$_4$;[30−3230−32] however, by comparison of the samples, there is no difference in the signals of the peaks. Hence, it has the presence of the CoPd alloy on the surface, having two spectra in their oxidation state. The quantitative evaluation of each peak was obtained by dividing the area of the peak, which was calculated from the cross sections and the mean depth of the escape electrons. XPS data were interpreted using Avantage Thermo software with angular resolution (ARXPS), where molar proportions were obtained as Co0.72Pd0.1, in addition to calculating the percentage of the relative weight of the sample, where also, 18% C was found,[24,28] where there is a higher percentage of Pd^{2+} with 40.3% than Pd^0 at 30.5% for the PdCo-OV sample.[33]

The 3d spectra of Pd collected during the pretreatment processes showed that on the surface of the aerogels, the Pd was partially oxidized, as expected.[34] However, the Co remained oxidized, with few perceptible changes in the region of the Co 2p spectrum. In comparison, for the PdCo-MW sample, there is a higher concentration of Pd^0 at 35.8%. This shows that PdCo aerogels can oxidize during the carbonization process in the heating techniques presented, resulting in greater oxidation of the Pd-MW sample. In contrast, the PdCo-MW sample presents the stability of the material by not undergoing total oxidation, which is consistent with the results of TEM and electrochemical tests presenting a better response in microwave heating of the sample PdCo-MW.[35]

3.2. Electrochemical Performance.

Aerogel samples were evaluated by cyclic voltammetry (CV) to determine their electrocatalytic activity toward the ethanol oxidation reaction (EOR) in potential ranges between −0.1 and 1.8 V vs RHE (all potential values were normalized vs RHE). Electrochemical profiles in the absence of ethanol were obtained in 1 M KOH at ambient conditions and 20 mV s^{-1} scan rate (Figure 6). The resulting voltammograms show the peaks attributed to Pd activity: (i) the hydrogen desorption in the range of 0.3−0.5V, (ii) hydrogen adsorption at 0.35 V, (iii) Pd(II) oxide reduction at 0.75 V, and (iv) Pd(II) oxide formation at 1.38 V. However, the samples obtained in this work also contain Co; therefore, there are other peaks that may be attributed to the oxidation (v) and reduction (vi) of Co metal species (Figure 6a). For the PdCo aerogels, oxidation and reduction processes are observed between 0.9 and 1.55 V vs RHE.

The use of microwave heating during the synthesis steps clearly improves the electrochemical activity of PdCo-MW. The lower particle size detected by TEM and the higher content of the Pd^0 present in the PdCo-MW evaluated by XPS show clearly that this synthesis procedure has a great impact on the electrochemical performance of the aerogels compared to that obtained using a convectional heating process as in the case of PdCo-OV.

The evaluation of the EOR was carried out in the same range of potential as the CV tests, where it can be seen that the mass current for the PdCo-MW aerogel was clearly superior to that obtained when PdCo-OV was used (Figure 6b). Furthermore, compared with the sample that only contains Pd, the current density value obtained with the material based on PdCo-MW was almost 3 times greater than that obtained

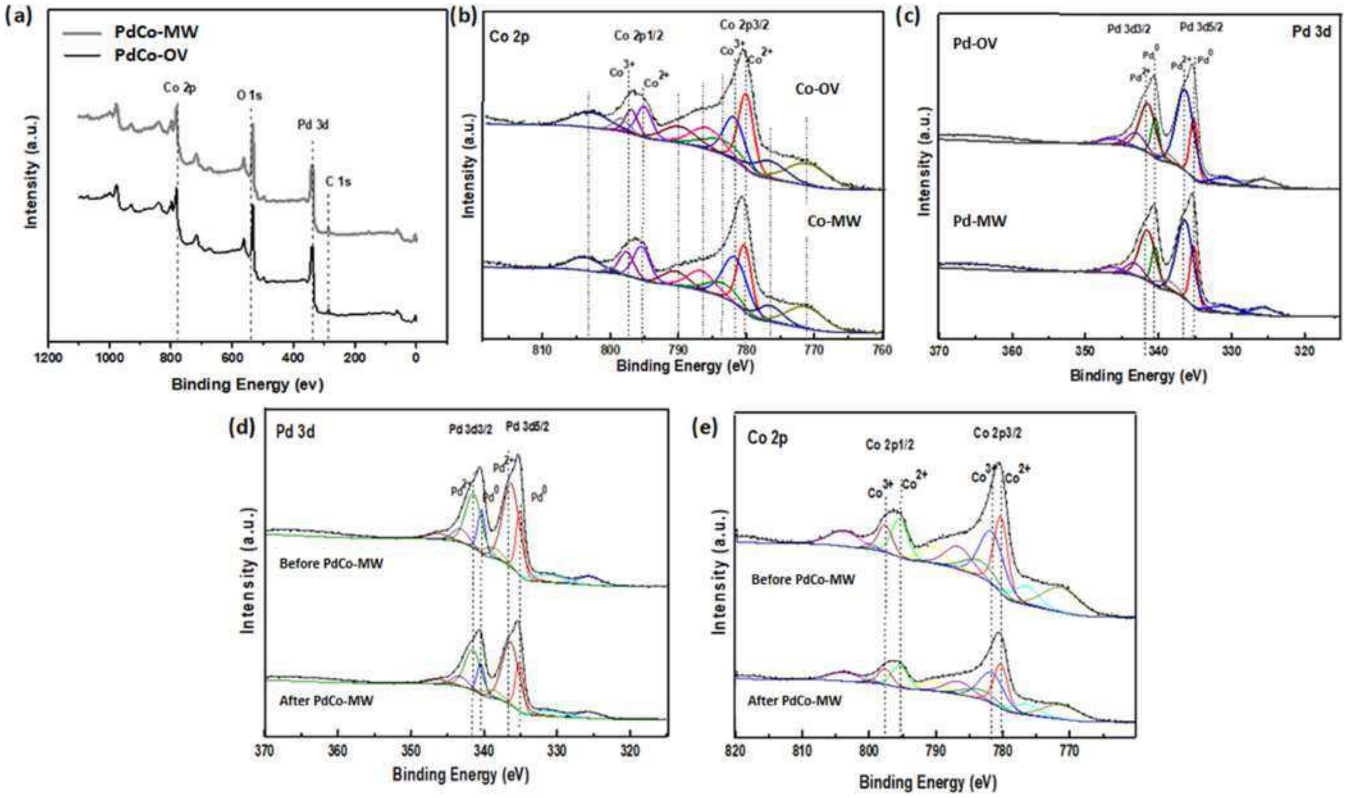

Figure 5. XPS analysis for Pd and Co species in PdCo aerogels. (a) High-resolution general spectra of PdCo aerogels. (b) Evaluation of spectra in the Co 2p region. (c) Evaluation of spectra in the Pd 3d region. (d) Comparison of spectra in the Pd 3d region before and after the stability test of the PdCo-MW aerogel. (e) Comparison of spectra in the Co 2p region before and after the stability test of the PdCo-MW aerogel.

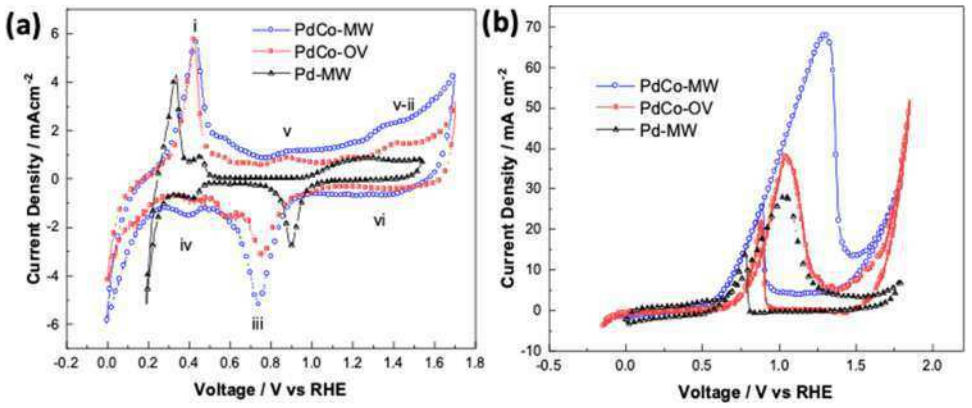

Figure 6. Comparative voltammograms of PdCo-MW, PdCo-OV, and Pd-MW in 1 M KOH (a) in the absence of ethanol and (b) in the presence of 0.5 M ethanol.

Table 1. Comparison of Electrocatalysts Used for the EOR in Alkaline Media Reported to Date

Sample	Ethanol Concentration	Electrolyte	Maximum ell Voltage	Maximum Current Density (mA cm^{-2})	Reference
Pd/C	1 M	1 M KOH	0.78 V vs RHE	30	36
Ni@Pd-Ni NAs	0.5 M	1 M KOH	−0.25 V	50	37
NiPd	1 M	1 M NaOH	0.82 V vs RHE	4.1	38
Au@Pd/C	1 M	1 M KOH	−0.19 V vs MMO	10.5	39
NCNT-Pd	0.1 M	1 M KOH	−0.39 V vs Ag/AgCl	10.30	40
cPd(DBA)$_2$	0.5 M Gly/KOH	1 M KOH	0.08 V vs NHE	16	41
Pd-MW	1 M	1 M KOH	1.03 V vs RHE	28	this work
PdCo-OV	1 M	1 M KOH	1.05 V vs RHE	37	this work
PdCo-MW	1 M	1 M KOH	1.28 V vs RHE	70	this work

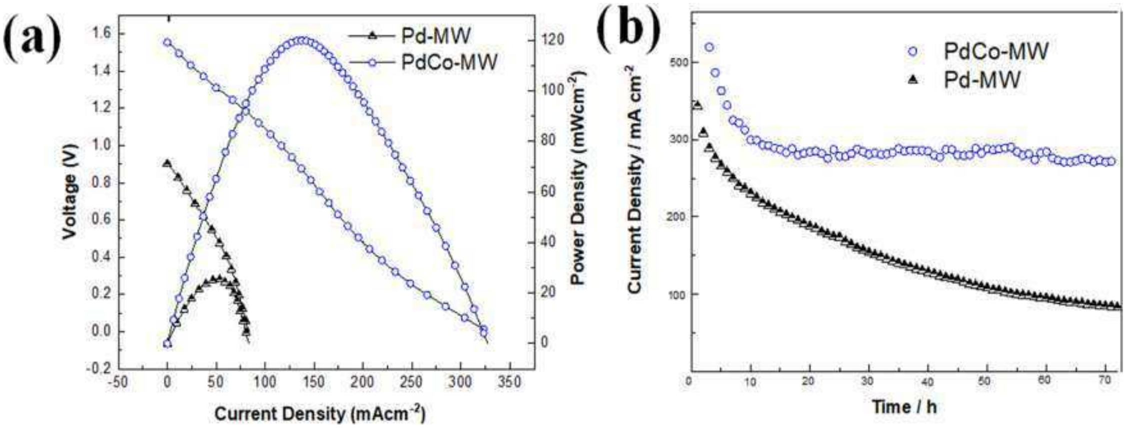

Figure 7. (a) Polarization and power density curves of MFC using 1 M ethanol as fuel and O_2 as an oxidant and Pd-based aerogels as anodic electrocatalysts. (b) Stability test performance of the MFC using PdCo-MW and Pd-MW aerogels.

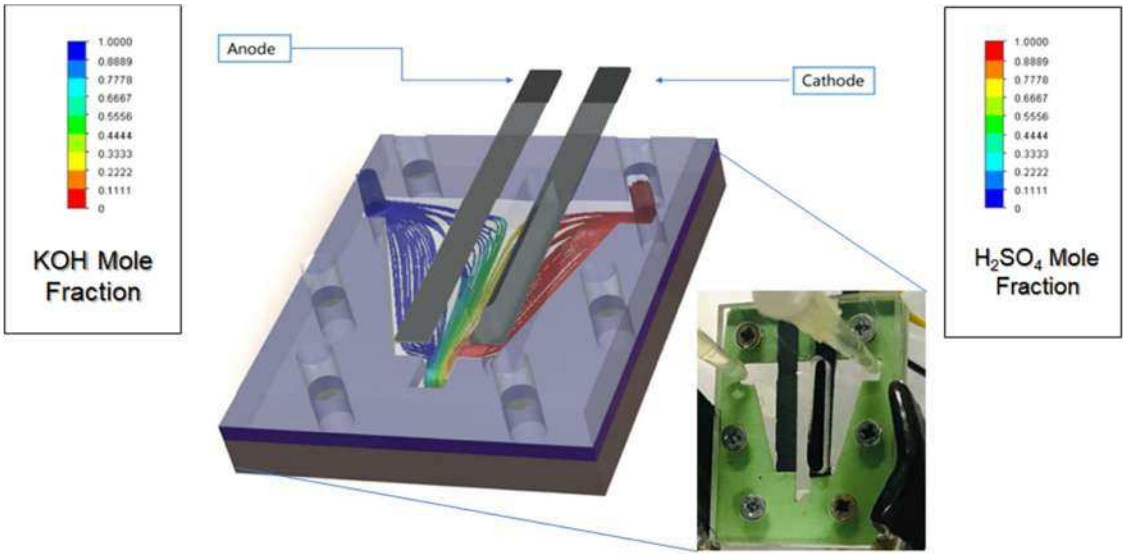

Figure 8. Distribution of the electrolytes injected in the MFC, acid and alkaline, for the catholyte and anolyte, respectively.

with the Pd-MW electrocatalyst, exhibiting the advantage of using the combination of Pd and Co besides the microwave heating during synthesis. This novel procedure can be compared with other studies previously reported, where other materials that are not aerogels do not reach current densities as high as that of the PdCo-MW aerogel (see Table 1).

Based on the results in the half-cell, PdCo-MW vs Pd-MW aerogels were selected to be compared in the MFC (Figure 7) in order to corroborate the contribution of Co in the electrocatalytic activity of the materials.

In the case of the results obtained with the Pd-MW electrocatalyst, 22 mW cm^{-2} as maximum power density was obtained with an OCV of 0.88 V; meanwhile, when PdCo-MW was used as the anodic electrocatalyst, an increase of 1 order of magnitude in the maximum power density value (120 mW cm^{-2}) and an OCV of 1.59 V were achieved. In addition, maximum current densities of 330 and 80 mA cm^{-2} were achieved with PdCo-MW and Pd-MW, respectively (Figure 7a). It is important to note that the high OCV values are due to the properties of the catalytic material in combinations with the pH gradient in the system (anolyte and catholyte), as has already been reported in some studies.[49−51]

Finally, the electrochemical stability of the synthesized materials was also evaluated in the microfluidic fuel cell for a prolonged period of time (70 h). Figure 7b shows a stable performance for the MFC that uses the PdCo-MW aerogel compared to that of the sole palladium aerogel (Pd-MW), which is maintained along the time. Therefore, the presence of cobalt in the aerogel not only improves the catalytic performance toward the EOR but also clearly improves the material stability by maintaining the excellent performance for more than 70 h.

Figure 8 presents a schematic representation of the homogeneous distribution of the electrolytes, which have different characteristics such as pH and density, used in the microfluidic device. This profile was obtained by simulation experiments using Open FOAM CFD simulation software, where at 200 μL min^{-1} flux rate, the interface formation under the laminar flux is guaranteed.

Furthermore, Figure 5d,e shows a comparative XPS study for the sample of PdCo-MW before and after current−time stability tests of the electrocatalyst for 70 h (Figure 7b), where the oxidation states in Pd 3d are observed, with the peaks in Pd^0 and Pd^{2+}, Co 2p, with the peaks of Co^{2+} and Co^{3+}. It can be appreciated that no change in the average width of the peak

Table 2. Comparison of MFC Performance Using Ethanol as Fuel

Anode	Cathode	Electrode Area (cm^2)	Fuel	Electrolyte	Flow Rate (μL/min)	OCV (V)	Power Density (mW cm^{-2})	Maximum Current Density (mA cm^{-2})	Reference
Pd−Ag/MWCNT (2 mg)	Pt/C (30 wt %) (2 mg)	0.09	3 M ethanol; air-breathing	1 M KOH	200	0.95	14.5	34	42
Pt−Ru (1:1) (4 mg cm^{-2})	Ag−Pt/graphene (0.04 mg cm^{-2})	0.015	2 M ethanol; air-breathing	0.5 M KOH	2.8	0.75	10	54	43
PtRu/C-Sb	Pt-C (60 wt %) (5 mg)	0.1963	1 M ethanol	0.1 M H_2SO_4	200	0.74	23.27	68.06	44
Pd/C			1.5 M ethanol; air-breathing	0.5 M H_2SO_4 and 0.3 M KOH		1.03	99.66	400	45
Pd−NiO/C (1 mg)	Pt/C (1 mg)	0.015	1.5 M ethanol; air-breathing	0.5 M H_2SO_4 and 0.3 M KOH	2.5	1.11	108	242	46
$Pt_{80}Sn_{10}Ni_{10}/C$	C (2 mg cm^{-2})	0.3	1 M ethanol; 0.1 M sodium percarbonate	0.5 M H_2SO_4		0.71	37.77	226.61	47
Pt−Sn−Ru/C (7:1:2) (2 mg cm^{-2})	Pt/C (2 mg cm^{-2})	0.3	1 M ethanol; 0.1 M sodium	0.5 M H_2SO_4	300	0.63	36	230.2	48
PdCo-MW	Pt/C (2 mg cm^{-2})	0.02	1 M ethanol	1 M KOH	200	1.59	120	330	this work
Pd-MW	Pt/C (2 mg cm^{-2})	0.02	1 M ethanol	1 M KOH	200	0.88	22	80	this work

for both elements occurred, which indicates that there was no oxidation state change of the material. However, it is observed that the intensity of the high peak decreases; this behavior is attributed to the fact that the material remains stable in the polarization tests of MFC.

Finally, for comparative purposes with the aerogels presented in this work, Table 2 presents the MFC performance previously published using several electrocatalysts (not aerogels) in the presence of ethanol as fuel.

4. CONCLUSIONS

The PdCo-MW aerogel was successfully synthesized by an innovative method based on microwave heating. The use of microwaves significantly increases the specific surface area and the presence of Pd^0, which are relevant for further electrochemical reactions. Furthermore, the combination of cobalt with palladium not only increases the specific surface area but also leads to a significant increase in mesoporosity (also called as feeder pores). On the other hand, the interplanar spacing of Pd(111) measured by HR-TEM shows an increase for the PdCo aerogels compared to that of the Pd aerogel alone and a slight increase in the case of using microwave heating during the synthesis, indicating the presence of Pd−Co metallic alloys and a beneficial effect of using microwaves.

All of these physicochemical properties of the PdCo-MW aerogel offer a great advantage for electrochemical applications, especially for the ethanol oxidation reaction, even in microfluidic fuel cells, where the current density reached a value of 330 mA cm^2 (more than 3 times that of the palladium aerogel), besides a much greater stability over time. Moreover, this type of electrocatalytic material with high surface area, active sites, and stability could be widely used for oxidation reactions of several fuels and applied in electrochemical energy systems.

■ ASSOCIATED CONTENT

Supporting Information

The Supporting Information is available free of charge at https://pubs.acs.org/doi/10.1021/acsaem.3c00173.

Additional experimental details of the aerogel synthesis procedure, including photographs of the experimental setup (PDF)

■ AUTHOR INFORMATION

Corresponding Authors

J. Ledesma-García − *División de Investigación y Posgrado, Facultad de Ingeniería, Universidad Autónoma de Querétaro, 76010 Santiago de Querétaro, Mexico*; orcid.org/0000-0002-0677-4280; Email: janet.ledesma@uaq.mx

A. Arenillas − *Instituto de Ciencia y Tecnología del Carbono, INCAR-CSIC, 33011 Oviedo, Spain*; Email: aapuente@incar.csic.es

Authors

A. Martínez-Lázaro − *División de Investigación y Posgrado, Facultad de Ingeniería, Universidad Autónoma de Querétaro, 76010 Santiago de Querétaro, Mexico*

A. P. Mendoza-Camargo − *División de Investigación y Posgrado, Facultad de Ingeniería, Universidad Autónoma de Querétaro, 76010 Santiago de Querétaro, Mexico*

M. H. Rodriguez-Barajas − *División de Investigación y Posgrado, Facultad de Ingeniería, Universidad Autónoma de Querétaro, 76010 Santiago de Querétaro, Mexico*

F. I. Espinosa-Lagunes − *Centro de Investigación y Desarrollo Tecnológico en Electroquímica, 76703 Santiago de Querétaro, Mexico*

Y. Salazar-Lara − *Centro de Investigación y Desarrollo Tecnológico en Electroquímica, 76703 Santiago de Querétaro, Mexico*

A. Herrera-Gomez − *Centro de Investigación y de Estudios Avanzados, 76230 Santiago de Querétaro, Mexico*

O. Cortazar-Martínez − *Centro de Investigación y de Estudios Avanzados, 76230 Santiago de Querétaro, Mexico*

N. Rey-Raap − *Instituto de Ciencia y Tecnología del Carbono, INCAR-CSIC, 33011 Oviedo, Spain*

L. G. Arriaga − *Centro de Investigación y Desarrollo Tecnológico en Electroquímica, 76703 Santiago de Querétaro, Mexico*; orcid.org/0000-0001-5052-2294

Complete contact information is available at:

https://pubs.acs.org/10.1021/acsaem.3c00173

Notes

The authors declare no competing financial interest.

■ ACKNOWLEDGMENTS

The authors thank Consejo Nacional de Humanidades, Ciencias y Tecnologías (CONAHCYT) for funding through the Ciencia de Frontera 2020-845132.

■ REFERENCES

(1) Safdar, M.; Jänis, J.; Sánchez, S. Microfluidic fuel cells for energy generation. *Lab Chip* **2016**, *16*, 2754−2758.

(2) Liu, C.; Sun, C.; Gao, Y.; Lan, W.; Chen, S. Improving the Electrochemical Properties of Carbon Paper as Cathodes for Microfluidic Fuel Cells by the Electrochemical Activation in Different Solutions. *ACS Omega* **2021**, *6*, 19153−19161.

(3) Pihosh, Y.; Uemura, J.; Turkevych, I.; Mawatari, K.; Kazoe, Y.; Smirnova, A.; Kitamori, T. From Extended Nanofluidics to an Autonomous Solar-Light-Driven Micro Fuel-Cell Device. *Angew. Chem., Int. Ed.* **2017**, *56*, 8130−8133.

(4) Santoro, C.; Kodali, M.; Herrera, S.; Serov, A.; Leropoulos, I.; Atanassov, P. Power generation in microbial fuel cells using platinum group metal-free cathode catalyst: Effect of the catalyst loading on performance and costs. *J. Power Sources* **2018**, *378*, 169−175.

(5) Oezaslan, M.; Liu, W.; Nachtegaal, M.; Frenkel, A. I.; Rutkowski, B.; Werheid, M.; Herrmann, A. K.; Laugier-Bonnaud, C.; Yilmaz, H. C.; Gaponik, N.; Czyrska-Filemonowicz, A.; Eychmüller, A.; Schmid, T. J. Homogeneity and elemental distribution in self-assembled bimetallic Pd-Pt aerogels prepared by a spontaneous one-step gelation process. *Phys. Chem. Chem. Phys.* **2016**, *18*, 20640−20650.

(6) Wen, D.; Liu, W.; Haubold, D.; Zhu, C.; Oschatz, M.; Holzschuh, M.; Wolf, A.; Simon, F.; Kaskel, S.; Eychmüller, A. Gold Aerogels: Three-Dimensional Assembly of Nanoparticles and Their Use as Electrocatalytic Interfaces. *ACS Nano* **2016**, *10*, 2559−2567.

(7) Wang, J.; Chen, F.; Jin, Y.; Guo, L.; Gong, X.; Wang, X.; Johnston, R. L. In situ high-potential-driven surface restructuring of ternary AgPd-Ptdilute aerogels with record-high performance improvement for formate oxidation electrocatalysis. *Nanoscale* **2019**, *11*, 14174−14185.

(8) Henning, S.; Ishikawa, H.; Kühn, L.; Herranz, J.; Müller, E.; Eychmüller, A.; Schmidt, T. J. Unsupported Pt-Ni Aerogels with Enhanced High Current Performance and Durability in Fuel Cell Cathodes. *Angew. Chem., Int. Ed.* **2017**, *56*, 10707−10710.

(9) Liu, W.; Herrmann, A. K.; Bigall, N. C.; Rodriguez, P.; Wen, D.; Oezaslan, M.; Schmidt, T. J.; Gaponik, N.; Eychmüller, A. Noble metal aerogels-synthesis, characterization, and application as electrocatalysts. *Acc. Chem. Res.* **2015**, *48*, 154−162.

(10) Gao, F.; Zhang, Y.; Ren, F.; Shiraishi, Y.; Du, Y. Universal Surfactant-Free Strategy for Self-Standing 3D Tremella-Like Pd−M (M = Ag, Pb, and Au) Nanosheets for Superior Alcohols Electrocatalysis. *Adv. Funct. Mater.* **2020**, *30*, No. 2000255.

(11) Gao, F.; Zhang, Y.; Wu, Z.; You, H.; Du, Y. Universal strategies to multi-dimensional noble-metal-based catalysts for electrocatalysis. *Coord. Chem. Rev.* **2021**, *436*, No. 213825.

(12) Zhao, Q.; Chu, C.; Xiao, X.; Chen, B. Selectively coupled small Pd nanoparticles on sp2-hybridized domain of graphene-based aerogel with enhanced catalytic activity and stability. *Sci. Total Environ* **2021**, *771*, No. 145396.

(13) Zhou, Q.; Su, Z.; Tang, Y.; Ai, L.; Fu, G.; Wu, Z.; Sun, D.; Tang, Y. Pt-Like Oxygen Reduction Activity Induced by Cost-Effective MnFeO 2 /N-Carbon. *Chem. − Eur. J.* **2019**, *25*, 6226−6232.

(14) Lee, J. Y.; Kwak, D. H.; Lee, Y. W.; Lee, S.; Park, K.W. Synthesis of cubic PtPd alloy nanoparticles as anode electrocatalysts for methanol and formic acid oxidation reactions. *Phys. Chem. Chem. Phys.* **2015**, *17*, 8642−8648.

(15) Zhu, C.; Liu, D.; Chen, Z.; Li, L.; You, T. Superior catalytic activity of Pt/carbon nanohorns nanocomposites toward methanol and formic acid oxidation reactions. *J. Colloid Interface Sci.* **2018**, *511*, 77−83.

(16) Han, A.; Zhang, Z.; Yang, J.; Wang, D.; Li, Y. Carbon-Supported Single-Atom Catalysts for Formic Acid Oxidation and Oxygen Reduction Reactions. *Small* **2021**, *17*, No. 2004500.

(17) Yu, X.; Dos Santos, E. C.; White, J.; Salazar-Alvarez, G.; Pettersson, L. G. M.; Cornell, A.; Johnsson, M. Electrocatalytic Glycerol Oxidation with Concurrent Hydrogen Evolution Utilizing an Efficient MoOx/Pt Catalyst. *Small* **2021**, *17*, No. 2104288.

(18) Wu, X.; Fang, G.; Tong, Y.; Jiang, D.; Liang, Z.; Leng, W.; Liu, L.; Tu, P.; Wang, H.; Ni, J.; Li, X. Catalytic Upgrading of Ethanol to n-Butanol: Progress in Catalyst Development. *ChemSusChem* **2018**, *11*, 71−85.

(19) Feng, Y.; Long, S.; Tang, X.; Sun, Y.; Luque, R.; Zeng, X.; Lin, L. Earth-abundant 3d-transition-metal catalysts for lignocellulosic biomass conversion. *Chem. Soc. Rev.* **2021**, *50*, 6042−6093.

(20) Hu, K.; Ohto, T.; Nagata, Y.; Wakisaka, M.; Aoki, Y.; Fujita, J.; Ito, Y. Catalytic activity of graphene-covered non-noble metals governed by proton penetration in electrochemical hydrogen evolution reaction. *Nat. Commun.* **2021**, *12*, No. 203.

(21) Habibullah, G.; Viktorova, J.; Ruml, T. Current Sstrategies for noble metal nanoparticle synthesis. *Nanoscale Res. Lett.* **2021**, *16*, 47.

(22) Gurrola, M. P.; Ortiz-Ortega, E.; Farias-Zuñiga, C.; Chávez-Ramírez, A. U.; Ledesma-García, J.; Arriaga, L. G. Evaluation and coupling of a membraneless nanofluidic device for low-power applications. *J. Power Sources* **2016**, *307*, 244−250.

(23) Choi, S.; Oh, M. Well-arranged and confined incorporation of PdCo nanoparticles within a hollow and porous metal−organic framework for superior catalytic activity. *Angew. Chem., Int. Ed.* **2019**, *58*, 866−871.

(24) Zhao, C.; Yan, X.; Wang, G.; Jin, Y.; et al. PdCo bimetallic nano-electrocatalyst as effective air-cathode for aqueous metal-air batteries. *Int. J. Hydrogen Energy* **2018**, *43*, 5001−5011.

(25) Zhu, X.; Zhang, B.; Ye, D. D.; Li, J.; Liao, Q. Air-breathing direct formic acid microfluidic fuel cell with an array of cylinder anodes. *J. Power Sources* **2014**, *247*, 346−353.

(26) Sen, B.; Acidereli, H.; Karaman, N.; Sen, F. Monodisperse palladium−cobalt alloy nanocatalyst supported on activated carbon (AC) as highly effective catalyst for the DMAB dehydrocoupling. *Sci. Rep.* **2020**, *10*, No. 11755.

(27) Anicai, L.; Costovici, S.; Cojocaru, A.; Manea, A.; Visan, T. Electrodeposition of Co and CoMo alloys coatings using choline chloride based ionic liquids − evaluation of corrosion behaviour. *Trans. IMF* **2015**, *93*, 302−312.

(28) Eftekhari, A.; Fang, B. Electrochemical hydrogen storage: opportunities for fuel storage, batteries, fuel cells, and supercapacitors. *Int. J. Hydrogen Energy* **2017**, *42*, 25143−25165.

(29) Oh, H. J.; Dao, V. D.; Choi, H. S. Cost-effective CoPd alloy/reduced graphene oxide counter electrodes as a new avenue for high-efficiency liquid junction photovoltaic devices. *J. Alloys Compd.* **2017**, *705*, 610−617.

(30) Xu, G. R.; Han, C. C.; Zhu, Y. Y.; Zeng, J. H.; Jiang, J. X.; Chen, Y. PdCo Alloy Nanonetworks−Polyallylamine Inorganic−Organic Nanohybrids toward the Oxygen Reduction Reaction. *Adv. Mater. Interfaces* **2018**, *5*, No. 1701322.

(31) Zhang, J. W.; Zhang, B.; Zhang, X. Enhanced catalytic activity of ternary NiCoPd nanocatalyst dispersed on carbon nanotubes toward methanol oxidation reaction in alkaline media. *J. Solid State Electrochem.* **2017**, *21*, 447−453.

(32) Cabrera-German, D.; Gomez, G.; Herrera, A. Accurate peak fitting and subsequent quantitative composition analysis of the spectrum of Co 2p obtained with Al Kα radiation: I: cobalt spinel. *Surf. Interface Anal.* **2016**, *48*, 252−256.

(33) Chakraborty, A.; Kunnikuruvan, S.; Kumar, S.; Markovsky, B.; Aurbach, D.; Dixit, M.; Major, D. T. Layered cathode materials for lithium-ion batteries: review of computational studies on LiNi_{1-x-y}

Co_x Mn_y O_2 and $LiNi_{1-x-y}$ $Co_xAl_yO_2$. *Chem. Mater.* **2020**, *32*, 915−952.

(34) Prieto, P.; Marco, J. F.; Serrano, A.; Manso, M.; De la Figuera, J. Highly oriented (111) CoO and Co_3O_4 thin films grown by ion beam sputtering. *J. Alloys Compd.* **2019**, *810*, No. 151912.

(35) Melo, R. S.; Silva, F. C.; Moura, K. R. M.; De Menezes, A. S.; Sinfrônio, F. S. M. Magnetic ferrites synthesised using the microwave-hydrothermal method. *J. Magn. Magn. Mater.* **2015**, *381*, 109−115.

(36) Asim, M.; Saba, N.; Sapuan, S. M.; Nasir, I. M.Potential of Natural Fiber/biomass Filler-Reinforced Polymer Composites in Aerospace Applications. In *Sustainable Composites for Aerospace Applications*; Woodhead Publishing, 2018; pp 253−268.

(37) Guo, F.; Li, Y.; Fan, B.; Liu, Y.; Lu, L.; Lei, Y. Carbon- and binder-free core−shell nanowire arrays for efficient ethanol electro-oxidation in alkaline medium. *ACS Appl. Mater. Interfaces* **2018**, *10*, 4705−4714.

(38) Park, C. E.; Lee, H.; Senthil, R. A.; Jeong, G. H.; Choi, M. Y. Bimetallic nickel-palladium nanoparticles with low Ni content and their enhanced ethanol oxidation performance: using a pulsed laser as modification machinery. *Fuel* **2022**, *321*, No. 124108.

(39) Ruiz-Montoya, J. G.; Nunes, L.M.S.; Baena, A. M.; Tremiliosi, G.; Morales, J. C. Effect of palladium on gold in core-shell catalyst for electrooxidation of ethanol in alkaline medium. *Int. J. Hydrogen Energy* **2021**, *46*, 23670−23681.

(40) Yasmin, S.; Roy, N.; Kabir, M. H.; Jeon, S. Nitrogen-functionalized carbon nanotube based palladium nanoparticles as an efficient catalyst for oxygen reduction and ethanol oxidation reaction. *Appl. Surf. Sci. Adv.* **2022**, *9*, No. 100235.

(41) Zhiani, M.; Rostami, H.; Majidi, M.; Karami, K. Bis (dibenzylidene acetone) palladium (0) catalyst for glycerol oxidation in half cell and in alkaline direct glycerol fuel cell. *Int. J. Hydrogen Energy* **2013**, *38*, 5435−5441.

(42) Armenta-González, A.; Carrera, R.; Moreno, A.; Álvarez, L.; Ledesma, J.; Cuevas, F. M.; Arriaga, L. G. An improved ethanol microfluidic fuel cell based on a PdAg/MWCNT catalyst synthesized by the reverse micelles method. *Fuel* **2016**, *167*, 240−247.

(43) Estrada-Solís, M.; Abrego-Martínez, J. C.; Moreno, A.; Arriaga, L. G.; Sun, S.; Cuevas, F. M.; Mohamedi, M. Use of a bilayer platinum-silver cathode to selectively perform the oxygen reduction reaction in a high concentration mixed-reactant microfluidic direct ethanol fuel cell. *Int. J. Hydrogen Energy* **2019**, *44*, 18372−18381.

(44) Figueiredo, M. C.; Sorsa, O.; Arán, R. M.; Doan, N.; Feliu, J. M.; Kallio, T. Trimetallic catalyst based on PtRu modified by irreversible adsorption of Sb for direct ethanol fuel cells. *J. Catal.* **2015**, *329*, 69−77.

(45) López-Rico, C. A.; Galindo de la Rosa, J.; Álvarez, L.; Ledesma, J.; Guerra, M.; Arriaga, L. G.; Arjona, N. Direct Ethanol Membraneless Nanofluidic Fuel Cell With High Performance. *ChemistrySelect* **2016**, *1*, 3054−3062.

(46) López-Rico, C.; Galindo de la Rosa, J.; Ortiz, E.; Álvarez, L.; Ledesma, J.; Guerra, M.; Arriaga, L. G.; Arjona, N. High performance of ethanol co-laminar flow fuel cells based on acrylic, paper and Pd-NiO as anodic catalyst. *Electrochim. Acta* **2016**, *207*, 164−176.

(47) Ponmani, K.; Kiruthika, S.; Muthukumaran, B. Investigation of nanometals (Ni and Sn) in platinum-based ternary electrocatalysts for ethanol electro-oxidation in membraneless fuel cells. *J. Electrochem. Sci. Technol.* **2015**, *6*, 95−105.

(48) Ponmani, K.; Nayeemunisa, S. M.; Kiruthika, S.; Muthukumaran, B. Electrochemical characterization of platinum-based anode catalysts for membraneless fuel cells. *Ionics* **2016**, *22*, 377−387.

(49) Arun, A.; Gowdhamamoorthi, M.; Kiruthika, S.; Muthukumaran, B. Analysis of Membraneless Methanol Fuel Cell Using Percarbonate as an Oxidant. *J. Electrochem. Soc.* **2014**, *161*, F311−F317.

(50) Chandra, S.; Lal, S.; Janardhanan, V.; Chandra Sahu, K.; Deepa, M. Ethanol Based Fuel Cell on Paper Support. *J. Power Sources* **2018**, *396*, 725−733.

(51) Priya, M.; Arun, A.; Elumalai, M.; Kiruthika, S.; Muthukumaran, B. A Development of Ethanol / Percarbonate Membraneless Fuel Cell. *Adv. Phys. Chem.* **2014**, *2014*, No. 862691.

Journal of Alloys and Compounds 969 (2023) 172390

Contents lists available at ScienceDirect

Journal of Alloys and Compounds

journal homepage: www.elsevier.com/locate/jalcom

Palladium – Cobalt aerogels for ethanol oxidation: Electrochemical study of chemical ratio effects

M.H. Rodríguez-Barajas [a], A. Gutiérrez [a], A. Martínez-Lázaro [a], F.I. Espinosa-Lagunes [a], N. Rey-Raap [c], A. Arenillas [c,*], J. Ledesma-García [a,*], L.G. arriaga [b]

[a] División de Investigación y Posgrado, Facultad de Ingeniería, Universidad Autónoma de Querétaro, 76010 Santiago de Querétaro, Mexico.
[b] Centro de Investigación y Desarrollo Tecnológico en Electroquímica, 76703 Santiago de Querétaro, Mexico.
[c] Instituto de Ciencia y Tecnología del Carbono, INCAR-CSIC, Francisco Pintado Fe, 26, 33011 Oviedo, Spain

ARTICLE INFO

Keywords:
Metal aerogels
Microwave assisted synthesis
Microfluidic fuel cells
Ethanol electrooxidation reaction

ABSTRACT

The present work presents a simple method based on a microwave-assisted sol-gel process to obtain various PdCo aerogels. Different Pd:Co chemical ratios were used and the obtained bimetallic aerogels exhibit different physicochemical properties such as morphology, surface area, crystalline size and oxidation state of the metal components. These unsupported bimetallic aerogels present interesting properties to be used as electrocatalysts for the ethanol oxidation reaction. Samples with different compositions were electrochemically characterized in a three-electrode cell configuration towards the ethanol oxidation reaction. The result was good performance for PdCo [80:20] and PdCo [50:50] aerogels in terms of current density and reaction potential, respectively. The series of aerogels were also tested as anodes in a real device such as a hybrid (acid-alkaline) microfluidic fuel cell for ethanol oxidation reaction, and the PdCo [80:20] aerogel was found to be the most effective electrocatalyst with 68 mW cm^{-2} and 227 mA cm^{-2} as power density and current density, respectively. The results revealed that the electrochemical performance of this unsupported electrocatalyst is even better than that of the Pd aerogel alone, since the synergies with the transition metal Co are minimized in addition to the use of the noble metal.

1. Introduction

The design and synthesis of new nanomaterials has been of great interest in recent years due to the their interesting properties and multiple applications in catalysis [1], adsorption [2] and separation processes [3,4]. Their physicochemical properties are of great interest due to their large surface area in addition to the pore size distribution and chemical structures that can be modified by the synthesis process. Synthesis strategies for the production of these nanomaterials are crucial, since the synthesis process determines not only the morphology and properties of the material [5], but also the effectiveness of their mass production. This is essential for certain areas such as impurity removal [6], biomolecules manipulation [7], gas storage [8], and electrochemistry (electrocatalysis [9], batteries [10] and other promising applications). Among the porous nanomaterials currently under investigation is a particular type known as aerogels, whose synthesis process involves sol-gel technology. Such materials are of great interest due to their exceptional physicochemical properties. Noble metals [11–13], silica supports [14], oxides [15] and carbon supports [16–19] have been studied mainly for electrocatalysis applications due to their electrochemical properties in electrooxidation of several molecules [20,21]. In this work, aerogels based neither on silica nor on carbon matrices but composed of a combination of noble (Pd) and transition metal (Co) are investigated. Noble metals exhibit great electrochemical activity; however, their scarcity and high price make it necessary to minimize their use. Thank to the optimization of metal content carried out in this work, it is possible to obtain highly efficient, unsupported bimetallic electrocatalysts while minimizing the use of noble metals.

Among the newer electrochemical devices, microfluidic fuel cells (MFCs) are of greatest interest [22]. These devices have received special attention due to their innovation, effectiveness, and small size and weight. The electrooxidation of ethanol in the anode of the MFC requires an electrocatalyst [23], and the PdCo aerogels obtained in this work were also tested for this specific application and device.

---

* Corresponding author.
E-mail addresses: aapuente@incar.csic.es (A. Arenillas), janet.ledesma@uaq.mx (J. Ledesma-García).

https://doi.org/10.1016/j.jallcom.2023.172390
Received 24 May 2023; Received in revised form 5 September 2023; Accepted 1 October 2023

2. Methodology

2.1. Synthesis of aerogels

The synthesis procedure was based on previous work on Pd aerogels published by Martínez-Lázaro et al. [24], changing the stoichiometry of the noble and transition metals. A series of PdCo aerogels was synthesized from 20 mL of 2 mg mL^{-1} $PdCl_2$ solution (99 %, Sigma-Aldrich ReagenPlus®, anhydrous powder, St Louis, MO, USA) and $CoCl_2$ * 6 H_2O (98 %, Sigma-Aldrich ®, ACS reagent, St Louis, MO, USA) with the concentrations of each metal precursor listed in Table 1. The mixture was reduced in a sodium carbonate ($\geq$ 99.5 %, JT. Baker R®) and glyoxylic acid monohydrate solution (98 % Sigma-Aldrich) at a volume ratio of 6:1 [25] in 80 mL of deionized water. The synthesis was carried out at 67 ^{0}C for 7 h. The heating time is divided into two stages: the first one corresponds to the first two hours, when the precipitation of the particles starts; the second stage consists of the formation of the wet gel during the following 5 h. Heating was carried out by microwave radiation using a conventional microwave oven (MW) with a thermocouple inserted into the precursor mixture to control the synthesis temperature and maintain it at 67 °C for 7 h. To continue the gelation process, allowed the resulting wet gel to cool at room temperature for 24 h. To remove unreacted compounds and synthesis by-products, the resulting gel was washed several times with deionized water, ethanol, and acetone. The final step of the synthesis was to dry the aerogels with about 2 mL of deionized water residual volume. For this purpose, the mixture was frozen with liquid N_2 and the solvent was removed by lyophilization (HyperCOOL, model: HC3110) at a temperature of − 110 °C for 24 h.

2.2. Physicochemical characterization

The morphology of the aerogels was characterized using a scanning electron microscope (SEM, Quanta FEG 650 microscopes from FEI). Specific surface area was determined by nitrogen adsorption-desorption isotherms at − 196 °C using Micrometrics ASAP 2020 after degasing the samples overnight at 120 °C. Crystal structures were characterized by X-ray diffraction (XRD; D8-Advance diffractometer Bruker) equipped with a CuKα X-ray source ($\lambda = 0.1541$ nm, 40 kV, 40 mA) at a step size of 0.02° 2Θ and a scan step time of 5 s. The crystallite size (D_{111}) was calculated using the Scherrer equation:

$$D_{111} = \frac{K\lambda}{\beta_{111}\cos\Theta} \tag{1}$$

Where K is the Scherrer constant corresponding to cubic symmetry, and (β_{111}) is the line broadening of the width at half maximum. The electronic structure of the elements in the aerogels was measured using the Phoibos 100 X-ray photoelectron spectroscopy (XPS) analyzer, SPECS, Germany.

2.3. Electrochemical characterization of aerogels obtained in half-cell configuration

2.3.1. Electrocatalytic activity

The aerogels were first studied in a conventional three-electrode system, also called half-cell. The electrochemical evaluation was carried out in alkaline media at a scan rate of 50 mV s^{-1}. The working electrode was a glassy carbon electrode (3 mm diameter), an Ag/AgCl as the reference electrode, and a Pt as the counter electrode. The electrocatalyst ink was prepared from one milligram of aerogel in a mixture of 500 μL deionized water and 50 μL Nafion ® (5 %) of each aerogel sample. The ink was sonicated for 30 min and then 10 μL was applied to the surface of the working electrode.

Table 1
Concentrations of the aerogels for a volume of 20 mL.

Aerogel	Precursor salts proportions	
	Pd (mg)	Co (mg)
Pd	40	–
PdCo [80:20]	32	8
PdCo [50:50]	20	20
PdCo [20:80]	8	32
Co	–	40

Electrochemical profiles were obtained by cyclic voltammetry (CV) experiments in 0.5 M KOH in a potential range of − 0.25–1.6 V vs RHE for each sample. The electrolyte was bubbled with N_2 for 40 min before electrochemical measurement.

2.3.2. Performance of the ethanol oxidation reaction

The electrocatalytic activity of the PdCo aerogels towards the ethanol electrooxidation reaction was tested by cyclic voltammetry (CV) in a 0.5 M KOH + 0.5 M ethanol solution. This mixture was bubbled with N_2 for 40 min at a potential range between − 0.25 and 1.6 V vs. RHE before each electrochemical measurement.

2.3.3. Stability of electrochemical performance

Chronoamperometry was used as a stability test. For this purpose, the half-cell system was stored in 0.5 M ethanol with 0.5 M KOH as electrolyte at 0.8 V vs. RHE for 5 h.

2.4. Evaluation of the obtained aerogels as electrocatalysts in a microfluidic fuel cell system

The microfluidic fuel cell (MFC) settings used for this work are shown in Fig. 1. Toray Carbon Paper-060 (TCP) with a transversal area of 0.02 cm^2 was used for the electrodes in the cell. These electrodes were subjected to pretreatment to remove the hydrophobicity of the paper before ink application. The electrocatalyst ink of each aerogel tested for the anode was prepared from one milligram of aerogel in a mixture of 200 μL deionized water and 50 μL Nafion ® (5 %) of each aerogel sample. The mixture was sonicated for 30 min and then 20 μL were deposited on Toray carbon paper. Ink for the cathode was prepared from 3 mg Pt/C (20 %) in 1 mL deionized water and 500 μL Nafion ® (5 %), and 20 μL were also deposited on Toray carbon paper. Linear sweep voltammetry (LSV) was performed at a flow rate of 200 μL min^{-1} by injecting 0.5 M ethanol with 0.5 M KOH as electrolyte into the anode with the evaluated catalyst and 0.5 M H_2SO_4 into the cathode with commercial Pt/C.

2.4.1. Electrochemical performance

Chronoamperometry was used as a stability test for the synthesized nanomaterials in the anode of the microfluidic fuel cell. At a flow rate of 200 μL min^{-1}, 0.5 M ethanol with 0.5 M KOH as electrolyte was injected into the anode with the catalyst to be evaluated and 0.5 M H_2SO_4 was injected into the cathode with commercial Pt/C.

3. Results and discussion

3.1. Physico.chemical characterization

The crystallinity of the aerogels was measured by XRD (Fig. 2). In the XRD pattern of the Pd and PdCo aerogels (Fig. 2a), the four main diffraction peaks appear at 2Θ values of 40.1°, 46.6°, 68.1° and 82.1° which are assigned to (111), (200), (220) and (311) reflection planes, respectively, according to JCPDS #46–1043. These peaks are consistent with a face-centered cubic (FCC) crystal structure. The resulting aerogels revealed characteristic Pd peaks and a shift in Pd peaks was observed for PdCo aerogels, indicating the formation of Pd-Co alloys.

The crystallite sizes determined using the Scherrer equation were 9.4 nm, 3.7 nm, 2.9 nm, and 5.1 nm for Pd, PdCo [80:20], PdCo [50:50] and PdCo [20:80], respectively. The crystallite sizes of the bimetallic

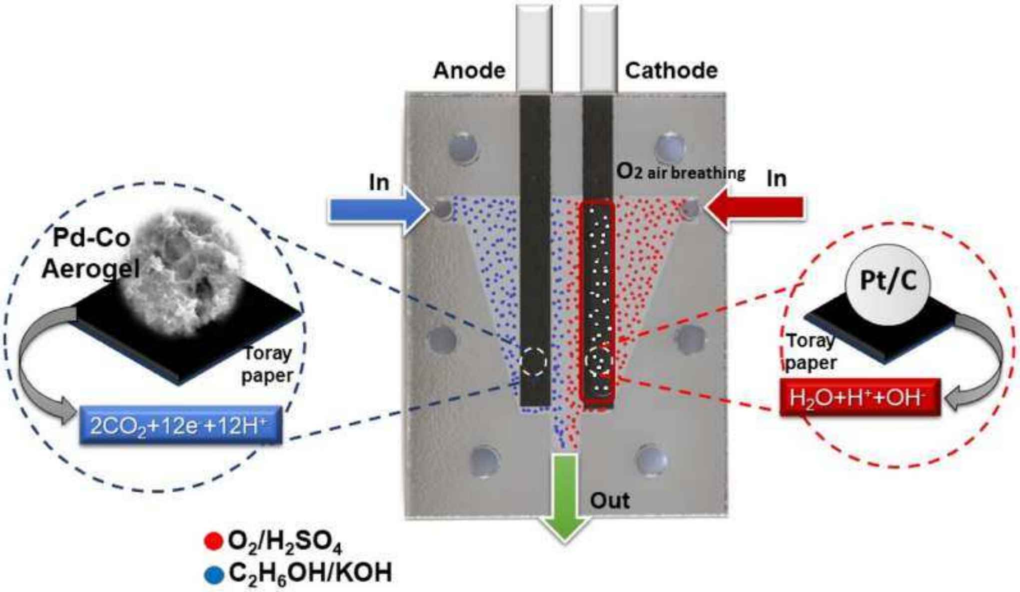

Fig. 1. Schematic representation of the microfluidic fuel cell system used in this work for the ethanol oxidation reaction.

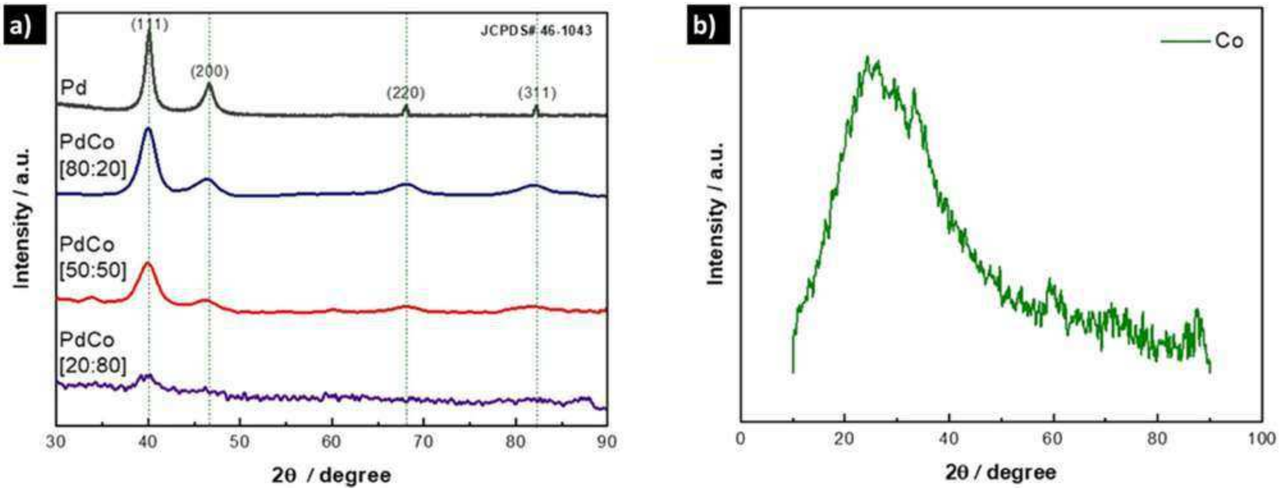

Fig. 2. XRD patterns of a)Pd and PdCo aerogels and b) Co aerogel.

aerogels are very different from those of the Pd aerogel. The latter exhibits the largest crystallite size and when Co is added to Pd, the sizes decrease and reach a minimum in the aerogel with the same amount of the two metals (i.e., PdCo [50:50]). It should be noted that for the PdCo [20:80] aerogel with a higher Co content, a lower crystallinity can be seen in the XRD pattern compared to the other bimetallic aerogels. Fig. 2b shows the XRD pattern of the Co aerogel, in which a peak at 22.46° can be seen. This peak is not observed in any other spectrum of PdCo aerogels. Also, a strong noise can be seen indicating low crystallinity.

The morphology of the aerogels was characterized by scanning electron microscopic analysis (SEM). The micrographs are shown in Fig. 3. The Pd and PdCo [80:20] aerogels present a foam-like morphology with a 3-dimensional open porous network. By adding more transition metal in the synthesis, the change of the structure to a cloud-like structure can be observed, which shows better transparency and more similarity with Co aerogel. The images with different magnifications show chains of nanoclusters of different sizes defining different porosity for each aerogel. PdCo [80:20] and PdCo [50:50] aerogels have nanoclusters of 2–4 nm in size, while PdCo [20:80] has larger nanoclusters of 3–5 nm.

The aerogels were also characterized by high-resolution transmission electron microscopy (HRTEM). The interplanar spacing for Pd-Co [80:20], PdCo [50:50], and PdCo [20:80] is 0.225, 0.221, and 0.218 nm, respectively. These values are very similar to those of the Pd aerogel (0.226 nm). The slight shortening of the spacings can be attributed to the presence of cobalt within the crystal.

The Brunauer-Emmett-Teller method (BET) applied to the nitrogen adsorption-desorption isotherms was used to analyze the specific surface area of the Pd, Co, and PdCo aerogels (Fig. 4a) yielded values of 56, 66, 68, 60, and 53 $m^2\,g^{-1}$ for Pd, PdCo [80:20], PdCo [50:50], PdCo [20:80] and Co aerogels, respectively. This indicates the presence of some microporosity in these samples, with increases slightly in the case of the bimetallic aerogels. The PdCo [50:50] sample exhibits the largest surface area value. However, the shape of the N_2 adsorption isotherm (type II) reveals that all samples are mainly meso/macroporous materials, which is consistent with the open pore structure observed by SEM.

By applying 2D-NLDFT to the adsorption isotherms, a pore size distribution (PSD) can be determined (Fig. 4b). It can be observed that all samples have pores in the mesopore range. Among them, the Pd aerogel

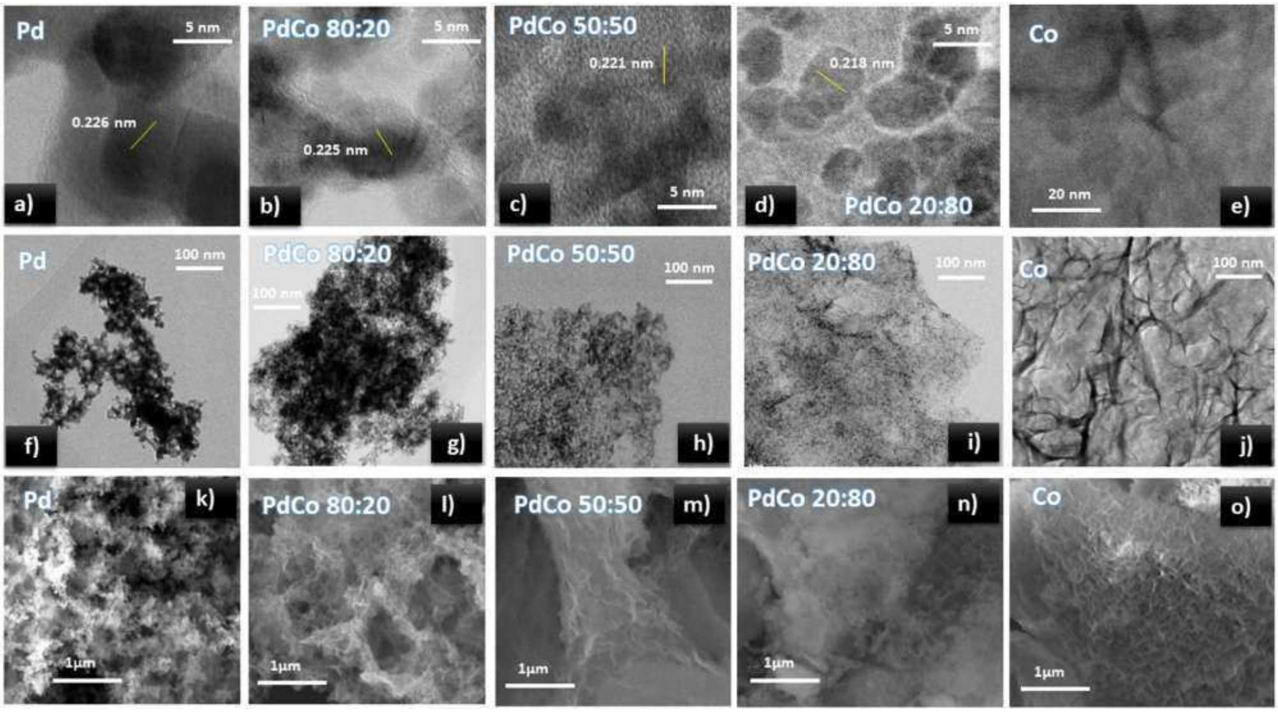

Fig. 3. HRTEM (a-j) and SEM (k-o) images of aerogel.

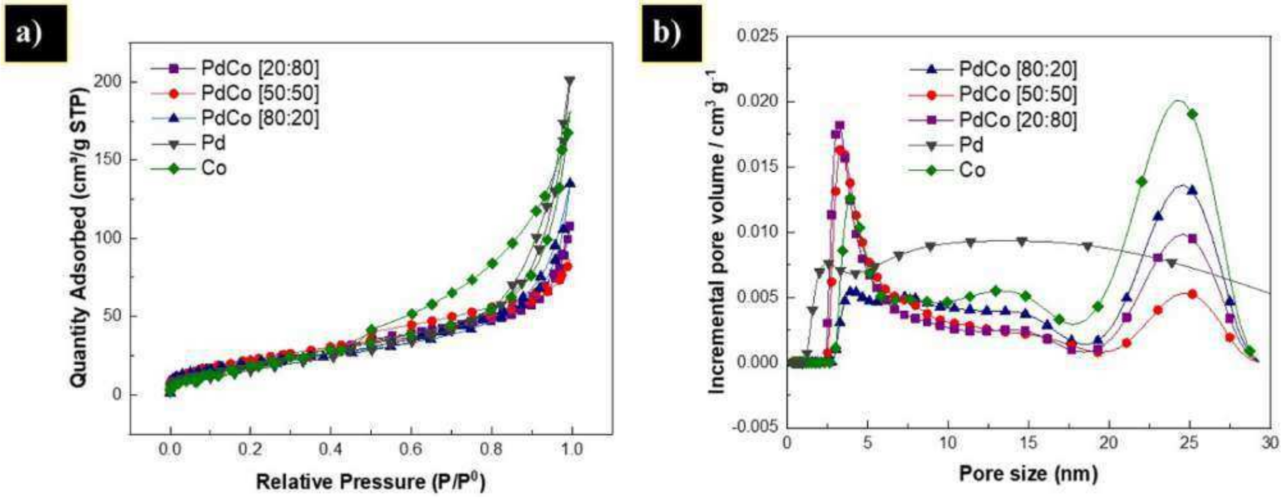

Fig. 4. a) N_2 adsorption-desorption isotherms and b) pore size distribution for the Pd, Co and PdCo aerogels.

is the one with the widest mesopore distribution. The Co aerogel shows a multimodal PSD with the main peaks around 4 and 25 nm. The bimetallic aerogels resemble the PSD of the Co aerogel, indicating the great influence of the presence of Co in their structures, especially in the development of pores of about 25 nm. Among the bimetallic aerogels, the PdCo [80:20] sample is the one with a higher pore volume, as shown by the N_2 adsorption isotherms.

According to the bibliography [26–28], the Pd aerogels should be in the range of 32–62 $m^2\ g^{-1}$. In fact, the surface area of the Pd aerogel is reported to be 50 $m^2 g^{-1}$ [28]. Compared to these values, the porous properties of Pd are preserved in the microwave-assisted methodology performed in this work. Moreover, the obtained bimetallic aerogels have a higher specific surface area.

X-ray photoelectron spectroscopy (XPS) was used to characterize the chemical composition of the synthesized aerogels (Fig. 5). The broad spectra of the bimetallic aerogels PdCo [80:20], PdCo [50:50] and PdCo [20:80] were compared with those of Pd and Co aerogels (Fig. 5a). It can be clearly seen that mainly Co, Pd, O and some C are present, besides certain impurities of Na and Si originating from the precursors used for the synthesis. A decrease in Pd 3d is obviously observed in the PdCo [20:80] sample, while a decrease in Co 2p is observed in the PdCo [80:20] sample. High resolution scans of Co 2p for PdCo [80:20], PdCo [50:50], PdCo [80:20] and Co samples are shown in Fig. 5b. The spectra of Co 2p exhibit two broad main peaks with binding energies at 780 and 796 eV corresponding to Co 2p3/2 and Co 2p1/2, respectively. However, a difference between the deconvoluted peaks of Co 2p is due to the different composition of each material. The oxidation state of the cobalt ions was determined using the Lorentz-Gaussian fitting method. Peaks at 780.5 eV and 795.4 eV corresponding to Co^{2+} and peaks at 782.2 eV and 797.7 eV relating to Co^{3+} were obtained. This could correspond to Co_3O_4 [29–31]. It can be observed that Co^{2+} is present at a higher percentage in PdCo [80:20] and PdCo [20:80] samples. In contrast, an

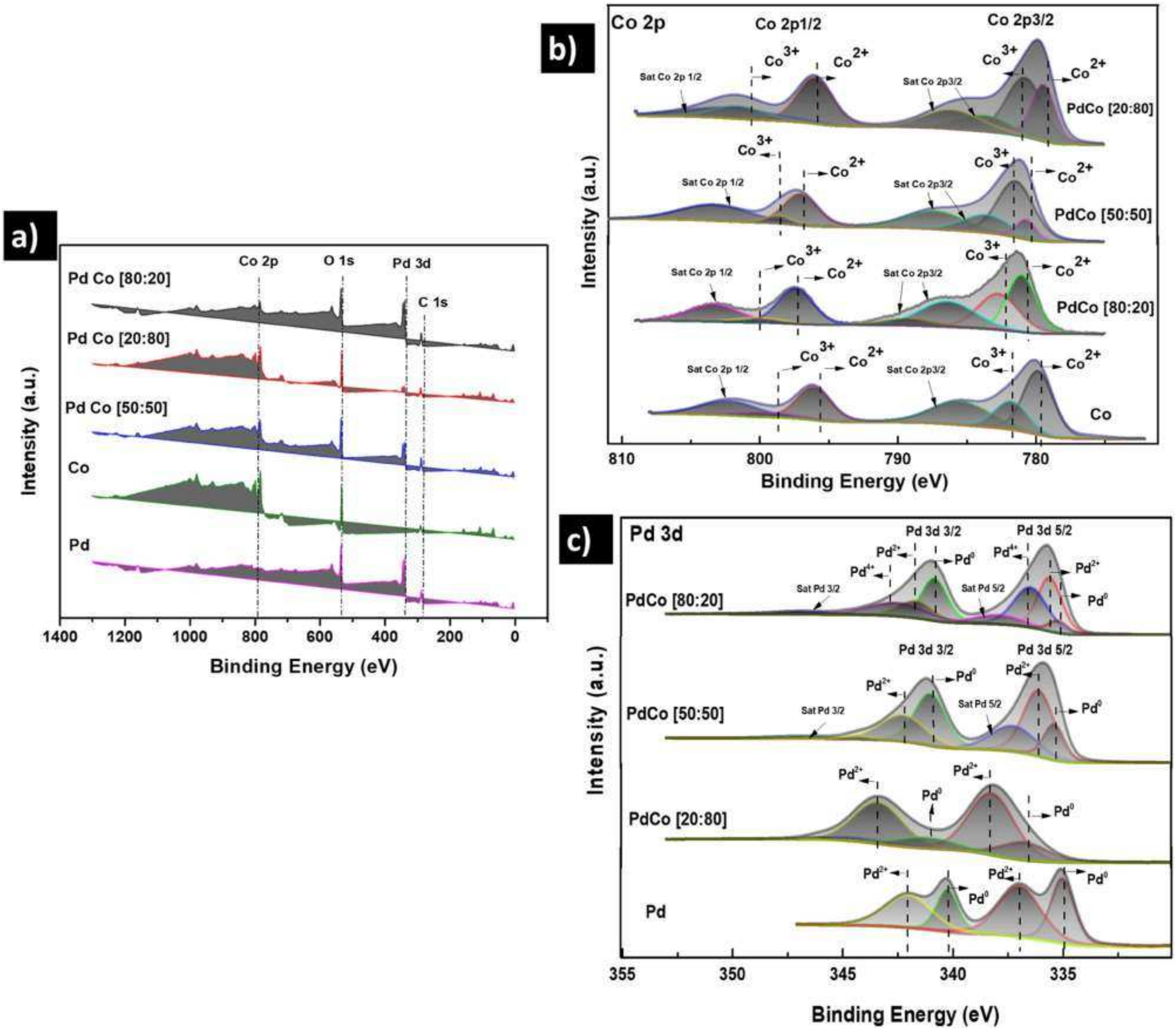

Fig. 5. XPS analysis of PdCo [80:20], PdCo [50:50], PdCo [20:80], Co and Pd aerogels. a) high-resolution XPS total spectra b) high-resolution spectrum in Co 2p region, c) high-resolution spectrum in Pd 3d region.

increase in Co^{3+} is observed for PdCo [50:50].

The spectrum of Pd 3d is shown in Fig. 5c, with binding energies for Pd 3d3/2 at 340.7 eV and Pd 3d5/2 at 355.55 eV in the case of Pd aerogel. However, the bimetallic aerogels PdCo [80:20], PdCo [50:50], and PdCo [20:80] exhibit a signal shift. The deconvoluted spectrum shows the energy band values at peaks with 336.43 eV and 341.76 eV for Pd^{2+}. In contrast, the peaks at 335.15 eV and 340.5 eV refer to Pd^0 [32], indicating the presence of Pd/PdO. Comparison of the different synthesized PdCo aerogels also reveals a higher concentration of Pd^{2+} in PdCo [20:80] compared to PdCo [50:50] and PdCo [80:20]. The PdCo [80:20] sample can be deconvoluted into Pd 3d 5/2 and Pd 3d 3/2. The peaks at 335.1 eV and 340.8 eV correspond to Pd^{2+} and, 336.25 ev and 342.5 eV correspond to Pd^{4+}, while the peaks at 335.51 eV and 340.5 eV refer to Pd^0. Therefore, this could be attributed to the $Pd/PdO/PdO_2/Pd_xO$ structure [33,34].

When comparing the different aerogels obtained in this work, a quantitative difference in the signals can be observed. The quantitative evaluation of each peak was performed by dividing the area of the peak calculated from the cross sections and the average depth of the outgoing electrons. The XPS data were interpreted using Advantage Thermo angular resolution software (ARXPS), where molar fractions such as Co0.72Pd0.1 were determined for the Pd and Co samples in addition to calculating the percentage of the relative weight of the sample [32,35]. For the PdCo [20:80] sample, a higher percentage of Pd^{2+} (40.3 %) than Pd^0 (10.5 %) was found, while for the PdCo [50:50] sample, 30.2 % of Pd^{2+} and 15.6 % of Pd^0 were present. In contrast, the PdCo [80:20] sample contains 20.8 % Pd^{2+}, 18.9 % Pd^{4+} and only 5.4 % Pd^0.

3.2. *Electrochemical performance*

To evaluate the electrocatalytic activity of the synthesized aerogels in the ethanol oxidation reaction (EOR), cyclic voltammetry (CV) was performed in a range of − 0.25 to 1.6 V vs. RHE. The electrochemical profiles are shown in Fig. 6a. They were obtained in an electrolyte of 0.5 M KOH at ambient conditions and a sweep rate of 50 mV s^{-1}. For comparison purposes, Pd aerogel and Co aerogel samples prepared by the same synthesis method were also characterized. The experimental CVs show the peaks attributed to Pd activity: (i) hydrogen desorption in the range of 0.1–0.2 V vs RHE, (ii) hydrogen adsorption at 0.3 V vs. RHE, (iii) reduction of Pd (II) oxide from 0.55 to 0.8 V vs. RHE and (iv) formation of Pd (II) oxide at 1–1.4 V vs. RHE. All of these phenomena are present in the cyclic voltammograms to a greater or lesser extent for

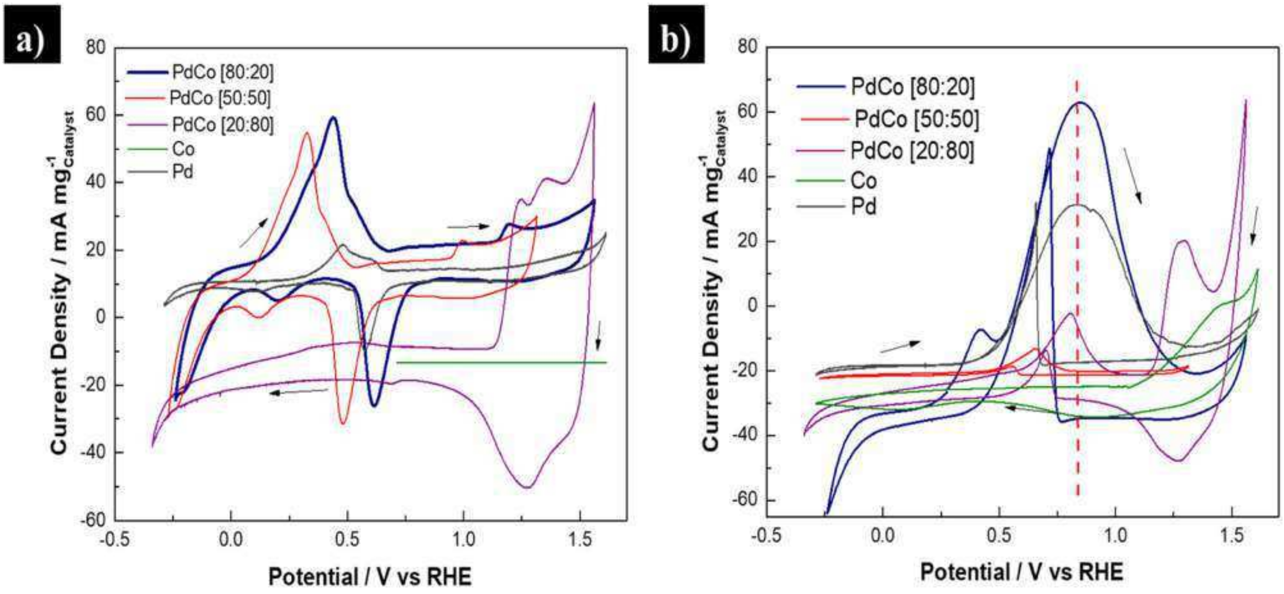

Fig. 6. a) CVs for PdCo, Pd and Co aerogels at 50 mV s^{-1} in 0.5 M KOH. b) EOR activity for PdCo, Pd and Co aerogels at 50 mV s^{-1} in 0.5 M C_2H_6O and 0.5 M KOH.

all aerogels tested. However, the samples containing transition metals show peaks due to the oxidation and reduction of these metallic species. The redox processes of the noble metal (Pd) species can be observed at different potentials for the oxidation and reduction processes of the PdCo aerogels (i.e., between 1.1 and 1.3 V vs. RHE). This could be due to the presence of alloys, which was also inferred from XRD analysis and represents a clear advantage for electron transfer compared to the Pd aerogel.

To compare the electrochemical performance of the Pd, Co and PdCo electrocatalysts for the ethanol oxidation reaction (EOR), the aerogels were evaluated by CV experiments in an electrolyte containing 0.5 M C_2H_6O + 0.5 M KOH. EOR was performed in the same potential range as the CV tests (i.e., from −0.25 to 1.6 V vs. RHE). The electrochemical profiles for EOR demonstrate that the PdCo aerogels exhibit high performance at room temperature in the range of 0.5–1.1 V vs. RHE (Fig. 6b).

It can be observed that the mass current activity of the PdCo [80:20] aerogel is improved compared to the Pd aerogel (49.5 mA mg^{-1}), following the trend PdCo [80:20]>PdCo 50:50 >PdCo [20:80], with 96.1, 11.5 and 4.4 mA mg^{-1}, respectively. The PdCo [80:20] aerogel shows the best electroactivity towards EOR in terms of current activity, however, the thermodynamic reaction potential is slightly in favor of PdCo [20:80], whose highest peak current can be observed at a slightly lower potential (0. 80 V vs. RHE) than that of PdCo [80:20] (0.86 V vs. RHE). However, the difference in the reaction potential with respect to OER is so small that it can be assumed that the most effective catalyst obtained in this work is PdCo [80:20]. These two values are also too close to the potential obtained with the Pd aerogel (i.e., 0.88 V vs. RHE). The Co aerogel does not appear to be an efficient catalyst for EOR, as the species associated with this reaction are not seen on CV [28,36].

The overall reaction of ethanol oxidation can be considered as reaction 1 (R1) and the mechanism of ethanol oxidations with these PdCo aerogels (R2–5) occurs when the CH_3CO or other derivative intermediates are adsorbed on the surface of PdCo aerogels (R2). The ethanol uses the hydroxide ions present in the solution to decompose and become acetic acid. This acidification step is considered a key factor in the reaction [37,38].

$$CH_3CH_2OH + 3H_2O \rightarrow 2CO_2 + 12e^- + 12H^+ \tag{R1}$$

$$PdCo + CH_3CH_2OH + 3OH^- \rightarrow PdCo\text{-}CH_3CO_{ads} + 3\ H_2O + 3e \tag{R2}$$

$$PdCO + OH^- \rightarrow OH_{ads}e^- \tag{R3}$$

$$PdCo\text{-}CH_3CO_{ads} + PdCo\text{-}OH_{ads} \rightarrow PdCo\text{-}CH_3COOH + PdCo \tag{R4}$$

$$PdCo\text{-}CH_3COOH + OH^- \rightarrow PdCo + CH_3COO^- + H_2O \tag{R5}$$

This process allows the elimination of adsorbed intermediate species and the PdCo catalysts promote the oxidation of the fuel according the trend: PdCo [80:20] > PdCo [50:50] > PdCo [20:80]. The maximum electrochemical activity of all investigated PdCo aerogels was found in the range of 0.5–1.2 V vs. RHE. In comparison with the literature [39], R5 also shows the formation of water and the resulting CH_3CO adsorbed on the surface of the PdCo catalysts. The combination of transition and noble metal significantly accelerates this EOR.

The Co aerogel shows a completely different behavior when ethanol and KOH are used. This is probably due to the hydroxyl ions present in R3 and the properties of Co aerogel that promote the evolution of oxygen (OER) to the detriment of EOR in this case (Fig. 6b) [40,41].

Chronoamperometry was performed as a stability test at 0.8 V vs. RHE for 24 h, as shown in Fig. 7. The high catalytic performance of the

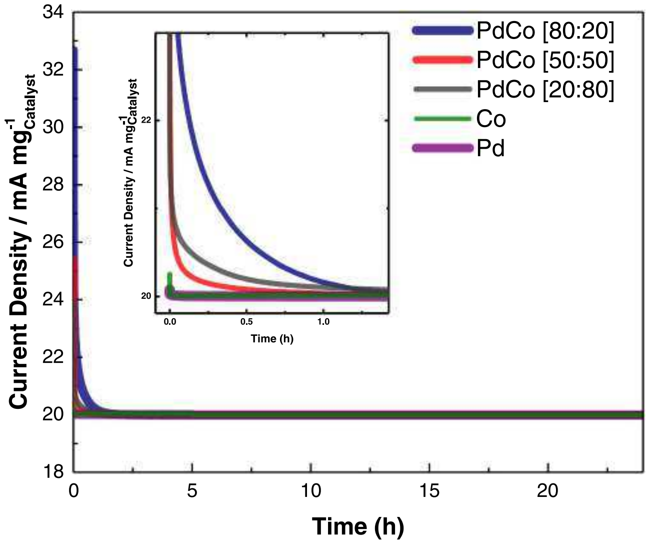

Fig. 7. Stability behavior for PdCo, Pd, and Co aerogels measured at 0.8 V vs. RHE in 0.5 M C_2H_6O and 0.5 M KOH.

PdCo [80:20] aerogel is clear, as is its great stability over time.

3.3. Performance of the microfluidic fuel cell

A microfluidic cell was used to test samples to evaluate their activity under real operating conditions, using 0.5 M C_2H_6O + 0.5 M KOH for the anodic reaction. Five materials were tested: PdCo [80:20], PdCo [50:50], PdCo [20:80], Co and Pd aerogels, the latter two being used as reference materials. The microcell operates by pumping 200 μL min^{-1} into both electrodes. The electrodes were normalized to the mass of the respective material loaded onto an area of 0.02 cm^2. Polarization curves were obtained for a stable open circuit voltage (OCV). The values for the PdCo [80:20], PdCo [50:50], PdCo [20:80], Pd, and Co aerogels were 1.4 V, 0.57 V, 1.22 V, 1.21 V and 1.17 V, respectively.

These results were normalized in three different ways: according to the specific surface area of each aerogel, the mass of the loaded catalyst, and the mass of Pd according to the XPS measurements. The profiles normalized by the specific surface area (Fig. 8a) show favorable results for the aerogel PdCo [80:20], with the highest mass current, in addition to the highest values of power and current density (68 $mWcm^{-2}$ and 227 mA cm^{-2}, respectively). This superior catalytic activity was due to a combination of a favorable morphology with high open porosity (see Fig. 3), a high specific surface area, and a favorable chemical composition with the alloy between Pd and Co. Normalization by loaded mass (Fig. 8c) gave the same results as by area, with PdCo [80:20] being the more efficient catalyst with 26 mW mg^{-1} and 90 mA mg^{-1} for power and current density, respectively. Normalization by mass of Pd (Fig. 8b) was performed according to XPS characterization and considering that Pd is known to be more active for EOR [23,28,36]. Fig. 8b shows interesting and different results, where PdCo [80:20] is with the best performing catalyst, showing 92 $mWmg_{\%Pd}^{-1}$ and 222 $mAmg_{\%Pd}^{-1}$ for power and current density values, respectively. The significance of this result resides in the small amount of noble metal used in this catalyst. Nevertheless, and considering all the tests performed, PdCo [80:20] aerogel is the catalyst with the best performance for EOR, even better than pure Pd aerogel, which is a great progress in minimizing noble metals for electrocatalysts.

Table 2 shows the performance of the different microfluidic devices compared to the one presented in this work, where PdCo [80:20] shows the best and most competitive results. The above results can be summarized in the following two parameters: The PdCo sample achieved the highest OCV value and power density compared to the other aerogels. This is mainly due to the chemical composition observed by XPS, where three oxidation states of the aerogels coexist: Pd (20.8 % Pd^{2+}, 18.9 % Pd^{4+} and 5.4 % Pd^0).

Chronoamperometry was also performed for the MFC during 24 h at 0.8 V, as shown in Fig. 9. The stability tests show variations for the Pd and Co aerogels. However, the bimetallic aerogels exhibit good stability.

4. Conclusions

The PdCo bimetallic aerogels were successfully synthesized using a simple synthesis method that avoided critical temperature and pressure conditions. These aerogels exhibit a highly crystalline FCC structure and alloys between their components. Depending on the ratio of noble and transition metal used during the synthesis process, different physicochemical properties were observed in the obtained samples. The crystallite sizes determined were 9.4 nm, 3.7 nm, 2.9 nm and 5.1 nm for Pd, PdCo [80:20], PdCo [50:50] and PdCo [20:80], respectively. SEM analysis show different morphology as a function of the Co content in the

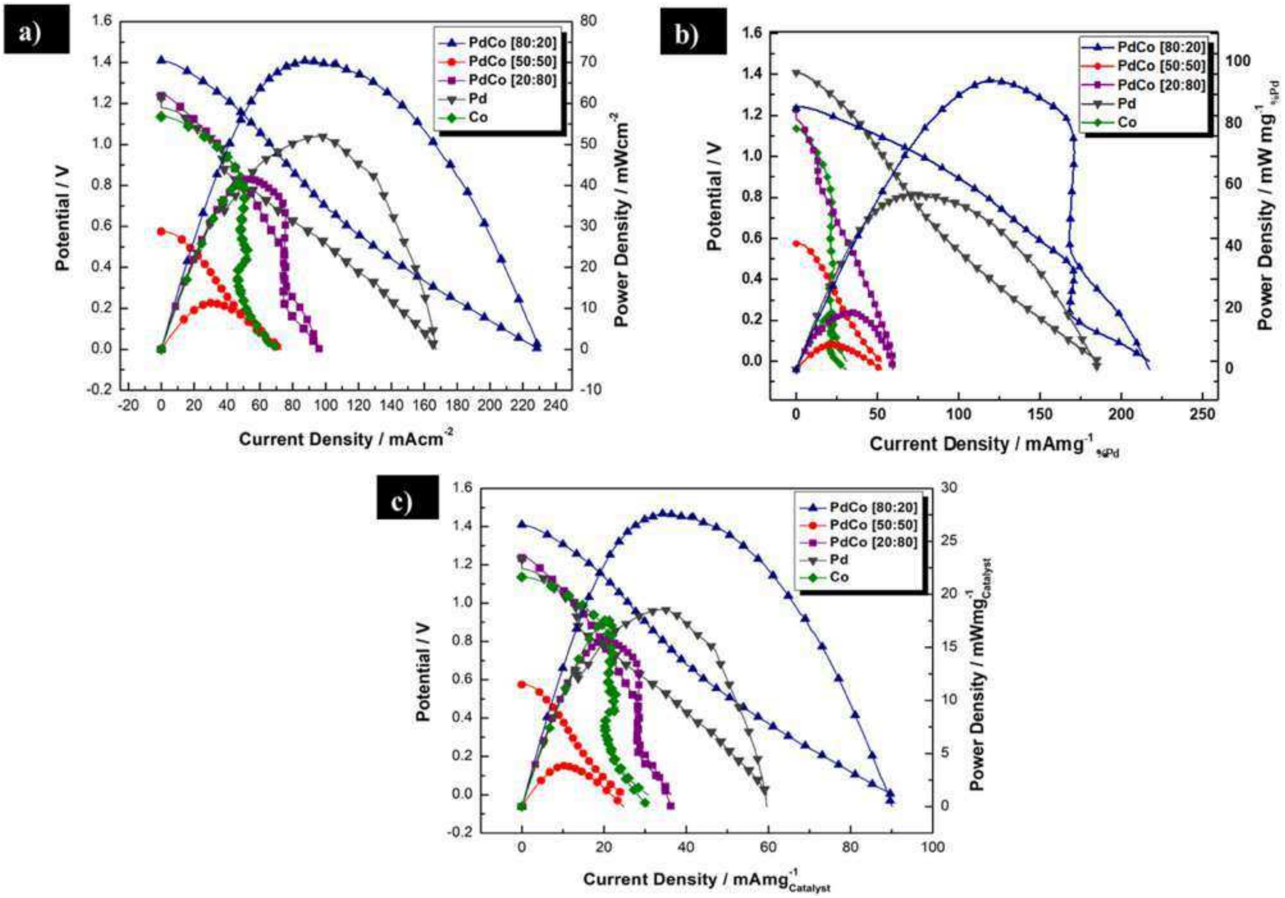

Fig. 8. MFC performance for PdCo, PdCo, PdCo, Pd, and Co aerogels in 0.5 M C_2H_6O and 0.5 M KOH at 10 mV s^{-1}. Normalized by a) area, b) Pd mass according to XPS results and c) by mass of catalyst loaded.

Table 2
Anode electrocatalyst comparison toward ethanol electrooxidation reaction.

Reference	Cell structure design	Anode	Fuel & Oxidant	Electrolyte	Flow rate (μL/min)	OCV (V)*	PPD (mW cm^{-2})*	MCD (mA cm^{-2})*
Brushett et al. [42]	Co-flow;	Pt-Ru (10 $mgcm^{-2}$)	1 M ethanol; Air breathing	1 M KOH	300	0.7	12.1	88
Gónzalez et al. [43]	Co-flow;	Pd-Ag-MWCNT(2 mg)	3 M ethanol; Air breathing	1 M KOH	200	0.95	14.5	34
Solis et al. [44]	Counter-flow; Flow-through; Mixed reactant;	Pt-Ru (1:1) (4 mg cm^{-2})	2 M ethanol; Air breathing	0.5 M KOH	2.8	0.75	10	54
Rico et al. [45]	Counter-flow; Flow through; Dual-electrolyte;	Pd-NiO/C(1 mg)	1.5 M ethanol; Air breathing	0.5 M H2SO4 Y 0.3 M KOH	2.5	1.11	108	242
This work	Co-flow;	PdCo 80:20 aerogel (1.8 $mgcm^{-2}$)	0.5 M ethanol; Air breathing	0.5 M KOH	200	1.4	70	228
This work	Co-flow;	PdCo 50:50 aerogel (1.8 $mgcm^{-2}$)	0.5 M ethanol; Air breathing	0.5 M KOH	200	0.57	11	73
This work	Co-flow;	PdCo 20:80 aerogel (1.8 $mgcm^{-2}$)	0.5 M ethanol; Air breathing	0.5 M KOH	200	1.22	41	95
This work	Co-flow;	Pd aerogel (1.8 $mgcm^{-2}$)	0.5 M ethanol; Air breathing	0.5 M KOH	200	1.21	51	166
This work	Co-flow;	Co aerogel (1.8 $mgcm^{-2}$)	0.5 M ethanol; Air breathing	0.5 M KOH	200	1.17	47	70

* OCV Open circuit voltage.
* MCD maximum current density.
* PPD peak power density.

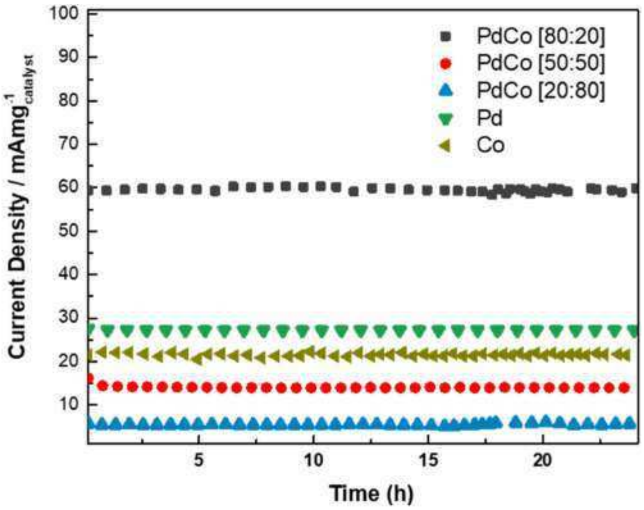

Fig. 9. MFC stability tests for aerogels measured at 0.8 V in 0.5 M ethanol + 0.5 M KOH.

aerogel, but in all cases an open macrostructure typical of aerogel samples. In terms of specific surface area, the bimetallic aerogels present a significant increase in BET surface area compared to the Pd aerogel. Therefore, the combination of the smaller size of the crystallites, the open macroporous structure observed by SEM, and the higher surface area of the bimetallic PdCo aerogels makes these materials very interesting for use as electrochemical electrocatalysts.

The electrochemical performance of the obtained bimetallic aerogels was investigated using a three-electrode-system and a microfluidic fuel cell, in both cases with the aim of characterizing the materials for the ethanol electrooxidation. The obtained current density follows the trend PdCo [80:20] >PdCo[50:50]>PdCo [20:80] with 96.1, 11.5 and 4.4 mA mg^{-1}, respectively, in the ethanol electrooxidation reaction. The PdCo [80:20] aerogel exhibits the highest value, even higher than the Pd aerogel (49.5 mA mg^{-1}). The reaction potentials also compare favorably with the Pd aerogel. As for the incorporation of the aerogels into the microfluidic fuel cell, the PdCo [80:20] aerogel again exhibits the highest values for current and power density (68 $mWcm^{-2}$ and 227 mA cm^{-2}), respectively, as well as great stability with respect to time.

CRediT authorship contribution statement

M.H. Rodriguez-Barajas: Writing – original draft, Methodology. **A. Gutiérrez:** Writing – original draft, Methodology. **A. Martínez-Lázaro:** Writing – original draft, Methodology. **F.I. Espinosa-Lagunes:** Data curation. **N. Rey-Raap:** Investigation, Visualization, Supervision. **A. Arenillas:** Supervision, Resources. **J. Ledesma-García:** Project administration, Resources, Supervision. **L.G. arriaga:** Writing – review & editing, Project administration, Supervision.

Declaration of Competing Interest

The authors declare the following financial interests/personal relationships which may be considered as potential competing interests. J. Ledesma-García reports financial support provided by Mexican Council for Science and Technology.

Data Availability

No data was used for the research described in the article.

Acknowledgements

The authors would like to thank the Mexican Council of Humanistics, Sciences and Technologies (CONAHCYT, Mexico) for financial support through the Ciencia de Frontera (Frontier Science) 2019 project, grant no. 845132. A. Gutiérrez thanks to CONAHCYT, Mexico for postdoctoral fellowship (2023-2025).

References

[1] A.P. Pandey, M.A. Shaz, V. Sekkar, R.S. Tiwari, Highly efficient catalytic derived synthesis process of carbon aerogel for hydrogen storage application, Int. J. Hydrogen Energy (2022), https://doi.org/10.1016/j.ijhydene.2022.02.102.
[2] Y. Saharan, et al., Nanoporous and hydrophobic new Chitosan-Silica blend aerogels for enhanced oil adsorption capacity, J. Clean. Prod. 351 (2022), https://doi.org/10.1016/j.jclepro.2022.131247.
[3] Y.X. Qu, et al., Facile synthesis of mechanically flexible and super-hydrophobic silicone aerogels with tunable pore structure for efficient oil-water separation, Mater. Today Chem. 26 (2022), https://doi.org/10.1016/j.mtchem.2022.101068.
[4] S. Wang, et al., Rechargeable nanofibrillated cellulose aerogel with excellent biocidal properties for efficient oil/water separation, Sep Purif. Technol. 301 (2022), 121955, https://doi.org/10.1016/j.seppur.2022.121955.
[5] A.S. Douk, H. Saravani, M. Noroozifar, K.H. Kim, Tuning the morphology of Pd aerogels for advanced electrocatalysis of formic acid, Microporous Mesoporous Mater. 344 (2022), https://doi.org/10.1016/j.micromeso.2022.112206.

[6] M. Mariana, et al., Recent trends and future prospects of nanostructured aerogels in water treatment applications, J. Water Process Eng. Elsevier Ltd 45 (2022), https://doi.org/10.1016/j.jwpe.2021.102481.

[7] T. Ferreira-Gonçalves, C. Constantin, M. Neagu, C.P. Reis, F. Sabri, R. Simón-Vázquez, Safety and efficacy assessment of aerogels for biomedical applications, Biomed. Pharmacother., Elsevier Mass. S. R. l 144 (2021), https://doi.org/10.1016/j.biopha.2021.112356.

[8] C. Shi, et al., Pyrolytic aerogels with tunable surface groups for efficient methane solidification storage via gas hydrates, Fuel 331 (2023), https://doi.org/10.1016/j.fuel.2022.125716.

[9] H. Guo, D.-H. Si, H.-J. Zhu, Q.-X. Li, Y.-B. Huang, R. Cao, Ni single-atom sites supported on carbon aerogel for highly efficient electroreduction of carbon dioxide with industrial current densities, eScience 2 (2022) 295–303, https://doi.org/10.1016/j.esci.2022.03.007.

[10] M. Shen, et al., Cellulose nanofibers carbon aerogel based single-cobalt-atom catalyst for high-efficiency oxygen reduction and zinc-air battery, J. Colloid Interface Sci. 629 (2023) 778–785, https://doi.org/10.1016/j.jcis.2022.09.035.

[11] M. Farsadrooh, H. Saravani, A. Shafaei Douk, Unique superstructure of Pd–Ir aerogel as a robust three-dimensional electrocatalyst, Int. J. Hydrogen Energy 47 (2022) 25638–25646, https://doi.org/10.1016/j.ijhydene.2022.06.018.

[12] S. Mohammad Mostashari, R. Amiri Dehkharghani, M. Farsadrooh, F. Afshar-Taromi, Engineering three-dimensional superstructure of Pd aerogel with enhanced performance for ethanol electrooxidation, J. Mol. Liq. 360 (2022), https://doi.org/10.1016/j.molliq.2022.119363.

[13] L. Calvillo, L. Mendez De Leo, S.J. Thompson, S.W.T. Price, E.J. Calvo, A.E. Russell, In situ determination of the nanostructure effects on the activity, stability and selectivity of Pt-Sn ethanol oxidation catalysts, J. Electroanal. Chem. 819 (2018) 136–144, https://doi.org/10.1016/j.jelechem.2017.09.060.

[14] L. Wang, et al., High catalytic activity and stability quasi homogeneous alkali metal promoted Ni/SiO2 aerogel catalysts for catalytic cracking of n-decane, Fuel 268 (2020), https://doi.org/10.1016/j.fuel.2020.117384.

[15] L. Solà-Hernández, F. Claudel, F. Maillard, C. Beauger, Doped tin oxide aerogels as oxygen evolution reaction catalyst supports, Int. J. Hydrogen Energy 44 (2019) 24331–24341, https://doi.org/10.1016/j.ijhydene.2019.07.152.

[16] Z. Mai, Z. Liu, S. Liu, X. Zhang, Z. Cui, Z. Tang, Atomically dispersed Co atoms in nitrogen-doped carbon aerogel for efficient and durable oxygen reduction reaction, Int. J. Hydrogen Energy 46 (2021) 36836–36847, https://doi.org/10.1016/j.ijhydene.2021.08.163.

[17] T. He, et al., Atomically dispersed ruthenium in carbon aerogels as effective catalysts for pH-universal hydrogen evolution reaction, Chem. Eng. J. 442 (2022), https://doi.org/10.1016/j.cej.2022.136337.

[18] Y. Zhang, Y. Li, Z. Yao, J. Wang, Q. Zhong, Iron-nickel aerogels anchored on GO nanosheets as efficient oxygen evolution reaction catalysts under industrial conditions, Int. J. Hydrogen Energy 47 (2022) 6996–7004, https://doi.org/10.1016/j.ijhydene.2021.12.078.

[19] T. Kocer, F.E. Saraç-Öztuna, S.F. Kurtoğlu-Öztulum, U. Unal, A. Uzun, Effect of nickel precursor on the catalytic performance of graphene aerogel-supported nickel nanoparticles for the production of COx-free hydrogen by ammonia decomposition, Energy Technol. 10 (2022), https://doi.org/10.1002/ente.202100794.

[20] M. Niu, et al., Synthesis of nanoporous CuO/TiO2/Pd-NiO composite catalysts by chemical dealloying and their performance for methanol and ethanol electro-oxidation, J. Power Sources 362 (2017) 10–19, https://doi.org/10.1016/j.jpowsour.2017.07.011.

[21] Q. Tan, C. Du, Y. Sun, L. Du, G. Yin, Y. Gao, A palladium-doped ceria@carbon core-sheath nanowire network: a promising catalyst support for alcohol electrooxidation reactions, Nanoscale 7 (2015) 13656–13662, https://doi.org/10.1039/c5nr03023d.

[22] H. Ning, F. Zhao, T. Zhou, Advances in microfluidic electrochemical fuel cells in recent years, J. Chem. Technol. Biotechnol. 977 (2022) 1625–1639, https://doi.org/10.1002/jctb.7026.

[23] C. Li, K. Wang, D. Xie, A review of approaches for the design of high-performance electrocatalysts for ethanol electrooxidation, Surf. Interfaces 28 (2022), https://doi.org/10.1016/j.surfin.2021.101594.

[24] A. Martínez-Lázaro, et al., Facile synthesis of unsupported Pd aerogel for high performance formic acid microfluidic fuel cell, Materials 15 (2022) 1422, https://doi.org/10.3390/ma15041422.

[25] A.S. Douk, H. Saravani, M. Farsadrooh, Three-dimensional inorganic polymer of Pd aerogel as a highly active support-less anode catalyst toward formic acid oxidation, Int. J. Hydrogen Energy 44 (2019) 18028–18037, https://doi.org/10.1016/j.ijhydene.2019.05.084.

[26] W. Liu, et al., Noble metal aerogels-synthesis, characterization, and application as electrocatalysts, Acc. Chem. Res. 48 (2015) 154–162, https://doi.org/10.1021/ar500237c.

[27] W. Liu, et al., High-performance electrocatalysis on palladium aerogels, Angew. Chem. - Int. Ed. 51 (2012) 5743–5747, https://doi.org/10.1002/anie.201108575.

[28] A. Shafaei Douk, H. Saravani, M. Noroozifar, Three-dimensional assembly of building blocks for the fabrication of Pd aerogel as a high performance electrocatalyst toward ethanol oxidation, Electrochim. Acta 275 (2018) 182–191, https://doi.org/10.1016/j.electacta.2018.04.073.

[29] S.C. Petitto, M.A. Langell, Surface composition and structure of Co3O4(110) and the effect of impurity segregation, J. Vac. Sci. Technol. A Vac. Surf. Film. 22 (2004) 1690–1696, https://doi.org/10.1116/1.1763899.

[30] D. Cabrera-German, G. Gomez-Sosa, A. Herrera-Gomez, Accurate peak fitting and subsequent quantitative composition analysis of the spectrum of Co 2p obtained with Al Kα radiation: I: cobalt spinel, Surf. Interface Anal. 48 (2016) 252–256, https://doi.org/10.1002/sia.5933.

[31] R. Tholkappiyan, K. Vishista, Tuning the composition and magnetostructure of dysprosium iron garnets by Co-substitution: an XRD, FT-IR, XPS and VSM study, Appl. Surf. Sci. 351 (2015) 1016–1024, https://doi.org/10.1016/j.apsusc.2015.05.193.

[32] H.J. Oh, V.D. Dao, H.S. Choi, Cost-effective CoPd alloy/reduced graphene oxide counter electrodes as a new avenue for high-efficiency liquid junction photovoltaic devices, J. Alloy. Compd. 705 (2017) 610–617, https://doi.org/10.1016/j.jallcom.2017.02.180.

[33] J. Wan, Z. Liu, X. Yang, P. Cheng, C. Yan, Cyanogel-derived synthesis of porous pdfe nanohydrangeas as electrocatalysts for oxygen reduction reaction, Nanomaterials 11 (2021) 1–9, https://doi.org/10.3390/nano11123382.

[34] C.H. Wu, C. Liu, D. Su, H.L. Xin, H.T. Fang, B. Eren, S. Zhang, C.B. Murray, M. B. Salmeron, Bimetallic synergy in cobalt–palladium nanocatalysts for CO oxidation, Nat. Catal. 2 (2019) 78–85, https://doi.org/10.1038/s41929-018-0190-6.

[35] J.W. Zhang, B. Zhang, X. Zhang, Enhanced catalytic activity of ternary NiCoPd nanocatalyst dispersed on carbon nanotubes toward methanol oxidation reaction in alkaline media, J. Solid State Electrochem. 21 (2017) 447–453, https://doi.org/10.1007/s10008-016-3331-3.

[36] H. Zhao, et al., Ultrafast generation of nanostructured noble metal aerogels by a microwave method for electrocatalytic hydrogen evolution and ethanol oxidation, ACS Appl. Nano Mater. 4 (2021) 11221–11230, https://doi.org/10.1021/acsanm.1c02746.

[37] M.T.X. Nguyen, M.K. Nguyen, P.T.T. Pham, H.K.P. Huynh, S.T. Nguyen, Pd coated one-dimensional Ag nanostructures: Controllable architecture and their electrocatalytic performance for ethanol oxidation in alkaline media, Int. J. Hydrogen Energy 46 (2021) 3909–3921, https://doi.org/10.1016/j.ijhydene.2020.10.226.

[38] J. Zhang, et al., Ethanol electrooxidation on highly active palladium/graphene oxide aerogel catalysts, Chem. Phys. 534 (2020), https://doi.org/10.1016/j.chemphys.2020.110753.

[39] A. Martínez-Lázaro, et al., Novel and high electrocatalytic activity aerogel Pd-TM (TM=Co, Ni, Fe), Mater. Today Nano (2023), 100308, https://doi.org/10.1016/j.mtnano.2023.100308.

[40] C. Gao, X. Zhang, J. Zhan, B. Cai, Engineering of aerogel-based electrocatalysts for oxygen evolution reaction, Electrochem. Sci. Adv. (2022), https://doi.org/10.1002/elsa.202100113.

[41] S. Yan, M. Zhong, C. Wang, X. Lu, Amorphous aerogel of trimetallic FeCoNi alloy for highly efficient oxygen evolution, Chem. Eng. J. 430 (2022), https://doi.org/10.1016/j.cej.2021.132955.

[42] F.R. Brushett, R.S. Jayashree, W.P. Zhou, P.J.A. Kenis, Investigation of fuel and media flexible laminar flow-based fuel cells, Electrochim. Acta 54 (2009) 7099–7105, https://doi.org/10.1016/j.electacta.2009.07.011.

[43] A.J. Armenta-González, et al., An improved ethanol microfluidic fuel cell based on a PdAg/MWCNT catalyst synthesized by the reverse micelles method, Fuel 167 (2016) 240–247, https://doi.org/10.1016/j.fuel.2015.11.057.

[44] M.J. Estrada-Solís, et al., Use of a bilayer platinum-silver cathode to selectively perform the oxygen reduction reaction in a high concentration mixed-reactant microfluidic direct ethanol fuel cell, Int. J. Hydrogen Energy 44 (2019) 18372–18381, https://doi.org/10.1016/j.ijhydene.2019.05.078.

[45] C.A. López-Rico, et al., High performance of ethanol co-laminar flow fuel cells based on acrylic, paper and Pd-NiO as anodic catalyst, Electrochim. Acta 207 (2016) 164–176, https://doi.org/10.1016/j.electacta.2016.05.002.

3.3. Conclusiones

La combinación de metales de transición (Fe, Ni, Co) con Pd, resultan una alternativa muy efectiva para disminuir la cantidad del metal noble necesaria para la oxidación de etanol por via electroquímica. La presencia del metal de transición mejora el transporte de oxigeno al interactuar con el electrolito, lo que hace a los aerogeles bimetálicos catalizadores excelentes hacia la ROE. Al ser utilizados en una microcelda que funciona con etanol estos materiales incrementan la densidad de corriente emitida por la celda. Además también el potencial de circuito abierto aumenta. La potencia de corriente también aumenta, al ser directamente proporcional a la corriente emitida. Las combinaciones PdNi y PdCo resultaron ser las mas eficientes para llevar a cabo la ROE en los dispositivos microfluidicos evaluados.

Referencias

Abbas, S. A., Iqbal, M. I., Kim, S. H., & Jung, K. D. (2017). Catalytic Activity of Urchin-like Ni nanoparticles Prepared by Solvothermal Method for Hydrogen Evolution Reaction in Alkaline Solution. *Electrochimica Acta*, *227*, 382–390. https://doi.org/10.1016/j.electacta.2017.01.039

Corbo, P., Migliardini, F., & Veneri, O. (2011). Hydrogen Fuel Cells for Road Vehicles. In *Control*. Springer London. https://doi.org/10.1007/978-0-85729-136-3

Douk, A. S., & Saravani, H. (2020). *Porous 3D Inorganic Superstructure of Pd − Ir Aerogel as Advanced Support-Less Anode Electrocatalyst toward Ethanol Oxidation*. https://doi.org/10.1021/acsomega.0c01661

Douk, A. S., & Saravani, H. (2022). *Is the Pd Aerogel Assembled by Nanosheets as an Advanced Three- Dimensional Support-less Electrocatalyst in Renewable Energy?* https://doi.org/10.1021/acsaenm.2c00019

Douk, A. S., Saravani, H., & Noroozifar, M. (2018). Electrochimica Acta Three-dimensional assembly of building blocks for the fabrication of Pd aerogel as a high performance electrocatalyst toward ethanol oxidation. *Electrochimica Acta*, *275*, 182–191. https://doi.org/10.1016/j.electacta.2018.04.073

Eshghi, A., Sadati, E., & Kheirmand, M. (2019). ScienceDirect Pd , Pd e Ni and Pd e Ni e Fe nanoparticles anchored on MnO 2 / Vulcan as efficient ethanol electro-oxidation anode catalysts. *International Journal of Hydrogen Energy*, *44*(52), 28194–28205. https://doi.org/10.1016/j.ijhydene.2019.08.236

Morales-Acosta, D., Rodríguez G., H., Godinez, L. A., & Arriaga, L. G. (2010). Performance increase of microfluidic formic acid fuel cell using Pd/MWCNTs as catalyst. In *Journal of Power Sources* (Vol. 195, Issue 7, pp. 1862–1865). https://doi.org/10.1016/j.jpowsour.2009.10.007

Wang, H., Chen, H., Wang, H. Q., Ou, C. R., Li, R., & Liu, H. B. (2020). Synthesis of ultrafine low loading Pd–Cu alloy catalysts supported on graphene with excellent electrocatalytic performance for formic acid oxidation. *International Journal of Hydrogen Energy*, *45*(18), 10735–10744. https://doi.org/10.1016/j.ijhydene.2020.02.019

Yazdan-abad, M. Z., Noroozifar, M., Douk, A. S., Modarresi-alam, A. R., & Saravani, H. (2019). Applied Catalysis B : Environmental Shape engineering of palladium aerogels assembled by nanosheets to achieve a high performance electrocatalyst. *Applied Catalysis B: Environmental*, *250*(March), 242–249. https://doi.org/10.1016/j.apcatb.2019.02.064

CAPÍTULO 4

AEROGELES DE METALES DE TRANSCION PARA SU USO EN CELDAS MICROFLUIDICAS

4.1. HIDROGENO: COMO VECTOR ENERGETICO SUSTENTABLE

La utilización de combustibles fósiles para generación de energía está ligada a multiples desventajas, como sus reservas limitadas y focalizadas solo en ciertos países con sus consecuencias en el precio y disponibilidad, pero sobre todo por su alto grado contaminante entre los que destaca la generación de CO_2 y su contribución al efecto invernadero. El aumento de la temperatura global del planeta está asociado con el aumento considerable de estos gases de origen antropogénico. Durante la última década se ha detectado un incremento de 0,18 ◦C cada año en la temperatura del planeta, lo que ha llevado a que la media global haya aumentado 1,5 ◦C en comparación con la temperatura registrada antes de la era industrial. Esto tiene consecuencias graves en cuanto a la estabilidad climática con efectos directos en los ecosistemas e incluso en la vida de las personas.

En la actualidad, aunque la electricidad es aun generada en gran medida por el uso de combustibles fósiles, se está potenciando enormemente el uso de fuentes de energía renovable con el fin de por una parte asegurar el suministro energético y por otra minimizar el impacto ambiental. Sin embargo, las principales fuentes renovables de energía son altamente discontínuas, mientras que la demanda energética es constante. Por lo tanto, este nuevo escenario trae consigo una nueva necesidad de almacenamiento de energía. En este contexto, el hidrógeno surge como un vector energético altamente efectivo. La combustión del hidrógeno no produce gases de efecto invernadero ni contaminantes solidos o acuosos, por lo que se puede definir como un vector de energía verde y limpia. Tiene un alto poder calorífico y muestra una excelente energía densidad por peso.

Se considera el combustible del futuro por su sostenibilidad, alto potencial energético y alta eficiencia de conversión ya que 1 kg de hidrógeno contiene una energía de aproximadamente 120-140 Mega Joules (MJ).

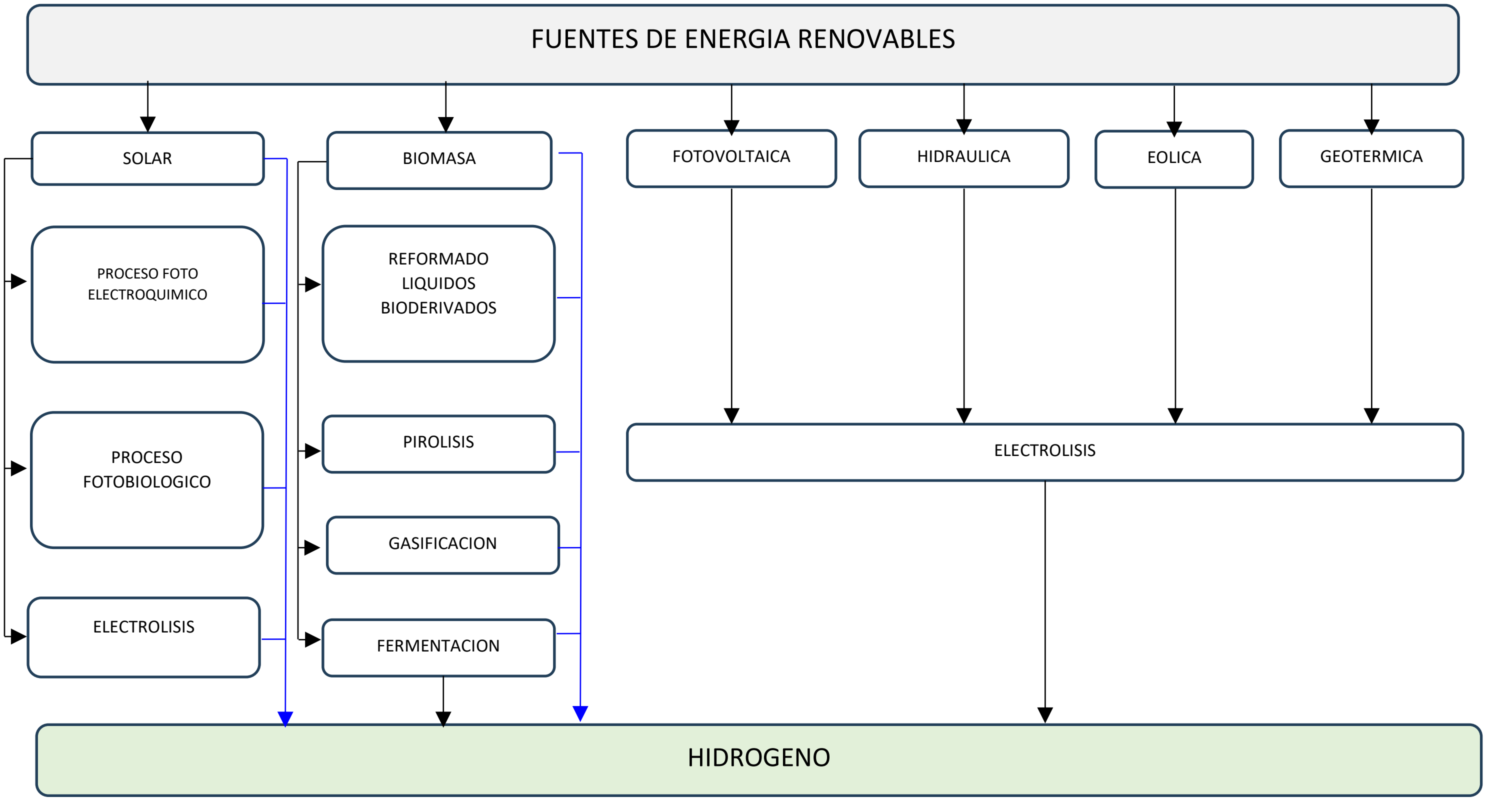

Figura 4.1 Esquema de distintas fuentes de energía renovable que son utilizadas para producir hidrogeno.

El hidrógeno tiene diversas aplicaciones en diferentes sectores además del energético, como producción de calor, transporte, elaboración de fertilizantes, entre otras. Sin embargo, presenta una gran dificultad para ser almacenado de forma eficiente. Para evitar este problema se puede generar y ser utilizado de forma inmediata a través de distintos procesos para generar energía que se almacene en baterías de alta potencia. Esta última se está volviendo una alternativa atractiva debido a que el hidrógeno tiene una energía específica mucho mayor que cualquier otro combustible.

Entre las diversas formas de producir H_2 existen algunas alternativas renovables **(Figura 4.1**). Para una mayor eficiencia del proceso, es necesario enfocarse en aquellos procesos que no generen subproductos o procesos simples, por ejemplo, en aquellos que llevan a cabo la electrolisis a partir de energías limpias como la solar, eólica, fotovoltaica, hidráulica y geotérmica.

El dispositivo más eficiente para generar energía a partir del hidrógeno es una celda de combustible de intercambio protónico, también llamada celda de combustible de electrolito de polímero solido (CCEPS). Este tipo de celda utiliza hidrógeno como combustible y un polímero de conducción iónica como electrolito **(Figura 4.2**).

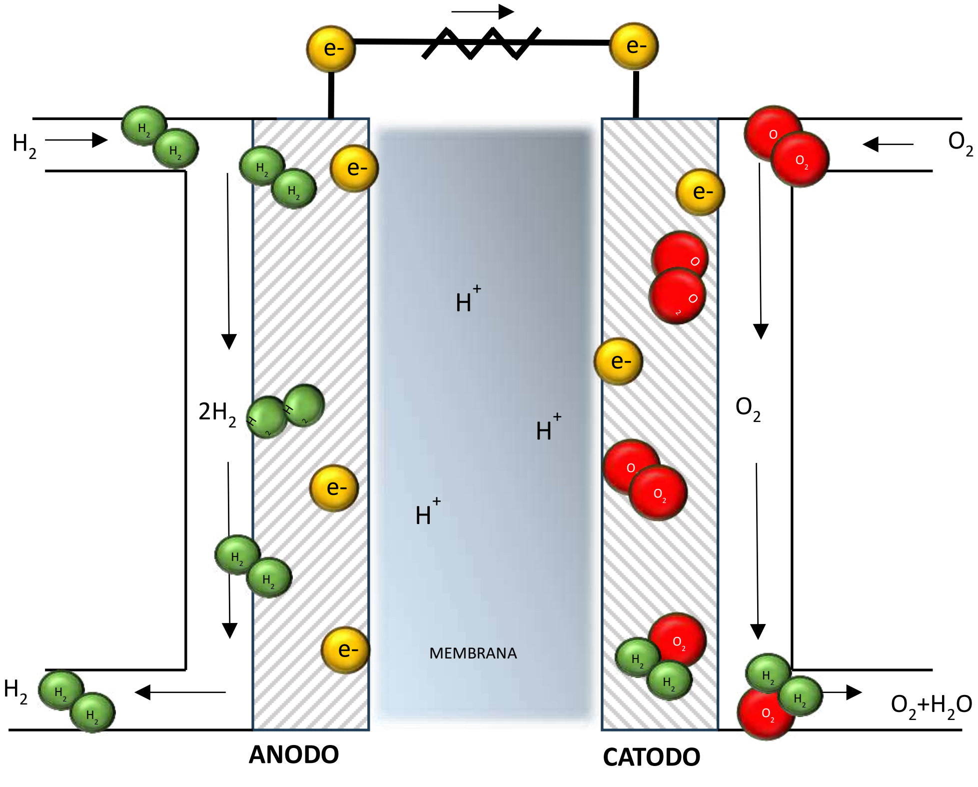

Figura 4.2 Esquema de funcionamiento de una celda de hidrogeno .

El combustible (hidrógeno) se inyecta a través del ánodo, mientras que el catalizador separa los átomos de hidrógeno en protones (H^+) y electrones (e^-). Los protones circulan a través del electrolito, mientras que los electrones son recolectados por un circuito externo para generar una corriente eléctrica. Los protones y electrones se combinan con el oxígeno que se suministra en el lado del cátodo para formar agua y vapor, debido a la liberación de energía en forma de calor. Los excedentes de combustible que no se utilizan en el proceso son expulsados a través de las compuertas de salida del ánodo y cátodo (Anantharaj et al., 2016). El interés en el uso de H_2 como fuente de energía se ha incrementado de manera considerable, debido a que en la actualidad es la tecnología con la que se genera una mayor cantidad de energía eléctrica, gracias a su alta eficiencia. La popularidad de la CCEPS es debido a sus numerosas ventajas, las cuales son: tamaño relativamente pequeño, diseño simple, operación a bajas temperaturas, alta eficiencia en la conversión de energía, alta densidad de corriente generada por unidad de área, bajos costos de mantenimiento y gran durabilidad.

4.2. GENERACION DE HIDROGENO VIA ELECTROLISIS

La electrolisis es un proceso electroquímico simple que ha tenido muchas aplicaciones en los últimos años ya que a través de la electrólisis es posible descomponer diferentes compuestos, la única condición es que estos compuestos combinados o disueltos liberen iones. La electrólisis se utiliza a nivel comercial en galvanoplastia para recubrir ciertos metales con otros para mejorar sus prestaciones y/o evitar la corrosión. Los metales que suelen depositarse son el oro, la plata, el cromo y el estaño.

La electrolísis también es utilizada como herramienta para la inmovilización de biomoléculas en los electrodos cambiando el pH de la superficie en las proximidades de los electrodos. Es el caso de la ascorbato oxidasa inmovilizada en el electrodo de oro con desprendimiento de hidrógeno (Patil et al., 2012).

Se han desarrollado un gran número de dispositivos basándose en estos procesos electroquímicos, como por ejemplo las baterías de metal-aire y las pilas de combustible de hidrógeno (Schmidt et al., 2003). El almacenamiento de hidrógeno obtenido por electrólisis del agua (EA) tiene un gran potencial para dispositivos portátiles para vehículos eléctricos, así como redes de almacenamiento a gran escala. Entre los diversos sistemas, la batería de metal-aire es el más prometedor, debido a su alta densidad de energía teórica de 40,1 MJ/kg, casi acercándose a los 40,6 MJ/kg de la gasolina (Tahir et al., 2017).

4.2.1. Mecanismo de reacción

El potencial estándar teórico de la EA es 1,23 V frente al electrodo reversible de hidrógeno (ERH) a 25 °C y 1 atm, independientemente del medio de reacción. La división electroquímica del agua es la combinación de dos reacciones de media celda, la reacción de desprendimiento o evolución de hidrógeno (REH) y la reacción de desprendimiento o evolución de oxígeno (REO). La primera ocurre a 0,0 V en el cátodo frente a ERH mientras que la segunda ocurre a 1,23 V frente a ERH en el ánodo.

Las reacciones de REH y REO pueden ocurrir en medio acido (Ecuaciones 4.1-4.2) y en medio neutro o básico (Ecuaciones 4.3-4.4).

$$4H^{+} + 4e^{-} \longrightarrow 2H_2 \quad E^0 = 0.0\ V \qquad \text{(Ec. 4.1)}$$

$$2H_2O \longrightarrow O_2 + 4H^{+} + 4e^{-} \quad E^0 = +1.23\ V \qquad \text{(Ec. 4.2)}$$

$$4H_2O + 4e^{-} \longrightarrow 2H_2 + 4OH^{-} \quad E^0 = -0.828\ V \qquad \text{(Ec. 4.3)}$$

$$4OH^{-} \longrightarrow O_2 + H_2O + 4e^{-} \quad E^0 = +0.401\ V \qquad \text{(Eq. 4.4)}$$

Para superar los obstáculos de activación como la resistencia de contacto y la resistencia de la solución se requiere un potencial mayor que los potenciales termodinámicos. Este potencial adicional necesario para la división del agua después de deducir el potencial termodinámico estándar se describe como sobrepotencial (η). Por lo tanto, minimizar el sobrepotencial requerido para la división del agua es el aspecto clave que se puede lograr seleccionando el catalizador o catalizadores adecuados y optimizando el diseño del electrolizador.

En los últimos años han surgido varias propuestas mediante las cuales se han evaluado diversas combinaciones de electrocatalizadores en media celda en condiciones de equilibrio (1 atm y 25 °C) para demostrar que la transferencia de electrones en la REH Y REO puede ocurrir a través de superficies con diferentes sustancias químicas y composiciones morfológicas, desde los metales nobles como Pt, Pd, Au hasta diversas combinaciones de metales de transición y compuestos orgánicos. La abundante disponibilidad, la fuerte actividad, las actividades electrocatalíticas sustanciales y ventajas económicas de los metales de transición los convierten en una alternativa muy atractiva para reemplazar los electrocatalizadores nobles para EA.

4.3. SINTESIS DE AEROGELES DE METALES DE TRANSICION CON APLICACIONES ELECTROQUIMICAS.

Los aerogeles metálicos se elaboraban principalmente con fines industriales, principalmente la industria aeroespacial para atrapar partículas de polvo espacial. También, se empleaba en distintas industrias como la petrolera (recubrimiento de tuberías) y la automotriz. A nivel comercial se aplica como aislante térmico en ventanas de los edificios. Además, de la producción de mantas aislantes y en equipamiento deportivo como raquetas de tenis, squash, bádminton, guantes de ciclismo, plantillas en botas de escaladores, entre otras. Por su alto poder de absorción, permite purificar el agua (Lim et al., 2015; Oschatz et al., 2017), posteriormente aerogeles de SiO_2 y TiO_2 se utilizaron como soporte de algunos metales por sus excelentes propiedades fisicoquímicas para ser utilizados como catalizadores en algunas reacciones químicas de absorcion (Heinrichs et al., 1997; Moussaoui et al., 2017; Sashkina et al., 2018). Los últimos 5 años en el campo de la catálisis electroquímica se ha experimentado un aumento considerable en la utilización de aerogeles de metales nobles para llevar a cabo reacciones de oxidación y reducción. Así por ejemplo se ha utilizado Pt para la reducción de oxígeno (J. Wang et al., 2019), Pt-Au para oxidación de alcoholes (Saravani et al., 2023), Ag-Cu para reducción de CO_2 (W. Wang et al., 2021), entre otros. Estos trabajos de investigación justifican el uso de estos metales nobles, escasos y de elevado coste, por las grandes aéreas superficiales que presentan, (Smirnova & Gurikov, 2018). Sin embargo, el uso de metales nobles sigue siendo cuestionable por su escasa disponibilidad. Por este motivo, ha surgido la necesidad de elaborar electrocatalizadores libres de metales nobles. Kim y colaboradores (Kim et al., 2023) hacen una interesante propuesta sobre aerogeles basados en Zn- Co **(Figura 4.3)**, estos materiales resultaron ser excelentes materiales para ser utilizados como electrodos de supercondensadores.

Este estudio muestra un método interesante de crecimiento de partículas 0D y 1D que arrojaron distintos tipos de histéresis (I Y III respectivamente) y aleaciones entre los metales de las sales precursoras, que lograron una sinergia con el medio en que se evaluaron. Así mismo, este trabajo mostro una novedosa propuesta para sintetizar aerogeles en forma de nanocables para aplicaciones de almacenamiento de energía que requieren rutas cortas de electrones/iones y con excelente conductividad eléctrica y áreas superficiales altas.

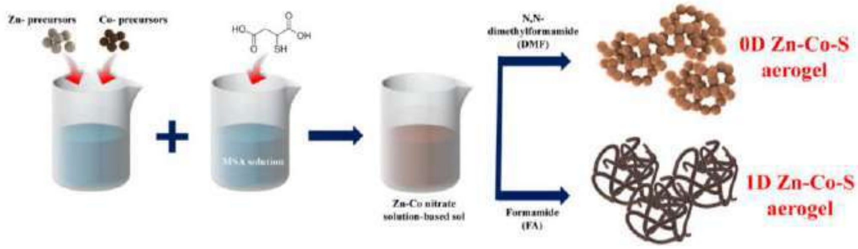

Fig. 4.3. Síntesis de aerogeles 0D y 1D Zn-Co-S via metal-coordinación asistido por sol-gel (Kim et al., 2023).

Por otro lado, Moreti y colaboradores (Moretti et al., 2018) obtuvieron aerogeles de Ni y Mn que posteriormente se doparon con óxidos de vanadio. Esta novedosa ruta de síntesis de aerogeles de metales no nobles demostró que aplicar sonicación en las soluciones precursoras durante de la etapa de síntesis permite reducir el tiempo necesario para el proceso sol-gel, aunque al realizar esta acción la cristalinidad de los aerogeles decae significativamente. Este hecho puede evitarse controlando el ritmo de adición de los precursores metálicos en la solución precursora. En este trabajo estos aerogeles se doparon con oxido de vanadio (10% molar), otorgando a los aerogeles resistencia a la corrosión, aunque la concentración de vanadio afecta claramente a la morfología de los "sono-aerogeles".

El análisis XPS de estos aerogeles mostro estructuras coordinadas octaédricamente, que cuando el Ni y Mn están pre-intercalados en el espacio entre capas se mejoran los sitios activos del material en términos de capacidad entregada y capacidad de velocidad. Otros aerogeles de metales de transición han sido adoptados como soportes para metales nobles como aerogeles de Fe funcionalizados con nanopartículas de Ag (Cha et al., 2023) y aerogeles Fe, Ni, Co dopados con Pd (Rodriguez-barajas et al., 2023). Sin embargo, aún quedan muchos aspectos que optimizar tanto en lo relativo al proceso de síntesis como de las propiedades de los multiples aerogeles metálicos basados en metales de transición que se pueden obtener. Por lo tanto ésta sigue siendo un área de oportunidad muy relevante en la catálisis electroquímica.

Publicaciones cientificas

En el capítulo anterior se mostraba un estudio detallado sobre la aleación de Pd con metales como el Fe, Ni y Co. Sin embargo, la presencia del metal noble hace que los catalizadores elaborados no favorezcan otras reacciones como la reacción de evolución de oxígeno y la reacción de evolución de hidrogeno, las cuales son las reacciones involucradas en la electrolisis del agua. A continuación, se presentan los trabajos científicos relacionados con el diseño y síntesis de aerogeles elaborados exclusivamente a partir de metales de transición y su actividad en reacciones para producir hidrogeno. Estos artículos científicos resultan muy relevantes en el área de la catálisis electroquímica debido a la ausencia de trabajos en la literatura sobre aerogeles de metales de transición autosoportados.

Nickel-Cobalt Aerogel as Highly Efficient Electrocatalyst for dual Microfluidic Applications: Hydrogen Generation and Power Energy from Nitrogenous Compounds

A. Martínez-Lázaro[a], A. Rodriguez-Buenrostro[a], M.H. Rodríguez-Barajas[a], N. Rey-Raap[b], F. I. Espinosa[c], Y. Salazar-Lara[c], A. Arenillas[b], J. Ledesma-García[a], L.G. Arriaga[c].*

[a]División de Investigación y Posgrado, Facultad de Ingeniería, Universidad Autónoma de Querétaro, 76010, Santiago de Querétaro, México.

[b]Instituto de Ciencia y Tecnología del Carbono, INCAR-CSIC. Francisco Pintado Fe, 26. 33011 Oviedo, Spain.

[c]Centro de Investigación y Desarrollo Tecnológico en Electroquímica, 76703, Santiago de Querétaro, México.

*Corresponding author: larriaga@cideteq.mx

Abstract

This research work presents a novel unsupported NiCo aerogel with high electrocatalytic activity was synthesised by an ultrafast method combining microwave heating and lyophilisation. The novel aerogel was used as electrocatalyst for the oxidation reactions of two different nitrogen compounds: Urea and Ammonium, with the aim of reducing the pollutant content in water and generating clean energy from the reduced hydrogen of oxidising species. The NiCo aerogel was incorporated/evaluated in a microfluidic device in two ways: as an ammonium fuel cell and an alkaline urea electrolyser, producing clean hydrogen in both systems. The unique physicochemical properties, particle size smaller than 0.1 nm, surface area of 52 m^2g^{-1} and the presence of NiCo metal alloys with the addition of species Ni-O, Ni-OH and a higher percentage of Ni^{2+} enable the effective oxidation of species in the alkaline medium. Hydrogen production and power densities of up $3x10^{-4}$ μgs^{-1} and 0.74 mW cm^{-2}, respectively. This work demonstrates for the first time an aerogel structure of non noble metal (NiCo) used in two different microfluidic devices that oxidise nitrogenous compounds such as urea and ammonium and produce clean fuel as hydrogen.

Keywords: Aerogel materials, non-noble electrocatalyst, ammonia oxidation reaction, urea oxidation reaction, hydrogen generation.

1.Introduction

Currently, electrochemical water splitting has become in the most promising technologies for H_2 generation. However, the required voltage of 1.23 V vs SHE and the slow electron transfer in the oxygen evolution reaction (OER) at the anode have a significant negative impact on the overall efficiency of water splitting [1], [2]. To address these limitations, nitrogen compounds such as ammonia (NH_3) and urea ($CO(NH_2)_2$) have been proposed to assist water electrolysis, by replacing OER with ammonia oxidation reaction (AOR) and urea oxidation reaction (UOR) [3], [4]. The anodic reactions are [5],[6]:

AOR: $2NH_{3(aq)} + 6OH^- \rightarrow N_2(g) + 6H_2O + 6e^-$

$E_o = -0.77$ V vs SHE (1)

UOR: $CO(NH_2)_2 + 6OH^- \rightarrow N_2 + 5H_2O + CO_2 + 6e^-$ $E_o = 0.37$ V vs SHE (2)

Both NH_3 and $CO(NH_2)_2$, are present in large quantities in domestic and industrial wastewater and are associated with water pollution problems [7], [8]. Therefore, AOR and UOR are also a possibility for wastewater remediation [9]. Although these reactions, (1) and (2), have low theoretical oxidation potentials, the six electrons transfer involved result in sluggish kinetics and a high overpotential. Noble metal-based catalyst such as Pt [10], RuO_2[11] and IrO_2[12] exhibit high AOR and UOR activity, but their use results limited and high cost. As alternative, transition metal-based materials have also shown high performance for AOR and

UOR, proving to be a great alternative to noble metal-based electrocatalysts [13]. Nickel is an abundant element in the nature and Ni-based catalysts as oxides [14]–[16], selenides[17], hydroxides[18] and phosphides[19], [20] have been successfully used for the electrooxidation of ammonia and urea as anodic half-reactions in H_2 generation[21]–[23].

Another low-cost transition metal with interesting electronic properties is cobalt, which has been shown to improve the electrochemical activity of bimetallic electrocatalysts [24], [25]. Co and Ni atoms have similar atomic radius, so the combination of both elements can be result highly compatible. In addition, Co is advantageous in the oxidation of Ni^{2+} to $Ni^{3+,}$ resulting in good electrical conductivity and a fast electron transfer rate [26]– [28].

A three-dimensional $Ni_1Cu_1Co_{0.5}$-S-T/CP nanoflower-like structure was designed by Wang [29] as an electrocatalyst for AOR. The introduction of Co enhanced the synergistic effect between Ni and Cu, resulting in a decrease in the potential required to generate the active species for the adsorption/desorption of NH_3 and other intermediates [29]. Almomani [30] prepared a Co/Ni–C catalyst with spherical (particle size ~10-20 mm) and porous structure by solvothermal method. At 20% Co concentration, the generated power and initial potential were higher as Co enhances the electrochemical polarization of ammonia. He reported NiCo2N nanosheets with high stability and high AOR activity at low voltages [31]. According to a theoretical simulation, the long-lasting electrocatalytic activity is caused by the downward shift of the metal-d band. Yang [32] found that in a spring-like NiCoP/NF, OER and UOR are promoted by the synergistic effect of Ni and Co bimetallic atoms. Cao et. al. [33] reported that doping a Ni-P-O film with Co intervenes in the amount of Ni, Co, O and thus affected the electron structure, which lowered the conversion potential for Ni^{2+} and Ni^{3+} and the offset potential for starting UOR. Xu [34] prepared a carboxyferrocene-modulated bimetallic metal-organic Ni/Co framework, in which defect tailoring and bimetallic coupling effect are integrated and this effect changed the coordination environment of the active Ni sites and optimised the electronic structure, enhancing the UOR performance. In the present work, NiCo aerogels for the production of hydrogen from nitrogen-containing compounds were analysed for the first time: urea and ammonium hydroxide, which, in addition to improving electrochemical production, also allow the elimination of environmentally harmful by-products in water, based on two operating principles: electrolyzer and fuel cell.

Chemical reagents

Deionized water was provided with the UPT-IV-10L system (19 MΩ cm). Precursor salts used in this work were $CoCl_2 * 6H_2O$ (98%, Sigma-Aldrich ®, ACS reagent, St Louis, MO, USA) and $NiCl_2 * 6H_2O$ (99.9%, Sigma-Aldrich®, St Louis, MO, USA). For reduction solution Na_2CO_3 anhydrous (99.5%, JT. Baker R®) and Glyoxylic acid (98% Sigma-Aldrich) were used.

2. Materials and methods

2.1. Aerogels synthesis

NiCo aerogels were prepared from two solutions: a precursor solution and a reduction solution. The synthesis procedure described elsewhere [35], [36] was used. The precursor solution was prepared in equal proportions of Ni and Co precursor salts, the precursors was dispersed in a concentration of 2 mg ml^{-1}. For the reduction solution, a mixture of glyoxylic acid monohydrate and sodium carbonate in a of ratio 1:6 was used.

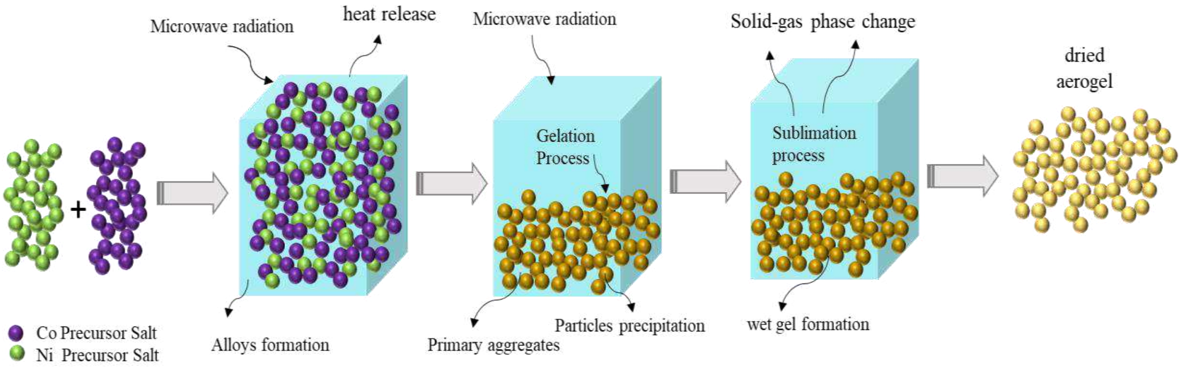

Figure 1. Synthesis process of NiCo aerogels.

The radiation source used was a microwave (MW) with a coupled thermoregulator. The reducing solution was heated to 68 ℃ beforehand, and later the precursor solution was added and both solutions were heated to 68 ℃ again. The reaction was almost instantaneous. Microwave heating was maintained for 7 hours to ensure the alloying and gelation phases, for 2 and 5 hours respectively. The reaction vessel was left at room temperature for 24 hours before washing. Washing was done continuously with deionized water and ethanol to remove reaction by-products. Finally, the solutions were sublimed in ethanol for 24 hours to induce a solid-gas phase change, which is crucial to prevent the collapse of the wet gel pores and eventually obtain a low-density aerogel. This process is graphically illustrated in Figure 1.

2.2 Physico-chemical characterization

To observe NiCo aerogels morphology a scanning electron microscope (SEM, Quanta FEG 650 microscopes from FEI) and a high–resolution transmission electron microscope

(HR-TEM, JEM–2200FS microscope) were used. Nitrogen adsorption-desorption isotherm were performed in a (Micromeritics ASAP 2020) at -196 ºC with a outgassing for 12 hours. X-ray photoelectron spectroscopy (XPS) analyzer Phoibos 100, SPECS, Germany was used to find the elements electronic structure.

2.3 Electrochemical measurements

2.3.1. Electrochemical measurements in a half-cell configuration

Aerogels electrochemical performance was evaluated in a Biologic VMP3 potentiostat/galvanostat using a three-electrode cell at a scan rate of 20 mV s^{-1}, which consist in a glass-carbon electrode (3 mm) as used as the working electrode, Ag/AgCl electrode as the reference electrode and a Pt wire as counter electrode. NiCo aerogel inks were prepared using a mixture of deionized water and Nafion® (5%) (4:1) and 5 mg of the sample. The ink was sonicated for one hour and then 10 μL was deposited over the electrode surface. 1 M KOH was prepared as electrolyte and another solution was prepared by adding urea until a concentration of 0.3 M urea in 1 M KOH was reached. The same process was followed for the ammonia measurements, but 1 M NH_4OH was added to the electrolyte. The solutions were bubbled with N_2 for 30 minutes for each electrochemical measurement. To obtain electrochemical profiles, each sample was evaluated by cyclic voltammetry (CV) in 1 M KOH in a potential range of 0.75 to 1.56 V vs. RHE for NiCo aerogel in urea and -0.3 to 1.65 V vs. RHE for NH_4OH measurements, with faradaic processes visible in a current (j) measured in $mAcm^{-2}$.

2.3.2 Design of microfluidic device

Figure 2A and B show the microfluidic cell (MFC) system, where (1) corresponds to Urea microfluidic electrolyzer (UME) module. The anode with NiCo aerogel is placed in a solution with urea/KOH, and the cathode with Pt/C (commercial) is placed in the alkaline solution (1 M KOH). A power density (V at 10 mAcm^{-2}) was applied across the electrodes. (2) Represents the Ammonia microfluidic fuel cell (AMFC) module. The same configuration was used in terms of anode and cathode as in the last case for UME, but in this case the NH_4OH solution is added to the anode in combination with 1 M KOH. (3) Shows the Hydrogen chamber: In this module it is possible to collect the hydrogen from UME and AMFC. This shows how urea and ammonia can be used as a source of hydrogen and provide a simple and safe alternative for the transport and storage of hydrogen (Figure 2B).

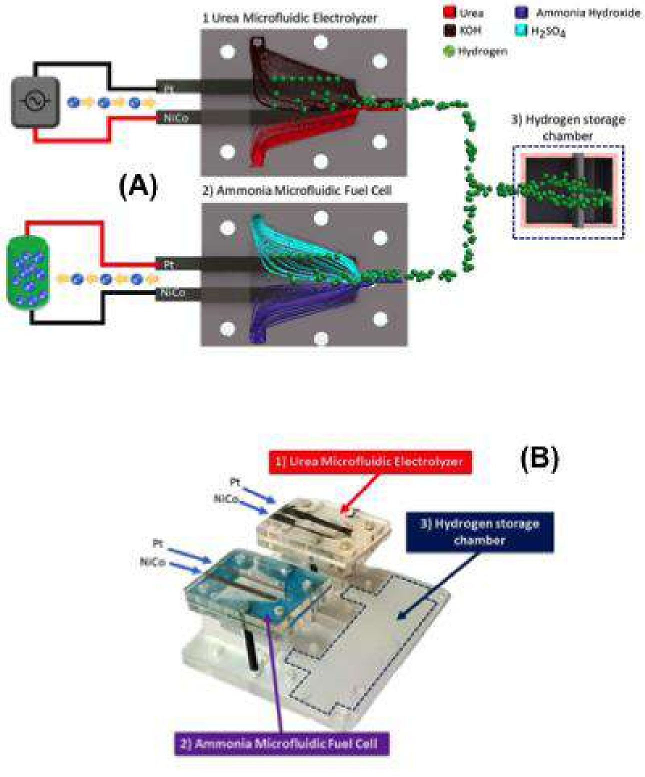

Figure 2. (A) Schematic representation of microfluidic cell device. (B) Microfluidic prototype

To evaluate hydrogen production, the behavior of the microcell is compared with nitrogen-containing compounds in alkaline medium. In the first case with 0.3 M urea with 1 M KOH and in the second case with 3 M ammonium hydroxide with 1 M KOH. The hydrogen production was calculated from the current obtained by chronoamperometry and with the formula:

$$\dot{m} = \frac{MI}{nF} \qquad (3)$$

Variables can be defined in the next way: ***F*** = Faraday´s Constant, M = Molecular weight, n = Number of electrons and I= Current, the stability and performance of hydrogen production were studied using chronoamperometry (CA) over a period of 35 hours.

3. Results

3.1 Physico-chemical analysis

SEM images (Figure 3a) show a uniform morphology in which the morphology of the aerogel with large pores on the surface predominates. HR-TEM (Figures 3c and 3d) show that NiCo aerogels consist of ultra-small particles whose size is less than 0.1 nm. In the analysis (Figure 3d), interplanar distances of 0.087 nm are also observed, so we are talking about an interatomically bound material. Specific surface area and pore size distribution of the aerogels were investigated using BET analysis (Figure 3b). The N_2 adsorption-desorption analysis shows a isotherm with hysteresis loop type IV, which represents a typical meso/macroporous material at a relative pressure (P/P_0) between 0.5 and 1, [37], [38], [39]. The pore size favored majorly the range between 2-80 nm, also this analysis shows a pore volume and surface area were 0.3 $cm^3\ g^{-1}$, respectively and 58 $m^2\ g^{-1}$.

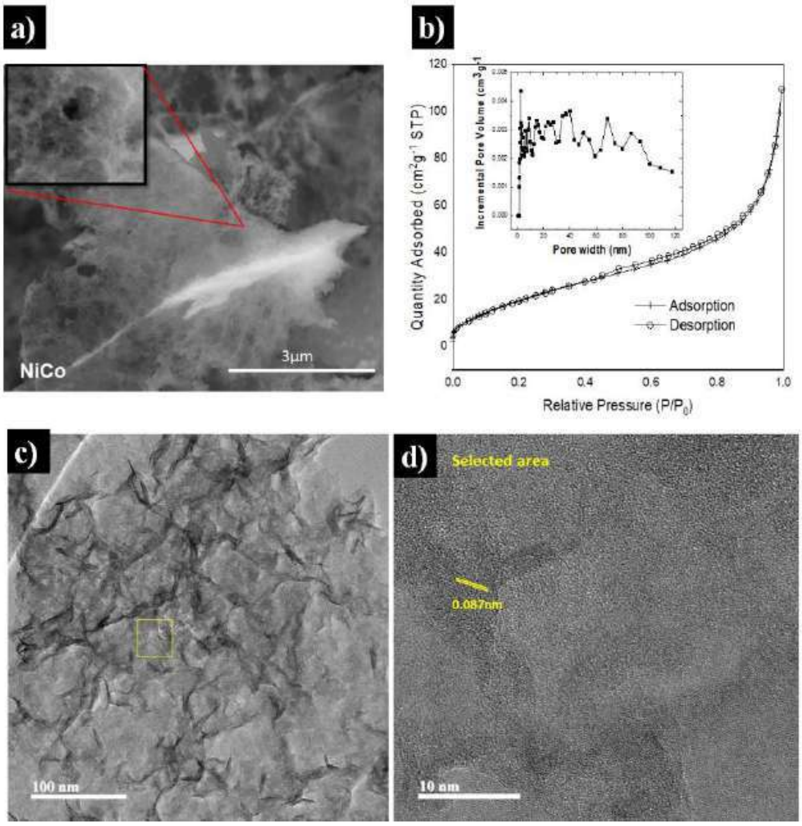

Figure 3. a) SEM images of NiCo aerogel; b) BET Analysis: isotherms and porosity of NiCo aerogel; c) and d) HR-TEM images of NiCo aerogel.

X-ray photoelectron spectroscopy (XPS) for the NiCo aerogel was performed to determinate the oxidation state and chemical composition, as shown in Figure 4. It exhibits the presence of C 1s, Co 2p, O 1s and Ni 2p, which are the most comun for the synthesis of the study material. The spectrum by high-resolution shows Co 2p and it can be observed in Figure 4b. The spectra of Co 2p3/2 in the energy band of 779.89 eV and Co 2p1/2 in 795.92 eV deconvoluted yield peaks 780.8 eV and 796.43 corresponding to Co^{2+} and peaks 779.48 eV and 795.11 related to Co^{3+} [40]–[42] corresponding to the structure Co_2O_4, where an increase of 42.5% in the oxidized species of Co^{2+} was observed with respect to Co^{3+}. This shows that the synthesis of NiCo leads to Co_2O_4, so you get the stability of the material by a lower oxidation of Co^{2+} to Co^{3+}. The spectrum by high-resolution shows Ni 2p and it can be observed in Figure 4c. It shows as orbitals Ni 2p3/2 in 854.77 eV and Ni 2p1/2 in 872.37 eV; on deconvolution, the peaks at 854.77 eV and 872.17 eV correspond to Ni^{2+}, while the peaks at 856.61 eV and 873.67 eV refer to Ni^{3+}, so they are due to an oxidation state [43]–[45]. The percentage of the relative weight of the sample was determined, with the percentage of Ni^{2+} at 61.8% being higher than that of the oxidized species of Ni^{3+} at 28.7%. This shows that the synthesis of NiCo exhibits an oxidation state due to the synthesis of the material leading to a greater oxidation of Ni^{2+} to Ni^{3+}. It thus corresponds to the results of cyclic voltammetry in the characteristic signals of the oxidation state. The high-resolution spectrum for C 1s is shown in Figure 4d. It shows three deconvolution peaks, the first peak at 287.05 eV characteristic of sp^3 hybridization, the second peak at 287.86 eV for C-O and the third peak at 287.8 eV for C=O, the bonds present are attributed to the synthesis of the material [46], [47], the percent of C in the sample is 2.1%. Other spectrum that can be observed is O1s and it is shown in Figure 4a is attributed to the O_2^- anions produced by the metal-oxygen bonds of the synthesis structure, with Co-O, Ni-O, OH groups and oxygen vacancies present in different oxidation states where the presence of Co and Ni alloys can be seen on the surface [48], [49].

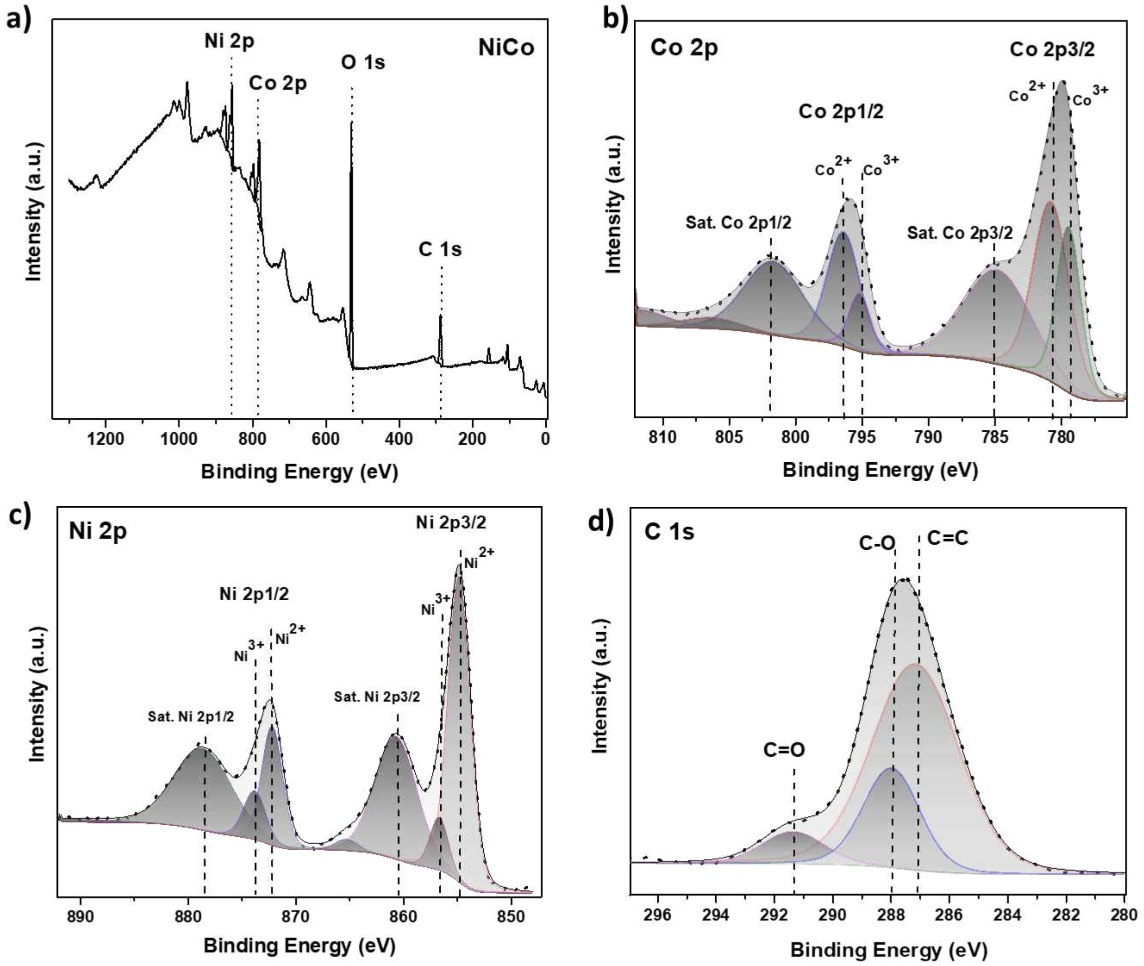

Figure 4. High-resolution XPS spectra for: a) NiCo in general; b) Co 2p; c) Ni 2p; and d) C 1s.

The adjusted results confirm that microwave heating and cold drying improve the degree of oxidation of the materials and reduce the concentration of heteroatomic defects. At the same time, the presence of heteroatoms causes point defects on the surface of the material, which leads to the segregation of electron clouds and the polarization of defects that are not present in these samples. Oxygen therefore reaches the surface efficiently, as demonstrated by comparison with electrochemical analysis, where the relevant signals for each sample are those corresponding to that analysis.

3.2. Electrochemical performance

3.2.1 UOR performance for NiCo aerogel

The electrocatalytic performance of NiCo aerogel was evaluated in two different solutions: 1 M KOH and 1 M KOH + 0.3 M urea. In a first step, the electrochemical profiles of the samples were determined using the cyclic voltammetry technique in a voltage range from 0.76 to 1.55 V vs RHE to observe the electrochemical profile of the material and to determine the starting voltage of the OER (Figure 5). The difference between using without urea is seen in the improvement of the OER, with a difference of 22 mV for NiCo, although there appears to be no significant change between testing in 1 M KOH and the adding urea to the electrolyte. It can be seen that the reaction starts at 1.35 V vs RHE and tends to evolve oxygen rapidly (Figure 5a).

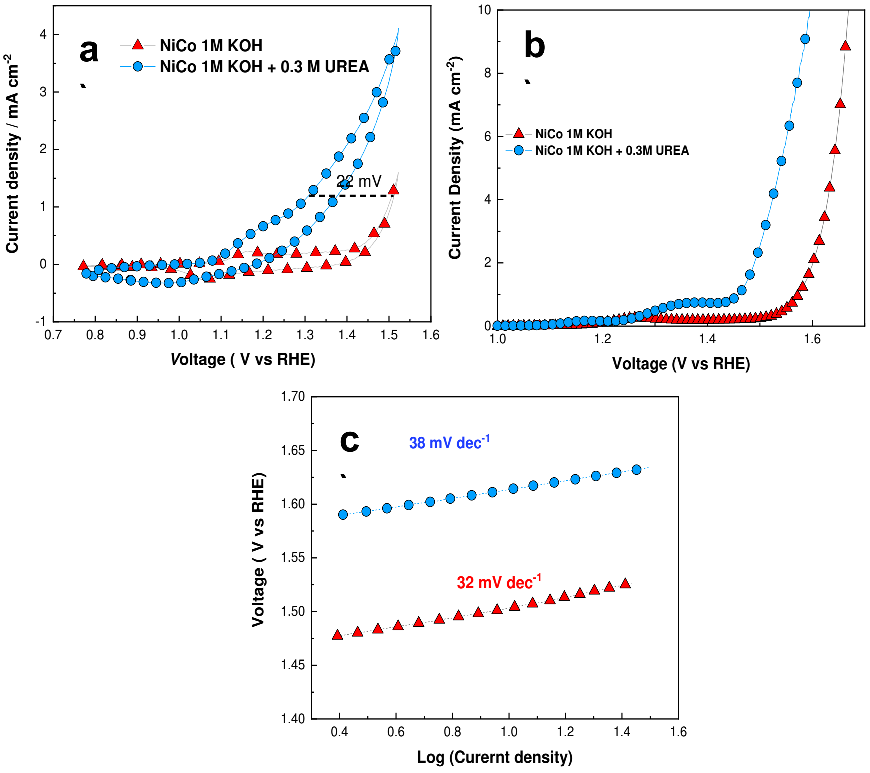

Figure 5. Electrochemical performance of the urea oxidation reaction (UOR).

On the other hand, for the NiCo sample, the potential difference between the sample with and without electrolyte is almost 150 mV, since for the aerogel in 1M KOH the reaction produces 1 mAcm^{-2} at 1.5 V vs RHE while adding urea to the electrolyte the reaction occurs at 1.3 V vs RHE[50].At 1.17 V vs. RHE it can be identify a peak in the cyclic voltammetry that correnponds to NiOOH presence, in the same way UOR starts to increase its current in this potential, which indicated that NiOOH species are the active site for UOR catalysis in the same thermodynamic potential[31], [51], [52].

Nickel has strong influence on the UOR, but the addition of cobalt favors the OER. NiCo aerogels shows how the reaction reaches 10 mAcm^{-2} at 1.58 and 1.65 (V vs RHE) for NiCo for UOR and the OER respectively[39], [53], [54].

Tafel slopes were calculated for the kinetic analysis on the surface of the electrodes towards the OUR (Fig. 5c), showing that the reaction NiCo with the lowest slope value favours 32 mV dec^{-1} in the presence of urea, while NiCo in KOH reaches a value of 38 mV dec^{-1}, the presence of nickel favours the transport of OH- species to the electrode surface in the presence of urea.

3.2.2 AOR performance for NiCo Aerogels

To evaluate the preliminary catalytic activity of the aerogels on ammonium, the cyclic voltammetry technique was evaluated in two solutions: 1M KOH and 1M KOH+ NH_4OH (Fig. 6). In a first step, the electrochemical profiles of the samples were determined using the cyclic voltammetry technique in a voltage range of -0.33 to 1.55 V vs RHE to observe the electrochemical profile of the material and determine the start voltage of the OER

(Fig. 6a). The use of ammonium hydroxide improves the oxidation process as the current density of the aerogel increases significantly.[55], [56].

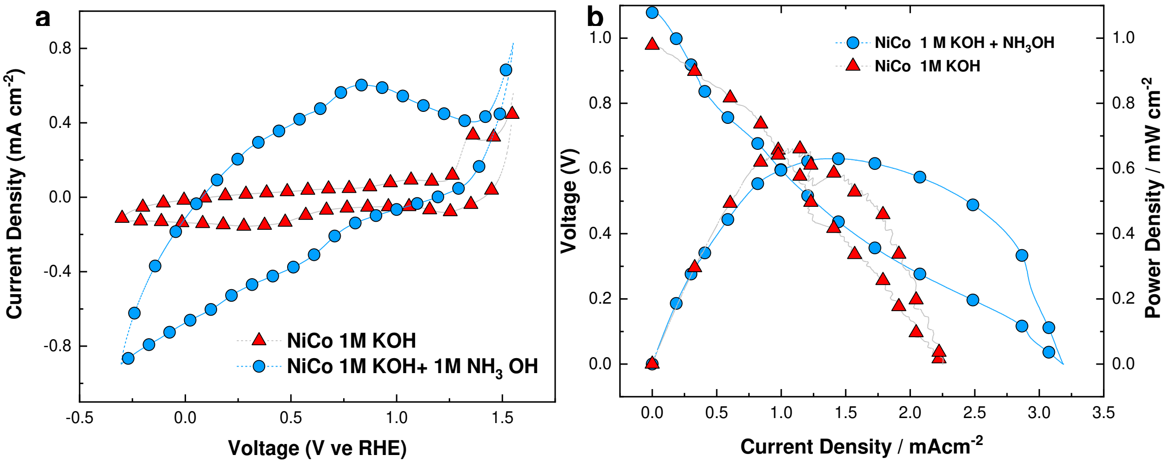

Figure 6. Electrochemical fuel cell performance towards ammonia oxidation reaction (AOR).

In the case of AMFC, the catalyst NiCo was used at the anode electrode and Pt/C (commercial) as the cathode (Pt/C||NiCo). The AMFC used an alkaline analyte and an acidic catholyte with an OCV of 1.1 V, wich is very close to the theoretical potential Eq.4 [22].

$$2NH_3\,H_2O + 3/2O_2 \rightarrow N_2 + 5H_2O \qquad E0 = 1.17\ V \quad (4)$$

The obtained OCV (Fig. 6b) shows that the microcell operates efficiently with a difference of only 0.07 V compared to the theory. This is due to the good interaction between the anode containing the NiCo aerogel with the AOR and the cathode containing Pt/C with the ORR. In addition, the difference in pH between the anolyte and catholyte plays an important role in the efficiency of the cell. In the polarization curves for NiCo with ammonia, three zones can be seen: the activation zone (0 – 0.75 mA cm^{-2}); the ohmic loss zone (0.75 – 2.7 mA cm^{-2}), and an electrolyte/catalyst concentration loss region (2.7 – 3.25 $mAcm^{-2}$). Of these three zones, the ohmic loss zone is the main cause of cell performance degradation due to significant OCV drop. In general, the cell has a maximum power density of 0.66 $mWcm^{-2}$, and the maximum discharge current density achieved by ammonia in the cell is about 3.25 mA cm^{-2}.

3.3. Hydrogen production in the microfluidic device

To demonstrate the high electrochemical performance of the aerogels, hydrogen production was tested in a microfluidic cell with/without a nitrogen-containing sample to show that the aerogel is capable of producing significant amounts of H2. A chronoamperometry was performed for 35 hours with a transverse flow rate of 200 µL min^{-1} for two processes: Electrolysis and fuel cell with NH_4OH.

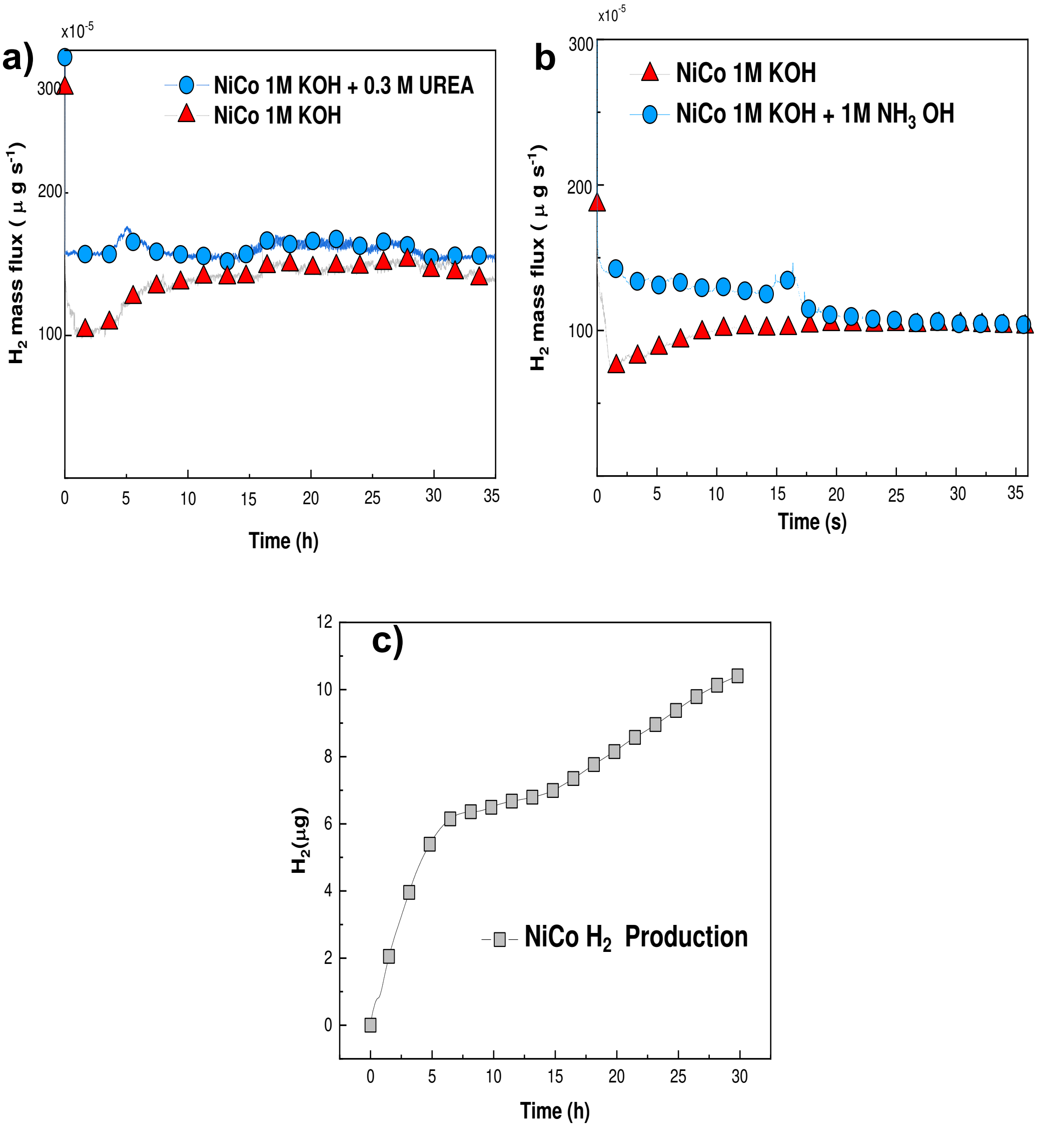

Figure 7. a) Chronoamperometric evaluation of NiCo aerogel. a) with urea, b) with NH_4OH and c) H_2 production.

These processes were performed simultaneously in two microfluidic devices to collect the produced H_2 in a chamber anchored to the two microfluidic systems. NiCo aerogel was investigated as the anode in the cells, while Pt/C was chosen as the cathode in both microfluidic systems [34]–[36].

3.3.1. Electrolysis assisted by NiCo aerogel

In order to make an effective evaluation of the electrochemical separation, a chronoamperometry was carried out for 35 hours. To compare the performance of the MFC in the presence or absence urea, the catalyst was evaluated in two different anolytes: 1 M KOH and 1 M KOH + 0.3 M urea. Water splitting was performed in the MFC with the electrolyte with and without urea (Figure 7a). The decrease in the potential required for the OER by adding urea to the solution indicates that its use in the electrolysis cell can reduce the energy consumption for hydrogen production significantly, and that the UOR is more efficient than the OER in production. of hydrogen via water splitting. The results show that the urea in combination with the electrolyte (Figure 7a) arrives abundantly at the surface of the anode at the beginning and the H_2 production in the MFC is higher than in the configuration without urea in the anolyte. Throughout the test, the H2 production of the configuration containing urea in the anolyte decreases until it is very similar to the configuration containing only KOH. This is because several active sites of the NiCo aerogel have reaction intermediates or can be saturated with other species, as well as the continuous flow of the anolyte, although the material loses its stability after 25 hours when the urea on the surface is constantly renewed (Also see Table 1).

Table 1. Water splitting in microfluidic fuel cell in the literature for comparison

EA: Electroactive area/ MCD: Maximum Current density

Cell feature	**Anode**	**Cathode**	**EA (cm^2)**	**Anolyte**	**Catholyte**	**Flux**	**Potential (V)**	**MCD (mAcm^{-2})**	**References**
With a Nafion membrane	Pt(99.95%)	Pt(99.95 %)	0.2	0.5 M H$_2$SO$_4$	1 M KOH	1 ccm	2.5	228	[57]
Co-flow	NiFe$_2$O$_4$/XC-72 0.93 mg	NiFe$_2$O$_4$/XC-72 0.93 mg	0.02	0.5 M H$_2$SO$_4$	1 M KOH	300 ml h^{-1}	1.8	—	[51]
microEC	Pt	Pt	0.018	0.5 M H$_2$SO$_4$	0.5 M H$_2$SO$_4$	1.4 ml min^{-1}	2.5	67.04	[58]
microEC	Pt/NF	Pt/NF	—	1 M KOH	1 M KOH	0.34 m s^{-1}	2.5	747	[59]
MFC co-flow	NiCo aerogel	Pt/C	0.021	1M KOH+0.3 M urea	1 M KOH	200µl min^{-1}	1.58	250	This work

3.3.2. NiCo Aerogel in the MFC using ammonium hydroxide as fuel

The stability of the MFC was investigated using ammonium hydroxide as fuel and is shown in Figure 7b. There it can be seen that at OCV voltage, the ammonia fuel cell can maintain hydrogen production between 150-125 µgs-1 10-5 for 20 hours, with production later dropping to 100 µgs-1 10-5 until it reaches hour 35. This could be due to the presence of a sufficient concentration of ammonium hydroxide in the anolyte at the beginning of cell operation, which interacts directly with the NiCo aerogel on the entire surface of the electrode.

As the fuel oxidizes, residues or half-processes may remain on the surface of the electrodes that prevent the ammonium hydroxide species from continuing to fully interact with the electrode, so that when the 20-hour mark is reached, the current and thus the amount of hydrogen prouduced decreases. It should be noted, however, that significant disturbances in the decay of the current do not occur until 20 hours after the start of the process. During hours 3-10, a high stability of the cell is observed, mainly due to the unique morphology of the material. However, as time on the catalyst increases, the AOR effectively ceases and by the end of hour 35 the production of hydrogen without NH4OH is very similar to when the nitrogenous species is not used and only the KOH electrolyte is used.

The OCV obtained in the present work can be compared with other reports in the literature (See Table 2), where other Ni-containing materials contribute significantly to the performance of microfluidic cells using ammonium species as fuel.

Table 2. Comparison of electrocatalysts used in MFC in the presence of urea and ammonia as fuels.

Cell feature	**Anode**	**Cathode**	**Fuel & Oxidant**	**Electrolyte**	**Flow Rate (µl min^{-1})**	**OCV (V)**	**PPD (mW cm^{-2})**	**MCD (mAcm^{-2})**	**References**
Co-flow	$Ni_{50}Cu_{50}$/CNTs 2.3 mg cm^{-2}	Pt/C 2mgcm^{-2}	1 M NH_3 Air-breathing	3 M KOH	500	1.31	10.84	184	[60]
Counter-flow	NiCu@ NiCuOOH-NF 5.8 mg cm^{-2}	Pt/C 2mgcm^{-2}	3 M NH_4Cl Air-breathing	2 M NaOH	760	0.72	17.1	102	[61]
AEM	$Ni_4Cu_1Co_{1.5}$-BP 10 mg cm^{-2}	Mn-Co-BP2000	3 M NH_3 Air	3 M KOH	5000	0.75	115.7	—	[62]

AEM	PtIr/C 1 mg$_{PtIr}$ cm^{-2}	1.5 mg cm^{-2} Pt/C 1 mg$_{Pt}$ cm^{-2}	0.1 M NH_3 Air (21% O_2)	1 M KOH	40,000	0.5	1.68	6.6	[63]
Co-flow	NiCo aerogel	Pt/C	NH_3OH+1 M KOH	0.5 M H_2SO4	200	1.1	0.74	3.2	This work

PPD: Peak Power Density / AEM: Anion Exchange membrane

3.3.3. Hydrogen production in both configuration devices

The above system contains a chamber where hydrogen from UME and AMFC reactions can be stored (Figure 7c), which is essential for evaluating the performance of the configuration. The hydrogen production was estimated by theoretical methods based on a fundamental equation using the current obtained by chronoamperometry and equation 1.

This equation allows calculating the molar flow of hydrogen produced by each source, both for the modules in the presence of urea and/or NH_4OH. In this way is possible to estimate the amount of hydrogen produced per unit time. Subsequently, this calculation is applied to each unit of time, giving an estimate of the total hydrogen production. Since the chamber is the final destination of the hydrogen, it can be inferred that the production of both sources is combined. The results of this procedure can be seen in Figure 7c. The system used allows the quantification of hydrogen production, which is essential for evaluating its performance. Using theoretical methods and the equation mentioned above, the hydrogen production of each source can be estimated.

Conclusions

NiCo aerogels were synthesised using a rapid synthesis method by microwave heating and cold drying. The method of obtaining the aerogels provided unique physicochemical properties that enabled excellent performance in the extraction of hydrogen from nitrogen-rich compounds (urea and ammonia). TEM analysis revealed a fine network of interatomically bound angstrom-sized particles. XPS analysis shows that the particles are tightly bound in NiCo alloys, which allow oxygen to efficiently reach the reaction surface due to the existence of oxygen-containing functional groups, which can be attributed to the synthesis of the material. NiCo aerogel proved to be an excellent catalyst towards UOR, improving the EOR by reducing the thermodynamic potential of the material by 22 mV in the presence of urea. Moreover, in ammonium oxidation, a better response of the catalyst is observed in half a cell when it is in contact with the fuel than when it is only in the presence of the electrolyte. The tests in the microfluidic cell arrangement showed efficient hydrogen production according to two principles: Fuel cell (ammonia) and electrolyser (urea). The hydrogen produced was collected in a chamber over the course of 30 hours. The amount collected during this period was 10.7 µg of H_2. In summary we can say that NiCo aerogels are a good alternative for to clean and efficient production of hydrogen in combined microfluidic devices.

Acknowledgements

The authors would like to thank the Mexican Council for Humanistics, Sciences and Technologies (CONAHCYT) for financial support through the Ciencia de Frontera (Frontier Science) 2019 project, grant no. 845132.

Conflicts of interest

There are no conflicts to declare

References

[1] C. Shuai, Z. Mo, X. Niu, P. Zhao, Q. Dong, Y. Chen, N. Liu, R. Guo, Nickel/cobalt bimetallic phosphides derived metal-organic frameworks as bifunctional electrocatalyst for oxygen and hydrogen evolution reaction. *J. Alloys Compd.* **2020**, 847, 156514.

[2] B.K. Martini, G. Maia, Using a combination of Co, Mo, and Pt oxides along with graphene nanoribbon and $MoSe_2$ as efficient catalysts for OER and HER. *Electrochim. Acta* **2021**, 391, 138907.

[3] Y. Wu, Z. Sun, Y. Wang, L. Yin, Z. He, Z. Zhang, M.D. Hayat, Q. Zang, J. Lian, Cyclic voltammetric deposition of binder-free Ni-Se film on Ni foams as efficient bifunctional electrocatalyst for boosting overall urea-water electrolysis. *J. Alloys Compd.* **(2023)** 937, 168460.

[4] M.H. Tsai, T.C. Chen, Y. Juang, L.C. Hua, C. Huang, High catalytic performance of CuCo/nickel foam electrode for ammonia electrooxidation. *Electrochem. Commun.* **2020**, 121, 106875.

[5] D.T. Tran, T.H. Nguyen, H. Jeong, P.K.L. Tran, D. Malhotra, K.U. Jeong, N.H. Kim, J.H. Lee, Recent engineering advances in nanocatalysts for NH_3-to-H_2 conversion technologies, *Nano Energy* **2022,** 94, 106929.

[6] M. He, S. Hu, C. Feng, H. Wu, H. Liu, H. Mei, Interlaced rosette-like MoS2/Ni3S2/NiFe-LDH grown on nickel foam: A bifunctional electrocatalyst for hydrogen production by urea-assisted electrolysis, *Int. J. Hydrogen Energy* **2020**, 45, 23–35.

[7] W. Ruan, C. Yuan, F. Teng, H. Liao, A.O. Ibhadon, Boosting hydrogen production

in ultrathin birnessite nanosheet arrays-based electrolytic cell by glycerol and urea oxidation reactions, *Mater. Today Chem.* **2022**, 26, 101086.

[8] W. Xu, R. Lan, D. Du, J. Humphreys, M. Walker, Z. Wu, H. Wang, S. Tao, Directly growing hierarchical nickel-copper hydroxide nanowires on carbon fibre cloth for efficient electrooxidation of ammonia. *Appl. Catal. B Environ.* **2017**, 218, 470–479.

[9] S.A. Patil, S. Cho, Y. Jo, N.K. Shrestha, H. Kim, H. Im, Bimetallic Ni-Co@hexacyano nano-frameworks anchored on carbon nanotubes for highly efficient overall water splitting and urea decontamination. *Chem. Eng. J.* **2021**, 426, 130773.

[10] K. Siddharth, Y. Hong, X. Qin, H.J. Lee, Y.T. Chan, S. Zhu, G. Chen, S. Il Choi, M. Shao, Surface engineering in improving activity of Pt nanocubes for ammonia electrooxidation reaction. *Appl. Catal. B Environ.* **2020**, 269, 118821.

[11] H.M. Wang, P. Ning, Q.L. Zhang, X. Liu, T.X. Zhang, J. Hu, L.Y. Wang, Effect of different RuO_2 contents on selective catalytic oxidation of ammonia over RuO2-Fe2O3 catalysts, Ranliao Huaxue Xuebao. *Journal Fuel Chem. Technol.* **2019**, 47, 215–223.

[12] D. Sun, X. Hong, K. Wu, K.S. Hui, Y. Du, K.N. Hui, Simultaneous removal of ammonia and phosphate by electro-oxidation and electrocoagulation using RuO_2–IrO_2/Ti and microscale zero-valent iron composite electrode. Water Res. **2020**, 169, 115239.

[13] Z. Chen, W. Wei, B.J. Ni, Transition metal chalcogenides as emerging electrocatalysts for urea electrolysis. *Curr. Opin. Electrochem.* **2022**, 31, 100888.

[14] C. Alex, G. Shukla, N.S. John, Introduction of surface defects in NiO with effective removal of adsorbed catalyst poisons for improved electrochemical urea oxidation. *Electrochim. Acta* **2021**, 385, 138425.

[15] S. Gopi, A.M. Al-Mohaimeed, M.S. Elshikh, K. Yun, Facile fabrication of bifunctional SnO–NiO heteromixture for efficient electrocatalytic urea and water oxidation in urea-rich waste water. *Environ. Res.* **2021**, 201, 111589.

[16] F. Almomani, R. Bhosale, M. Khraisheh, A. Kumar, M. Tawalbeh,

Electrochemical oxidation of ammonia on nickel oxide nanoparticles. *Int. J. Hydrogen Energy* **2020**, 45, 10398–10408.

[17] H. Hosseini, S. Shahrokhian, Self-supported nanoporous Zn–Ni–Co/Cu selenides microball arrays for hybrid energy storage and electrocatalytic water/urea splitting, *Chem. Eng. J.* **2019**, 375, 122090.

[18] S. Hu, Y. Tan, C. Feng, H. Wu, J. Zhang, H. Mei, Synthesis of N doped NiZnCu-layered double hydroxides with reduced graphene oxide on nickel foam as versatile electrocatalysts for hydrogen production in hybrid-water electrolysis, *J. Power Sources* **2020**, 453, 227872.

[19] R. Wang, H. Liu, K. Zhang, G. Zhang, H. Lan, J. Qu, Ni(II)/Ni(III) redox couple endows Ni foam-supported Ni2P with excellent capability for direct ammonia oxidation, *Chem. Eng. J.* **2021***,* 404, 126795.

[20] T. Wang, X. Cao, L. Jiao, Ni_2P/NiMoP heterostructure as a bifunctional electrocatalyst for energy-saving hydrogen production, *EScience* **2021**, 1, 69–74.

[21] B. Patil, M.P. Gurrola, L.G. Arriaga, Electrochemical Water Splitting. Nanochemistry: Synthesis, Characterization and Applications **2021**, 378–395. Taylor and Francis ebook.

[22] Y. Liu, Z. Pan, O.C. Esan, X. Huo, X. Shi, L. An, Development and performance evaluation of a passive direct ammonia fuel cell, *J. Power Sources* **2023**, 570, 233057.

[23] N. Mahmood, Y. Yao, J.W. Zhang, L. Pan, X. Zhang, J.J. Zou, Electrocatalysts for Hydrogen Evolution in Alkaline Electrolytes: Mechanisms, Challenges, and Prospective Solutions, *Adv. Sci.* **2018**, 5, 1700464.

[24] S. Gopi, D. Choi, A.G. Ramu, J. Theerthagiri, M.Y. Choi, K. Yun, Hybridized bimetallic Ni–Fe and Ni–Co spinels infused N-doped porous carbon as bifunctional electrocatalysts for efficient overall water splitting, *Int. J. Hydrogen* **2022**, 47, 42122-42135.

[25] H.M. Abd El-Lateef, M.M. Khalaf, A.O. Alnajjar, I.M.A. Mohamed, Facile synthesis of Co/Ni bimetallic phosphate as electrode material for urea fuel cells: Effect of synthetic strategy on the physicochemical and electrocatalytic behavior,

Fuel **2023**, 334, 126671.

[26] J. Jin, F. Chen, Y. Feng, J. Zhou, W. Lei, F. Gao, Co-Ni-Mo phosphides hierarchical nanoarrays as bifunctional electrocatalysts for excellent overall water splitting, *Fuel* **2023**, 332, 126131.

[27] H. Roh, C. Lim, D. Kim, T. Park, K. Yong, Hierarchically nanostructured Ni(Mo,Co)-WOx electrocatalysts for highly efficient urea electrolysis. *Appl. Surf. Sci.* **2023***,* 610, 155520.

[28] Y.T. Wang, X.F. He, X.M. Chen, Y. Zhang, F.T. Li, Y. Zhou, C. Meng, Laser synthesis of cobalt-doped Ni3S4-NiS/Ni as high-efficiency supercapacitor electrode and urea oxidation electrocatalyst, *Appl. Surf. Sci.* **2022***,* 596, 153600.

[29] H. Wang, X. Tong, L. Zhou, Y. Wang, L. Liao, S. Ouyang, H. Zhang, Unique three-dimensional nanoflower-like NiCu electrodes constructed by Co, S co-doping for efficient ammonia oxidation reaction. *Sep. Purif. Technol.* 2022, 303, 122293.

[30] F. Almomani, M. Ali H Salah Saad, Electrochemical oxidation of ammonia (NH4+/NH3) ON synthesized nickel-cobalt oxide catalyst, *Int. J. Hydrogen Energy* **2021***,* 46, 4678–4690.

[31] S. He, Y. Chen, M. Wang, K. Liu, P. Novello, X. Li, S. Zhu, J. Liu, Metal nitride nanosheets enable highly efficient electrochemical oxidation of ammonia, Nano Energy 2021, 80, 105528.

[32] L. Yang, F. Ru, J. Shi, T. Yang, C. Guo, Y. Chen, E. Wang, Z. Du, K.C. Chou, X. Hou, Trifunctional electrocatalysts based on feather-like NiCoP 3D architecture for hydrogen evolution, oxygen evolution, and urea oxidation reactions, *Ceram. Int.* **2023**, 49, 659–668.

[33] J. Cao, Z. Jiao, R. Zhu, H. Long, Y. Zheng, J. Pan, J. Wang, F. Luo, C. Li, Q. Wei, Enhancing hydrogen evolution through urea electrolysis over Co-doped Ni-P-O film on nickel foam. *J. Alloys Compd.* **2022***,* 914, 165362.

[34] L. Xu, X. Wang, L. Zhang, H. Sun, X. Xie, Y. Zhang, B. Tan, R. Yuan, Carboxyferrocene modulated Ni/Co bimetallic metal-organic framework for highly efficient electrocatalysis of urea oxidation reaction. *Electrochim. Acta*

2022, 428, 140877.

[35] H. Electrocatalytic, A. Aerogel, P.T.M. Co, L.G. Arriaga, Materials Today Nano Editors-in-Chief, (n.d.).

[36] A. Martínez, L.A. Ramirez, J. Ledesma, M.A. Montes, M.P. Gurrola, J.A. Menendez, A. Arenillas, L.G. Arriaga, Facile Synthesis of Unsupported Pd Aerogel for High Performance Formic Acid Microfluidic Fuel Cell. *Materials* **2022**, 15, 1422.

[37] A. Mukherjee, S. Chakrabarty, W.N. Su, S. Basu, Nanostructured nickel ferrite embedded in reduced graphene oxide for electrocatalytic hydrogen evolution reaction, *Mater. Today Energy* **2018**, 8, 118–124.

[38] L. Chen, H. Dai, Y. Shen, J. Bai, Size-controlled synthesis and magnetic properties of NiFe 2 O 4 hollow nanospheres via a gel-assistant hydrothermal route. Journal of Alloys and Compounds **2010**, 491, 33–38.

[39] C. Si, Y. Zhang, C. Zhang, H. Gao, W. Ma, L. Lv, Z. Zhang, Mesoporous nanostructured spinel-type MFe2O4 (M = Co, Mn, Ni) oxides as efficient bi-functional electrocatalysts towards oxygen reduction and oxygen evolution, Electrochim. Acta **2017**, 245, 829–838.

[40] Y. Wang, X. Di, J. Chen, L. She, H. Pan, B. Zhao, R. Che, Multi-dimensional C@NiCo-LDHs@Ni aerogel: Structural and componential engineering towards efficient microwave absorption, anti-corrosion and thermal-insulation, *Carbon N. Y.* **2022**, 191, 625–635.

[41] L.K. Wu, W.Y. Wu, J. Xia, H.Z. Cao, G.Y. Hou, Y.P. Tang, G.Q. Zheng, Nanostructured NiCo@NiCoOx core-shell layer as efficient and robust electrocatalyst for oxygen evolution reaction. *Electrochim. Acta* **2017**, 254, 337–347.

[42] B. Li, Z. Tian, H. Li, Z. Yang, Y. Wang, X. Wang, Self-supporting graphene aerogel electrode intensified by NiCo2S4 nanoparticles for asymmetric supercapacitor, *Electrochim. Acta* **2019**, 314, 32–39.

[43] K. Zhao, X. Sun, Z. Wang, C. Huang, D. Li, J. Liu, Sheet-like NiCo-layered double hydroxide anchored on N self-doped hierarchical porous carbon aerogel from

chitosan for high-performance supercapacitors. *J. Alloys Compd.* **2022**, 921, 166036.

[44] Y. Zhang, J. He, Z. Fu, H. Yang, Lightweight porous NiCo-SiC aerogel with synergistically dielectric and magnetic losses to enhance electromagnetic wave absorption performances. *J. Alloys Compd.* **2022**, 926, 166758.

[45] M. Irfan, X. Liu, H.G. Abrha, J. Cabrera, S. Mushtaq, Y. Dai, P. Zhang, Synergistic approach of high-performance N-NiCo/PC environment benign electrode material for energy storage device. *J. Mater. Sci. Mater. Electron.* **2021**, 32, 22245–22255.

[46] G. Fu, Y. Chen, Z. Cui, Y. Li, W. Zhou, S. Xin, Y. Tang, J.B. Goodenough, Novel Hydrogel-Derived Bifunctional Oxygen Electrocatalyst for Rechargeable Air Cathodes. *Nano Lett.* **2016**,16, 6516–6522.

[47] R. Guo, L. Dang, Z. Liu, Z. Lei, Incorporation of electroactive $NiCo_2S_4$ and Fe_2O_3 into graphene aerogel for high-energy asymmetric supercapacitor. *Colloids Surfaces A Physicochem. Eng. Asp.* **2020***,* 602, 125110.

[48] X. Chang, W. Li, Y. Liu, M. He, X. Zheng, X. Lv, Z. Ren, Synthesis and characterization of $NiCo_2O_4$ nanospheres/nitrogen-doped graphene composites with enhanced electrochemical performance. *J. Alloys Compd.* **2019***,* 784, 293–300.

[49] M. Ranjani, N. Senthilkumar, G. Gnana Kumar, A. Manthiram, 3D flower-like hierarchical NiCo2O4 architecture on carbon cloth fibers as an anode catalyst for high-performance, durable direct urea fuel cells. *J. Mater. Chem. A.* **2018***,* 6, 23019–23027.

[50] A. Martinez-lazaro, A. Caprì, I. Gatto, J. Ledesma-garcía, N. Rey-raap, A. Arenillas, NiFe 2 O 4 hierarchical nanoparticles as electrocatalyst for anion exchange membrane water electrolysis. *J. Power Sources* **2023** 556, 232417.

[51] A. Martínez-Lázaro, A. Rico-Zavala, F.I. Espinosa-Lagunes, J. Torres-González, L. Álvarez-Contreras, M.P. Gurrola, L.G. Arriaga, J. Ledesma-García, E. Ortiz-Ortega, Microfluidic water splitting cell using 3D NiFe2O4 hollow spheres. *J. Power Sources* **2019***,* 412 (2019) 505–513.

[52] X. Luo, P. Ji, P. Wang, X. Tan, L. Chen, S. Mu, Spherical Ni3S2/Fe-NiPx Magic

Cube with Ultrahigh Water/Seawater Oxidation Efficiency. *Adv. Sci.* **2022**, 9, 1–11.

[53] K. Feng, D. Zhang, F. Liu, H. Li, J. Xu, Y. Xia, Y. Li, H. Lin, S. Wang, M. Shao, Z. Kang, J. Zhong, Highly Efficient Oxygen Evolution by a Thermocatalytic Process Cascaded Electrocatalysis Over Sulfur-Treated Fe-Based Metal–Organic-Frameworks. *Adv. Energy Mater.* **2020**, 10, 1–8.

[54] A. Wu, Y. Xie, H. Ma, C. Tian, Y. Gu, H. Yan, X. Zhang, G. Yang, H. Fu, Integrating the active OER and HER components as the heterostructures for the efficient overall water splitting. *Nano Energy* **2018,** 44, 353-363.

[55] S.C. Tsai, M.S. Wu, Hydrothermal growth of pompon-like manganese oxide microspheres with embedded nickel ions as single-atom catalysts for urea oxidation. *J. Alloys Compd.* **2022**. 894, 162515.

[56] B. You, X. Liu, G. Hu, S. Gul, J. Yano, D.E. Jiang, Y. Sun, Universal Surface Engineering of Transition Metals for Superior Electrocatalytic Hydrogen Evolution in Neutral Water. *J. Am. Chem. Soc.* **2017**, 139, 12283–12290.

[57] G. Yang, S. Yu, Y. Li, K. Li, L. Ding, Z. Xie, W. Wang, Y. Dohrmann, F.Y. Zhang, A simple convertible electrolyzer in membraneless and membrane-based modes for understanding water splitting mechanism. *J. Power Sources* **2021***,* 487, 229353.

[58] B. Samir De, J. Cunningham, N. Khare, J.L. Luo, A. Elias, S. Basu, Hydrogen generation and utilization in a two-phase flow membraneless microfluidic electrolyzer-fuel cell tandem operation for micropower application. *Appl. Energy* **2022**, 305, 117945.

[59] B. Samir De, A. Singh, R. Ji Dixit, N. Khare, A. Elias, S. Basu, Hydrogen generation in additively manufactured membraneless microfluidic electrolysis cell: Performance evaluation and accelerated stress testing. *Chem. Eng. J.* **2023**, 452, 139433.

[60] H.M. Zhang, Y.F. Wang, Y.H. Kwok, Z.C. Wu, D.H. Xia, D.Y.C. Leung, A Direct Ammonia Microfluidic Fuel Cell using NiCu Nanoparticles Supported on Carbon Nanotubes as an Electrocatalyst. *ChemSusChem*. **2018**, 11, 2889–2897.

[61] H. Zhang, W. Chen, H. Wang, X. Tong, Y. Wang, X. Yang, Z. Wu, Z. Liu, A core-shell NiCu@NiCuOOH 3D electrode induced by surface electrochemical reconstruction for the ammonia oxidation reaction. *Int. J. Hydrogen Energy* **2022**, 47, 16080–16091.

[62] Z. Hu, S. Lu, F. Tang, D. Yang, C. Zhang, Q. Xiao, P. Ming, High-performance precious metal-free direct ammonia fuel cells endowed by Co-doped Ni4Cu1 anode catalysts. *Appl. Catal. B Environ.* **2023**, 334, 122856.

[63] R. Chen, S. Zheng, Y. Yao, Z. Lin, W. Ouyang, L. Zhuo, Z. Wang, Performance of direct ammonia fuel cell with PtIr/C, PtRu/C, and Pt/C as anode electrocatalysts under mild conditions. *Int. J. Hydrogen Energy* **2021**, 46, 27749–27757.

FeNiCo Aerogel for Oxygen Evolution Reaction in Alkaline Systems: Microfluidic and Anion Exchange Membrane Electrolysers

A.Martínez-Lázaro[a], A. Rodríguez-Buenrostro[a], J. Ledesma-García[a], A. Arenillas[b], C. Lo Vecchio[d], I. Gatto[d], Vincenzo Baglio[d], L.G. Arriaga*[c].

[a]División de Investigación y Posgrado, Facultad de Ingeniería, Universidad Autónoma de Querétaro, 76010, Santiago de Querétaro, México

[b]Instituto de Ciencia y Tecnología del Carbono, INCAR-CSIC. Francisco Pintado Fe, 26. 33011 Oviedo, Spain

[c]Centro de Investigación y Desarrollo Tecnológico en Electroquímica, 76703, Santiago de Querétaro, México.

[d]Istituto di Tecnologie Avanzate per l'Energia, Nicola Giordano, CNR-ITAE, Salita Santa Lucia sopra Contesse, 5, 98126, Messina (Italy)

*Corresponding author: larriaga@cideteq.mx

Abstract

In this work, FeNiCo and NiCo aerogels were prepared by a simple and rapid synthesis method. These aerogels were used as catalysts in two systems: Microfluidics and anion exchange membrane electrolysers. These novel catalysts explore the effect of Fe under a NiCo alloy and its influence on water splitting. Physiochemical differences between the two aerogels are evident. BET analysis shows that Fe content is twice as high in FeNiCo compared to the NiCo sample, TEM analysis shows a similar morphology in both aerogels and the crystallographic structure of the NiCo alloy is predominant. XPS analysis shows that Fe can efficiently transport oxygen to the reaction surface, as Fe^{2+} *and* Fe^{3+} *can help stabilize the high-valent metal sites and thus improve the reaction activity of the FeNiCo aerogel. The electrochemical performance of FeNiCo over OER evaluated in a microfluidic electrolysis cell showed a hydrogen production of 220* $\mu g\ s^{-1}\ 10^{-7}$ *after 35 hours, while and* *then an anion exchange membrane electrolyser with a catalyst-coated membrane using FeNiCo as an anode was prepared at different temperatures between 30°C and 60°C. A stability test of 50 hours at 2 V and 60°C was then successfully carried out, achieving a current density of almost 2.1 Acm*$^{-2}$.

KEYWORDS: Aerogel, non-noble electrocatalyst, oxygen evolution reaction, water splitting, electrolysis.

Graphical Abstract

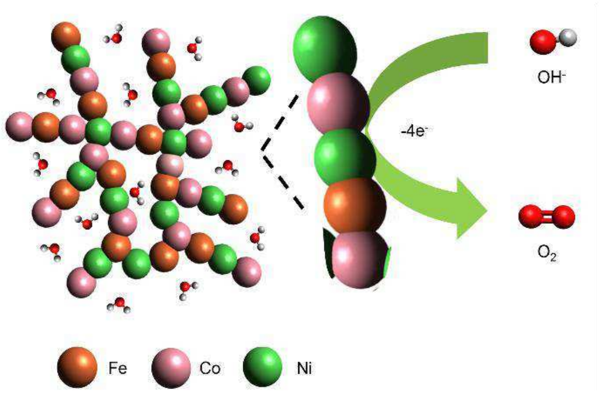

Introduction

Hydrogen (H_2) energy is seen as a promising approach to reducing global energy demand. Water electrolysis is one of the most promising approaches for green H2 production and has a high energy density (~282 kJ mol^{-1})[1]. Electrochemical water splitting comprises two half reactions: the hydrogen evolution reaction (HER) and the oxygen evolution reaction (OER), which take place at the cathode and the anode respectively [2].

Anode (OER): $4OH^- \rightarrow O_2 + 2H_2O + 4e^-$ (1)

Cathode (HER): $4H_2O + 4e^- \rightarrow 2H_2 + 4OH^-$ (2)

The slow four-electron transfer and the complicated gas evolution steps in OER lead to slow kinetics, therefore highly active catalysts with a large electron transfer capacity are required[3]. Recently, interest in catalysts based on transition metals such as oxides [4–6], phosphides[7–9], sulphides [10–12], hydroxides[13–15] and bimetallic alloys has increased. In addition, most of these materials have porous and 2D or 3D hierarchical structures that provide highly exposed electroactive sites[16–18].

Iron (Fe) is an abundant metal element characterised by its good conductivity and multiple oxidation states and has a suitable radius to Co and Ni ions [19]. Therefore, nickel-based materials with Fe as a catalyst for OER in alkaline media have been studied in detail. It has been reported that in nickel-iron layered silicate nanomembranes [20] and hierarchical nanocomposites of ultrathin nickel/iron double hydroxide nanosheets strongly coupled with nanocarbon networks [21], the introduction of iron improves the fast electrocatalytic kinetics. Fe has a low electron density, which facilitates the adsorption of intermediates (*OH, *O, *OOH). In addition, iron ions have a stronger adsorption effect on the *O intermediate reducing the energy barrier for the conversion of *OH to *O, a potentially crucial OER step. The surface-oxidised iron-nickel nanorods coupled with reduced graphene architectures (FeNi-O-rGA) synthesised by Yu's team[22] exhibit surface hydrophilicity, and the presence of iron promotes the formation of electroactive sites to improve the kinetics of OER. After activation, an FeNi-based sulphide and (oxy)hydroxide nanorod based on MIL-88 exhibits FeOOH and amorphous FeNiOOH as active sites, the latter providing adequate free adsorption energy for reaction intermediates [23].

All these studies clearly show the positive effect of including Fe in the catalyser. However, in most cases it involves lengthy and complex syntheses of the electrocatalyst materials themselves, and in other cases it is necessary to support them on another material that provides porosity to favour diffusion and access to the active centres. Aerogels have been shown to be effective catalysts as they reduce the mass of charged species, provide excellent diffusion and offer high stability for electrochemical applications[24]. Therefore, this work demostrates for the first time how Fe can be effectively incorporated into a self-supporting NiCo electrocatalyst (i.e. NiCo aerogel) and the impact this has on electrolysis in two different devices: a microfluidic and an anion exchange membrane electrolyser.

2. Experimental Procedures

2.1 Microwave-assisted synthesis of NiCo and FeNiCo aerogels

To carry out the sol-gel reaction, precursor salts were first prepared: For NiCo aerogel, a solution with a concentration of 2 mg ml^{-1} of the precursor salts $NiCl_2$* $6H_2O$ (99.9%, Sigma-Aldrich®, St Louis, MO, USA) and $CoCl_2$*$6H_2O$ (Sigma-Aldrich ®, ACS reagent, St Louis, MO, USA) in equal parts. In the case of FeNiCo, a solution with the same concentration of the three metals was prepared from Ni and Co salts with the addition of $FeCl_2$ (98%, Sigma-Aldrich ®, St Louis, MO, USA). The reducing solution consisted of a mixture (6:1) of sodium carbonate (≥ 99.5%, JT. Baker R®) and glyoxylic acid monohydrate (98% Sigma-Aldrich) using 1 ml of water per mg of glyoxylic acid. Following previous reports [25,26], microwave heating at 67ºC was used for this synthesis process. The reaction lasted 2 hours and the gelation process was carried out for 7 hours at the same temperature. Finally, the NiCo and FeNiCo samples were washed with water, ethanol and acetone and later a sublimation process was applied to remove the excess liquid.

2.2. Physico-chemical characterisation

The specific pore size distribution and surface area were determined by N_2 adsorption-desorption isotherms (Micromeritics ASAP 2020) with degassing for 24 hours and using the BET equation and the NLDFT model. The morphology of the NiCo and FeNiCo aerogels was characterised using a high–resolution transmission electron microscope (HR-TEM, JEM–2200FS microscope). The diffractions patterns were measured with an X-ray diffractometer (XRD; D8-Advance diffractometer Bruker) equipped with a CuKα X-ray source ($\lambda = 0.1541$ nm, 40 kV, 40 mA,) using a step size of 0.5º 2θ and a scan step time of 3 s. The electronic structure of the elements was measured by X-ray photoelectron spectroscopy (XPS; K-Alpha+ spectrometer equipped with the Avantage Data System from Thermo Scientific^{TM}).

2.3. Electrochemical measurements

2.3.1. Electrocatalytic activity in half-cell configuration

The electrochemical activity of the aerogels was evaluated in an electrochemical alkaline three-electrode cell (20 mV $s^{-}1$) with a potentiostat/galvanostat VMP3 Biologic. For the three-electrode system, an Ag/AgCl electrode was used as the reference, a glassy-carbon electrode (3 mm) as the working electrode and a Pt wire as the counter electrode. NiCo and FeNiCo aerogel inks were prepared with and 50 µL Nafion® (5%) and 250 µL deionised water per mg aerogel sample. The ink was shaken vigorously in a vortex and then sonicated for 30 minutes. 10 µL of each ink were deposited on the electrode surface. 1M KOH was prepared as electrolyte, which was bubbled with N_2 for 30 minutes before electrochemical measurement. To obtain electrochemical profiles, each sample was evaluated by cyclic voltammetry (CV) experiments in 1M KOH in a potential range of 0.75 to 1.37 V vs. RHE for FeNiCo aerogel and a range of 0.75 to 1.56 V vs. RHE for NiCo aerogel.

The electrocatalytic activity of NiCo and FeNiCo aerogels towards OER was tested by Linnear sweep voltammetry in the aforementioned three electrode half-cell configuration, using a potential range between 1.0 and 1.7 V vs. RHE.

2.3.3. Hydrogen production

A microfluidic cell was prepared to evaluate the hydrogen production in alkaline medium in the presence of FeNiCo aerogel. The H_2 production was calculated from:

$$\dot{m} = \frac{MI}{nF}$$

Where $\boldsymbol{M}$ is the molecular weight, $\boldsymbol{I}$ is the current, $\boldsymbol{n}$ the number of electrons transferred, and $\boldsymbol{F}$ is the Faraday constant.

The stability and performance of hydrogen production were analysed using chronoamperometry technique (CA) for 35 hours in a nitrogen atmosphere for the catholyte and in an oxygen atmosphere for the anolyte solution. The aerogel was used for the anode and a commercially available Pt/C (20%) for the cathode. The inks were prepared in a mixture of water, etanol and Nafion(5%) on Toray Carbon paper-060 (TCP) and a transverse flow rate of 200 µL min^{-1} was used.

1.1.Electrolyser electrochemical measurements

The electrochemical measurements were performed in a single cell configuration in a temperature range between 30°C and 60°C using a 1 M KOH solution in the anode compartment (flow rate 5 mL/min). The LSV curves were performed at a scan rate of 5 mV/s.

Anode and cathode electrodes with an area of 5 cm^2 were prepared according to the following procedures: An ink of 40 wt% platinum on carbon (Pt/C, Alfa Aesar) and commercially available 20 wt% FAA3 ionomer (FumaTech) was prepared under sonication for 1 hour. The ink was spray-coated onto the Sigracet 25-BC gas diffusion layer (SGL Carbon), with a final charge of 0.5 mg/cm^2. For the anodes, FeNiCo aerogel was mixed with 20 wt% FAA3 ionomers to form an ink, which was deposited on a FAA3-50® membrane (FumaTech) until a loading of 3 mg/cm^2 was reached. All these parts were assembled in a cold-assembly process to realise a membrane-electrode assembly (MEA). A Ni-felt current collector (NV BEKAERT SA, Belgium) was used in the anode compartment. For the stability test, a chronopotentiometric analysis was carried out at 1 A cm-2 in the electrolyser, with a 1 M KOH solution being continuously supplied.

3. Results

3.1 Physico-chemical analysis

The specific surface area and pore size distribution of the aerogels were analysed using N_2 adsorption-desorption isotherms **(Fig. 1a).** The surface areas were 79 and 167 m^2g^1 for NiCo and FeNiCo, respectively. The isotherms showed a type II for both samples, indicating the mainly macroporous nature of the samples, although FeNiCo has a larger adsorbed volume due to the higher porosity of this sample. Thus, the total pore volume calculated at the saturation point (i.e. p/p0 = 0.99) shows values of 0.17 cm^3g^{-1} for NiCo and 0.61 cm^3 g^{-1} for FeNiCo. FeNiCo also presents a type 3a hysteresis loop at a relative pressure (p/p^0) between 0 and 0.7, indicating the presence of mesopores in addition to macropores in this aerogel. The pore size distribution was determined by applying the NLDFT model[27,28] **(Fig. 1b**) and clear differences between the two aerogels can be recognised.

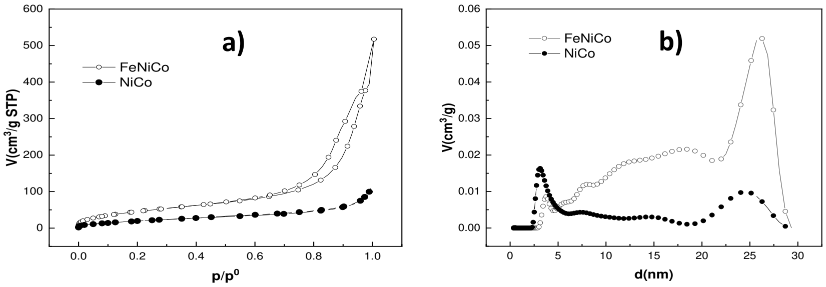

Fig. 1 N_2 isotherms using the BET technique: a) N_2 adsorption-desorption, b) Porosity analysis.

FeNiCo exhibits a significant increase in mesopores in the 20-30 nm range compared to NiCo, while the NiCo aerogel has a higher volume of mesopores in the 2-5nm range.

The morphology and structure of the samples can be seen in the TEM micrographs (Figure 2). The network of interconnected nanoparticles is very similar for both aerogels, although NiCo appears to have a more compact structure than FeNiCo, as can be seen in Fig. 2b and Fig. 2e. This is consistent with the porosity results obtained from the N_2 adsorption isotherms. The size of the pores can be recognised in the TEM images as an interconnected network of angstrom-sized particles. The morphology of NiCo is similar to that of FeNiCo, although NiCo shows slight agglomerations in rod form of the metals Ni and Co. The XRD patters are shown in Fig. 2c, where a NiCo alloy with FCC structure is favoured [29].

X-ray photoelectron spectroscopy (XPS) allows NiCo and FeNiCo aerogels to be analysed in terms of the chemical composition and oxidation states of their constituents. Fig.3 shows the presence of C1s, Co2p, O1s and Ni2p, for both samples. While Fe2p is, as expeted, only found in the FeNiCo aerogel.

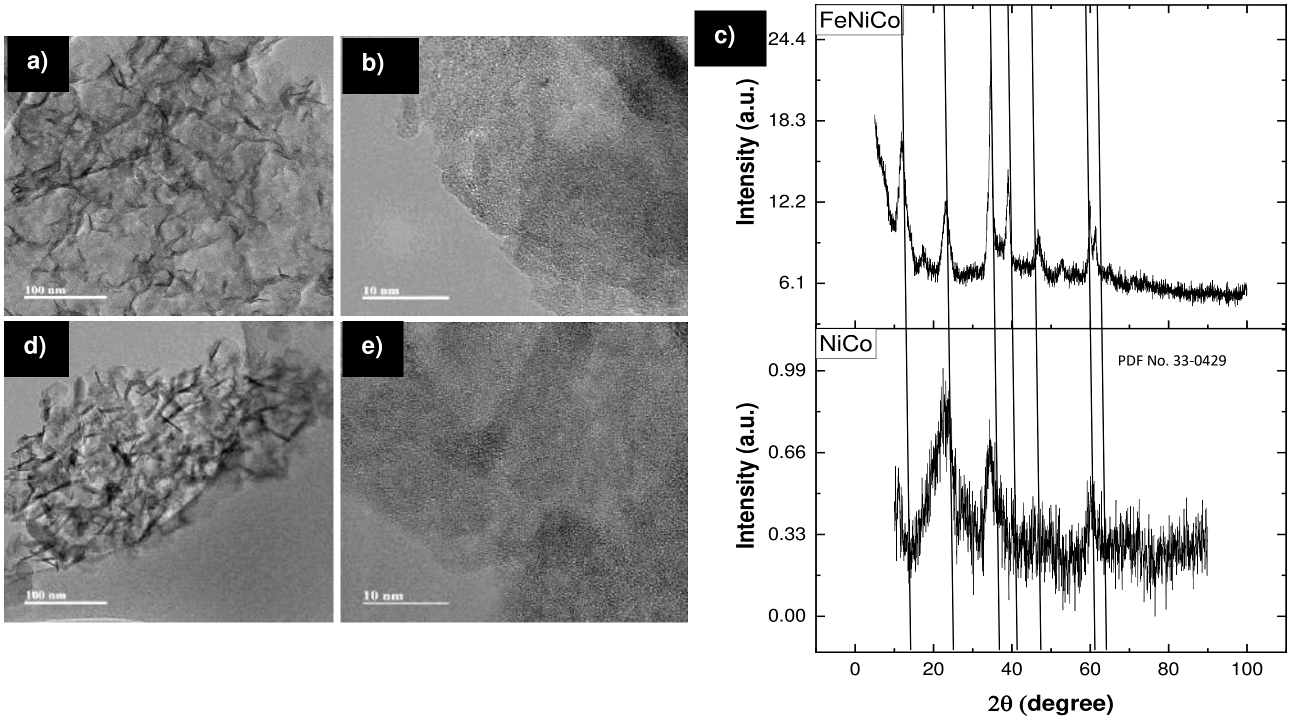

Fig. 2 Physo-chemical characterisations of aerogels: TEM images of (a-b) NiCo and (d-e) FeNiCo. XRD patterns of NiCo and FeNiCo.

The high-resolution spectrum of the Co2p comparison is shown in Fig. 3b. The spectra of Co2p3/2 in the energy band 779.89 eV and Co2p1/2 in 795.92 eV were deconvoluted, resulting in the peaks at 780.8 and 796.43 eV corresponding to Co^{2+} and the peaks located at 779.48 and 795.11 eV relating to Co^{3+}. These correspond to the structure Co_2O_4 [30,31].

An increase of Co^{2+} by 42.5% compared to Co^{3+} can be observed in the NiCo sample. In the FeNiCo sample, however, it can be seen that the Co^{2+} species occur in a lower ratio than Co^{3+}.

The comparison of the spectrum for Ni2p in NiCo and FeNiCo aerogels is shown in Fig. 1c. Ni2p3/2 is at 854.77 eV and Ni2p1/2 at 872.37 eV. After deconvolution, peaks appear at similar positions (854.77 eV and 872.17 eV) corresponding to Ni^{2+}, while the peaks at 856.61

eV and 873.67 eV refer to Ni^{3+}[31–34]. In the NiCo sample there is also a higher proportion of Ni^{2+}(61.8 wt%) than Ni^{3+} (28.7 wt%), the rest is mainly oxygen.

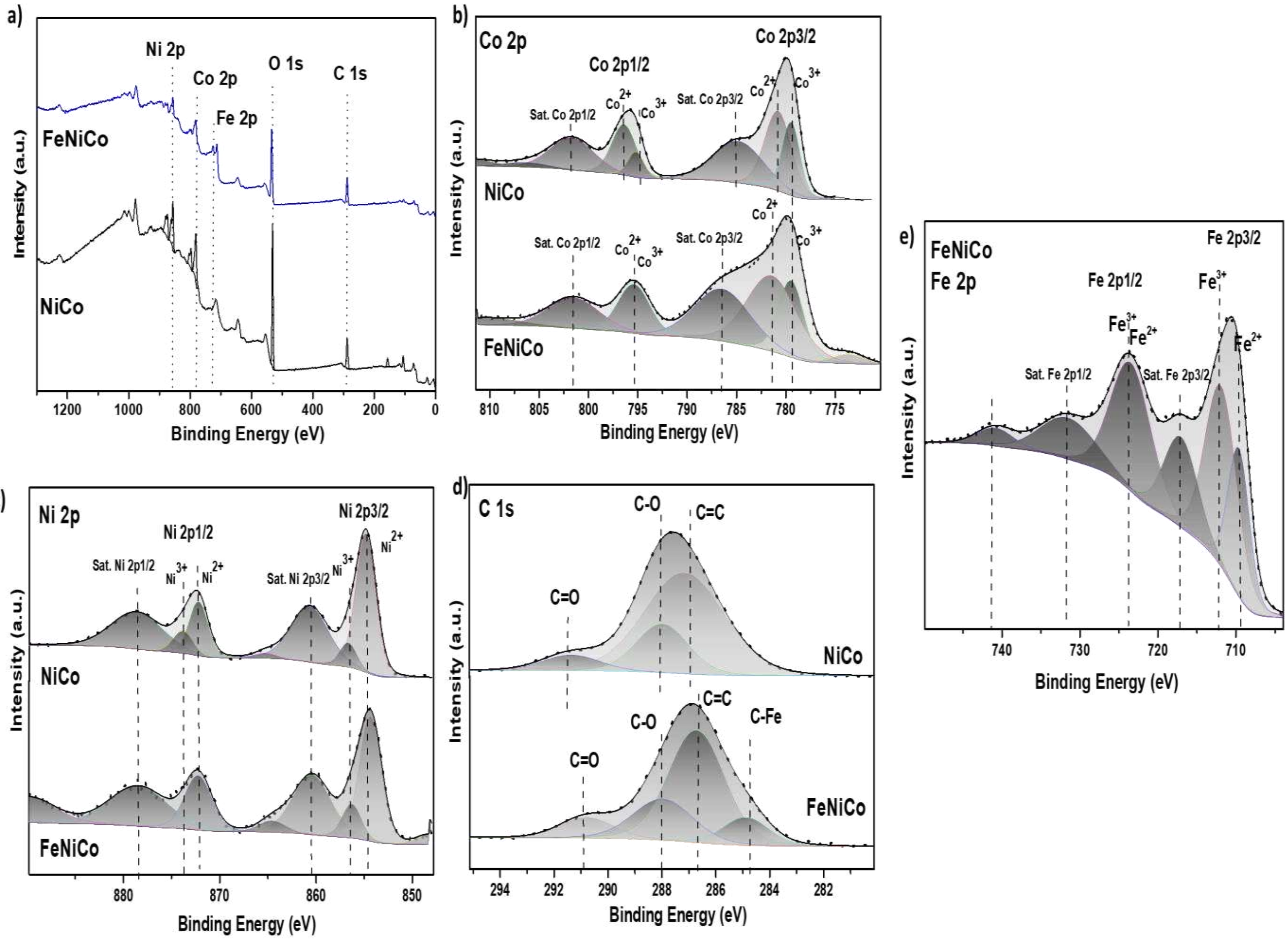

Fig. 3 Comparison of high-resolution XPS for NiCo and FeNiCo aerogels. a) General spectra of FeNiCo and NiCo, b) Co 2p for NiCo and FeNiCo, c) Ni 2p for NiCo and FeNiCo, d) C 1s for NiCo and FeNiCo, and d) Fe 2p for FeNiCo aerogel.

The results obtained show that the synthesis of NiCo exhibits an oxidation state that is due to the synthesis of the material leads to a stronger oxidation of Ni^{2+} than Ni^{3+}. However, when compared with FeNiCo aerogel, it is found that doping with iron changes the Ni-Co ratio by replacing some nickel atoms with iron. This means a decrease of Ni^{2+} to 51.51 wt% and an increase of Ni^{3+} species to 38.86 wt% compared to the NiCo aerogel.

The high-resolution C1s spectrum for NiCo and FeNiCo aerogels is shown in Figure 3d. The NiCo aerogel shows three peaks after deconvolution, the first peak at 287.05 eV, which is characteristic of sp3 hybridisation, the second peak at 287.86 eV for C-O and the third peak at 287.8 eV for C = O [31,35,36]. The percentage of C in NiCo aerogel is 2.1 wt%, while it is 3.2 wt% in FeNiCo samples. In addition, a fourth peak at 284.7 eV is detected in FeNiCo aerogel, which corresponds to metallic bonds.

The high-resolution spectrum of Fe 2p is shown in Figure 3e. The peak at 709.75 eV corresponds to Fe^{2+}, at 712.11 eV to Fe^{3+}[37,38], and the satellite peaks of band 2p3/2 and 2p1/2 at 717.47 and 721.67 eV, respectively. These results confirm the interaction due to the transfer of electrons at the NiCo interface by the addition of Fe during the synthesis of FeNiCo. The presence of Fe^{3+} is due to the partial oxidation of Fe^{2+} during the synthesis process. Fe^{2+} and Fe^{3+} can help stabilise the high-valent metal sites and thyus improve the reaction activity of the FeNiCo sample.

In summary, it can be concluded that NiCo and FeNiCo aerogels were successfully prepared by the sol-gel process using microwave heating and exhibit different physicochemical properties.

3.2 Electrochemical performance

3.2.1 OER performance for NiCo and FeNiCo aerogels

In a first approach, the electrochemical profiles of the samples were determined using cyclic voltammetry in 1 M KOH (Fig. 4a). In this analysis, the peak located at 1.17 V vs. RHE can be attributed to the formation of NiOOH for both FeNiCo and NiCo aerogels, while Ni^{3+} and Fe^{3+} reductions occur at 1.05 and 1.18 V vs. RHE, respectively [11,39,40].

To understand how OER is generated at the aerogels surface, linnear sweep voltammetry was performed at 20 mVs^{-1} in a range of 1 to 1.7 V vs. RHE (Fig. 4b). The anode current of OER starts to increase at the potential of NiOOH formation (i.e. 1.17 V vs. RHE), indicating that these species are the active sites for OER catalysis. Although nickel strongly influences OER, the addition of iron significantly favours OER. The presence of iron allows the OH- ions to easily reach the electrode surface, so that the OER is energetically favoured as the OH- ions are rapidly supplied to the reaction surface and reach 10 mAcm^{-2} at 1.4 V in the FeNiCo aerogel. In the case of NiCo, however, this value is reached at a higher voltage (1.62 V vs. RHE).

For the kinetic analysis of the surface of the electrodes towards the OER, Tafel slopes were calculated (Fig. 4c), which show that the reaction is favoured by the use of FeNiCo aerogel, as a slope value of 25 mV dec^{-1} is achieved, while NiCo aerogel has 38 mV dec^{-1} under the same conditions.

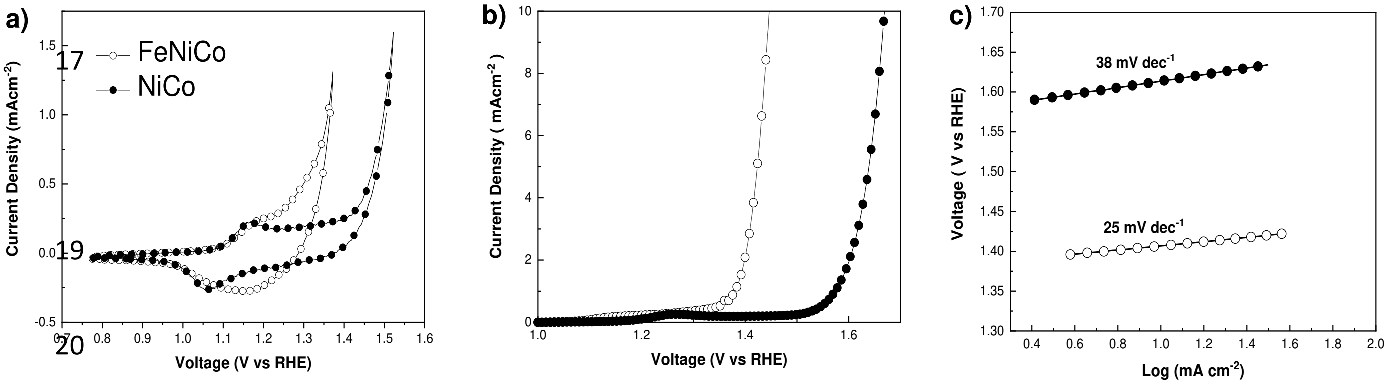

Fig. 4 Electrochemical performance of NiCo and FeNiCo aerogels. a) Cyclic voltammetry, b) Linnear sweep voltammetry and c) Tafel plots.

3.2.2. Hydrogen production

To demonstrate the high electrochemical performance of the FeNiCo aerogel, it was evaluated in a microfluidic cell prototype (Fig. 5a), which demonstrated the ability to produce significant amounts of H_2 in alkaline medium. Chronoamperometry was performed for 35 hours at 200 μL min^{-1} flow rate. FeNiCo was investigated as the anode in the microfluidic cell shown in Fig. 5a, with Pt/C chosen as the commercial catalyst for the cathode[41–43]. The hydrogen production achieved for the FeNiCo aerogel after 35 hours was 220 μg s^{-1} 10^{-7} (Fig. 5b).

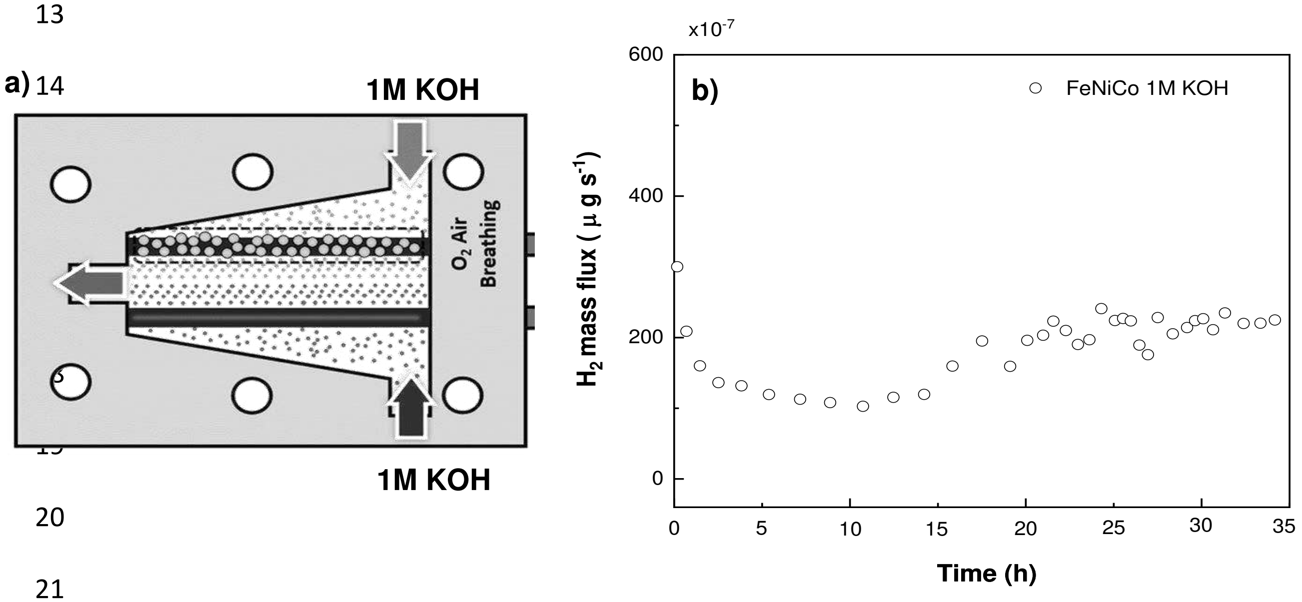

Fig. 5 a) Schematic of the microfluidic fuel cell used in this work and b) Hydrogen production using aerogels as electrocatalysers in 1M KOH.

3.2.3. FeNiCo performance in an electrolysis system

The best material performance can be attributed to the FeNiCo aerogel tested in an electrolysis system where an electrolysis cell was used to perform the electrochemical measurements[44]. The cell consists of a simple 5cm^2 serpentine that collect the flow and recirculates it through Ni plates. The current collectors are made of gold plate. The AEM consists of a CCM for the anode side, where the FeNiCo was deposited by spraying onto a FAA3-50® membrane, the system was coupled with a gas diffusion electrode (GDE) containing Pt/C for the cathode anode. LSV was performed at 5 mV·s^{-1} at different temperatures (30°C, 40°C, 50°C and 60°C) with a 1 M KOH solution continuously flowing through the anode at 5 ml.min flow rate.

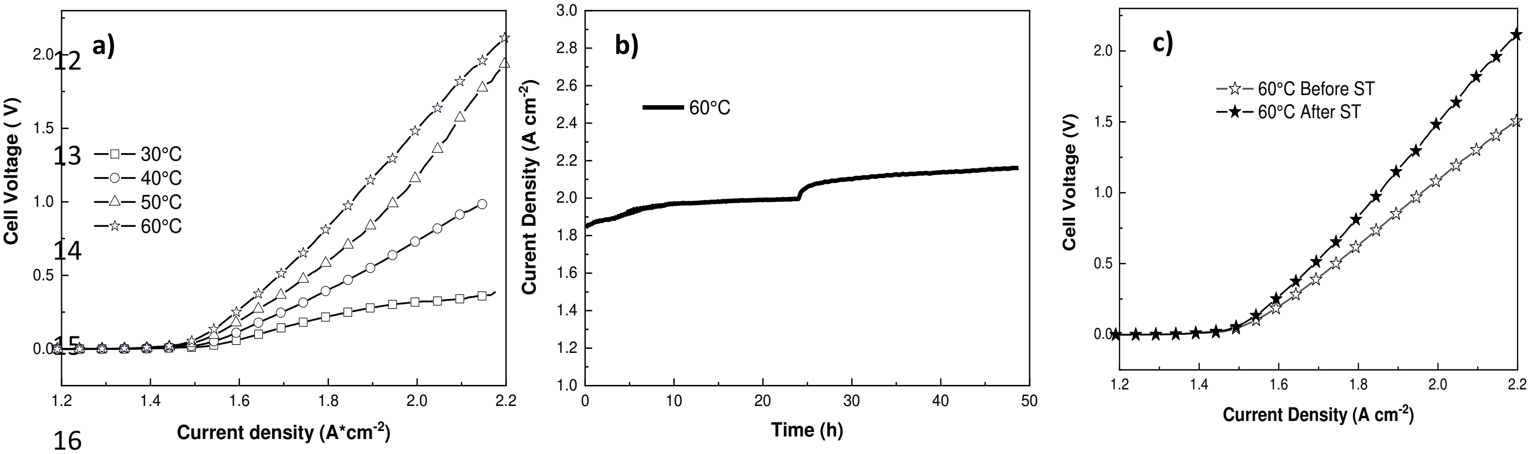

Fig. 6 Performance of the electrolyser using FeNiCo aerogel in the anode. a) LSV curves at different temperatures, b) Stability test over 50 hours and c) LSV at 60 ºC before and after the stability test (ST).

The LVS measurements were performed at temperatures not exceeding the limit of the commercial membrane (60°C) to avoid stress. The I-V curves are shown in Fig. 6a. They show an increase in electrolysis potential at low temperatures, while the best electrolysis performance is observed at 60 °C.

To verify whether the catalyst can withstand the long-term potential, a stability test was carried out using chronopotentiometry (@ 1 A cm-2). The results are presented in Fig. 6b. In this analysis, 1 M KOH solution was recirculated from the anode side and after 24 hours the 1M KOH solution was changed (Fig. 6c). A slight increase in current density was observed during the second 24-hour period. This effect could be attributed to various reasons, namely the activation of the catalysts or membrane permeability or the elimination of the accumulation of H_2 and O_2 gas bubbles. This could be the reason for the recovery in performance after 24 hours of operation, in addition to the replacement of the solution.

4. Conclusions

NiCo and FeNiCo aerogels were successfully produced by microwave-assisted sol gel method. The results clearly show that the incorporation of Fe greatly improves the electrocatalytic activity towards the EOR in a microfluidic electrolysis cell. This excellent performance is due to a very good porosity with a relatively high surface area besides the presence of meso- and macropores, a low density morphology with cross-linked nanoparticles and a specific chemistry. XPS analysis shows that the particles are strongly bound in NiCo and FeNiCo alloys, where the Fe can efficiently transport the oxygen to the reaction surface. Fe^{2+} and Fe^{3+} can help to stabilise high valent metal sites and thus improve the reaction activity of the FeNiCo aerogel. The performance in a microfluidic cell for hydrogen production shows that a larger amount of gas was obtained with the FeNiCo aerogel.

To summarise, the FeNiCo aerogels exhibit higher catalytic activity than NiCo in OER and are presented as a highly competitive alternative to produce hydrogen in different electrolyser configurations with and without membrane.

5. Acknowledgements

The authors thanks to the Mexican Council of Humanistics, Sciences and Technologies (CONAHCYT) for financial support.

6. References

[1] N. Chen, Y.X. Du, G. Zhang, W.T. Lu, F.F. Cao, Amorphous nickel sulfoselenide for efficient electrochemical urea-assisted hydrogen production in alkaline media, Nano Energy. 81 (2021) 105605. https://doi.org/10.1016/j.nanoen.2020.105605.

[2] Q. Zhou, L. Liao, H. Zhou, D. Li, D. Tang, F. Yu, Innovative strategies in design of transition metal-based catalysts for large-current-density alkaline water/seawater electrolysis, Mater. Today Phys. 26 (2022) 100727. https://doi.org/10.1016/j.mtphys.2022.100727.

[3] Y. Guo, X. Liu, Y. Li, F. Ma, Q. Zhang, Z. Wang, Y. Liu, Z. Zheng, H. Cheng, B. Huang, Y. Dai, P. Wang, Anion-modulation in CoMoO4 electrocatalyst for urea-assisted energy-saving hydrogen production, Int. J. Hydrogen Energy. 47 (2022) 33167–33176. https://doi.org/10.1016/j.ijhydene.2022.07.219.

[4] J. Ge, Z. Liu, M. Guan, J. Kuang, Y. Xiao, Y. Yang, C.H. Tsang, X. Lu, C. Yang, Investigation of the electrocatalytic mechanisms of urea oxidation reaction on the surface of transition metal oxides, J. Colloid Interface Sci. 620 (2022) 442–453. https://doi.org/10.1016/j.jcis.2022.03.152.

[5] W. Wen, X. Du, X. Zhang, Controlled synthesis of M doped N-Ni3S2 (M = Cu, Fe, Co and Ce) on Ni foam as efficient electrocatalyst for urea oxidation reaction and oxygen evolution reaction, J. Alloys Compd. 918 (2022) 512–525. https://doi.org/10.1016/j.jallcom.2022.165739.

[6] S.C. Tsai, M.S. Wu, Hydrothermal growth of pompon-like manganese oxide

microspheres with embedded nickel ions as single-atom catalysts for urea oxidation, J. Alloys Compd. 894 (2022) 162515. https://doi.org/10.1016/j.jallcom.2021.162515.

[7] T. Wang, X. Cao, L. Jiao, Ni2P/NiMoP heterostructure as a bifunctional electrocatalyst for energy-saving hydrogen production, EScience. 1 (2021) 69–74. https://doi.org/10.1016/j.esci.2021.09.002.

[8] C. Chen, L. Jin, L. Hu, T. Zhang, J. He, P. Gu, Q. Xu, J. Lu, Urea-oxidation-assisted electrochemical water splitting for hydrogen production on a bifunctional heterostructure transition metal phosphides combining metal–organic frameworks, J. Colloid Interface Sci. 628 (2022) 1008–1018. https://doi.org/10.1016/j.jcis.2022.08.127.

[9] Y. Zhang, C. Wang, Yolk-shell nanostructural Ni2P/C composites as the high performance electrocatalysts toward urea oxidation, Chinese Chem. Lett. 32 (2021) 2222–2228. https://doi.org/10.1016/j.cclet.2020.11.040.

[10] M. Zhong, W. Li, C. Wang, X. Lu, Synthesis of hierarchical nickel sulfide nanotubes for highly efficient electrocatalytic urea oxidation, Appl. Surf. Sci. 575 (2022) 151708. https://doi.org/10.1016/j.apsusc.2021.151708.

[11] Y. Wang, N. Chen, X. Du, X. Han, X. Zhang, Transition metal atoms M (M = Mn, Fe, Cu, Zn) doped nickel-cobalt sulfides on the Ni foam for efficient oxygen evolution reaction and urea oxidation reaction, J. Alloys Compd. 893 (2022) 162269. https://doi.org/10.1016/j.jallcom.2021.162269.

[12] X. Du, Y. Ding, X. Zhang, MOF-derived Zn–Co–Ni sulfides with hollow nanosword arrays for high-efficiency overall water and urea electrolysis, Green Energy Environ. 8 (2021) 798-811. https://doi.org/10.1016/j.gee.2021.09.007.

[13] X.H. Wang, Q.L. Hong, Z.N. Zhang, Z.X. Ge, Q.G. Zhai, Y.C. Jiang, Y. Chen, S.N. Li, Two-dimensional nickel–cobalt bimetallic hydroxides towards urea electrooxidation, Appl. Surf. Sci. 604 (2022) 154484. https://doi.org/10.1016/j.apsusc.2022.154484.

[14] L. Xiang, W. Da Zhang, H. Xu, M. Hu, J. Yang, J. Liu, Z.G. Gu, X. Yan,

Hierarchical microspheres constructed by hexagonal NiCo(OH)2 nanosheets with rich Ni3+ species and carboxylic groups for efficient urea oxidation reaction, J. Alloys Compd. 930 (2023) 167453. https://doi.org/10.1016/j.jallcom.2022.167453.

[15] Y. Zheng, K. Sun, J. Pang, J. Hou, G. Wang, W. Guo, L. Wang, X. Guo, L. Chen, Ternary cobalt–iron–manganese layered double hydroxides with 1D/2D hierarchical nanostructure for oxygen evolution reaction and urea oxidation reaction, J. Alloys Compd. 925 (2022) 166754. https://doi.org/10.1016/j.jallcom.2022.166754.

[16] W. Huang, Y. Yuan, K. Wang, Q. Cao, Y. Zhao, X. Sun, R. Ding, P. Gao, W. Cai, E. Liu, Tuning interface density and electronic structure of NiS/Ni3S4 by Mo, Co co-doping for efficient urea electrooxidation reaction, J. Electroanal. Chem. 911 (2022) 116242. https://doi.org/10.1016/j.jelechem.2022.116242.

[17] M. Li, X. Wu, K. Liu, Y. Zhang, X. Jiang, D. Sun, Y. Tang, K. Huang, G. Fu, Nitrogen vacancies enriched Ce-doped Ni3N hierarchical nanosheets triggering highly-efficient urea oxidation reaction in urea-assisted energy-saving electrolysis, J. Energy Chem. 69 (2022) 506–515. https://doi.org/10.1016/j.jechem.2022.01.031.

[18] J. Cao, H. Li, R. Zhu, L. Ma, K. Zhou, Q. Wei, F. Luo, Improved hydrogen generation via a urea-assisted method over 3D hierarchical NiMo-based composite microrod arrays, J. Alloys Compd. 844 (2020) 155382. https://doi.org/10.1016/j.jallcom.2020.155382.

[19] C. Wang, X. Du, X. Zhang, Controlled synthesis of Fe doped NiCoM (M=O, P, S and Se) as robust electrocatalyst for urea electrolysis, J. Alloys Compd. 928 (2022) 167094. https://doi.org/10.1016/j.jallcom.2022.167094.

[20] J. Zhang, Z. Li, G. Bai, Q. Wang, J. Zhang, W. Wang, L. Zhou, J. Yi, Z. Ma, Nickel-iron layered silicate nanomembrane as efficient electrocatalyst for oxygen evolution reaction in alkaline media, Fuel. 332 (2023) 126209. https://doi.org/10.1016/j.fuel.2022.126209.

[21] X. Yin, Y. Hua, W. Hao, J. Yang, Z. Gao, Hierarchical nanocomposites of nickel/iron-layered double hydroxide ultrathin nanosheets strong-coupled with nanocarbon networks for enhanced oxygen evolution reaction, Electrochim. Acta.

420 (2022) 140455. https://doi.org/10.1016/j.electacta.2022.140455.

[22] X. Yu, Z. Zhao, C. Pei, Surface oxidized iron-nickel nanorods anchoring on graphene architectures for oxygen evolution reaction, Chinese Chem. Lett. 32 (2021) 3579–3583. https://doi.org/10.1016/j.cclet.2021.03.040.

[23] W. Ke, Y. Zhang, A.L. Imbault, Y. Li, Metal-organic framework derived iron-nickel sulfide nanorods for oxygen evolution reaction, Int. J. Hydrogen Energy. 46 (2021) 20941–20949. https://doi.org/10.1016/j.ijhydene.2021.03.207.

[24] I. Smirnova, P. Gurikov, Aerogel production: Current status, research directions, and future opportunities, J. Supercrit. Fluids. 134 (2018) 228–233. https://doi.org/10.1016/j.supflu.2017.12.037.

[25] A.Martínez, M.H. Rodriguez, L.G. Arriaga, Novel and high electrocatalytic activity aerogel Pd-TM (TM=Co, Ni, Fe), Materials Today Nano (2023) 221003908. https://doi.org/10.1016/j.mtnano.2023.100308.

[26] A. Martínez, L.A. Ramirez, J. Ledesma-Garcia, M.A. Montes-Moran, M.P. Gurrola, J.A. Mendez, A. Arenillas, L.G. Arriaga, Facile Synthesis of Unsupported Pd Aerogel for High Performance Formic Acid Microfluidic Fuel Cell, (2022). https://doi.org/10.3390/ma15041422

[27] Y. Kong, Y. Zhong, X. Shen, S. Cui, M. Yang, K. Teng, J. Zhang, Facile synthesis of resorcinol-formaldehyde/silica composite aerogels and their transformation to monolithic carbon/silica and carbon/silicon carbide composite aerogels, J. Non. Cryst. Solids. 358 (2012) 3150–3155. https://doi.org/10.1016/j.jnoncrysol.2012.08.029.

[28] A. Martinez-lazaro, A. Caprì, I. Gatto, J. Ledesma-garcía, N. Rey-raap, A. Arenillas, NiFe2O4 hierarchical nanoparticles as electrocatalyst for anion exchange membrane water electrolysis, J. Power Sources. 556 (2023) 232417. https://doi.org/10.1016/j.jpowsour.2022.232417.

[29] J. Qian, Y. Zhang, Z. Chen, Y. Du, B. Ni, Chemosphere NiCo layered double hydroxides / NiFe layered double hydroxides composite (NiCo-LDH / NiFe-LDH)

towards efficient oxygen evolution in different water matrices, 345 (2023) 140472https://doi.org/10.1016/j.chemosphere.2023.140472.

[30] D. Cabrera-German, G. Gomez-Sosa, A. Herrera-Gomez, Accurate peak fitting and subsequent quantitative composition analysis of the spectrum of Co 2p obtained with Al Kα radiation: I: cobalt spinel, Surf. Interface Anal. 48 (2016) 252–256. https://doi.org/10.1002/sia.5933.

[31] J.F. Marco, J.R. Gancedo, M. Gracia, J.L. Gautier, E. Ríos, F.J. Berry, Characterization of the nickel cobaltite, NiCo2O4, prepared by several methods: An XRD, XANES, EXAFS, and XPS study, J. Solid State Chem. 153 (2000) 74–81. https://doi.org/10.1006/jssc.2000.8749.

[32] J. Haenen, W. Visscher, E. Barendrecht, Characterization of NiCo2O4 electrodes for O2 evolution. Part II. Non-electrochemical characterization of NiCo2O4 electrodes, J. Electroanal. Chem. 208 (1986) 297–321. https://doi.org/10.1016/0022-0728(86)80540-X.

[33] M.A. Ghanem, A.M. Al-Mayouf, J.P. Singh, P. Arunachalam, Concurrent Deposition and Exfoliation of Nickel Hydroxide Nanoflakes Using Liquid Crystal Template and Their Activity for Urea Electrooxidation in Alkaline Medium, Electrocatalysis. 8 (2017) 16–26. https://doi.org/10.1007/s12678-016-0336-8.

[34] R. BoopathiRaja, M. Parthibavarman, Hetero-structure arrays of MnCo2O4 nanoflakes@nanowires grown on Ni foam: Design, fabrication and applications in electrochemical energy storage, J. Alloys Compd. 811 (2019) 152084. https://doi.org/10.1016/j.jallcom.2019.152084.

[35] T.S. Munonde, H. Zheng, M.S. Matseke, P.N. Nomngongo, Y. Wang, P. Tsiakaras, A green approach for enhancing the electrocatalytic activity and stability of NiFe2O4/CB nanospheres towards hydrogen production, Renew. Energy. 154 (2020) 704–714. https://doi.org/10.1016/j.renene.2020.03.022.

[36] J. White, A. Anil, D. Martín-Yerga, G. Salazar-Alvarez, G. Henriksson, A. Cornell, Electrodeposited PdNi on a Ni rotating disk electrode highly active for glycerol electrooxidation in alkaline conditions, Electrochim. Acta. 403 (2022) 139714.

https://doi.org/10.1016/j.electacta.2021.139714.

[37] M.C. Biesinger, B.P. Payne, A.P. Grosvenor, L.W.M. Lau, A.R. Gerson, R.S.C. Smart, Resolving surface chemical states in XPS analysis of first row transition metals, oxides and hydroxides: Cr, Mn, Fe, Co and Ni, Appl. Surf. Sci. 257 (2011) 2717–2730. https://doi.org/10.1016/j.apsusc.2010.10.051.

[38] R. Tholkappiyan, K. Vishista, Tuning the composition and magnetostructure of dysprosium iron garnets by Co-substitution: An XRD, FT-IR, XPS and VSM study, Appl. Surf. Sci. 351 (2015) 1016–1024. https://doi.org/10.1016/j.apsusc.2015.05.193.

[39] M.S.E. Houache, E. Cossar, S. Ntais, E.A. Baranova, Electrochemical modification of nickel surfaces for efficient glycerol electrooxidation, J. Power Sources. 375 (2017) 310–319. https://doi.org/10.1016/j.jpowsour.2017.08.089.

[40] H. Zhang, W. Chen, H. Wang, X. Tong, Y. Wang, X. Yang, Z. Wu, Z. Liu, A core-shell NiCu@NiCuOOH 3D electrode induced by surface electrochemical reconstruction for the ammonia oxidation reaction, Int. J. Hydrogen Energy. 47 (2022) 16080–16091. https://doi.org/10.1016/j.ijhydene.2022.03.139.

[41] M.P. Marčeta Kaninski, V.M. Nikolić, T.N. Potkonjak, B.R. Simonović, N.I. Potkonjak, Catalytic activity of Pt-based intermetallics for the hydrogen production-Influence of ionic activator, Appl. Catal. A Gen. 321 (2007) 93–99. https://doi.org/10.1016/j.apcata.2007.01.036.

[42] S. Henning, H. Ishikawa, L. Kühn, J. Herranz, E. Müller, A. Eychmüller, T.J. Schmidt, Unsupported Pt-Ni Aerogels with Enhanced High Current Performance and Durability in Fuel Cell Cathodes, Angew. Chemie - Int. Ed. 56 (2017) 10707–10710. https://doi.org/10.1002/anie.201704253.

[43] D. Li, A.R. Motz, C. Bae, C. Fujimoto, G. Yang, F.Y. Zhang, K.E. Ayers, Y.S. Kim, Durability of anion exchange membrane water electrolyzers, Energy Environ. Sci. 14 (2021) 3393–3419. https://doi.org/10.1039/d0ee04086j.

[44] X. Zhang, X. Fang, K. Zhu, W. Yuan, T. Jiang, H. Xue, J. Tian, Fe-doping induced

electronic structure reconstruction in Ni-based metal-organic framework for improved energy-saving hydrogen production via urea degradation, J. Power Sources. 520 (2022) 230882. https://doi.org/10.1016/j.jpowsour.2021.230882.

Conclusiones

En este capítulo se describe como se obtuvieron aerogeles de metales de transición mediante la metodología de sol-gel asistida por microondas, los cuales resultaron ser catalizadores altamente selectivos para reacciones como oxidación de urea y evolución de oxígeno. Estos aerogeles se elaboraron a partir de sales precursoras de Fe, Ni y Co, que posteriormente fueron utilizados eficazmente en una celda microfluídica y en un electrolizador. Los resultados obtenidos a lo largo de esta Tesis Doctoral muestran claramente la eficacia de los materiales sintetizados, y específicamente la gran mejora obtenida con la incorporación de Fe en la actividad electrocatalítica hacía la reacción de evolución de oxígeno. Este hecho junto con el desarrollo de un proceso de obtención sencillo y rápido hace que sean unos materiales muy prometedores para su utilización en dispositivos para la producción de hidrogeno a partir de la hidrólisis del agua.

Referencias

Anantharaj, S., Ede, S. R., Sakthikumar, K., Karthick, K., Mishra, S., & Kundu, S. (2016). Recent Trends and Perspectives in Electrochemical Water Splitting with an Emphasis on Sulfide, Selenide, and Phosphide Catalysts of Fe, Co, and Ni: A Review. *ACS Catalysis*, *6*(12), 8069–8097. https://doi.org/10.1021/acscatal.6b02479

Cha, B., Yea, Y., Yun, K., Kim, T., Kim, H., Yoon, Y., Kim, S., & Min, C. (2023). *Enhanced catalytic oxidation of naproxen via activation of peroxymonosulfate by Fe-based metal – organic framework aerogels functionalized with Ag nanoparticles*. *458*(May).

Heinrichs, B., Noville, F., & Pirard, J. P. (1997). Pd/SiO2-cogelled aerogel catalysts and impregnated aerogel and xerogel catalysts: Synthesis and characterization. *Journal of Catalysis*, *170*(2), 366–376. https://doi.org/10.1006/jcat.1997.1772

Kim, Y., Parale, V. G., Kim, T., Kim, S., Choi, H., Patil, U. M., Kanamori, K., & Park, H. (2023). *Synthesis of Zn-Co-S nanowire bundle type aerogel electrodes for asymmetric supercapacitors*. *474*(September).

Lim, M. B., Hu, M., Manandhar, S., Sakshaug, A., Strong, A., Riley, L., & Pauzauskie, P. J. (2015). Ultrafast sol-gel synthesis of graphene aerogel materials. *Carbon*, *95*, 616–624. https://doi.org/10.1016/j.carbon.2015.08.037

Moretti, A., Giuli, G., Trapananti, A., & Passerini, S. (2018). *Electrochemical and structural investigation of transition metal doped V 2 O 5 sono-aerogel cathodes for lithium metal batteries*. *319*(September 2017), 46–52.

Moussaoui, R., Elghniji, K., ben Mosbah, M., Elaloui, E., & Moussaoui, Y. (2017). Sol–gel synthesis of highly TiO2aerogel photocatalyst via high temperature supercritical drying. *Journal of Saudi Chemical Society*, *21*(6), 751–760. https://doi.org/10.1016/j.jscs.2017.04.001

Oschatz, M., Boukhalfa, S., Nickel, W., Hofmann, J. P., Fischer, C., Yushin, G., & Kaskel, S. (2017). Carbide-derived carbon aerogels with tunable pore structure as versatile electrode material in high power supercapacitors. *Carbon*, *113*, 283–291. https://doi.org/10.1016/j.carbon.2016.11.050

Patil, B., Fujikawa, S., Okajima, T., & Ohsaka, T. (2012). Enzymatic direct electron transfer at ascorbate oxidase-modified gold electrode prepared by one-step galvanostatic method. *International Journal of Electrochemical Science*, *7*(6), 5012–5019.

Rodriguez-barajas, M. H., Rey-raap, N., & Espinosa, F. I. (2023). *Materials Today Nano Novel and high electrocatalytic activity aerogel Pd-TM (TM ¼ Co , Ni , Fe)*. *22*, 0–8. https://doi.org/10.1016/j.mtnano.2023.100308

Saravani, H., Mehdizadeh, K., & Elyasi, Z. (2023). Growing nanoparticles to assemble a modern three-dimensional nanoarchitecture of Pt-Ru aerogel for advanced electrocatalysis. *Journal of Molecular Liquids*, *384*(May), 122047. 149https://doi.org/10.1016/j.molliq.2023.122047

Sashkina, K. A., Gurikov, P. A., Ayupov, A. B., Smirnova, I., & Parkhomchuk, E. V. (2018). Zeolite/silica aerogel composite monoliths and microspheres. *Microporous and Mesoporous Materials*, *263*(December 2017), 106–112. https://doi.org/10.1016/j.micromeso.2017.12.010

Schmidt, T. J., Stamenkovic, V., Ross, P. N., & Markovic, N. M. (2003). Temperature dependent surface electrochemistry on Pt single crystals in alkaline electrolyte: Part 3. The oxygen reduction reaction. *Physical Chemistry Chemical Physics*, *5*(2), 400–406. https://doi.org/10.1039/b208322a

Smirnova, I., & Gurikov, P. (2018). Aerogel production: Current status, research directions, and future opportunities. *Journal of Supercritical Fluids*, *134*(December 2017), 228–233. https://doi.org/10.1016/j.supflu.2017.12.037

Tahir, M., Pan, L., Idrees, F., Zhang, X., Wang, L., Zou, J. J., & Wang, Z. L. (2017). Electrocatalytic oxygen evolution reaction for energy conversion and storage: A comprehensive review. *Nano Energy*, *37*(May), 136–157. https://doi.org/10.1016/j.nanoen.2017.05.022

Wang, J., Chen, F., Jin, Y., Guo, L., Gong, X., Wang, X., & Johnston, R. L. (2019). In situ high-potential-driven surface restructuring of ternary AgPd-Ptdilute aerogels with record-high performance improvement for formate oxidation electrocatalysis. *Nanoscale*, *11*(30), 14174–14185. https://doi.org/10.1039/c9nr03266e

Wang, W., Gong, S., Liu, J., Ge, Y., Wang, J., & Lv, X. (2021). *Journal of Colloid and Interface Science Ag-Cu aerogel for electrochemical CO 2 conversion to CO*. *595*, 159–167.

CONCLUSIONES GENERALES

En esta tesis de investigación se elaboraron aerogeles de Pd en combinación con los metales de transición Fe, Ni y Co para formar aleaciones Pd-M, estos aerogeles se evaluaron como ánodos en sistemas microfluidicos de etanol y ácido fórmico, donde las aleaciones Pd-Ni y Pd-Co fueron las combinaciones que más favorecieron ambos sistemas, la proporción ideal entre los metales es 4:1, la ligera presencia del metal de transición en la estructura del aerogel permitió aumentar los sitios activos para las oxidaciones de los combustibles mejorando la actividad catalítica del aerogel de Pd por sí solo. La incorporación de ambos metales (Pd-M) muestra una innovadora propuesta hacia el uso de metales nobles, ya que la morfología y composición química del aerogel disminuyen la cantidad de catalizador utilizado a la vez que permiten al sistema microfluíco alcanzar densidades de potencia de hasta 120 mWcm^{-2} cuando se usa ácido fórmico y 110 mWcm^{-2} cuando se usa etanol, además el uso de un anolito básico y catolito ánodo permitió alcanzar voltajes de circuito abierto de hasta 1.6 V en los sistemas con etanol y 1.1 V en sistemas con ácido fórmico. La estabilidad electroquímica de los aerogeles también resulto prometedora ya que los aerogeles toleran altos potenciales por periodos de tiempo de hasta 35 horas sin perder su desempeño catalítico.

Por otro lado los aerogeles de metales de transición resultaron ser excelente catalizadores en sistemas microfluidicos de electrolisis, aprovechando combustibles como urea y amonio para potenciar el desempeño de los sistemas de separación electroquímica de agua, brindando una perspectiva de eliminación de residuos ambientales por un método electroquímico sencillo y practico, las propiedades catalíticas de estos aerogeles se atribuyen a su morfología de partículas ultrafinas y la presencia de Fe y Ni que mejoran el transporte de OH- a la superficie de los ánodos, brindando una combinación de excelente desempeño catalítico y estabilidad electroquímica.

ANEXO I

TECNICAS DE CARACTERIZACION

A1.1. Fisisorción de nitrógeno

El análisis de la adsorción de nitrógeno en diversos materiales es una de las técnicas más empleadas en el estudio de la textura porosa de un material. Para el caso de los aerogeles esta técnica permitió determinar parámetros como el área superficial específica, el volumen y la distribución de tamaño de poro obtenido por síntesis sol-gel. En este análisis se adsorbe un gas a temperatura constante obteniéndose así una isoterma de adsorción. Dicha isoterma se analiza gravimétricamente, esto quiere decir que se mide la ganancia de peso experimentada por la muestra como consecuencia de la adsorción, a cada presión relativa de gas. Dicha isoterma también puede ser obtenida volumétricamente donde la cantidad adsorbida se calcula mediante la aplicación de las leyes de los gases a la presión y volumen de adsorbato antes y después de la adsorción.

El análisis de los resultados de las isotermas de adsorción puede llevarse a cabo a través de varios métodos semi-empíricos. En la presente tesis se ha utilizado el método BET (Brunauer, Emmett y Teller) para calcular el área superficial específica, el método BJH (Barrett, Joyner y Halenda) para el cálculo del volumen de mesoporo y el método de t-plot para el cálculo del volumen de microporo. Los análisis presentados en este trabajo se han llevado a cabo en el equipo para medidas volumétricas de adsorción Micromeritics ASAP 2020.

A1.2. Difracción de Rayos X

La difracción de rayos X está basada en las interferencias ópticas que se producen cuando una radiación monocromática atraviesa una rendija de espesor comparable a la longitud de onda de la radiación. Los rayos X tienen longitudes de onda de Angstroms, del mismo orden que las distancias interatómicas de los componentes de las redes cristalinas. Al ser irradiados sobre la muestra a analizar, los rayos X se difractan con ángulos que dependen de las distancias interatómicas. El método analítico del polvo al azar o de Debye-Scherrer consiste en irradiar con rayos X sobre una muestra formada por multitud de cristales colocados al azar en todas las direcciones posibles. Para ello es aplicable la Ley de Bragg:

$$n\lambda = 2d\ \mathrm{sen}\theta \qquad \text{(Ec. A1.1)}$$

En la que “d” es la distancia entre los planos interatómicos que producen la difracción. La difracción de rayos-x es un método de alta tecnología no destructivo para el análisis de una amplia gama de materiales, incluso fluidos, metales, minerales, polímeros, catalizadores, plásticos, productos farmacéuticos, recubrimientos de capa fina, cerámicas y semiconductores. La aplicación fundamental de la difracción de Rayos X es la identificación cualitativa de la composición mineralógica de una muestra cristalina.

En este caso se someterán a análisis por difracción de rayos X las muestras elaboradas de geles secos para determinar la cristalinidad de las muestras y su similitud con el Pd metálico previamente reportado.

A1.3. Microscopía Electrónica de Barrido (SEM)

La técnica microscopía electrónica permitIO de producir imágenes de alta resolución de la superficie de los aerogeles utilizando las interacciones electrón-materia. Utiliza un haz de electrones en lugar de un haz de luz para formar una imagen. Al incidir el haz de electrones sobre la muestra, interactúa con ella y se producen diversos efectos que serán captados y visualizados en función del equipo que utilicemos. Un microscopio electrónico de barrido (SEM, por sus siglas en inglés) se encuentra principalmente compuesto por un emisor de electrones, una columna y diferentes lentes electromagnéticas. La función del emisor es generar un haz de electrones (electrones incidentes) con una aceleración entre 200 V y 30 keV, el cual viaja a través de la columna (Vacío de 10-4 Pa). En la columna el haz de electrones pasa a través de las diferentes lentes electromagnéticas y un sistema de deflexión que permite manipular el haz de electrones para poder llevar a cabo un barrido superficial de la muestra. Esta técnica nos permitirá conocer la morfología de la superficie del material elaborado.

A1.4. Microscopía electrónica de transmisión de electrones de alta resolución (HRTEM)

La microscopía electrónica de transmisión de electrones de alta resolución HRTEM (High-resolution transmission electron microscopy) es una técnica que mediante el microscopio electrónico de transmisión (TEM) nos dio la formación de imágenes que nos permitieron de la estructura morfológica y cristalográfica de los aerogeles en una escala atómica.

Se eligió esta técnica debido a su alta resolución que permitió atribuir características a nivel atómico a las partículas de los materiales sintetizados por solgel.

A1.5. Espectrometría Fotoelectrónica (XPS)

La espectrometría fotoelectrónica X o espectrometría de fotoelectrones inducidos por rayos X (X-Ray photoelectron spectrometry) es una técnica que permite evaluar la pureza del Pd presente en las muestras, esta técnica implico la medición de los espectros de los fotoelectrones inducidos por fotones de rayos X sobre las muestras elaboradas. La estructura electrónica de los elementos presentes en las muestras fue medida en un equipo Thermo ScienticTM Avantage Data System, K-Alpha+.

A1.6. Experimentos en media celda electroquímica

El análisis de la actividad electroquímica de los catalizadores sintetizados se llevó a cabo mediante experimentos montados en un -celda electroquímica convencional de tres electrodos. Para el análisis de las reacciones evaluadas de los aerogeles sintetizados elaborados se empleó como electrodo de trabajo, carbón vítreo (GC), de 3 mm de diámetro y otro de 5 mm de diámetro para las mediciones en disco rotatorio.

Previo a depositar la tinta del catalizador sobre la superficie del electrodo, el GC se somete a un tratamiento de pulido con una dispersión de alúmina en agua. Una vez limpio y pulido, se depositan 5 µL de tinta del catalizador, compuesta por el electrocatalizador basado en el material de Pd. objeto de estudio, el ionómero (Nafion®) y agua, la tinta se dispersa en un baño ultrasónico durante 30 minutos.

La tinta se deja secar sobre el GC a 85ºC por 6 horas, estas condiciones se establecieron tras varias pruebas sobre tiempo de secado y estabilidad de la tinta sobre el electrodo a simple vista. Durante la evaluación de la actividad electroquímica cabe aclarar sólo la superficie cubierta del catalizador se mantiene en contacto con la solución electrolítica.

Como electrodo de referencia se empleó un electrodo de Hg/$HgSO_4$, como contra-electrodo se utilizó un de alambre de Platino.

El electrolito utilizado para obtener los perfiles electroquímicos del material fue H_2SO_4 0.5 M y para todos los sistemas fue ajustado con la ecuación de Nernst (11) para el electrodo reversible de hidrogeno (RHE).

A1.7. Técnicas electroquímicas utilizadas para la evaluación de la actividad catalítica

La caracterización electroquímica de los aerogeles de Pd estudiados se llevó a cabo el uso de diversas técnicas: voltamperometría cíclica (CV), voltamperometría lineal (LV) y cronoamperometría, que se diferencian entre sí en la forma en la que varía el potencial aplicado frente al tiempo. Se utilizó un potenciostato/galvanostato Biologic VSP. En esta sección se describen los distintos procedimientos utilizados.

A1.7.1. Activación de la Superficie del Electrodo (GC)

Antes de evaluar el desempeño de cada catalizador es necesario activar la superficie del electrodo sometiéndolo a ciclos continuos en una ventana de potencial entre -1.0 V y +1,10 V vs RHE a una velocidad de barrido de 100 mVs^{-1}, en el electrolito soporte (H_2SO_4 0.5M) a temperatura ambiente, hasta lograr un perfil electroquímico estable en la medición.

A1.7.2. Voltamperometría Cíclica

Esta técnica se basa en aplicar un barrido de potencial al electrodo de trabajo tanto en el sentido directo como en el inverso, es decir realizando lo que se denomina barrido triangular de potencial.

Para obtener un barrido de potencial deseado, es necesario programar el potenciostato en un valor inicial E_i hasta un valor de corte denominado E_f, estos valores son establecidos con base en la actividad de las muestras sintetizadas, es decir, el potencial aplicado no es aleatorio, sino que es establecido por la actividad catalítica del Pd. Para aplicar esta técnica sobre los materiales elaborados se aplicó un barrido de potencial a modo de ciclo mientras se registró la corriente obtenida. Para las mediciones sobre esta técnica se una velocidad de barrido de 20 mV s^{-1}, entre dos valores de potencial dados (+0.05 V y +1.4 V vs RHE) en el electrolito base (H_2SO_4 0.5M).

A1.7.3. Superficie electroquímicamente activa (ECSA)

Para evaluar la actividad electroquímica de los aerogeles sintetizados, el área superficial electroquímica activa (ECSA) de un catalizador es un parámetro que proporciona información acerca del comportamiento de la superficie de un catalizador. Determinar el área superficial electroquímicamente activa del catalizador permite obtener un aproximado de la cantidad real de la masa por unidad de área de catalizador que interactúa con la solución.

La voltamperometría cíclica fue utilizada para obtener esta información a partir del pico correspondiente a la carga de la reducción del óxido de Pd (II) a partir de la siguiente ecuación:

$$ECSA = \frac{Q_m}{m_{Pd}ed_m} \qquad \text{(Ec. A1.2)}$$

Donde, Q_m denota la carga culombica (Q por μCcm^{-2}) para la reducción del óxido de Pd (II) obtenida integrando las cargas relacionadas con la reducción del óxido de Pd (II) para las diferentes muestras y Pd / C; m_{Pd} es la cantidad de masa de Pd (g cm^{-2}) presente en la superficie del electrodo GC y con una carga constante (424 μCcm^{-2}), que corresponde a la reducción de una monocapa de óxido de Pd (II).

A1.7.4. Voltamperometría lineal

La voltamperometría de barrido lineal es una técnica en la que se mide la corriente en el electrodo de trabajo mientras se hace un barrido lineal del potencial entre el electrodo de trabajo y el electrodo de referencia. La oxidación o la reducción del analito son registrados como un pico en la señal, obtenido en el potencial al cual la especie comienza a oxidarse o reducirse.

La técnica de Voltamperometría lineal o polarización fue aplicada para analizar la actividad electrocatalítica de los materiales en la reacción de reducción de oxígeno (ORR) y la reacción de evolución de oxígeno (OER). Para la primera reacción las soluciones se saturaron de O_2 y para la segunda reacción de N_2 por 30 minutos.

LISTA DE FIGURAS

CERTIFICATE OF ATTENDANCE

presented to

Alejandra Martínez-Lázaro

for giving the oral presentation "Un-supported PdCo Aerogel electrocatalyst to ethanol electrooxidation reaction"
at the

XVI HYdrogen POwer THeoretical & Engineering Solutions International Symposium

November 8-10, 2021

Conference Chair
Giulia Monteleone

Organised by

AMWEB IT Solutions

CGS

Sociedad Mexicana de
Ciencia y Tecnología
de Membranas, A.C.

XI CONGRESO ANUAL

**17, 18 y 19
octubre 2022
Zacatecas, México.**

LA SOCIEDAD MEXICANA DE CIENCIA Y TECNOLOGÍA DE MEMBRANAS
Otorga la presente:

CONSTANCIA

A:

Alejandra Martínez Lázaro

Por su asistencia al XI Congreso Anual de la Sociedad Mexicana de Ciencia y Tecnología de Membranas.

Dra. Janet Ledesma García
Presidente de la SMCyTM

Dr. Sergio Miguel Durón Torres
Presidente Comité Organizador

cideteq

FI

Laboratorio
Nacional de
Micro y Nano
Fluídica

CONSEJO ZACATECANO DE
CIENCIA, TECNOLOGÍA
E INNOVACIÓN

CICY

EDUCACIÓN
SECRETARÍA DE EDUCACIÓN PÚBLICA

TECNOLÓGICO NACIONAL DE MÉXICO

Sociedad Mexicana de Ciencia y Tecnología de Membranas, A.C.

EL TECNOLÓGICO NACIONAL DE MÉXICO
A TRAVÉS DEL INSTITUTO TECNOLÓGICO DE CHETUMAL

OTORGA LA PRESENTE

CONSTANCIA

A

M.E.Q. ALEJANDRA MARTÍNEZ LÁZARO

Por haber fungido como moderadora durante el X Congreso Anual de la Sociedad Mexicana de Ciencia y Tecnología de Membranas, A.C.

CHETUMAL, QUINTANA ROO, OCTUBRE 2021

DRA. JANET LEDESMA GARCÍA
PRESIDENTA DE LA SOCIEDAD MEXICANA DE CIENCIA Y TECNOLOGÍA DE MEMBRANAS, A.C.

ING. MARIO VICENTE GONZÁLEZ ROBLES
DIRECTOR

DRA. MAYRA POLETT GURROLA
PRESIDENTA DEL COMITÉ ORGANIZADOR

cideteq

COQCYT
CONSEJO QUINTANARROENSE DE CIENCIA Y TECNOLOGÍA

Laboratorio Nacional de Micro y Nano Fluídica

CICY

X CONGRESO ANUAL
21 y 22 de octubre del 2021.
Chetumal, Quintana Roo, México.

MINISTERIO
DE CIENCIA
E INNOVACIÓN

CSIC
CONSEJO SUPERIOR DE INVESTIGACIONES CIENTÍFICAS

Dirección del Departamento de Postgrado y Especialización

Dña. Alejandra Martínez Lazaro

Con ID: G35880073

Ha realizado el curso:
Síntesis, Caracterización y Aplicaciones de Materiales de Carbono organizado por el Instituto de Ciencia y Tecnología del Carbono (INCAR) de la Agencia Estatal Consejo Superior de Investigaciones Científicas (CSIC) con una duración de 20 horas, durante los días 9 de mayo de 2022 al 13 de mayo de 2022, y en el cual ha alcanzado el grado de suficiencia establecido.

Madrid, a 13 de mayo de 2022

La Dirección,

La Dirección del Curso,

Carmen Simón Mateo

FIRMANTE(1) : MARIA MERCEDES DIAZ SOMOANO | FECHA : 06/05/2022 09:27
FIRMANTE(2) : FABIAN SUAREZ GARCIA | FECHA : 09/05/2022 08:49
FIRMANTE(3) : FERNANDO RUBIERA GONZALEZ | FECHA : 10/05/2022 17:14
FIRMANTE(4) : M.CARMEN SIMON MATEO | FECHA : 13/05/2022 13:14 | Sin acción específica

Electrochimica Acta 463 (2023) 142851

Contents lists available at ScienceDirect

Electrochimica Acta

journal homepage: www.journals.elsevier.com/electrochimica-acta

Three-dimensionally ordered macroporous trimetallic spinel for anion exchange membrane water electrolysis

Angela Caprì [a,1], Alejandra Martínez-Lázaro [b,1], José Béjar [c], Irene Gatto [a], Lorena Álvarez-Contreras [c], Mayra Polett Gurrola [d], Janet Ledesma-García [b], Vincenzo Baglio [a,*], Luis Gerardo Arriaga [e,*]

[a] Institute for Advanced Energy Technologies "Nicola Giordano" - CNR-ITAE, Via S. Lucia sopra Contesse 5 -, Messina 98126, Italy
[b] División de Investigación y Posgrado, Facultad de Ingeniería, Universidad Autónoma de Querétaro, Santiago de Querétaro 76010, Mexico
[c] Centro de Investigación en Materiales Avanzados S. C., Complejo Industrial Chihuahua, Chihuahua, Chihuahua, CP 31136, México
[d] Tecnológico Nacional de México/ Instituto Tecnológico de Chetumal. Av. Insurgentes 330, David Gustavo Gutiérrez, Chetumal, Quintana Roo 77013, México
[e] Centro de Investigación y Desarrollo Tecnológico en Electroquímica, Santiago de Querétaro 76703, México

ARTICLE INFO

Keywords:
Trimetallic spinel catalyst
Electrolyser
Anionic exchange membrane
Oxygen evolution reaction
Hydrogen production

ABSTRACT

Here, the synthesis of a $Ni_{0.5}Mn_{0.5}Co_2O_4$ trimetallic catalyst with a spinel structure and three-dimensionally ordered macroporous (3DOM) morphology is reported. A polymethylmethacrylate (PMMA) template, characterized by spheres with an average diameter of 160 nm, is used in the preparation procedure.

The material is investigated by X-ray diffraction, transmission and scanning electron microscopy analyzes to corroborate the incorporation of Mn and Ni into the Co_3O_4 crystal structure and the formation of the 3DOM morphology, respectively. Furthermore, the sample is evaluated as an oxygen evolution reaction catalyst in an electrolyzer based on an anion exchange membrane (Fumasep® FAA3-50 from FuMaTech) as the electrolyte in different conditions. The performance is compared to that obtained using benchmarked IrO_2 electrocatalysts. The maximum current density achieved with the developed catalyst is 2.5 A cm^{-2} at 2.2 V, higher than that obtained with IrO_2 (2 A cm^{-2} at 2.2 V). Proper stability of 150 h is recorded for the cell based on the trimetallic catalyst.

1. Introduction

Hydrogen is a substitute for fossil fuels, since it affords pathways to expand the production of renewable energy to meet the growing energy demand [1–3]. The anion exchange membrane water electrolysis (AEMWE) process is considered as a novel generation of green hydrogen production method, with the advantages of using non-noble metal oxide electrocatalysts and cheap membranes as electrolytes and separators [4–8]. The oxygen evolution reaction (OER), occurring at the anode, is the rate-determining step of the water splitting process [9]. Therefore, the research is focused on identify the appropriate catalysts to increase the reaction rate for the oxygen evolution and improve the stability. The activity of this reaction is controlled by the electronic structure of the active sites of the catalyst and the metal-oxygen (M-O) bond; since the reaction takes place at the electrode-electrolyte interface, the possible candidates as electrocatalysts for OER must comply with a high specificity [10], high surface area and good electrical conductivity [11–14]. The current benchmark electrocatalyst for OER applications is based on precious metals (Ir) and their oxides (IrO_2) thanks to their high catalytic activity, low overpotential and good chemical stability in basic and acid environment [15,16], however, these precious metal catalysts are expensive and scarce, limiting large-scale and commercial applications [17,18]. On the other hand, layered double hydroxides (LDHs), oxyhydroxides, and non-Platinum Group Metal (PGM) electrocatalysts are used as OER electrocatalysts for AEMWE [11,19–21] this has given a tremendous boost to interest in water electrolyzers that use anion exchange membranes [66,67].

There are perovskite-based electrocatalysts that have attracted significant attention as double-layered perovskites ($A_2B_2O_{6-\delta}$), perovskites with Ruddlesden - Popper (RP) phases ($A_{n+2}B_nO3_{n+1}$) and single-layered perovskites ($ABO_{3-\delta}$), where larger A-site cation is a rare-earth or alkaline earth element and smaller B-site cation is a transition

---

[*] Corresponding authors.
E-mail addresses: vincenzo.baglio@itae.cnr.it (V. Baglio), larriaga@cideteq.mx (L.G. Arriaga).
[1] These authors contributed equally to the work.

https://doi.org/10.1016/j.electacta.2023.142851
Received 28 December 2022; Received in revised form 22 May 2023; Accepted 6 July 2023

metal element [22–25]. As another important alternative to precious materials and within the oxides and (oxy)hydroxides, there are those that contain metals of the first transition period, which have been studied as OER electrocatalysts in alkaline medium [26–29]. The use of spinel-type Ni [30], Mn [28], and Co [31] based metal oxides as OER electrocatalysts in alkaline media has recently been reported. In the present work, a trimetallic catalyst ($Ni_{0.5}Mn_{0.5}Co_2O_4$) with a spinel structure and three–dimensionally ordered macroporous (3DOM) morphology, obtained using a poly–methylmethacrylate (PMMA) template made of spheres with an average diameter of 160 nm, is reported [32]. This material was already synthesized and used as a bifunctional catalyst for oxygen reduction and evolution reactions in Zn-air batteries [32]. It showed good reversibility and proper OER activity in half-cell configuration [32]. For this reason, the catalyst was synthesized again, physicochemically characterized by different techniques and evaluated in an electrolyser based on an anion exchange membrane (FAA3-50 from FuMaTech) as the electrolyte in different conditions. Additionally, the performance was compared to that obtained using a benchmark IrO_2 electrocatalyst.

2. Experimental

2.1. Synthesis of 3DOM trimetallic spinel $Ni_{0.5}Mn_{0.5}Co_2O_4$

The 3DOM trimetallic spinel catalysts were prepared by using the colloidal crystal template (CCT) method as reported elsewhere [32]. This method uses PMMA microspheres that act as a template for the 3DOM material. Briefly, the 3DOM trimetallic spinel was prepared as follows: 1 g of citric acid (Sigma–Aldrich, ≥ 99.5%) was solubilized in 20 mL of methanol (Sigma–Aldrich, ≥ 99.9%) and stirred for 1 h. Then, the proper amounts of cobalt nitrate hexahydrate (Sigma–Aldrich, ≥ 98%), nickel nitrate hexahydrate (Sigma–Aldrich, ≥ 97%) and manganese nitrate tetrahydrate (Sigma–Aldrich, ≥ 97%) were dissolved into the methanol solution and maintained under magnetic stirring at 35 °C for 4 h. The total metal ion concentration was 1 mol L^{-1}. The template impregnation procedure was carried out by vacuum filtration as follows: 3 mL of precursor solution was deposited on a piece of CCT under vacuum for 5 min; this passage was repeated six times. Then, a vacuum was applied for 2 h to eliminate any excess metal solution, before drying the sample at 50 °C for 24 h in an air atmosphere. To eliminate the template, and obtain the 3DOM structure formation, the sample was thermally treated in a tube furnace. At first, the sample was calcined using an N_2 flow at 90 mL min^{-1} and a temperature ramp of 1 °C min^{-1} until reaching 310 °C (for 3 h). Then, the atmosphere was changed from N_2 to air (at 90 ml min^{-1}) for 1 h. Finally, the temperature was increased to 400 °C with a temperature ramp of 1 °C min^{-1} and maintained for 4 h.

2.2. Physicochemical measurements

The 3DOM catalyst was characterized physicochemically to better understand its structure, morphology and surface properties. The X-ray diffractometer Bruker D8 Advance diffractometer was used to analyze the crystalline structure. The morphology was investigated by using field–emission scanning electron microscopy (FE-SEM, JEOL JSM–7401F microscope), and a high–resolution transmission electron microscope (HR-TEM, JEM–2200FS microscope) equipped with a Bruker EDX detector to perform the elemental mapping. The images were analyzed by using ImageJ software.

The surface characteristics of the catalysts were analyzed by X-ray photoelectron spectroscopy technique, using a Thermo Scientific Escalab 250 Xi XPS apparatus. BET analysis were performed using N_2 adsorption/desorption isotherms employing a Quantachrome ® S–BET Autosorb iQ2.

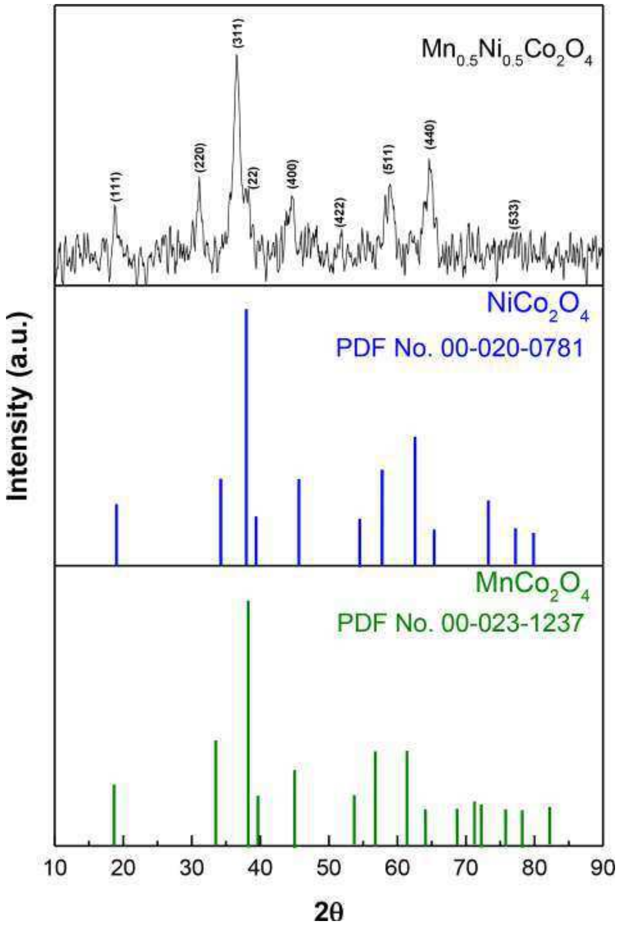

Fig. 1. XRD pattern of the trimetallic catalyst, together with the reference cards of $NiCo_2O_4$ and $MnCo_2O_4$.

2.3. Electrolyzer electrochemical measurements

For the electrochemical characterization in an electrolyzer, cathode electrodes were realized by using a spray coating technique. The catalyst ink, obtained by mixing in an ultrasonic ice bath a commercial 40% wt. Platinum on carbon (Alfa Aesar) and a 20 wt.% of FAA3 ionomer, was deposited onto a Sigracet 25-BC Gas Diffusion Layer (SGL) with a Pt loading of 0.5 mg cm^{-2}, as reported elsewhere [33].

For the anodes, the catalytic ink, consisting of a mixing of 3DOM catalyst and a 20 wt.% of FAA3 ionomer, was directly sprayed on the FAA3-50 membrane, by maintaining a catalyst loading of 3 mg cm^{-2}. Before the electrochemical test, anodes, cathodes and membranes were exchanged in a 1 M KOH solution for 1 h at room temperature. The electrochemical tests were performed in a single-cell configuration with an active area of 5 cm^2. A temperature range between 30 and 60 °C was investigated. A 1 M KOH solution was supplied during the test to the anode compartment (flow rate 5 ml min^{-1}), during the electrochemical experiments. The J-V curves, carried out at a scan rate of 5 mV s^{-1}, and the electrochemical impedance spectroscopy (EIS) measurements at a fixed cell voltage of 1.8 V in a frequency range 10 kHz - 100 mHz were performed by using a potentiostat-galvanostat device PGSTAT302N equipped with an FRA module (Autolab). A chronoamperometry test at 2 V was carried out, feeding a 1 M KOH solution.

3. Results and discussion

3.1. Physicochemical measurements

The X-ray diffraction (XRD) analysis has been carried out to get

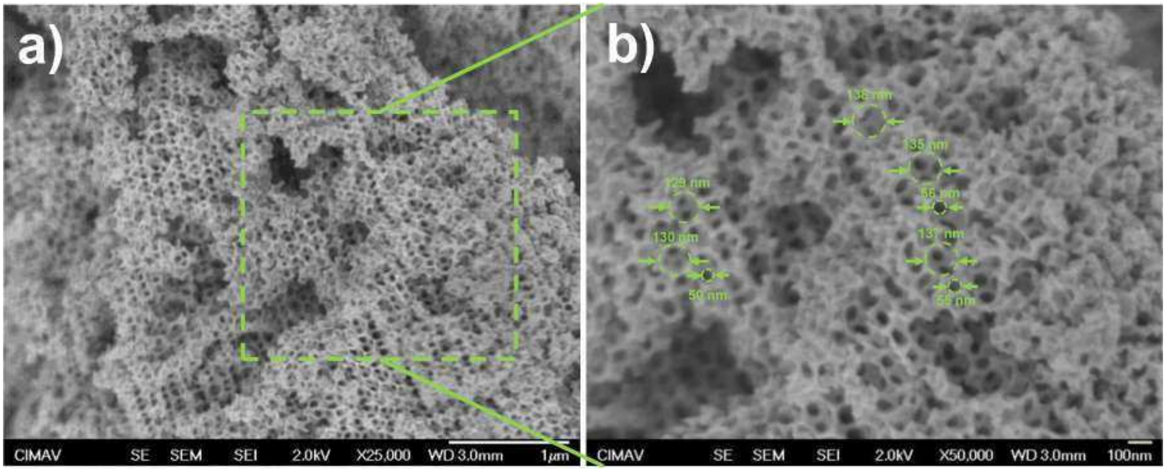

Fig. 2. SEM images of 3DOM catalyst: a) x25000 and b) x50000 magnifications.

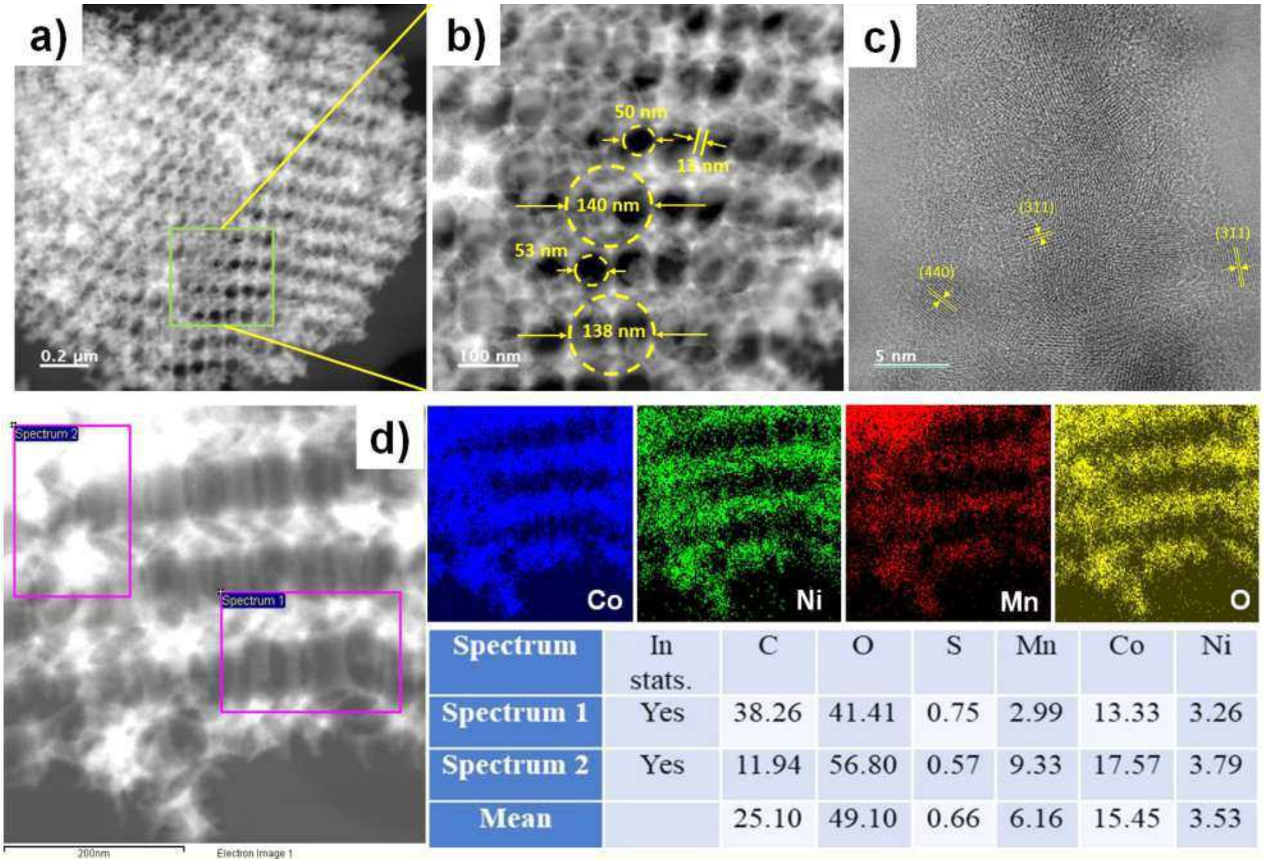

Spectrum	In stats.	C	O	S	Mn	Co	Ni
Spectrum 1	Yes	38.26	41.41	0.75	2.99	13.33	3.26
Spectrum 2	Yes	11.94	56.80	0.57	9.33	17.57	3.79
Mean		25.10	49.10	0.66	6.16	15.45	3.53

Fig. 3. (a–d) HR-TEM images of 3DOM $Ni_{0.5}Mn_{0.5}Co_2O_4$ and mapping for the elements Co, Ni, Mn, O.

information on the crystallographic structure of the catalyst (Fig. 1). The signals related to the (111), (220), (311), (222), (400), (422), (511), (440), and (533) planes of the cubic structures of $NiCo_2O_4$ and $MnCo_2O_4$ spinels (PDF No. 77–0471 and 74–2120, respectively) are recognizable. No other peaks were found during the analysis, meaning that $NiCo_2O_4$ and $MnCo_2O_4$ crystals coexist in a trimetallic spinel structure.

A crystallite size of 5.0 nm was calculated by using the Debye–-Scherrer equation. Scanning Electron Microscopy (SEM) and Transmission Electron Microscopy (TEM) analyzes were performed, to investigate the morphological and microstructural properties. The SEM images clearly show the 3D morphology of the catalyst, at x25000 (Fig. 2a) and x50000 (Fig. 2b), where a porously ordered material can be observed by a connected network of uniformly sized pores characteristic of a 3DOM material. The SEM analysis allows us to appreciate macropore sizes between 130-138 nm, this pore is obtained thanks to the PMMA template used and removed during the synthesis process. Within the macropores, a second smaller pore between 50-56 nm in diameter can be observed.

A deep morphology analysis was complemented with HR-TEM micrographs, which corroborated the 3DOM structure (Fig. 3a–d). The pore size was also measured through TEM micrographs for better precision, where it is verified that the largest pores are about 130 ± 10 nm

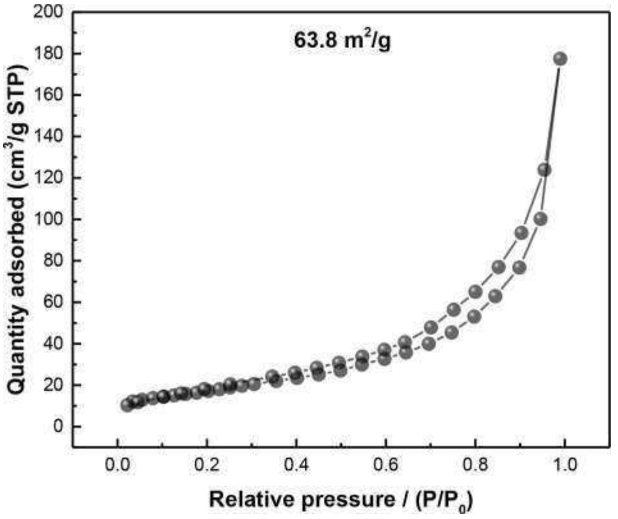

Fig. 4. BET analysis of the $Ni_{0.5}Mn_{0.5}Co_2O_4$ catalyst.

and the smallest ones around 50 ± 5, while the thickness of the wall is 13 ± 2 nm. Elemental mapping of the 3DOM trimetallic spinel indicated that there was a distribution between Ni, Mn and Co elements in the 3DOM material. In addition, the elemental analysis allowed calculating the dispersion of the elements on the catalyst surface that can be defined as $Ni_{0.5}Mn_{0.5}Co_2O_4$. To analyze the surface area and porosity of the catalyst, a BET analysis was carried out using N_2 adsorption/desorption isotherms (Fig. 4). The results suggest a mixture of types 2 and 4 isotherms, confirming the interconnected network of pores observed by HR-TEM. By considering that there is no limiting adsorption at high P/Po (range of 0.7–1), it is possible to assume that the catalyst is a mesoporous material. The BET data indicate a surface area of 63.8 $m^2\ g^{-1}$ and a pore volume of 0.23 $m^3\ g^{-1}$. This value of the surface area, similar to the value obtained in a previous paper [32], was correlated to the diameter (160 nm) of the PMMA spheres used as templates.

An X-ray photoelectron spectroscopy (XPS) analysis of the trimetallic spinel 3DOM $Ni_{0.5}Mn_{0.5}Co_2O_4$ (Fig. 5) was carried out to know the chemical composition and the oxidation states of the elements present in the sample, as is shown in Table 1. The high-resolution spectrum of Co 2p is presented in Fig. 5b, showing the signals of Co $2p_{3/2}$ at the binding energy of 780.6 eV and Co $2p_{1/2}$ at 792.65 eV, which were deconvoluted, giving the peaks at 780.4 eV and 795.2 corresponding to Co^{2+}, and those located at 782.5 eV and 797.2 refer to Co^{3+} [34,35].

In Fig. 5c, the high-resolution spectrum for Mn 2p is observed, where the peak of Mn $2p_{1/2}$ is located at 653.8 eV and the peak of Mn $2p_{3/2}$ at 642.5 eV. The deconvolutions of these peaks are positioned at 639.5 and 653.4 eV for Mn^{2+}, while they are at 642.3 and 654.7 eV for Mn^{3+}. Peaks at 645.32 and 656.4 eV are assigned to Mn^{4+} [35–37].

The spectrum of Ni 2p is observed in Fig. 5d, having orbitals Ni $2p_{3/2}$ at 855 eV and Ni $2p_{1/2}$ at 872.6 eV. After deconvolution, the peaks at 855.5 eV and 872.9 eV correspond to Ni^{2+}, while those located at 859.2 and 874.6 eV refer to Ni^{3+} [38,39]. Molar proportions such as

Table 1
Quantitative analysis by XPS of 3DOM $Ni_{0.5}Mn_{0.5}Co_2O_4$.

Name	Deconvolution	Position (eV)	Atomic %	Weight %
O 1s	O-Ni/O-Co/O-Mn	530.5	38.51	48.18
	C=O	532.11		31.90
	C-OH/C-O-C	533.9		19.81
Co 2p	Co^{2+}	780.4	14.72	73.2
	Co^{3+}	782.5		26.38
Ni 2p	Ni^{2+}	855.16	5.06	76.54
	Ni^{3+}	859.2		24.42
Mn 2p	Mn^{2+}	639.5	7.17	12.45
	Mn^{3+}	642.3		58.83
	Mn^{4+}	645.32		28.72

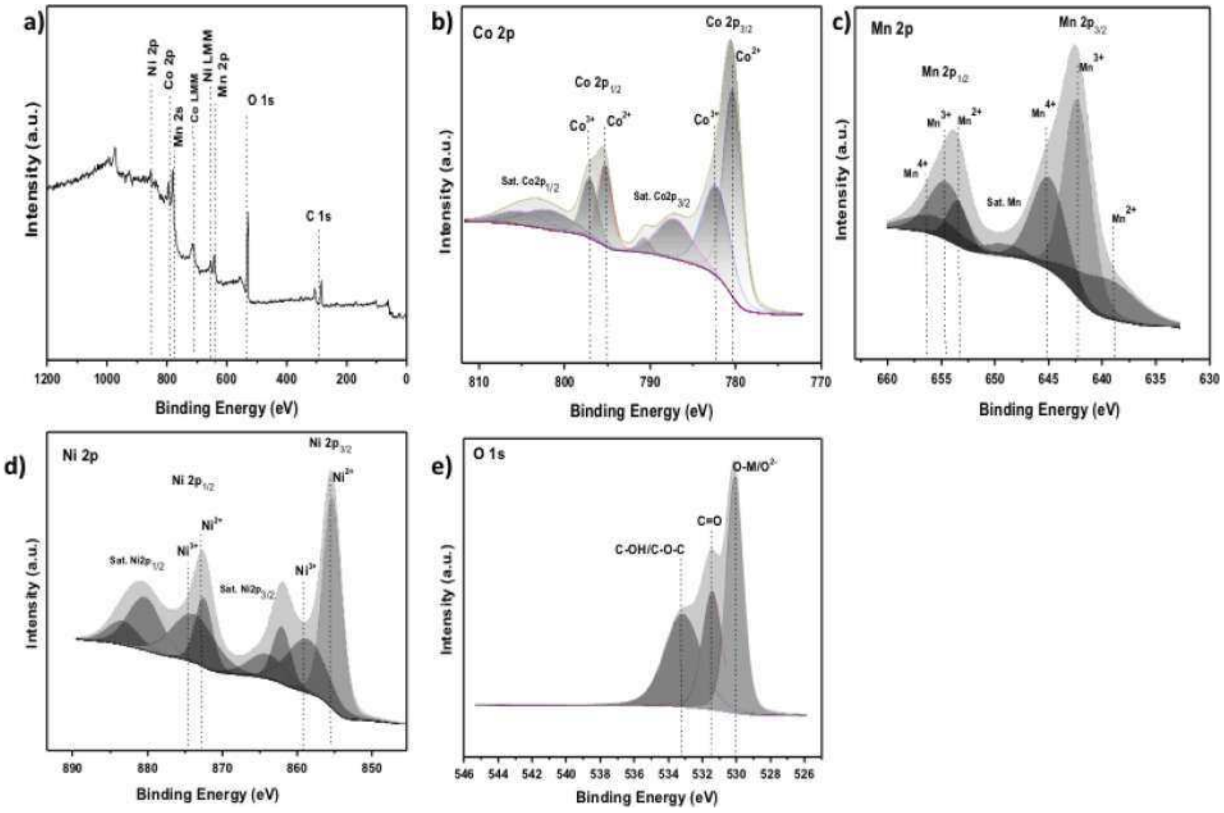

Fig. 5. (a) Survey XPS spectrum for 3DOM $Ni_{0.5}Mn_{0.5}Co_2O_4$ catalyst; high-resolution spectra of the (b) Co 2p, (c) Mn 2p, (d) Ni 2p, and (e) O 1s signals.

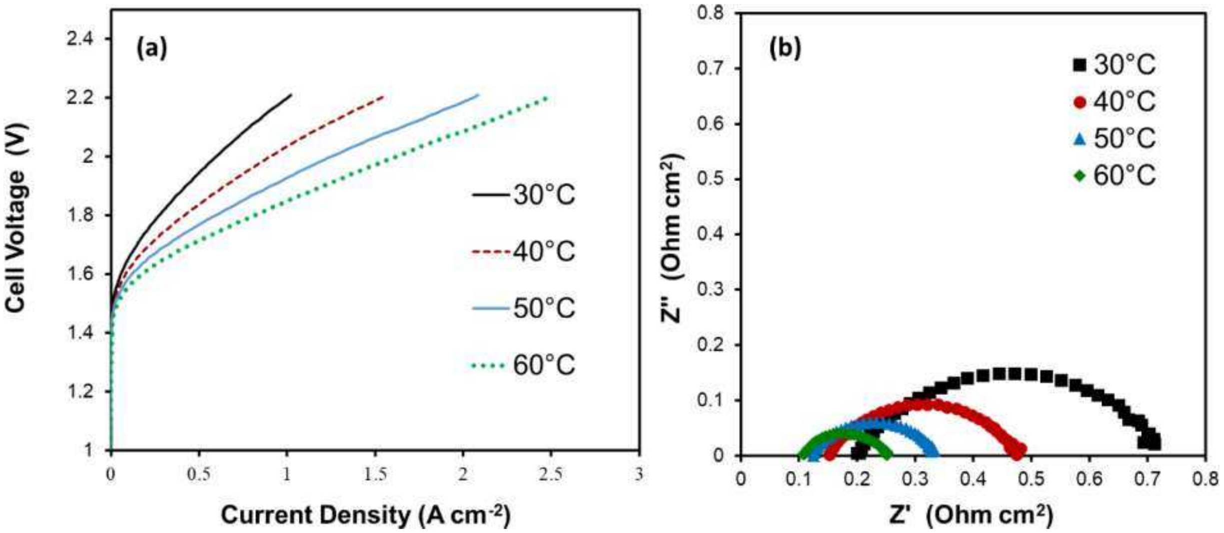

Fig. 6. (a) Performance at different temperatures (from 30 to 60 °C) for the cell equipped with c at the anode, in 1 M KOH as supporting electrolyte and (b) EIS for $Ni_{0.5}Mn_{0.5}Co_2O_4$-based cell at 1.8 V.

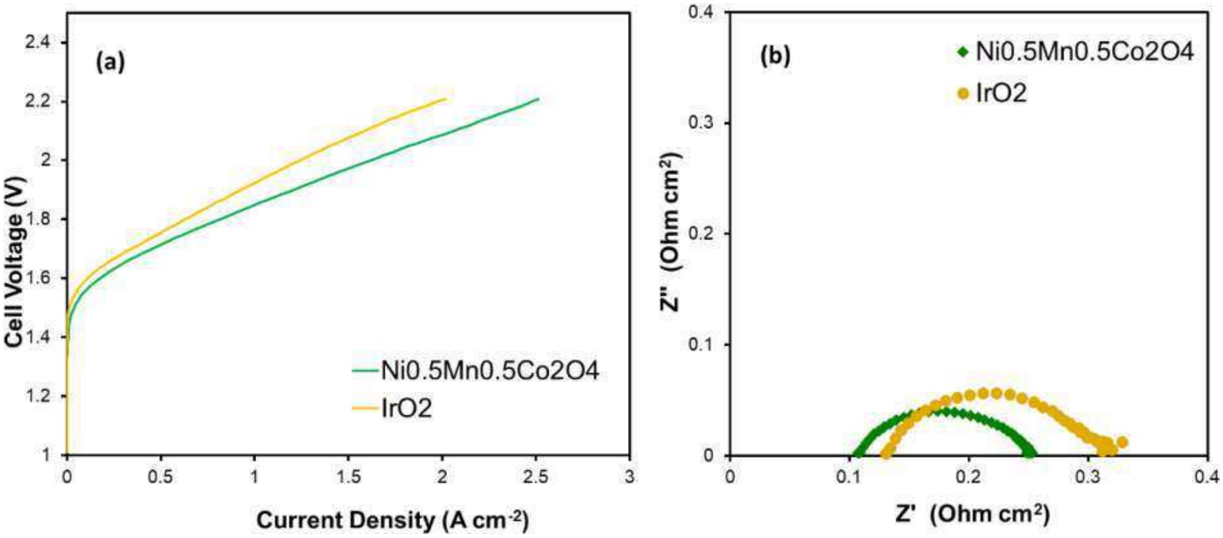

Fig. 7. (a) Performance and (b) EIS (at 1.8 V) data comparison at 60 °C for the cells equipped with $Ni_{0.5}Mn_{0.5}Co_2O_4$ and commercial IrO_2 at the anode, in 1 M KOH as supporting electrolyte.

$Ni_{0.52}Mn_{0.48}$ were obtained.

The high-resolution spectrum of O 1s presents three peaks of deconvolution, as shown in Fig. 5e. The first one at 530.1 eV is attributed to the O^{2-} anions generated by the metal-oxygen bonds of the structure of the spinel, where Co-O, Ni-O and Mn-O bonds are present in different oxidation states and are typical of the synthesis of the material. The second peak is at 531.4 eV, which is associated with oxygen ions on the surface, such as C=O bonds. The third peak has a signal at 533.2 eV and is characteristic of OH groups and oxygen vacancies [38].

3.2. Electrolyser electrochemical measurements

The 3DOM trimetallic spinel was mounted at the anode of an electrolysis cell to evaluate the performance for the oxygen evolution reaction at different temperatures (30–60 °C). The J-V curves in Fig. 6a show an improvement in performance as the temperature increases. Passing from 30–60 °C, a three-time growth in the maximum current density was obtained (0.85 A cm^{-2} vs. 2.5 A cm^{-2} at 2.2 V). This is due to the enhanced kinetics of the reactions occurring at the electrodes and to the higher ionic conductivity of the anionic membrane favored by the temperature, as observed in Fig. 6b. The Nyquist plot obtained at 1.8 V shows a charge transfer resistance (R_{ct}) and series resistance (R_s) reduction at higher temperatures. R_s, corresponding to the high-frequency intercept of the semicircles on the x-axis in the Nyquist plots, is related to the ohmic resistance and decreases at increased temperatures due to the higher ion mobility. Instead, R_{ct} is connected with the electrode-electrolyte interfacial properties indicating more favourable reaction kinetics (the semicircles become smaller). Both oxygen and hydrogen evolution reactions are here considered resulting in two overlapping semicircles in the Nyquist plots, although not clearly distinguished. A small semicircle (not easy to see) is occurring at high frequencies and is characterized by small resistance (the hydrogen evolution process is a fast reaction on Pt in an alkaline environment). The arc occurring at low frequency and characterized by higher resistance is attributed to the anode (the oxygen evolution is the slowest reaction determining the performance in the electrolysis) [40].

The performance of the developed catalyst was compared under the same operating conditions and loading (3 mg cm^{-2}) with a benchmark

Table 2
Literature survey of cell performance in an AEMWE.

Membrane	Anode	Cathode	Temperature [°C]	Feed	Performance @1.8V and 2V [Acm^{-2}]	Refs.
FAA-3-50	$Ni_{0.5}Mn_{0.5}Co_2O_4$	Pt/C	60	1M KOH	0.85 1.60	This work
FAA-3-50	$NiFe_2O_4$	Pt/C	60	1M KOH	1.43 2.35	[41]
FAA-3-50	Ni-Foam	Ni-Foam	60	10%wt KOH	0.02 0.03	[42]
FAA-3-50	g-CN-CNF-800	Pt/C	60	1M KOH	0.48 0.98	[43]
FAA-3-50	$NiMn_2O_4$/C	Pt/C	50	1M KOH	0.18 0.38	[44]
FAA-3-50	$NiMn_2O_4$/ CNF	Pt/C	50	6M KOH	0.13 -	[45]
Sustainion	$NiFe_2O_4$	NiFeCo	60	1M KOH	0.16 0.94	[46]
Sustainion 37-50	NiFe	NiFeCo	60	1M KOH	0.50 1.75	[12]
FAS-50	$NiFe_2O_4$	NiFeCo	60	1M KOH	0.25 0.90	[12]
Sustainion X37-50	$NiFe_2O_4$	Ni Raney	-	-	0.74 -	[47]
PTFE-Sustainion	$NiFe_2O_4$	Ni Raney	60	1M KOH	0.84 -	[48]
FAA-3-50	$NiFe_2O_4$	NiFeCo	60	1M KOH	0.24 -	[48]
Sustainion	$NiFe_2O_4$	NiFeCo	60	1M KOH	0.51 -	[49]
FAA-3-50	NiFe	Ni	60	1M KOH	0.15 0.6	[50]
Pap-TP-85	$NiFe_2O_4$	Pt black	60	H_2O	0.05 0.19	[51]
FAA-3-50	NiFeOx	Pt/C	50	1M KOH	1 -	[52]
FAA-3PE-30	$Ni_{80}Fe_{20}$	Pt/C	50	1M KOH	0.4 -	[53]
A-201	CuCoOx	Pt/C	50	10%wt K_2CO_3	0.18 0.87	[54]
Chloromethylated PSF (CMPSF)	$Pb_2Ru_2O_{6.5}$	Pt black	50	Water	0.40 0.60	[55]
A901	$CoFe_{0.25}Al_{1.75}O_4$	Pt/C	60	0.1M KOH	0.60 1.05	[56]
FAA-3-PK-130	$Ce_{0.2}MnFe_{1.8}O_4$	Ni 3.5	25	Water	0.3 0.38	[57]
FAA-3-PK-130	$MnFe_2O_4$	Ni 3.5	25	Water	0.025 0.06	[57]
AA-3PE-30	$Ni_{90}Fe_{10}$	Pt/C	50	1M KOH	1.35 -	[58]
AA-3PE-30	$Ni_{90}Fe_{10}$	Pt/C	50	0.1 M KOH	0.9 1.9	[58]
Pap-TP-85	$NiFe_2O_4$	Pt black 2	60	Water	0.05 0.19	[59]
Pap-TP-85	$Ni_{0.5}Co_{0.5}Fe_2O_4$	Pt black	60	Water	0.2 0.5	[59]
HTMA-DAPP	NiFe foam	PtRu/C	60	1M NaOH	5.3 -	[60]
Sustainion X37-50	$NiFe_2O_4$	Ni Raney	60	1M KOH	0.74 -	[61]
Fumapem-3-PE-30	$Ni0.6Co0.2Fe_{0.2}$	Pt/C	50	1M KOH	0.75 1.37	[62]
PiperIon	Ni-Foam	Pt/C	60	1M KOH	0.38 0.87	[63]
PBP	Ni-Foam	Pt/C	60	1M KOH	0.56 1.25	[63]
AQ720A4-Q	NiFeOx	Pt/C	60	1M KOH	0.19 -	[64]
AQ720A4-Q	NiFeOx	Pt/C	90	1M KOH	0.4 0.65	[64]
FAA-3-50	$NiFe_2O_4$	Pt/C	60	1M KOH	1.5 2.5	[65]

IrO_2 commercial catalyst. Linear sweep voltammetry curves are reported in Fig. 7a, together with the Nyquist plots of the two cells in Fig. 7b. Lower performance is observed for the cell based on the noble metal catalyst, together with a higher onset potential for the water-splitting process. Moreover, the maximum current density achieved with the developed catalyst is 2.5 A cm^{-2} at 2.2 V, higher than that obtained with IrO_2 (2 A cm^{-2} at 2.2 V). The EIS spectra comparison, reported in Fig. 7b, highlights both a higher R_s and R_{ct} for the IrO_2-based cell. This effect is a further confirmation of the J-V behavior, in which a lower onset potential and slope are observed for the 3DOM trimetallic catalyst,

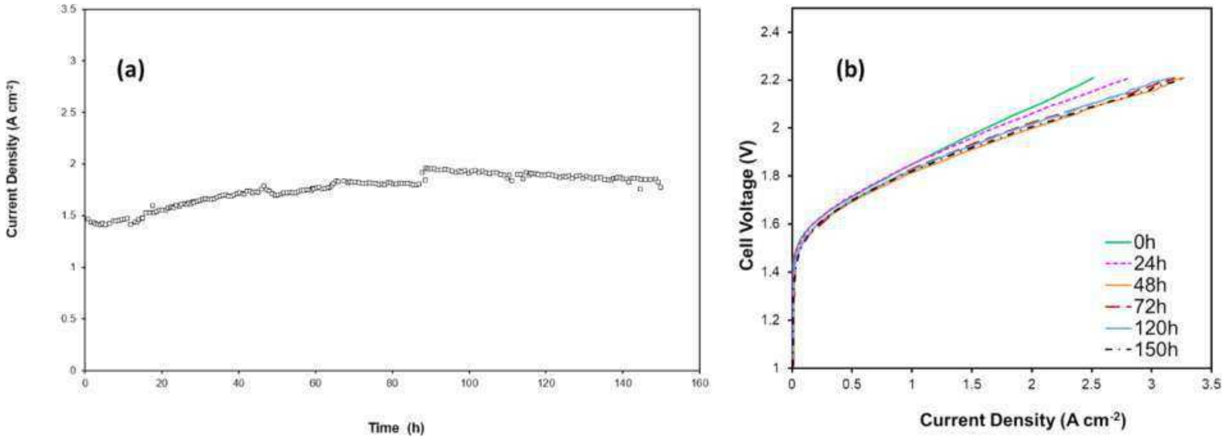

Fig. 8. (a) Chronoamperometric test for the cell equipped with $Ni_{0.5}Mn_{0.5}Co_2O_4$ at 60 °C and 2 V; (b) J-V curves at °C during the time-stability test, feeding 1 M KOH solution as supporting electrolyte.

indicating better catalytic activity and electronic conductivity. The latter aspect needs clarification since both catalysts are good electronic conductors, but most likely the 3DOM morphology favors better interaction with the ionomer compared with low-surface area IrO_2 (crystallite size in the order of 20 nm) resulting in a better interface and lower ohmic constraints. Furthermore, surface characteristics, together with the proper composition, structure, and the number of active sites of the developed catalyst produce a higher catalytic activity.

The performance obtained with this catalyst, although remarkable, is not the highest one compared with others reported in the literature (see Table 2 and Refs. [66,67]); however, it is pointed out that this catalyst presents high reversibility for the two reactions involving oxygen [32]. Accordingly, this catalyst could find a potential use also in Unitized Regenerative Fuel Cells (URFCs).

To study the behavior of the developed catalyst over time, a short stability test at 2 V for 150 h was performed. In Fig. 8a, the chronoamperometric data were reported. Approximately every 24 h, there is a slight increase in the current density correlated to the replacement of the KOH solution, recirculating at the anode side, and to the recorded polarization curves (Fig. 8b). From the results, it appears that the catalyst is highly stable during operation, showing also increased performance (as observed in the J-V curves) with time.

4. Conclusions

The $Ni_{0.5}Mn_{0.5}Co_2O_4$ trimetallic catalyst has been synthesized and characterized by using different techniques, confirming the spinel structure and three-dimensionally ordered macroporous (3DOM) morphology. The catalyst has been tested in an AEM electrolyzer, using commercial membranes and cathode catalysts, to evaluate the activity for the oxygen reduction reaction in a complete device. It showed a performance higher than a benchmark noble metal catalyst and other non-PGM catalysts reported in the literature, with excellent stability with time.

CRediT authorship contribution statement

Angela Caprì: Investigation, Data curation, Writing – original draft. **Alejandra Martínez-Lázaro:** Conceptualization, Methodology, Investigation. **José Béjar:** Investigation. **Irene Gatto:** Conceptualization, Supervision, Writing – review & editing. **Lorena Álvarez-Contreras:** Conceptualization, Investigation, Writing – review & editing. **Mayra Polett Gurrola:** Methodology, Investigation. **Janet Ledesma-García:** Conceptualization, Supervision, Writing – review & editing. **Vincenzo Baglio:** Conceptualization, Supervision, Funding acquisition, Writing – review & editing, Project administration. **Luis Gerardo Arriaga:** Conceptualization, Supervision, Funding acquisition, Writing – review & editing, Project administration.

Declaration of Competing Interest

The authors declare the following financial interests/personal relationships which may be considered as potential competing interests: V. Baglio reports financial support was provided by Italian Ministry MUR.

Acknowledgments

CNR-ITAE authors thank the Italian ministry MUR for funding through the FISR2019 project AMPERE (FISR2019_01294).

References

[1] K. Ayers, N. Danilovic, R. Ouimet, M. Carmo, B. Pivovar, M. Bornstein, Perspectives on low-temperature electrolysis and potential for renewable hydrogen at scale, Annu. Rev. Chem. Biomol. Eng. 10 (2019) 219–239, https://doi.org/10.1146/annurev-chembioeng-060718-030241.

[2] A.Y. Faid, A. Oyarce Barnett, F. Seland, S. Sunde, Highly active nickel-based catalyst for hydrogen evolution in anion exchange membrane electrolysis, Catalysts 8 (2018), https://doi.org/10.3390/catal8120614.

[3] X. Zhang, T. Yu, X. Ma, L. Guo, An efficient multi-agent negotiation algorithm for multi-period photovoltaic array reconfiguration with a hydrogen energy storage system, Energy Convers. Manag. 256 (2022), 115376, https://doi.org/10.1016/j.enconman.2022.115376.

[4] C. Duan, R. Kee, H. Zhu, N. Sullivan, L. Zhu, L. Bian, D. Jennings, R. O'Hayre, Author correction: highly efficient reversible protonic ceramic electrochemical cells for power generation and fuel production, Nat. Energy 5 (2020), https://doi.org/10.1038/s41560-020-0669-7, 729–729.

[5] D. Li, A.R. Motz, C. Bae, C. Fujimoto, G. Yang, F.Y. Zhang, K.E. Ayers, Y.S. Kim, Durability of anion exchange membrane water electrolyzers, Energy Environ. Sci. 14 (2021) 3393–3419, https://doi.org/10.1039/D0EE04086J.

[6] C. Santoro, A. Lavacchi, P. Mustarelli, V. Di Noto, L. Elbaz, D.R. Dekel, F. Jaouen, What is next in anion-exchange membrane water electrolyzers? Bottlenecks, benefits, and future, ChemSusChem 15 (2022), e202200027, https://doi.org/10.1002/cssc.202200027.

[7] J.R. Varcoe, P. Atanassov, D.R. Dekel, A.M. Herring, M.A. Hickner, P.A. Kohl, A. R. Kucernak, W.E. Mustain, K. Nijmeijer, K. Scott, T. Xu, L. Zhuang, Anion-exchange membranes in electrochemical energy systems, Energy Environ. Sci. 7 (2014) 3135–3191, https://doi.org/10.1039/C4EE01303D.

[8] M. Chatenet, B.G. Pollet, D.R. Dekel, F. Dionigi, J. Deseure, P. Millet, R.D. Braatz, M.Z. Bazant, M. Eikerling, I. Staffell, P. Balcombe, Y. Shao-Horn, H. Schäfer, Water electrolysis: from textbook knowledge to the latest scientific strategies and industrial developments, Chem. Soc. Rev. 51 (2022) 4583–4762, https://doi.org/10.1039/D0CS01079K.

[9] C. Li, J.B. Baek, The promise of hydrogen production from alkaline anion exchange membrane electrolyzers, Nano Energy 87 (2021), 106162, https://doi.org/10.1016/j.nanoen.2021.106162.

[10] A. Eftekhari, Tuning the electrocatalysts for oxygen evolution reaction, Mater. Today Energy 5 (2017) 37–57, https://doi.org/10.1016/j.mtener.2017.05.002.

[11] M. David, C. Ocampo-Martínez, R. Sánchez-Peña, Advances in alkaline water electrolyzers: a review, J. Energy Storage 23 (2019) 392–403, https://doi.org/10.1016/j.est.2019.03.001.

[12] J.E. Park, S.Y. Kang, S.H. Oh, J.K. Kim, M.S. Lim, C.Y. Ahn, Y.H. Cho, Y.E. Sung, High-performance anion-exchange membrane water electrolysis, Electrochim. Acta 295 (2019) 99–106, https://doi.org/10.1016/j.electacta.2018.10.143.

[13] M.E.G. Lyons, M.P. Brandon, A comparative study of the oxygen evolution reaction on oxidised nickel, cobalt and iron electrodes in base, J. Electroanal. Chem. 641 (2010) 119–130, https://doi.org/10.1016/j.jelechem.2009.11.024.

[14] D. Xu, M.B. Stevens, M.R. Cosby, S.Z. Oener, A.M. Smith, L.J. Enman, K.E. Ayers, C. B. Capuano, J.N. Renner, N. Danilovic, Y. Li, H. Wang, Q. Zhang, S.W. Boettcher, Earth-abundant oxygen electrocatalysts for alkaline anion-exchange-membrane water electrolysis: effects of catalyst conductivity and comparison with performance in three-electrode cells, ACS Catal. 9 (2019) 7–15, https://doi.org/10.1021/acscatal.8b04001.

[15] X. Wang, X. Wan, X. Qin, C. Chen, X. Qian, Y. Guo, Q. Xu, W.B. Cai, H. Yang, K. Jiang, Electronic structure modulation of RuO_2 by TiO_2 enriched with oxygen vacancies to boost acidic O_2 evolution, ACS Catal. 12 (2022) 9437–9445, https://doi.org/10.1021/acscatal.2c01944.

[16] H. Zhu, Z. Zhu, J. Hao, S. Sun, S. Lu, C. Wang, P. Ma, W. Dong, M. Du, High-entropy alloy stabilized active Ir for highly efficient acidic oxygen evolution, Chem. Eng. J. 431 (2022), 133251, https://doi.org/10.1016/j.cej.2021.133251.

[17] X. Xie, L. Du, L. Yan, S. Park, Y. Qiu, J. Sokolowski, W. Wang, Y. Shao, Oxygen evolution reaction in alkaline environment: material challenges and solutions, Adv. Funct. Mater. 32 (2022), 2110036, https://doi.org/10.1002/adfm.202110036.

[18] W. Li, H. Zhang, M. Hong, L. Zhang, X. Feng, M. Shi, W. Hu, S. Mu, Defective RuO_2/TiO_2 nano-heterostructure advances hydrogen production by electrochemical water splitting, Chem. Eng. J. 431 (2022), 134072, https://doi.org/10.1016/j.cej.2021.134072.

[19] X. Luo, P. Ji, P. Wang, X. Tan, L. Chen, S. Mu, Spherical Ni_3S_2/Fe-NiPx magic cube with ultrahigh water/seawater oxidation efficiency, Adv. Sci. 9 (2022), 2104846, https://doi.org/10.1002/advs.202104846.

[20] S. Wan, X. Wang, G. Zhang, Y. Wang, J. Chen, Q. Li, Y. Zhang, L. Chen, X. Wang, G. Meng, K. Jiang, Electrochemically activated Ni-Fe oxyhydroxide for mimic saline water oxidation, ACS Sustain. Chem. Eng. 10 (2022) 11232–11241, https://doi.org/10.1021/acssuschemeng.2c02923.

[21] A. Serov, K. Kovnir, M. Shatruk, Y.V. Kolen'ko, Critical review of platinum group metal-free materials for water electrolysis: transition from the laboratory to the market : earth-abundant borides and phosphides as catalysts for sustainable hydrogen production, Johnson Matthey Technol. Rev. 65 (2021) 207–226.

[22] C. Alegre, E. Modica, M. Rodlert-Bacilieri, F.C. Mornaghini, A.S. Aricò, V. Baglio, Enhanced durability of a cost-effective perovskite-carbon catalyst for the oxygen evolution and reduction reactions in alkaline environment, Int. J. Hydrog. Energy 42 (2017) 28063–28069, https://doi.org/10.1016/j.ijhydene.2017.03.216.

[23] Z.W. Gao, J.Y. Liu, X.M. Chen, X.L. Zheng, J. Mao, H. Liu, T. Ma, L. Li, W.C. Wang, X.W. Du, Engineering NiO/NiFe LDH intersection to bypass scaling relationship for oxygen evolution reaction via dynamic tridimensional adsorption of intermediates, Adv. Mater. 31 (2019), 1804769, https://doi.org/10.1002/adma.201804769.

[24] B. Hua, Y.Q. Zhang, N. Yan, M. Li, Y.F. Sun, J. Chen, J. Li, J.L. Luo, The excellence of both worlds: developing effective double perovskite oxide catalyst of oxygen reduction reaction for room and elevated temperature applications, Adv. Funct. Mater. 26 (2016) 4106–4112, https://doi.org/10.1002/adfm.201600339.

[25] M.E. Abrishami, M. Risch, J. Scholz, V. Roddatis, N. Osterthun, C. Jooss, Oxygen evolution at manganite perovskite ruddlesden-popper type particles: trends of activity on structure, valence and covalence, Materials 9 (2016), https://doi.org/10.3390/ma9110921.

[26] F. Lu, M. Zhou, Y. Zhou, X. Zeng, First-row transition metal based catalysts for the oxygen evolution reaction under alkaline conditions: basic principles and recent advances, Small 13 (2017), 1701931, https://doi.org/10.1002/smll.201701931.

[27] X. Wang, H. Luo, H. Yang, P.J. Sebastian, S.A. Gamboa, Oxygen catalytic evolution reaction on nickel hydroxide electrode modified by electroless cobalt coating, Int. J. Hydrog. Energy 29 (2004) 967–972, https://doi.org/10.1016/j.ijhydene.2003.05.001.

[28] H. Sim, J. Lee, T. Yu, B. Lim, Manganese oxide with different composition and morphology as electrocatalyst for oxygen evolution reaction, Korean J. Chem. Eng. 35 (2018) 257–262, https://doi.org/10.1007/s11814-017-0247-2.

[29] F. Song, L. Bai, A. Moysiadou, S. Lee, C. Hu, L. Liardet, X. Hu, Transition metal oxides as electrocatalysts for the oxygen evolution reaction in alkaline solutions: an application-inspired renaissance, J. Am. Chem. Soc. 140 (2018) 7748–7759, https://doi.org/10.1021/jacs.8b04546.

[30] R. Subbaraman, D. Tripkovic, K.C. Chang, D. Strmcnik, A.P. Paulikas, P. Hirunsit, M. Chan, J. Greeley, V. Stamenkovic, N.M. Markovic, Trends in activity for the water electrolyser reactions on 3d M(Ni,Co,Fe,Mn) hydr(oxy)oxide catalysts, Nat. Mater. 11 (2012) 550–557, https://doi.org/10.1038/nmat3313.

[31] C. Schoeberl, M. Manolova, R. Freudenberger, Sol-gel-deposited cobalt and nickel oxide as an oxygen evolution catalyst in alkaline media, Int. J. Hydrog. Energy 40 (2015) 11773–11778, https://doi.org/10.1016/j.ijhydene.2015.05.046.

[32] J. Béjar, L. Álvarez−Contreras, F. Espinosa−Magaña, J. Ledesma−García, N. Arjona, L.G. Arriaga, Zn−air battery operated with a 3DOM trimetallic spinel ($Mn_{0.5}Ni_{0.5}Co_2O_4$) as the oxygen electrode, Electrochim. Acta 391 (2021), 138900, https://doi.org/10.1016/j.electacta.2021.138900.

[33] A. Carbone, R. Pedicini, I. Gatto, A. Saccà, A. Patti, G. Bella, M. Cordaro, Development of polymeric membranes based on quaternized polysulfones for AMFC applications, Polymers 12 (2020), https://doi.org/10.3390/polym12020283.

[34] R. BoopathiRaja, M. Parthibavarman, Hetero-structure arrays of $MnCo_2O_4$ nanoflakes@nanowires grown on Ni foam: design, fabrication and applications in electrochemical energy storage, J. Alloy. Compd. 811 (2019), 152084, https://doi.org/10.1016/j.jallcom.2019.152084.

[35] K. Zeng, W. Li, Y. Zhou, Z. Sun, C. Lu, J. Yan, J.-H. Choi, R. Yang, Multilayer hollow $MnCo_2O_4$ microsphere with oxygen vacancies as efficient electrocatalyst for oxygen evolution reaction, Chem. Eng. J. 421 (2021), 127831, https://doi.org/10.1016/j.cej.2020.127831.

[36] G. Fu, Z. Liu, J. Zhang, J. Wu, L. Xu, D. Sun, J. Zhang, Y. Tang, P. Chen, Spinel $MnCo_2O_4$ nanoparticles cross-linked with two-dimensional porous carbon nanosheets as a high-efficiency oxygen reduction electrocatalyst, Nano Res. 9 (2016) 2110–2122, https://doi.org/10.1007/s12274-016-1101-2.

[37] K.J. Kim, J.W. Heo, Electronic structure and optical properties of inverse-spinel $MnCo_2O_4$ thin films, J. Korean Phys. Soc. 60 (2012) 1376–1380, https://doi.org/10.3938/jkps.60.1376.

[38] L. Zeng, T.S. Zhao, R.H. Zhang, J.B. Xu, $NiCo_2O_4$ nanowires@MnOx nanoflakes supported on stainless steel mesh with superior electrocatalytic performance for anion exchange membrane water splitting, Electrochem. Commun. 87 (2018) 66–70, https://doi.org/10.1016/j.elecom.2018.01.002.

[39] X. Chang, W. Li, Y. Liu, M. He, X. Zheng, X. Lv, Z. Ren, Synthesis and characterization of $NiCo_2O_4$ nanospheres/nitrogen-doped graphene composites with enhanced electrochemical performance, J. Alloy. Compd. 784 (2019) 293–300, https://doi.org/10.1016/j.jallcom.2019.01.036.

[40] S. Siracusano, S. Trocino, N. Briguglio, V. Baglio, A.S. Aricò, Electrochemical impedance spectroscopy as a diagnostic tool in polymer electrolyte membrane electrolysis, Materials 11 (2018), https://doi.org/10.3390/ma11081368.

[41] A. Martinez-Lazaro, A. Caprì, I. Gatto, J. Ledesma-García, N. Rey-Raap, A. Arenillas, F.I. Espinosa-Lagunes, V. Baglio, L.G. Arriaga, $NiFe_2O_4$ hierarchical nanoparticles as electrocatalyst for anion exchange membrane water electrolysis, J. Power Sources 556 (2023), 232417, https://doi.org/10.1016/j.jpowsour.2022.232417.

[42] P. Balasubramanian, S.B. He, A. Jansirani, H.H. Deng, H.P. Peng, X.H. Xia, W. Chen, Engineering of oxygen vacancies regulated core-shell N-doped carbon@$NiFe_2O_4$ nanospheres: A superior bifunctional electrocatalyst for boosting the kinetics of oxygen and hydrogen evaluation reactions, Chem. Eng. J. 405 (2021), 126732, https://doi.org/10.1016/j.cej.2020.126732.

[43] M.M. Titirici, M. Antonietti, A. Thomas, A generalized synthesis of metal oxide hollow spheres using a hydrothermal approach, Chem. Mater. 18 (2006) 3808–3812, https://doi.org/10.1021/cm052768u.

[44] M. Hua, L. Xu, F. Cui, J. Lian, Y. Huang, J. Bao, J. Qiu, Y. Xu, H. Xu, Y. Zhao, H. Li, Hexamethylenetetramine-assisted hydrothermal synthesis of octahedral nickel ferrite oxide nanocrystallines with excellent supercapacitive performance, J. Mater. Sci. 53 (2018) 7621–7636, https://doi.org/10.1007/s10853-018-2052-7.

[45] X. Ma, X. Liu, X. Zhang, C. Piao, Z. Liu, D. Fang, J. Wang, Construction of dual Z-scheme NiO/$NiFe_2O_4$/Fe_2O_3 photocatalyst via incomplete solid state chemical combustion reactions for organic pollutant degradation with simultaneous hydrogen production, Int. J. Hydrog. Energy 46 (2021) 31659–31673, https://doi.org/10.1016/j.ijhydene.2021.07.076.

[46] L. Liu, S. Hu, K. Gao, Natural nanofiber-based stacked porous nitrogen-doped carbon/$NiFe_2O_4$ nanohybrid nanosheets, Cellulose 27 (2020) 1021–1031, https://doi.org/10.1007/s10570-019-02843-w.

[47] J.E. Park, M.J. Kim, M.S. Lim, S.Y. Kang, J.K. Kim, S.H. Oh, M. Her, Y.H. Cho, Y. E. Sung, Graphitic carbon nitride-carbon nanofiber as oxygen catalyst in anion-exchange membrane water electrolyzer and rechargeable metal–air cells, Appl. Catal. B Environ. 237 (2018) 140–148, https://doi.org/10.1016/j.apcatb.2018.05.073.

[48] M.S. Cha, J.E. Park, S. Kim, S.H. Han, S.H. Shin, S.H. Yang, T.H. Kim, D.M. Yu, S. So, Y.T. Hong, S.J. Yoon, S.G. Oh, S.Y. Kang, O.H. Kim, H.S. Park, B. Bae, Y. E. Sung, Y.H. Cho, J.Y. Lee, Poly(carbazole)-based anion-conducting materials with high performance and durability for energy conversion devices, Energy Environ. Sci. 13 (2020) 3633–3645, https://doi.org/10.1039/D0EE01842B.

[49] N. Lee, D.T. Duong, D. Kim, Cyclic ammonium grafted poly (arylene ether ketone) hydroxide ion exchange membranes for alkaline water electrolysis with high chemical stability and cell efficiency, Electrochim. Acta 271 (2018) 150–157, https://doi.org/10.1016/j.electacta.2018.03.117.

[50] A. Carbone, S.C. Zignani, I. Gatto, S. Trocino, A.S. Aricò, Assessment of the FAA3-50 polymer electrolyte in combination with a $NiMn_2O_4$ anode catalyst for anion exchange membrane water electrolysis, Int. J. Hydrog. Energy 45 (2020) 9285–9292, https://doi.org/10.1016/j.ijhydene.2020.01.150.

[51] C. Busacca, S.C. Zignani, A. Di Blasi, O. Di Blasi, M. Lo Faro, V. Antonucci, A. S. Aricò, Electrospun $NiMn_2O_4$ and $NiCo_2O_4$ spinel oxides supported on carbon nanofibers as electrocatalysts for the oxygen evolution reaction in an anion exchange membrane-based electrolysis cell, Int. J. Hydrog. Energy 44 (2019) 20987–20996, https://doi.org/10.1016/j.ijhydene.2019.02.214.

[52] I.V. Pushkareva, A.S. Pushkarev, S.A. Grigoriev, P. Modisha, D.G. Bessarabov, Comparative study of anion exchange membranes for low-cost water electrolysis, Int. J. Hydrog. Energy 45 (2020) 26070–26079, https://doi.org/10.1016/j.ijhydene.2019.11.011.

[53] Z. Liu, S.D. Sajjad, Y. Gao, H. Yang, J.J. Kaczur, R.I. Masel, The effect of membrane on an alkaline water electrolyzer, Int. J. Hydrog. Energy 42 (2017) 29661–29665, https://doi.org/10.1016/j.ijhydene.2017.10.050.

[54] H. Ito, N. Kawaguchi, S. Someya, T. Munakata, Pressurized operation of anion exchange membrane water electrolysis, Electrochim. Acta 297 (2019) 188–196, https://doi.org/10.1016/j.electacta.2018.11.077.

[55] J. Parrondo, C.G. Arges, M. Niedzwiecki, E.B. Anderson, K.E. Ayers, V. Ramani, Degradation of anion exchange membranes used for hydrogen production by ultrapure water electrolysis, RSC Adv. 4 (2014) 9875–9879, https://doi.org/10.1039/C3RA46630B.

[56] T. Wu, S. Sun, J. Song, S. Xi, Y. Du, B. Chen, W.A. Sasangka, H. Liao, C.L. Gan, G. G. Scherer, L. Zeng, H. Wang, H. Li, A. Grimaud, Z.J. Xu, Iron-facilitated dynamic

active-site generation on spinel $CoAl_2O_4$ with self-termination of surface reconstruction for water oxidation, Nat. Catal. 2 (2019) 763–772, https://doi.org/10.1038/s41929-019-0325-4.

[57] T. Pandiarajan, L.John Berchmans, S. Ravichandran, Fabrication of spinel ferrite based alkaline anion exchange membrane water electrolysers for hydrogen production, RSC Adv. 5 (2015) 34100–34108, https://doi.org/10.1039/C5RA01123J.

[58] E. Cossar, A. Oyarce Barnett, F. Seland, E.A. Baranova, The performance of nickel and nickel-iron catalysts evaluated as anodes in anion exchange membrane water electrolysis, Catalysts 9 (2019), https://doi.org/10.3390/catal9100814.

[59] R.A. Krivina, G.A. Lindquist, S.R. Beaudoin, T.N. Stovall, W.L. Thompson, L. P. Twight, D. Marsh, J. Grzyb, K. Fabrizio, J.E. Hutchison, S.W. Boettcher, Anode catalysts in anion-exchange-membrane electrolysis without supporting electrolyte: conductivity, dynamics, and ionomer degradation, Adv. Mater. 34 (2022), 2203033, https://doi.org/10.1002/adma.202203033.

[60] D. Li, E.J. Park, W. Zhu, Q. Shi, Y. Zhou, H. Tian, Y. Lin, A. Serov, B. Zulevi, E. D. Baca, C. Fujimoto, H.T. Chung, Y.S. Kim, Highly quaternized polystyrene ionomers for high performance anion exchange membrane water electrolysers, Nat. Energy 5 (2020) 378–385, https://doi.org/10.1038/s41560-020-0577-x.

[61] B. Motealleh, Z. Liu, R.I. Masel, J.P. Sculley, Z.R. Ni, L. Meroueh, Next-generation anion exchange membrane water electrolyzers operating for commercially relevant lifetimes, Int. J. Hydrog. Energy 46 (2021) 3379–3386, https://doi.org/10.1016/j.ijhydene.2020.10.244.

[62] A.Y. Faid, A.O. Barnett, F. Seland, S. Sunde, Ternary NiCoFe nanosheets for oxygen evolution in anion exchange membrane water electrolysis, Int. J. Hydrog. Energy 47 (2022) 23483–23497, https://doi.org/10.1016/j.ijhydene.2022.05.143.

[63] T. Caielli, A.R. Ferrari, S. Bonizzoni, E. Sediva, A. Caprì, M. Santoro, I. Gatto, V. Baglio, P. Mustarelli, Synthesis, characterization and water electrolyzer cell tests of poly(biphenyl piperidinium) Anion exchange membranes, J. Power Sources 557 (2023), 232532, https://doi.org/10.1016/j.jpowsour.2022.232532.

[64] A. Carbone, S.C. Zignani, I. Gatto, R. Pedicini, C. Oldani, A. Cattaneo, A.S. Aricò, Aquivion-based anion exchange membranes: Synthesis optimization via dispersant agents and reaction time, Chem. Eng. J. (2022), 140765, https://doi.org/10.1016/j.cej.2022.140765.

[65] A. Caprì, I. Gatto, C. Lo Vecchio, S. Trocino, A. Carbone, V. Baglio, Anion exchange membrane water electrolysis based on nickel ferrite catalysts, ChemElectroChem 10 (2023), e202201056, https://doi.org/10.1002/celc.202201056.

[66] H.A. Miller, Green hydrogen from anion exchange membrane water electrolysis, Curr. Opin. Electrochem. 36 (2022), 101122, https://doi.org/10.1016/j.coelec.2022.101122.

[67] H.A. Miller, K. Bouzek, J. Hnat, S. Loos, C.I. Bernäcker, T. Weißgärber, L. Röntzschc, J. Meier-Haackd, Green hydrogen from anion exchange membrane water electrolysis: a review of recent developments in critical materials and operating conditions, Sustain. Energy Fuels 4 (2020) 2114–2133.

Journal of Power Sources 556 (2023) 232417

Contents lists available at ScienceDirect

Journal of Power Sources

journal homepage: www.elsevier.com/locate/jpowsour

$NiFe_2O_4$ hierarchical nanoparticles as electrocatalyst for anion exchange membrane water electrolysis

A. Martinez-Lazaro [a,1], A. Caprì [b,1], I. Gatto [b], J. Ledesma-García [a], N. Rey-Raap [c], A. Arenillas [c], F.I. Espinosa-Lagunes [d], V. Baglio [b,*], L.G. Arriaga [d,**]

[a] *División de Investigación y Posgrado, Facultad de Ingeniería, Universidad Autónoma de Querétaro, 76010, Santiago de Querétaro, Mexico*
[b] *Istituto di Tecnologie Avanzate per l'Energia, Nicola Giordano, CNR-ITAE, Salita Santa Lucia sopra Contesse, 5, 98126, Messina, Italy*
[c] *Instituto de Ciencia y Tecnología del Carbono, INCAR-CSIC, Francisco Pintado Fe, 26, 33011, Oviedo, Spain*
[d] *Centro de Investigación y Desarrollo Tecnológico en Electroquímica, 76703, Santiago de Querétaro, Mexico*

HIGHLIGHTS

- A $NiFe_2O_4$ catalyst is synthesized by hydrothermal treatment using glucose and urea.
- $NiFe_2O_4$ is investigated at the anode of an anion exchange membrane electrolyser.
- A Fumasep® FAA3-50 membrane is used as electrolyte.
- A current density of 2.7 A cm^{-2} is obtained at 2.2 V and 60 °C.
- A proper stability is demonstrated for the catalyst.

ARTICLE INFO

Keywords:
Water electrolysis
Anion exchange membrane
$NiFe_2O_4$ catalyst
Oxygen evolution reaction
Hydrogen production

ABSTRACT

A $NiFe_2O_4$ catalyst with nanoparticle morphology, obtained by hydrothermal treatment using glucose and urea as precursors, is investigated as an anode catalyst in an anion exchange membrane electrolyser. Structure, morphology and composition are confirmed by X-ray diffraction (XRD), scanning and transmission electron microscopy (SEM and TEM), and X-ray photoelectron spectroscopy (XPS) analyses. The catalyst is sprayed onto one side of the Fumasep® FAA3-50 anion-exchange membrane to produce a catalyst-coated membrane (CCM), which, assembled with a cathode based on a 40% Pt/C catalyst, is investigated in a single-cell configuration with a size of 5 cm^2, at a temperature of 30–60 °C. A current density of 2.7 A cm^{-2} is obtained at 2.2 V and 60 °C, a value more than 25% higher than that recorded with a benchmark IrO_2 catalyst at the anode, representing a breakthrough for an anion exchange membrane electrolyser based on FAA3-50 membrane. A time-stability test of 72 h demonstrates the promising durability of this catalyst, which makes it a new reference for future investigations.

1. Introduction

Hydrogen is considered a potential substitute for fossil fuels, because it is abundant, efficient and, unlike other alternatives, it offers the potential to be renewable and does not produce harmful emissions. Hydrogen can be used as an energy carrier to generate electrical energy by hydrogen fuel cells and hydrogen combustion engines; also, its energy density is 120 MJ kg which is more than 2.5 times that of gasoline (44 MJ kg) [1,2]. Its clean production avoids the emission of CO_2 or other greenhouse gases, making it one of the ideal green energy sources that can replace non-renewable energy sources such as fossil fuels [3].

Water is an abundant and highly available substance on the planet, it is made up of two hydrogen atoms and one oxygen atom. Thus, it can act as a source of hydrogen and oxygen if the elements are separated or bonds are broken in the H_2O molecule ($H_2O \rightarrow H_2 + ½ O_2$).

The process of breaking the water molecule is known as water

---

* Corresponding author.
** Corresponding author.
E-mail addresses: vincenzo.baglio@itae.cnr.it (V. Baglio), larriaga@cideteq.mx (L.G. Arriaga).
[1] Contributed equally to the work.

https://doi.org/10.1016/j.jpowsour.2022.232417
Received 15 July 2022; Received in revised form 9 November 2022; Accepted 14 November 2022

dissociation reaction. The water molecule is broken down into hydrogen and oxygen by using energy like solar light, electrical, thermal, nuclear, and so on. The electrochemical water dissociation (EWD) is one of the most efficient and greenest ways to produce pure hydrogen without any greenhouse gases if powered by renewable energies, making it a sustainable method [4,5]. Among the different EWD types, alkaline electrolysis is the most utilized technology due to its low cost. In fact, the high pH allows the use of platinum group metal (PGM)-free catalysts [6,7]. In this regard, there has been a recent surge in interest in electrolysers based on anion-exchange membranes (AEMs), since they combine the advantages of both the liquid alkaline and proton exchange membrane (PEM) technologies in terms of high purity of generated H_2, good efficiency, dynamic behavior, together with the possibility of using inexpensive catalysts and fluorine-free membranes [8–12]. One of the biggest challenges for AEM electrolysis to be efficient is the development of highly effective catalysts for oxygen evolution reaction (OER) [13–15].

Although noble metals dominate EWD catalysis [16–18], some combinations of transition metals have shown strong stability, cost-effectiveness, and substantial electrocatalytic activities, which make them an alternative to replace the noble-metal electrocatalysts.

The transition metals used for EWD are usually found in the form of chalcogenides, phosphides, nitrides, carbides, and oxides [19–30]. Some results obtained by these categories of materials are reported in Table S1, concerning the OER activity determined in half-cell configuration.

Transition metal oxides like $NiCo_2O_4$, $NiFe_2O_4$, or a combination of different transition metals show excellent OER catalysis due to the possibility of adjusting the stoichiometry of transition metals in the lattice [31–33]. Transition metal phosphides (TMPs) are widely studied materials in the entire pH range, including the neutral. Delocalization between the transition metal and P facilitates H_2O adsorption and their decomposition. Furthermore, the addition of two or more transition metals in the single-metal phosphides boosts the electrocatalytic activities of TMPs [34–36]. Transition metal oxides are poor in conductivity; however, the enormous amount of oxygen vacancies generated by electrocatalytic reduction promotes the adsorption/desorption process in the OER [37]. In addition, the orderly hierarchical growth in two-dimensional and three-dimensional structures provides transition metal catalysts with high yield and electrochemical stability towards the OER [38–40]. In summary, the unique properties of metal oxides make them ideal for application in alkaline water electrolysers. This work explores the activity in an anion-exchange-membrane (AEM) electrolyser of a $NiFe_2O_4$ catalyst, obtained by hydrothermal treatment using glucose and urea as precursors to promote particle hierarchical growth with nanoparticle morphology. The sample has shown high catalytic activity towards OER, which led to a performance in the AEM electrolyser higher than noble-metal catalysts.

2. Materials and methods

2.1. Preparation of $NiFe_2O_4$ hierarchical nanoparticles

The nanoparticles were synthesized by chemical synthesis following this procedure: 1.1 g of Ni $(NO_3)_2{\cdot}6H_2O$ and 0.8 g Fe $(NO_3)_3{\cdot}9H_2O$ were dissolved in deionized water, adding 1.5 g of glucose; the solution was stirred for 1 h at 800 rpm; afterward, 3 mmol of urea was added, and the aqueous solution was subjected to hydrothermal treatment at 180 °C for one day. The sample was washed with deionized water and ethanol to remove all impurities; the solution excess was dried at 80 °C for 24 h. Finally, the dry sample was calcined at 550 °C for 5 h to eliminate the remaining organic moieties.

2.2. Physicochemical measurements

The crystallographic structure of $NiFe_2O_4$ was determined by X-ray diffractometry (XRD; Bruker D8 Advance diffractometer). The morphology was observed by a scanning electron microscope (SEM, HITACHI SU3500) and a high-resolution transmission electron microscope (HR-TEM, JEOL JEM2200), with spherical aberration correction. The specific surface area and the pore size distribution were determined by isotherms of nitrogen sorption for mesopores and micropores by BET analysis at 77.261 K (TriStar II 3020 V1.03). X-ray photoelectron spectroscopy (XPS, Monochromatic Magics Thermo Scientifics, and K-Alpha + Surface analysis) was used to determine the surface composition and bonding configuration of the samples.

2.3. Electrolyser electrochemical measurements

In an ultrasonic ice bath, cathodes were realized by mixing a commercial 40 wt% Platinum on carbon (Pt/C, Alfa Aesar) and a 20 wt% of FAA3 ionomer (FumaTech) for 30 min. The ink was deposited by spray coating technique onto the Sigracet 25-BC Gas Diffusion Layer (SGL Carbon), with a final loading of 0.5 mg cm^{-2} [41]. Anodes were prepared using $NiFe_2O_4$ samples with 20 wt% FAA3 ionomer, spraying the anodic catalytic ink directly on the FAA3-50® membrane (FumaTech), with a final loading of 3 mg cm^{-2}, to form a catalyst-coated membrane (CCM). Anode and cathode were made with a geometrical area equal to 5 cm^2. Before the assembly, the CCMs and cathodes were exchanged separately in a 1 M KOH solution for 1 h. Then they were coupled together by a cold-assembling procedure to realize a membrane-electrode assembly (MEA) [42]. A Ni-felt (NV BEKAERT SA, Belgium) was used as the current collector/backing layer at the anode side. The electrochemical characterisations were carried out in a single-cell configuration with a size of 5 cm^2, in a temperature range between 30 °C and 60 °C, supplying a 1 M KOH solution to the anode compartment (flow rate 5 ml min^{-1}). I-V curves were performed at a scan rate of 5 mV/s. The electrochemical impedance spectroscopy (EIS) measurements were performed under potentiostatic control (at a cell voltage of 1.8 V) in a frequency range between 10 kHz and 100 mHz by frequency sweeping in the single sine mode. The amplitude of the sinusoidal excitation signal was 0.01 V r.m.s. Chronoamperometric tests were carried out at 2 V in the complete cell, feeding a 1 M KOH solution.

3. Results and discussion

The urea hydrolysis process was employed to succeed in hydrated metal nitrate incorporation as a precursor salt instead of ammoniacal salts or other inorganic compounds. This process allows that transition metals salts to be soluble in water and react with the hydroxide and ammonium ions formed during urea hydrolysis:

$$CO(NH_2)_2 + H_2O \rightarrow 2NH_4^+ + HCO_3\text{-} + OH^- \tag{1}$$

In this reaction, hydroxide ions (OH^-) react with metal ions (Fe^{3+} and Ni^{2+}) in the aqueous solution at high temperatures. The reaction is carried out at 180 °C to guarantee that all the precursor salts react; in addition, the ammonia and carbonic acid favor the reducing environment so that the ions of the metal salts can anchor to the OH^- ions; thus, during the hydrothermal process, it allows that all reactions occur in this way:

$$Fe^{3+} + 3OH\text{-}\rightarrow Fe\ (OH)_3 \tag{2}$$

$$Ni^{2+} + 2OH^- \rightarrow Ni\ (OH)_2 \tag{3}$$

The hydrothermal synthesis method has been explored under different conditions in works carried out by Kumar et al. [43], Majid et al. [44], and Peng et al. [45]. Analysing the literature results, the optimal synthesis conditions were selected, adding modifications to make easier the production of the catalysts. A synthesis with a smaller number of nitrogenous compounds (urea) is proposed, promoting the adequate growth of crystals and reducing the residues. It does not use

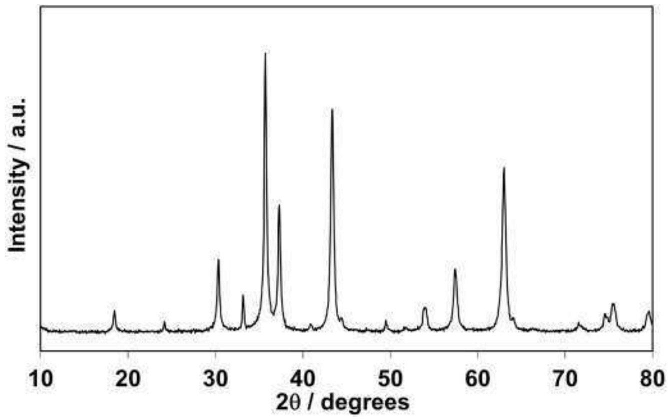

Fig. 1. XRD pattern of $NiFe_2O_4$ catalyst.

organic solvents, such as in the work of Kim [46], which facilitates the washing of the catalyst. Furthermore, glucose promotes the formation of nanospheres during the synthesis process. To obtain the oxides, an oxidation process is applied at high temperatures; posteriorly, the organic residues are removed by the final calcination step.

In addition, the synthesis method presented in this work is done in a single rapid step compared to other hydrothermal methods that require more than one set of steps at different temperatures, as reported by Boychuk et al. [47], Mahala et al. [48], and Wu et al. [49].

The crystallographic analysis of the synthesized catalyst shows diffraction peaks at 2 Θ degree positions: 18.3, 30.4, 37.2, 43.3, 54, 57.5, 63, 74.8, 79, which coincide with the indexed (111), (220), (311), (222), (400), (422), (511), (440) and (533) crystalline planes, respectively (Fig. 1). The observed diffractions indicate that the unit cell is a face-centered cubic (fcc) spinel according to JCPDS card n. 10-0325. Crystal size was calculated according to the Scherrer's equation, obtaining a crystallite size of 20–22 nm.

The N_2 adsorption-desorption isotherms exhibited a type IV hysteresis loop at a relative pressure (P/P_0) between 0.6 and 1, representing a typical mesoporous material. The specific surface area and the pore size distribution of the $NiFe_2O_4$ nanoparticles were studied by BET technique. In this sense, the pore size distribution obtained confirms the presence of pores in a range between 10 and 70 nm, and the main pore size is centered at 70 nm. The surface area and pore volume were 23.3 $m^2\ g^{-1}$ and 0.117 $cm^3\ g^{-1}$, respectively (Fig. 2).

The morphological analysis was done by SEM images, which showed that the $NiFe_2O_4$ is composed of a cluster structure type. The formation of this type of structure is favoured by the presence of glucose during the hydrothermal treatment, resulting in clusters of 30–50 nm (Fig. 3a–b) that correspond to the average size of glucose spheres in the initial solution. It is important to mention that the shape of the structure is dictated by the mold, so the use of different organic molds will contribute to a different cluster shape. The amount of glucose used in this work is greater than that reported in previous works [32,50–53], which allows a greater dispersion of the organic mold, and therefore clusters of smaller size are obtained. The size of the clusters depends on the amount of carbohydrate because it is to be assumed that the precursor salts adhere to the surface of the glucose spheres, and then, once the samples are calcined the glucose is removed, which is why sharper edges are marked around the clusters. On the other hand, the morphology of the spaces within the particles provides the active sites that allow the OER to be carried out effectively since the liquid can penetrate the catalyst more easily. To complement the crystallographic and morphological investigation, a TEM analysis was carried out to confirm the structure of the clusters. The analysis showed the occurrence of hexagonal particles favoring the plane (311), see Fig. 3c–f).

X-ray photoelectronic spectroscopy (XPS) was performed to know the chemical composition and oxidation state of the hierarchical nanoparticles of $NiFe_2O_4$, as presented in Fig. 4. The overall spectrum of the sample, as shown in Fig. 4a, indicates the presence of Fe, Ni, O, and C (adventitious and from the conductive tape substrate), without peaks of impurities found in the studied material.

The spectrum of Ni 2p is observed in Fig. 4b, having orbital deconvolution in Ni $2p_{3/2}$ and Ni $2p_{1/2}$, with the peaks of 855.1 eV and 872.5 eV corresponding to Ni^{2+}, while those located at 856.6 eV and 874.0 eV refer to Ni^{3+} [54,55]. The high-resolution scan of Fe 2p is presented in

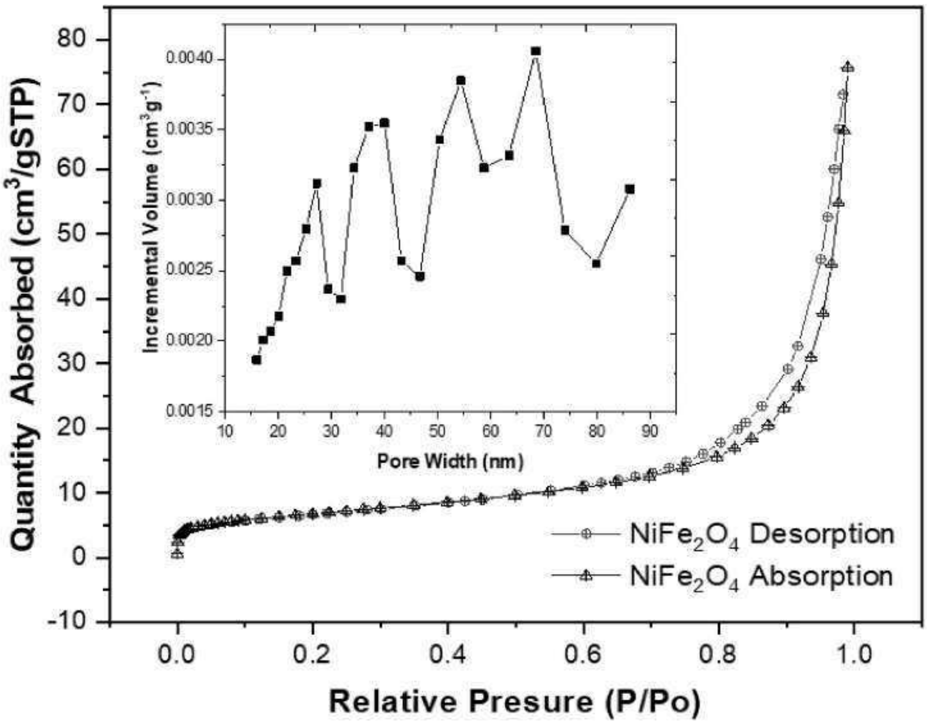

Fig. 2. BET analysis of $NiFe_2O_4$ catalyst.

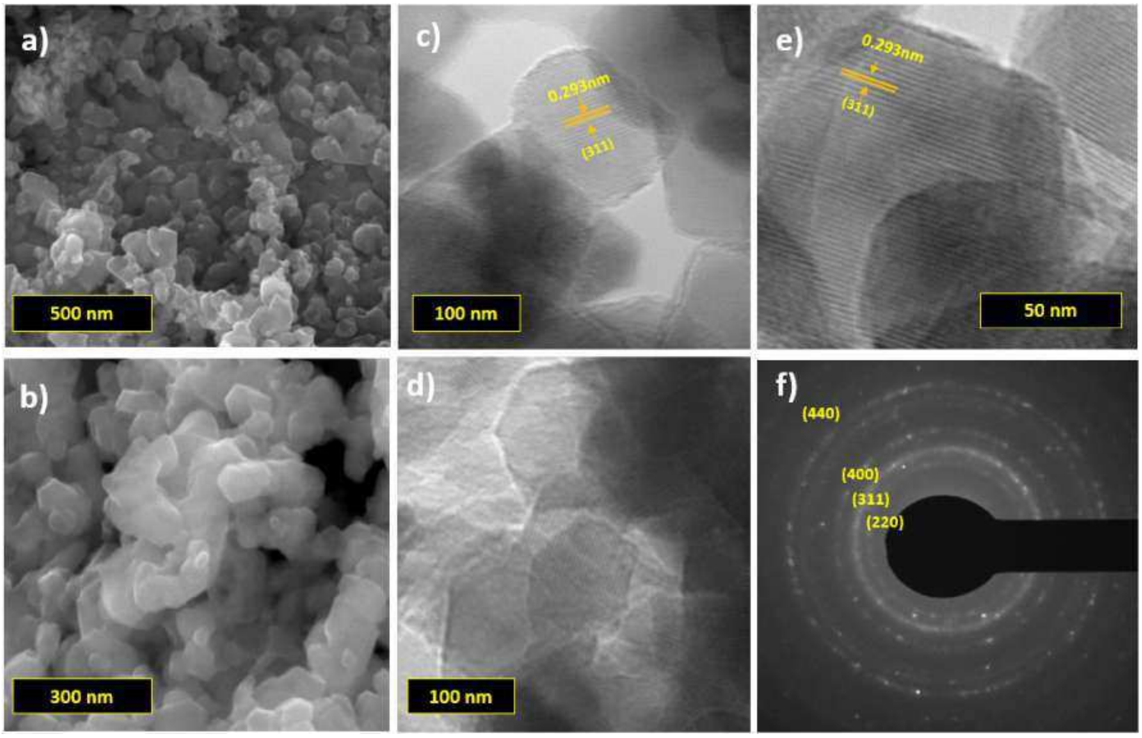

Fig. 3. (a–b) SEM images. (c–e) TEM images. f) Crystallinity patterns of $NiFe_2O_4$.

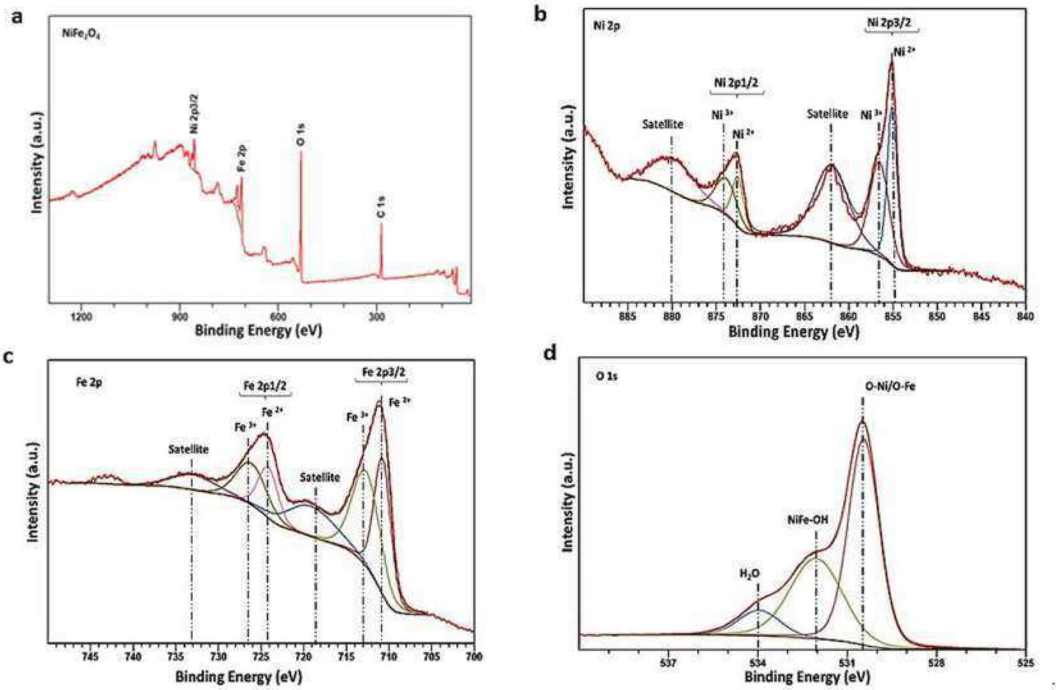

Fig. 4. XPS spectrum of $NiFe_2O_4$ hierarchical nanoparticles; (a) survey spectrum, high resolution (b) Ni 2p; (C) Fe 2p; and (d) O 1s.

Fig. 4c; the spectra of Fe $2p_{3/2}$ and Fe $2p_{1/2}$ were deconvoluted, giving the peaks at 710.2 eV and 724.2, which correspond to Fe $^{2+}$, while those located at 713.0 eV and 726.4 refer to Fe $^{3+}$. These characteristics are common in the $NiFe_2O_4$ structure reported in the literature [55]. Fig. 4d shows the deconvoluted spectrum of O 1s, having three peaks centered at 530.5 eV (associated with O–Ni/O–Fe), 532.1 eV (referred to NiFe–OH, oxygen defects on the surface or absorbed oxygen species), and 533.9 eV (associated with the presence of H_2O physically and chemically absorbed on the surface) [56–58]. The atomic ratio between Ni:Fe was found to 1:2 confirming the spinel structure.

Electrochemical measurements were carried out in an electrolysis cell based on Ni plates with a single-serpentine flow field of 5 cm^2 and gold-plated current collectors (Fig. S1). The MEA consisted of a CCM for the anode side (the $NiFe_2O_4$ catalyst was deposited by spray onto the FAA3-50® membrane) coupled with a gas diffusion electrode (GDE) loaded with a Pt/C catalyst for the cathode side. The electrochemical

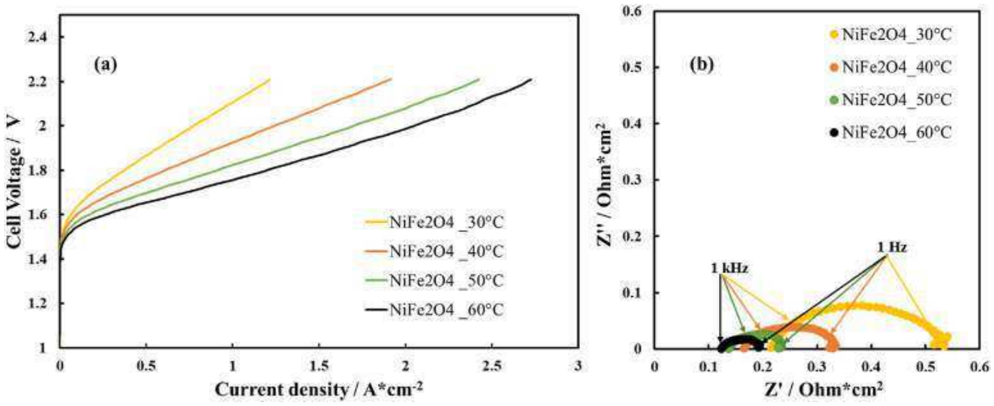

Fig. 5. (a) Linear sweep voltammetric curves and (b) electrochemical impedance spectroscopy plots (Nyquist), recorded at 1.8 V, at different temperatures for the electrolyser based on $NiFe_2O_4$ catalyst at the anode.

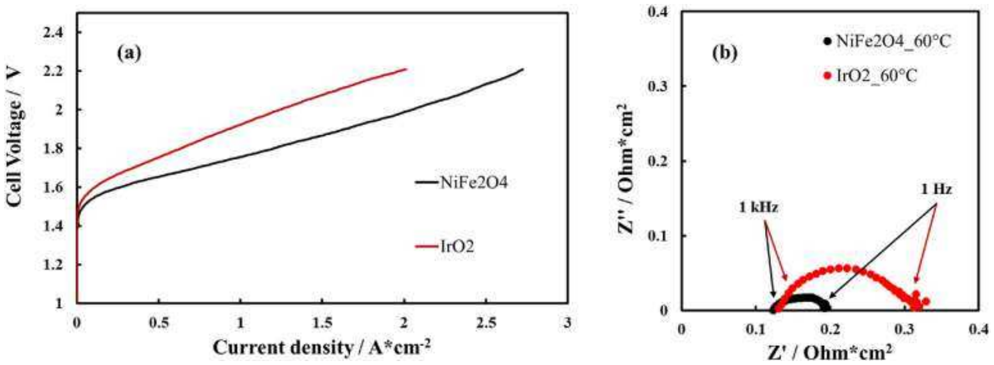

Fig. 6. (a) Linear sweep voltammetric curves and (b) electrochemical impedance spectroscopy plots (Nyquist), recorded at 1.8 V, for the electrolyser based on $NiFe_2O_4$ catalyst at the anode in comparison with a commercial IrO_2 sample at 60 °C.

performance of this cell was evaluated by using linear sweep voltammetry (LSV) at a scan rate of 5 mV s^{-1}, in a temperature range between 30 °C and 60 °C, supplying a 1 M KOH solution to the anode compartment (flow rate 5 ml min^{-1}).

Linear sweep voltammetry experiments were performed on the cell operating at different temperatures, from 30 to 60 °C (this upper limit was selected not to stress the commercial membrane used). The i-V curves are reported in Fig. 5a; they show a decrease in the onset potential for the water splitting with the increase of the temperature and a consequent improvement of the performance caused by the enhanced kinetics for the two processes occurring at the two electrodes (the oxygen and hydrogen evolution reactions).

This effect is clearly observed in Fig. 5b, where the diameter of the semicircle, corresponding to the charge transfer resistance (R_{ct}), decreases, raising the temperature. Furthermore, a higher temperature reduces the series resistance (R_s), the intercept at high frequency with the x-axis, indicating an increase in ionic conductivity. The maximum current density obtained at 60 °C is about 2.7 A cm^{-2} at 2.2 V, whereas at lower voltages of 1.8 V and 2 V, which require less energy, 1.2 and 2 A cm^{-2} are reached, respectively. This performance is higher than that observed in several papers with cells based on similar PGM-free catalysts at the anode or noble metals (IrO_2) [42,59–74]. A literature survey of the recent results obtained is reported in Table S2.

To further confirm the superior behavior of this catalyst with respect to state-of-the-art catalysts, the cell was compared with an analogous one equipped with a commercial IrO_2 catalyst at the anode under the same operating conditions [42]. The results at 60 °C are reported in Fig. 6. Details regarding the noble metal-based cell are reported in reference [42]. From Fig. 6a, a lower onset potential and a lower slope of the i-V curve are observed, which, considering that all other materials are the same for the two cells, indicates a high catalytic activity and a faster kinetic for the OER. This is confirmed by the EIS plots (Fig. 6b), in which a significantly lower charge transfer resistance (R_{ct}) was recorded for the non-PGM-based cell, together with a slightly lower series resistance (R_s), confirming the good conductivity and superb catalytic activity of the synthesized $NiFe_2O_4$ nanoparticles.

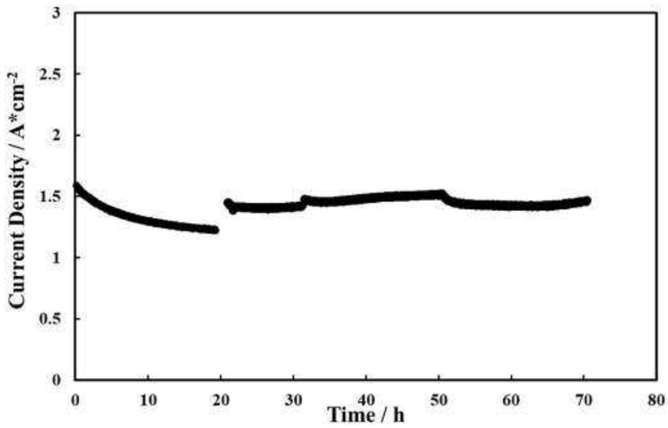

Fig. 7. Durability test carried out at 60 °C and 2 V for the cell based on $NiFe_2O_4$ catalyst at the anode and FAA-3–50 membrane.

The long-term behavior of the catalyst is an important issue for the development of the AEM electrolysis technology. Accordingly, the cell equipped with the $NiFe_2O_4$ nanoparticles was subjected to 72 h (3 days) durability test under potentiostatic operating conditions (@ 2 V). The

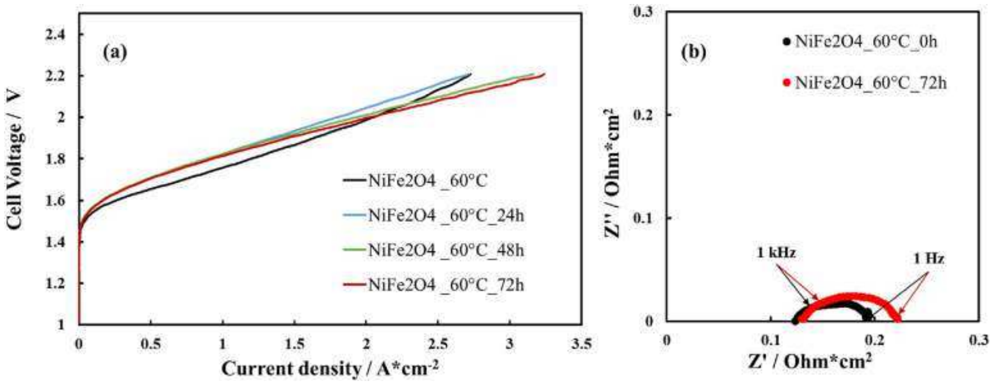

Fig. 8. (a) Linear sweep voltammetric curves at BoT and after 24, 48, and 72 h operation; (b) electrochemical impedance spectroscopy plots (Nyquist), recorded at 1.8 V, for the electrolyser based on $NiFe_2O_4$ catalyst at the BoT and after 72 h (EoT).

chronoamperometric curve is reported in Fig. 7. The experiment was carried out by recirculating 1 M KOH solution from the anode side. After 24 h approximatively, a polarization curve was registered to check the electrochemical behavior; moreover, after performing the i-V curve, the solution was replaced with a fresh one. The chronoamperometric investigation was continued and stopped again after the other 24 h and 48 h to reach a 72 h operation (recording the i-V curves after every 24 h stops and replacing the KOH solution). A slight decrease in performance was observed during the first 24 h. This effect could be ascribed to different reasons, i.e. catalysts deactivation, membrane degradation or poisoning, electrode constraints (flooded electrode with oxygen bubbles removal limitations), etc. Furthermore, carbonation phenomena may occur. CO_2 uptake in the cell from the external environment could produce carbonate species, which may initially poison both the membrane and electrodes. Afterward, during the LSV, carbonates decompose, cleaning the catalyst surface or the membrane. This may cause the performance recovery after 24 h operation and replacing the solution.

Fig. 8a shows the LSV curves recorded at the beginning of the test and after the interruptions, at 24, 48, and 72 h; whereas the EIS analysis at the beginning and after 72 h of operation is reported in Fig. 8b. Compared with the i-V curve recorded at the beginning of the test (BoT), the LSV after 24 h indicates a slightly higher onset potential and larger polarizations in the broad range of voltage considered. Only at 2.2 V the current densities appear similar for the two curves. The i-V curves after 48 and 72 h show similar behavior, in the onset potential and current up to 1.8 V, to the 24-h plot. Increased performance was observed at high voltages, agreeing with a better behavior recorded during the chronoamperometric test (Fig. 7) at 2 V. The Nyquist plot (Fig. 8b), recorded at 1.8 V, indicates a slight increase of R_s and R_{ct} after 72 h, which could be attributed to the carbonation process occurring during the time. These data are in good agreement with the polarization curves in Fig. 8a.

To better understand the reason for this behavior, and further assess the stability of the $NiFe_2O_4$ after the operation, post-mortem analyses, in terms of XRD, TEM and XPS, were carried out on the EoT catalyst. The results are reported in the Supplementary Information. Fig. S2 shows the X-ray diffraction patterns of the fresh and used sample, which are almost identical, indicating that no modification of the structure nor the crystallite size occurred after 72 h operation. This is confirmed by the TEM images recorded on the used catalyst scratched from the membrane (Fig. S3). The particle size and morphology are essentially the same, as a further confirmation of the stability of the sample. This was also analysed regarding the surface characteristics by XPS (Fig. S4). The survey and the Fe 2p signals of the used catalyst were investigated for comparison with the fresh sample. The survey spectrum shows the presence of K from the liquid electrolyte used in the anodic compartment; furthermore, the presence of Ni coming from the Ni foam backing layer does not allow a precise determination of the amount of this element, and the ratio between Ni and Fe. The high-resolution scan of Fe 2p is presented in Fig. S4 (right); the spectra of Fe $2p_{3/2}$ and Fe $2p_{1/2}$ were deconvoluted, giving the peaks at 710.2 eV and 724.2, which correspond to Fe^{2+}, whereas those located at 713.0 eV and 726.4 refer to Fe^{3+}. Accordingly, when comparing the sample before and after the operation, the two spectra are observed in the oxidation states typical of the presence of the $NiFe_2O_4$ structure, as reported in the literature [75].

Analysing all these post-operation results, the causes of performance degradation with time could be attributed to the carbonation phenomena, since the catalyst structure, morphology, size, and oxidation states appear unvaried after testing. Moreover, these losses can be recovered by replacing the KOH solution and/or sweeping the cell potential, confirming the above-mentioned hypothesis.

4. Conclusions

A $NiFe_2O_4$ catalyst, obtained by hydrothermal treatment using glucose and urea as precursors to promote particle hierarchical growth with nanoparticle morphology, has been investigated as an anode catalyst in an anion exchange membrane electrolyser. Promising performance and durability have been recorded, although a commercial membrane and an unoptimized electrodic structure have been used. Compared with other literature works dealing with the same commercial membrane or other polymeric electrolytes, these results can be considered a step forward in the future application of this technology.

CRediT authorship contribution statement

A. Martinez-Lazaro: Conceptualization, Methodology, Investigation. **A. Caprì:** Investigation, Data curation, Writing – original draft. **I. Gatto:** Conceptualization, Supervision, Reviewing. **J. Ledesma-García:** Conceptualization, Supervision, Reviewing. **N. Rey-Raap:** Investigation, Reviewing. **A. Arenillas:** Conceptualization, Investigation, Reviewing. **F.I. Espinosa-Lagunes:** Methodology, Investigation. **V. Baglio:** Conceptualization, Supervision, Funding acquisition, Writing – review & editing, Project administration. **L.G. Arriaga:** Conceptualization, Supervision, Funding acquisition, Writing – review & editing, Project administration.

Declaration of competing interest

The authors declare that they have no known competing financial interests or personal relationships that could have appeared to influence the work reported in this paper.

Data availability

Data will be made available on request.

Acknowledgments

CNR-ITAE authors thank the Italian Ministry of University and Research (MUR) for funding through the FISR2019 project AMPERE (FISR2019_01294). Mexican authors acknowledge the Mexican Council for Science and Technology (CONACYT) for financial support through project Ciencia de Frontera Grant no. 845132.

Appendix A. Supplementary data

Supplementary data to this article can be found online at https://doi.org/10.1016/j.jpowsour.2022.232417.

References

[1] A. Patonia, R. Poudineh, Cost-competitive Green Hydrogen: How to Lower the Cost of Electrolysers, EL, Oxford Institute for Energy Studies, 2022, p. 47.
[2] P. Nikolaidis, A. Poullikkas, A comparative overview of hydrogen production processes, Renew. Sustain. Energy Rev. 67 (2017) 597–611, https://doi.org/10.1016/j.rser.2016.09.044.
[3] F. Barbir, Transition to renewable energy systems with hydrogen as an energy carrier, Energy 34 (2009) 308–312, https://doi.org/10.1016/j.energy.2008.07.007.
[4] A.S. Arico, S. Siracusano, N. Briguglio, V. Baglio, A. Di Blasi, V. Antonucci, Polymer electrolyte membrane water electrolysis: status of technologies and potential applications in combination with renewable power sources, J. Appl. Electrochem. 43 (2013) 107–118, https://doi.org/10.1007/s10800-012-0490-5.
[5] M. Carmo, D.L. Fritz, J. Mergel, D. Stolten, A comprehensive review on PEM water electrolysis, Int. J. Hydrogen Energy 38 (2013) 4901–4934, https://doi.org/10.1016/j.ijhydene.2013.01.151.
[6] D. Xu, M.B. Stevens, M.R. Cosby, S.Z. Oener, A.M. Smith, L.J. Enman, K.E. Ayers, C. B. Capuano, J.N. Renner, N. Danilovic, Y. Li, H. Wang, Q. Zhang, S.W. Boettcher, Earth-abundant oxygen electrocatalysts for alkaline anion-exchange-membrane water electrolysis: effects of catalyst conductivity and comparison with performance in three-electrode cells, ACS Catal. 9 (2019) 7–15, https://doi.org/10.1021/acscatal.8b04001.
[7] J. Wang, J. Wang, X. Yue, Y. Yang, S. Sirisomboonchai, P. Wang, X. Ma, A. Abudula, G. Guan, Earth-abundant transition-metal-based bifunctional catalysts for overall electrochemical water splitting: a review, J. Alloys Compd. 819 (2020), 153346. https://doi: 10.1016/j.jallcom.2019.153346.
[8] C. Santoro, A. Lavacchi, P. Mustarelli, V. Di Noto, L. Elbaz, D.R. Dekel, F. Jaouen, What is next in anion-exchange membrane water electrolyzers? Bottlenecks, benefits, and future, ChemSusChem (2022), e202200027. https://doi:10.1002/cssc.202200027.
[9] D. Henkensmeier, M. Najibah, C. Harms, J. Žitka, J. Hnát, K. el Bouzeket, Overview: state-of-the art commercial membranes for anion exchange membrane water electrolysis, J. Electrochem. En. Conv. Stor. 18 (2021), 024001. https://doi:10.1115/1.4047963.
[10] J.R. Varcoe, P. Atanassov, D.R. Dekel, A.M. Herring, M.A. Hickner, P.A. Kohl, A. R. Kucernak, W.E. Mustain, K. Nijmeijer, K. Scott, T. Xuk, L. Zhuang, Anion-exchange membranes in electrochemical energy systems, Energy Environ. Sci. 7 (2014) 3135–3191, https://doi.org/10.1039/c4ee01303d.
[11] M. Chatenet, B.G. Pollet, D.R. Dekel, F. Dionigi, J. Deseure, P. Millet, R.D. Braatz, M.Z. Bazant, M. Eikerling, I. Staffell, P. Balcombe, Y. Shao-Horn, H. Schafer, Water electrolysis: from textbook knowledge to the latest scientific strategies and industrial developments, Chem. Soc. Rev. 51 (2022) 4583–4762, https://doi.org/10.1039/d0cs01079k.
[12] I. Vincent, A. Kruger, D. Bessarabov, Development of efficient membrane electrode assembly for low cost hydrogen production by anion exchange membrane electrolysis, Int. J. Hydrogen Energy 42 (2017) 10752–10761, https://doi.org/10.1016/j.ijhydene.2017.03.069.
[13] A. Eftekhari, Tuning the electrocatalysts for oxygen evolution reaction, Mater, Today Energy 5 (2017) 37–57, https://doi.org/10.1016/j.mtener.2017.05.002.
[14] C.C. Pavel, F. Cecconi, C. Emiliani, S. Santiccioli, A. Scaffidi, S. Catanorchi, M. Comotti, Highly efficient platinum group metal free based membrane-electrode assembly for anion exchange membrane water electrolysis, Angew. Chem. Int. Ed. 53 (2014) 1378–1381, https://doi.org/10.1002/anie.201308099.
[15] H.A. Miller, K. Bouzek, J. Hnat, S. Loos, C.I. Bernacker, T. Weißgarber, L. Rontzsch, J. Meier-Haackd, Green hydrogen from anion exchange membrane water electrolysis: a review of recent developments in critical materials and operating conditions, Sustain. Energy Fuels 4 (2020) 2114–2133, https://doi.org/10.1039/C9SE01240K.
[16] S. Siracusano, N. Hodnik, P. Jovanovic, F. Ruiz-Zepeda, M. Šalab, V. Baglio, A. S. Aricò, New insights into the stability of a high performance nanostructured catalyst for sustainable water electrolysis, Nano Energy 40 (2017) 618–632, https://doi.org/10.1016/j.nanoen.2017.09.014.
[17] A. Di Blasi, C. D'Urso, V. Baglio, V. Antonucci, A.S. Arico', R. Ornelas, F. Matteucci, G. Orozco, D. Beltran, Y. Meas, L.G. Arriaga, Preparation and evaluation of $RuO_2 – IrO_2$, IrO_2 – Pt and $IrO_2 – Ta_2O_5$ catalysts for the oxygen evolution reaction in an SPE electrolyzer, J. Appl. Electrochem. 39 (2009) 191–196, https://doi.org/10.1007/s10800-008-9651-y.
[18] S. Cherevko, S. Geiger, O. Kasian, N. Kulyk, J.-P. Grote, A. Savan, B.R. Shrestha, S. Merzlikin, B. Breitbach, A. Ludwig, K.J.J. Mayrhofer, Oxygen and hydrogen evolution reactions on Ru, RuO_2, Ir, and IrO_2 thin film electrodes in acidic and alkaline electrolytes: a comparative study on activity and stability, Catal. Today 262 (2016) 170–180, https://doi.org/10.1016/j.cattod.2015.08.014.
[19] M. Tahir, L. Pan, F. IIdrees, X. Zhang, L. Wang, J.-J. Zou, Z.L. Wang, Electrocatalytic oxygen evolution reaction for energy conversion and storage: a comprehensive review, Nano Energy 37 (2017) 136–157, https://doi.org/10.1016/j.nanoen.2017.05.022.
[20] M. Gu, S.-C. Wang, C. Chen, D. Xiong, R.-Y. Yi, Iron-based metal-organic framework system as an efficient bifunctional electrocatalyst for oxygen evolution and hydrogen evolution reactions, Inorg. Chem. 9 (2020) 6078–6086, https://doi.org/10.1021/acs.inorgchem.0c00100.
[21] L. Wang, Y. Wu, R. Cao, L. Ren, M. Chen, X. Feng, J. Zhou, B. Wang, Fe/Ni metal-organic frameworks and their binder-free thin films for efficient oxygen evolution with low overpotential, ACS Appl. Mater. Interfaces 26 (2016) 16736–16743, https://doi.org/10.1021/acsami.6b05375.
[22] S.W. Luo, R. Gua, P. Shi, J. Fan, Q. Xu, Y. Min, Π-Π interaction boosts catalytic oxygen evolution by self-supporting metal-organic frameworks, J. Power Sources 448 (2020), 227406, https://doi.org/10.1016/j.jpowsour.2019.227406.
[23] F. Song, X. Hu, Exfoliation of layered double hydroxides for enhanced oxygen evolution catalysis, Nat. Commun. 5 (2014) 1–9, https://doi.org/10.1038/ncomms5477.
[24] J. Masa, P. Weide, D. Peeters, I. Sinev, W. Xia, Z. Sun, C. Somsen, M. Muhler, W. Schuhmann, Amorphous cobalt boride (Co_2B) as a highly efficient nonprecious catalyst for electrochemical water splitting: oxygen and hydrogen evolution, Adv. Energy Mater. 6 (2016) 1–10, https://doi.org/10.1002/aenm.201502313.
[25] K. Fominykh, J.M. Feckl, J. Sicklinger, M. Döblinger, S. Böcklein, J. Ziegler, L. Peter, J. Rathousky, E.-W. Scheidt, T. Bein, D. Fattakhova-Rohlfing, Ultrasmall dispersible crystalline nickel oxide nanoparticles as high-performance catalysts for electrochemical water splitting, Adv. Funct. Mater. 24 (2014) 3123–3129, https://doi.org/10.1002/adfm.201303600.
[26] P. Chen, K. Xu, Z. Fang, Y. Tong, J. Wu, X. Lu, X. Peng, H. Ding, C. Wu, Y. Xie, Metallic Co_4N porous nanowire arrays activated by surface oxidation as electrocatalysts for the oxygen evolution reaction, Angew. Chem. 127 (2015) 14923–14927, https://doi.org/10.1002/ange.201506480.
[27] Y. Yang, H. Fei, G. Ruan, J.M. Tour, Porous cobalt-based thin film as a bifunctional catalyst for hydrogen generation and oxygen generation, Adv. Math. 27 (2015) 3175–3180, https://doi.org/10.1002/adma.201500894.
[28] Y. Gorlin, T.F. Jaramillo, A bifunctional nonprecious metal catalyst for oxygen reduction and water oxidation, J. Am. Chem. Soc. 132 (2010) 13612–13614, https://doi.org/10.1021/ja104587v.
[29] S. Mao, Z. Wen, T. Huang, Y. Hou, J. Chen, High-performance bi-functional electrocatalysts of 3D crumpled graphene-cobalt oxide nanohybrids for oxygen reduction and evolution reactions, Energy Environ. Sci. 7 (2014) 609–616, https://doi.org/10.1039/c3ee42696c.
[30] C. Alegre, C. Busacca, A. Di Blasi, O. Di Blasi, A.S. Aricò, V. Antonucci, E. Modica, V. Baglio, Electrospun carbon nanofibers loaded with spinel-type cobalt oxide as bifunctional catalysts for enhanced oxygen electrocatalysis, J. Energy Storage 23 (2019) 269–277, https://doi.org/10.1016/J.EST.2019.04.001.
[31] C.C.L. McCrory, S. Jung, J.C. Peters, T.F. Jaramillo, Heterogeneous electrocatalysts for the oxygen evolution reaction, J. Am. Chem. Soc. 135 (2013) 16977–16987, https://doi.org/10.1021/ja407115p.
[32] W. Shen, L. Zhang, B. Zhao, Y. Du, X. Zhou, Growth mechanism of octahedral like nickel ferrite crystals prepared by modified hydrothermal method and morphology dependent magnetic performance, Ceram. Int. 44 (2018) 9809–9815, https://doi.org/10.1016/j.ceramint.2018.02.219.
[33] C. Si, et al., Mesoporous nanostructured spinel-type MFe_2O_4 (M = Co, Mn, Ni) oxides as efficient bi-functional electrocatalysts towards oxygen reduction and oxygen evolution, Electrochim, Acta 245 (2017) 829–838, https://doi.org/10.1016/j.electacta.2017.06.029.
[34] Y. Shi, B. Zhang, Recent advances in transition metal phosphide nanomaterials: synthesis and applications in hydrogen evolution reaction, Chem. Soc. Rev. 45 (2016) 1529–1541, https://doi.org/10.1039/c5cs00434a.
[35] G. Li, Y. Sun, J. Rao, J. Wu, A. Kumar, Q.N. Xu, C. Fu, E. Liu, G.R. Blake, P. Werner, B. Shao, K. Liu, S. Parkin, X. Liu, M. Fahlman, S.-C. Liou, G. Auffermann, J. Zhang, C. Felser, X. Feng, Carbon-tailored semimetal MoP as an efficient hydrogen evolution electrocatalyst in both alkaline and acid media, Adv. Energy Mater. 8 (2018), 1801258, https://doi.org/10.1002/aenm.201801258.
[36] C. Huang, C. Pi, X. Zhang, K. Ding, P. Qin, J. Fu, X. Peng, B. Gao, P.K. Chu, K. Huo, In situ synthesis of MoP nanoflakes intercalated N-doped graphene nanobelts from MoO_3–amine hybrid for high-efficient hydrogen evolution reaction, Small 14 (2018), 201800667, https://doi.org/10.1002/smll.201800667.
[37] F. Luo, R. Xua, S. Ma, Q. Zhang, H. Hu, K. Qu, S. Xiao, Z. Yang, W. Ca, Engineering oxygen vacancies of cobalt tungstate nanoparticles enable efficient water splitting in alkaline medium, Appl. Catal. B Environ. 259 (2019), 118090, https://doi.org/10.1016/j.apcatb.2019.118090.
[38] X. Gao, et al., Hierarchical NiCo2O4 hollow microcuboids as bifunctional electrocatalysts for overall water-splitting, Angew. Chem., Int. Ed. 55 (2016) 6290–6294, https://doi.org/10.1002/anie.201600525.
[39] F. Song, K. Schenk, X. Hu, A nanoporous oxygen evolution catalyst synthesized by selective electrochemical etching of perovskite hydroxide $CoSn(OH)_6$ nanocubes, Energy Environ. Sci. 9 (2016) 473–477, https://doi.org/10.1039/c5ee03453a.
[40] J. Jiang, C. Zhang, L. Ai, Hierarchical iron nickel oxide architectures derived from metal-organic frameworks as efficient electrocatalysts for oxygen evolution

reaction, Electrochim. Acta 208 (2016) 17–24, https://doi.org/10.1016/j.electacta.2016.05.008.

[41] A. Carbone, R. Pedicini, I. Gatto, A. Saccà, A. Patti, G. Bella, M. Cordaro, Polymers 12 (2020) 283, https://doi.org/10.3390/polym12020283.

[42] I. Gatto, A. Caprì, C. Lo Vecchio, S. Zignani, A. Patti, V. Baglio, Optimal operating conditions evaluation of an anion-exchange-membrane electrolyzer based on FUMASEP® FAA3-50 membrane, Int. J. Hydrogen Energy (2022), https://doi.org/10.1016/j.ijhydene.2022.04.176 in press.

[43] D. Kumar, B. Das, R. Gopalan, B. Singh, Effects of surfactant on the structural and magnetic properties of hydrothermally synthesized NiFe2O4 nanoparticles, Mater. Chem. Phys. 218 (2018) 70–76, https://doi.org/10.1016/j.matchemphys.2018.07.020.

[44] F. Majid, J. Rauf, S. Ata, I. Bibi, A. Malik, S.M. Ibrahim, A. Ali, M. Iqbal, Synthesis and characterization of $NiFe_2O_4$ ferrite: sol–gel and hydrothermal synthesis routes effect on magnetic, structural and dielectric characteristics, Mater. Chem. Phys. 258 (2021), 123888, https://doi.org/10.1016/j.matchemphys.2020.123888.

[45] J. Peng, W. Dong, Z. Wang, Y. Meng, W. Liu, P. Song, Z. Liu, Recent advances in 2D transition metal compounds for electrocatalytic full water splitting in neutral media, Mater. Today Adv. 8 (2020), 100081, https://doi.org/10.1016/j.mtadv.2020.100081.

[46] H. Kim, Switchable p-n gas response for 3D-hierarchical $NiFe_2O_4$ porous microspheres for highly selective and sensitive toluene gas sensors, J. Alloys Compd. 886 (2021), 161281, https://doi.org/10.1016/j.jallcom.2021.161281.

[47] V. Boychuk, R. Zapukhlyak, M. Hodlevsky, V. Kotsyubynsky, Proceedings Surfactant-assisted hydrothermal synthesis of NiFe2O4/reduced graphene oxide composites, Mater. Today Proc. 62 (2022) 5705–5711, https://doi.org/10.1016/j.matpr.2022.01.485.

[48] C. Mahala, M.D. Sharma, M. Basu, 2D nanostructures of $CoFe_2O_4$ and $NiFe_2O_4$: efficient oxygen evolution catalys, Electrochim. Acta 273 (2018) 462–473, https://doi.org/10.1016/j.electacta.2018.04.079.

[49] A. Wu, Y. Xie, H. Ma, C. Tian, Y. Gu, H. Yan, X. Zhang, G. Yang, H. Fu, Integrating the active OER and HER components as the heterostructures for the efficient overall water splitting, Nano Energy 44 (2018) 353–363, https://doi.org/10.1016/j.nanoen.2017.11.045.

[50] K. Karuppasamya, B. Sharma, D. Vikraman, E.-B. Jo, P. Sivakumar, H.-S. Kim, Switchable p-n gas response for 3D-hierarchical $NiFe_2O_4$ porous microspheres for highly selective and sensitive toluene gas sensors, J. Alloys Compd. 886 (2021), 161281, https://doi.org/10.1016/j.jallcom.2021.161281.

[51] P. Hu, L. Yu, A. Zuo, C. Guo, F. Yuan, Fabrication of Monodisperse magnetite hollow spheres, J. Phys. Chem. C 113 (2009) 900–906, https://doi.org/10.1021/jp806406c.

[52] Y. Zhang, Z. Huang, F. Tang, J. Ren, Ferrite hollow spheres with tunable magnetic properties, Thin Solid Films 515 (2006) 2555–2561, https://doi.org/10.1016/j.tsf.2006.04.049.

[53] M.M. Titirici, M. Antonietti, A. Thomas, A generalized synthesis of metal oxide hollow spheres using a hydrothermal approach, Chem. Mater. 8 (2006) 3808–3812, https://doi.org/10.1021/cm052768u, 6.

[54] T.S. Munonde, H. Zheng, M.S. Matseke, P.N. Nomngongo, Y. Wang, P. Tsiakaras, A green approach for enhancing the electrocatalytic activity and stability of $NiFe_2O_4$/CB nanospheres towards hydrogen production, Renew. Energy 154 (2020) 704–714, https://doi.org/10.1016/j.renene.2020.03.022.

[55] P. Balasubramanian, S.-B. He, A. Jansirani, H.-H. Deng, H.-P. Peng, X.-H. Xi, W. Chen, Engineering of oxygen vacancies regulated core-shell N-doped carbon@ $NiFe_2O_4$ nanospheres: a superior bifunctional electrocatalyst for boosting the kinetics of oxygen and hydrogen evaluation reactions, Chem. Eng. J. 405 (2021), 126732, https://doi.org/10.1016/j.cej.2020.126732.

[56] M. Hua, L. Xu, F. Cui, J. Lian, Y. Huang, J. Bao, J. Qiu, Y. Xu, H. Xu, Y. Zhao, H. Li, Hexamethylenetetramine-assisted hydrothermal synthesis of octahedral nickel ferrite oxide nanocrystallines with excellent supercapacitive performance, J. Mater. Sci. 53 (2018) 7621–7636, https://doi.org/10.1007/s10853-018-2052-7.

[57] X. Ma, X. Liu, X. Zhang, C. Piao, Z. Liu, D. Fang, J. Wang, Construction of dual Z-scheme $NiO/NiFe_2O_4/Fe_2O_3$ photocatalyst via incomplete solid state chemical combustion reactions for organic pollutant degradation with simultaneous hydrogen production, Int. J. Hydrogen Energy 46 (2021) 31659–31673, https://doi.org/10.1016/j.ijhydene.2021.07.076.

[58] L. Liu, S. Hu, K. Gao, Natural nanofiber-based stacked porous nitrogen-doped carbon/$NiFe_2O_4$ nanohybrid nanosheets, Cellulose 27 (2020) 1021–1031, https://doi.org/10.1007/s10570-019-02843-w.

[59] J. Eun Park, S.Y. Kang, S.-H. Oh, J.K. Kim, M.S. Lim, C.-Y. Ahn, Y.-H. Cho, Y.-E. Sung, High-performance anion-exchange membrane water electrolysis, Electrochim. Acta 295 (2019) 99–106, https://doi.org/10.1016/j.electacta.2018.10.143.

[60] J. Eun Park, M.-J. Kim, M. Su Lim, S.Y. Kang, J.K. Kim, S.-H. Oh, M. Her, Y.-H. Cho, Y.-E. Sung, Graphitic carbon nitride-carbon nanofiber as oxygen catalyst in anion-exchange membrane water electrolyzer and rechargeable metal–air cells, Appl. Catal., B 237 (2018) 140–148, https://doi.org/10.1016/j.apcatb.2018.05.073.

[61] M. Suc Cha, J.E. Park, S. Kim, S.-H. Han, S.-H. Shin, S.H. Yang, T.-H. Kim, D.M. Yu, S. So, Y.T. Hong, S.J. Yoon, S.-G. Oh, S.Y. Kang, O.-H. Kim, H.S. Park, B. Bae, Y.-E. Sung, Y.-H. Cho, J.Y. Lee, Poly(carbazole)-based anion-conducting materials with high performance and durability for energy conversion devices, Energy Environ. Sci. 13 (2020) 3633–3645, https://doi.org/10.1039/D0EE01842B.

[62] N. Lee, D.T. Duong, D. Kim, Cyclic ammonium grafted poly (arylene ether ketone) hydroxide ion exchange membranes for alkaline water electrolysis with high chemical stability and cell efficiency, Electrochim. Acta 271 (2018) 150–157, https://doi.org/10.1016/j.electacta.2018.03.117.

[63] A. Carbone, S.C. Zignani, I. Gatto, S. Trocino, A.S. Aricò, Assessment of the FAA3-50 polymer electrolyte in combination with a $NiMn_2O_4$ anode catalyst for anion exchange membrane water electrolysis, Int. J. Hydrogen Energy 45 (2020) 9285–9292, https://doi.org/10.1016/j.ijhydene.2020.01.150.

[64] C. Busacca, S.C. Zignani, A. Di Blasi, O. Di Blasi, M. Lo Faro, V. Antonucci, A. S. Aricò, Electrospun $NiMn_2O_4$ and $NiCo_2O_4$ spinel oxides supported on carbon nanofibers as electrocatalysts for the oxygen evolution reaction in an anion exchange membrane-based electrolysis cell, Int. J. Hydrogen Energy 44 (2019) 20987–20996, https://doi.org/10.1016/j.ijhydene.2019.02.214.

[65] I.V. Pushkareva, A.S. Pushkarev, S.A. Grigoriev, P. Modisha, D.G. Bessarabov, Comparative study of anion exchange membranes for low-cost water electrolysis, Int. J. Hydrogen Energy 45 (2019) 26070–26079, https://doi.org/10.1016/j.ijhydene.2019.11.011.

[66] Z. Liu, S. Dawar Sajjad, Y. Gao, H. Yang, J.J. Kaczur, R.I. Masel, The effect of membrane on an alkaline water electrolyzer, Int. J. Hydrogen Energy 42 (2017) 29661–29665, https://doi.org/10.1016/j.ijhydene.2017.10.050.

[67] B. Motealleh, Z. Liu, R.I. Masel, J.P. Sculley, Z. Richard Ni, L. Meroueh, Next-generation anion exchange membrane water electrolyzers operating for commercially relevant lifetimes, Int. J. Hydrogen Energy 46 (2021) 3379–3386, https://doi.org/10.1016/j.ijhydene.2020.10.244.

[68] N. Chen, S.Y. Paek, J.Y. Lee, J.H. Park, S.Y. Lee, Y. Moo Lee, High-performance anion exchange membrane water electrolyzers with a current density of 7.68 A cm^2 and a durability of 1000 hours, Energy Environ. Sci. 14 (2021) 6338–6348, https://doi.org/10.1039/d1ee02642a.

[69] T. Feng, B. Lin, S. Zhang, N. Yuan, F. Chu, M.A. Hickner, C. Wang, L. Zhu, J. Ding, Imidazolium-based organic–inorganic hybrid anion exchange membranes for fuel cell applications, J. Membr. Sci. 508 (2016) 7–14, https://doi.org/10.1016/j.memsci.2016.02.019.

[70] E. López-Fernández, C. Gómez-Sacedón, J. Gil-Rostra, J.P. Espinós, A.R. González-Elipe, F. Yubero, A. de Lucas-Consuegra, Ionomer-Free Nickel-Iron bimetallic electrodes for efficient anion exchange membrane water electrolysis, J. Chem. Eng. 433 (2022), 133774, https://doi.org/10.1016/j.cej.2021.133774.

[71] R.A. Krivina, G.A. Lindquist, S.R. Beaudoin, T.N. Stovall, W.L. Thompson, L. P. Twight, D. Marsh, J. Grzyb, K. Fabrizio, J.E. Hutchison, S.W. Boettcher, Anode catalysts in anion-exchange-membrane electrolysis without supporting electrolyte: conductivity, dynamics, and ionomer degradation, Adv. Mater. 34 (2022), 2203033, https://doi.org/10.1002/adma.202203033.

[72] S.C. Zignani, M. Lo Faro, A. Carbone, C. Italiano, S. Trocino, G. Monforte, A. S. Aricò, Performance and stability of a critical raw materials-free anion exchange membrane electrolysis cell, Electrochim. Acta 413 (2022), 140078, https://doi.org/10.1016/j.electacta.2022.140078.

[73] E. Cossar, A.O. Barnett, F. Seland, R. Safari, G.A. Botton, E.A. Baranova, Ionomer content optimization in nickel-iron-based anodes with and without ceria for anion exchange membrane water electrolysis, J. Power Sources 514 (2021), 230563, https://doi.org/10.1016/j.jpowsour.2021.230563.

[74] P. Fortin, T. Khoza, X. Cao, S.Y. Martinsen, A.O. Barnett, S. Holdcroft, High-performance alkaline water electrolysis using Aemion™ anion exchange membranes, J. Power Sources 451 (2020), 227814, https://doi.org/10.1016/j.jpowsour.2020.227814.

[75] L. Wu, X. Zhou, G. Wan, S. Shi, G. Wang, $NiFe_2O_4$/CNTs fabricated by atomic layer deposition as highly stable peroxidase mimics for sensitive colorimetric detection of hydrogen peroxide and glucose, Mater. Res. Bull. 147 (2022), 111637, https://doi.org/10.1016/j.materresbull.2021.111637.

catalysts

MDPI

Article

Perspective of Use of Pd/rGO in a Direct Urea Microfluidic Fuel Cell

M. P. Gurrola [1,2,*], **J. C. Cruz** [2], **F. I. Espinosa-Lagunes** [3], **A. Martínez-Lázaro** [4], **J. Ledesma-García** [4], **L. G. Arriaga** [3,*] and **R. A. Escalona-Villalpando** [4]

[1] CONACYT-Tecnológico Nacional de México/Instituto Tecnológico de Chetumal, Av. Insurgentes 330, Chetumal 77013, Quintana Roo, Mexico
[2] Tecnológico Nacional de México/Instituto Tecnológico de Chetumal, Av. Insurgentes 330, Chetumal 77013, Quintana Roo, Mexico; jcruz@itchetumal.edu.mx
[3] Centro de Investigación y Desarrollo Tecnológico en Electroquímica, Querétaro 76703, Querétaro, Mexico; fespinosa@cideteq.mx
[4] División de Investigación y Posgrado, Facultad de Ingeniería, Universidad Autónoma de Querétaro, Santiago de Querétaro 76010, Querétaro, Mexico; aleem.lazaro@live.com (A.M.-L.); janet.ledesma@uaq.mx (J.L.-G.)
* Correspondence: mayra.pg@chetumal.tecnm.mx (M.P.G.); larriaga@cideteq.mx (L.G.A.)

Abstract: The urine/urea oxidation reaction through catalysts with a higher performance in direct urea microfluidic fuel cells (DUμFC) is a promising method for power generation due to the large amount of human and animal urine containing 2–2.5 wt% urea. This paper presents a study that used urea as fuel in a DUμFC in the presence of palladium supported by reduced graphene oxide (rGO) for power generation. Some parameters, such as urea, KOH and H_2SO_4 concentration and flux rate, among others, are optimized in order to carry out the evaluation of urine samples as fuel in an air-breathing microfluidic fuel cell. The results show that the Pd/rGo catalyst mixed with Nafion® in the anodic compartment is dispersed and attached to the paper fibers, generating electrical contact and giving rise to the reactions of interest. In addition, XRD analysis confirmed the successful deposition of Pd and rGo on the substrate. These electrochemical results are promising, since, despite the decrease in the general performance of the DUμFC under ideal conditions with respect to normal cells, the generation of energy from urine was demonstrated.

Keywords: UREA oxidation reaction; direct urea microfluidic fuel cell; reduced graphene oxide; palladium; alternative fuel

Citation: Gurrola, M.P.; Cruz, J.C.; Espinosa-Lagunes, F.I.; Martínez-Lázaro, A.; Ledesma-García, J.; Arriaga, L.G.; Escalona-Villalpando, R.A. Perspective of Use of Pd/rGO in a Direct Urea Microfluidic Fuel Cell. *Catalysts* **2023**, *13*, 788. https://doi.org/10.3390/catal13050788

Academic Editors: Jiefang Zhu, Jia Liu and Christian Julien

Received: 9 March 2023
Revised: 17 April 2023
Accepted: 19 April 2023
Published: 22 April 2023

1. Introduction

There are several published works that address the importance of energy production with wastewater treatment as a sustainable alternative through adequate waste management. In this context, urea is a residual compound to be used for wastewater treatment and energy production, because it is a non-toxic, innocuous molecule; is easy to handle; and has a high energy density of 16.9 MJ·L^{-1} [1,2]. Urea is considered an environmental problem due to its decomposition into ammonia and other nitrogenous components [3]. The most common treatments for urea removal are nitrification, denitrification and electrolysis [4]. The use of urea-rich wastewater has received recent attention as an alternative energy source, since a large amount of human and animal urine is produced every day, containing approximately 2–2.5% of urea by weight [5]. The urea oxidation through catalysts is an efficient alternative, since it can also generate energy, as is the case with the direct urea fuel cell (DUFC) [6].

In general, the reactions of the DUFCs have a high open circuit voltage (OCV) of 1.146 V, which is the contribution of the anodic reaction (−0.746 vs. SHE) and cathodic reaction (0.4 vs. SHE) obtained through the use of different catalysts [1,2,7]. There are several metallic catalysts used for the urea oxidation reaction, such as Ni [8,9]; Ni alloys with chalcogenides [10]; metallic mixes, such as $NiCo_2O_4$ [11], Ni-Cu/ZnO, $Ni_{1.5}Mn_{1.5}O_4$, $LaNiO_3$, and Co [12]; or precious metals, such as Pt [13], Ti, Ir, and Ru-TiO2 [1], which display a high performance in basic media. Pd as catalyst is an multifunctional alternative that can be used in DUFCs and the oxidation reaction in alternative fuels, such as glucose [14,15] or alcohols [16], although it has preferentially been used in oxygen reduction reaction as a Pt replacement [1].

In addition to the catalyst, the support is another important factor, since it is able to improve the active surface area and thermal stability and increase the catalytic efficiency. Preferably, carbon materials are used as supports, such as multi-walled carbon nanotubes (MWCNT), carbon nanotubes (CNT), sponges and rGO. In this context, thanks to its unique properties, rGO allows a better distribution of the catalyst, possess excellent electrical conductivity and the efficient collection of electrons generated in the oxidation of the fuel and also has a low cost compared to other carbon materials, which makes this material an excellent candidate to be used as a support [17,18].

For the optimal functioning of the DUFC, an anionic membrane is used, since this type of catalyst improves its performance in alkaline medium. A technological alternative is the use of microfluidic fuel cells (μFC), which have various advantages, such as the elimination of the use of the membrane, the use of different electrolytes in the anolyte and catholyte, the miniaturization of the electronic device, the reduction of manufacturing costs and versatility in the use of catalysts and fuels [19].

The literature related to the direct urea microfluidic fuel cell (DUμFC) is scarce compared to other conventional fuels with excellent prospects for study and application [20,21]. Therefore, in this work, a study of DUμFC was carried out using palladium supported on rGO (Pd/rGO) as anodic catalyst for power generation using urea as fuel and commercial platinum/C-based cathode (Pt/C) for oxygen reduction reaction. An air-breathing type microfluidic fuel cell was used, optimizing the flow rate of electrolytes, urea concentration and anolyte and catholyte concentration. Finally, the microdevice was tested in the presence of a urine sample with the prospect of being used for the remediation of wastewater and energy production [22,23].

2. Physicochemical Characterization

The morphology and microstructure of the Pd/rGO and Pt/C electrodes were investigated by scanning electron microscopy, SEM (JEOL, model JSM-6510LV), equipped with an energy-dispersive spectroscopy detector (EDS, BrukerXFlash 6I10). The crystal structures were measured by X-ray diffraction (XRD; D8-advance diffractometer Bruker) equipped with a CuKα X-ray source (λ = 0.1541 nm, 40 kV, 40 mA), using a step size of 0.02° 2θ and a scan step time of 5 s. The electronic structure of the elements was measured by X-ray photoelectron spectroscopy (XPS; K-Alpha+ spectrometer equipped with the Avantage Data System from Thermo Scientific^{TM}).

3. Results and Discussion

3.1. Physical Characterization

The anode and cathode surfaces of the electrodes corresponding to Pd/rGO and commercial Pt/C, respectively, were examined by SEM as is illustrated in Figure 1a. This figure shows different increments, where it can be seen, in both cases, that the electrocatalytic material is deposited on the Toray paper fibers, which is distinguished by its intense brightness. In the case of the anode, it can be seen that the mixture of Pd/rGo with Nafion® is dispersed and attached to the paper fibers, generating good electrical contact between the electrode and the supported catalyst particles [24]. In addition, it is also possible to observe that the catalytic mixture is embedded in the binder, which translates to a certain resistance to the flow of electrons [25,26]. In the case of the cathode, it can be seen that the electrocatalytic material presents a good dispersion and, therefore, the ability to react.

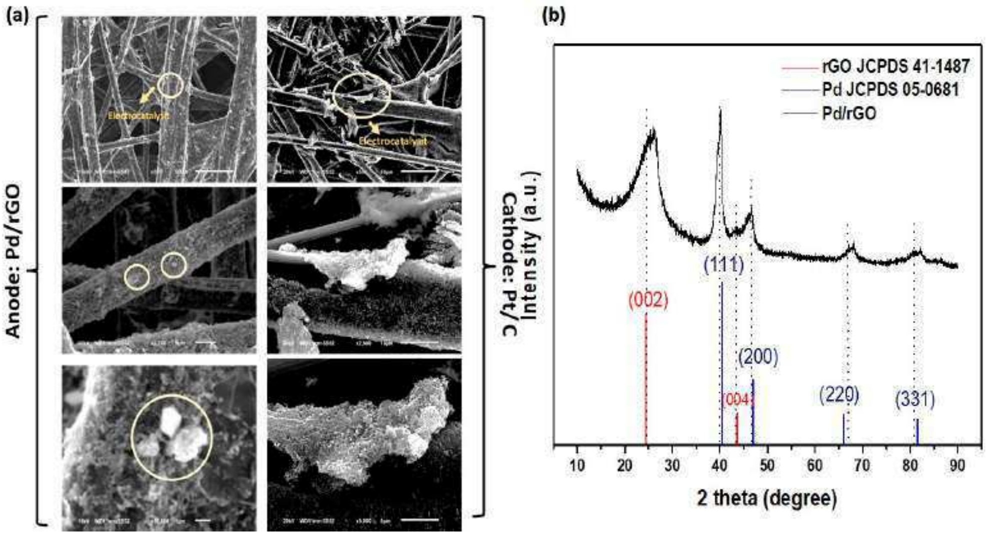

Figure 1. (**a**) SEM images of the electrodes (anode and cathode). (**b**) powder X-ray diffraction (XRD) pattern of Pd/rGO.

XRD patterns of Pd/rGO nanoparticles are presented in Figure 1b. The main diffraction peaks of Pd are observed at $2\theta = 40°$, 46.7°, 68.1° and 82.2°, corresponding to files (111), (200), (220) and (311), respectively, and also corresponding to files JPDS:41-1487 and JCPDS 05-0681, respectively. It is possible to observe two peaks for rGO at $2\theta = 26.1°$ and 43.5°. Through Rietveld's refinement analysis, the adjustment of the signals using the parameters of the crystallographic database (COD data) was performed, where the Bragg equation and the Scherrer equation were used to determine FWHM and the particle size of the mean peak of the Pd/rGO, where the average value of the crystallite size was 6.40 nm, with a microstrain of 3.41×10^{-3} and dislocation density of 49.13×10^{-3} nm^{-2}. For more details, see Figure S1 and Tables S1 and S2 in the Supplementary Materials. The maximum in the diffractogram can be related to the most probable intersegmental distance (spacing d) between the rGO and Pd using the Bragg equation, which is given in (111). The spacing d showed slight growth depending on the content of rGO chains; this can be attributed to the presence of bulky carbon chain units, which restricted the free rotation of the chains and hindered dense packing, which is observed at $2\theta = 26.1°$ [27].

Using the X-ray photoelectron spectroscopy technique (XPS), an analysis of Pd/rGO was performed to determine the chemical composition and oxidation state before and after of the evaluation of the electrocatalyst in the microfluidic fuel cell, and the comparison is presented in Figure 2. In Figure 2a the presence of C, Pd and O can be appreciated, which is typical of the material synthesis under study. However, a slight change in the intensity of peaks is observed for the analysis post-evaluation of the microfluidic cell, with greater material oxidation. The spectra of Pd 3d can be seen in Figure 2b, where a comparative analysis of the oxidation states present in the synthesis of Pd/rGO and those present after the analysis of the microfluidic cell is performed and can be seen to be deconvolution orbitals in Pd 3d 5/2 and Pd 3d 3/2, with the peaks of 335.1 eV and 340.8 eV corresponding to Pd^0. In comparison, those located at 336.25 eV and 342.5 correspond to Pd^{2+} [14,28], so they are attributed to a change in the oxidation state that constitutes the Pd/PdO structure for the Pd/rGO sample. A higher concentration of Pd^0 is observed in Pd/rGO, according to electrochemical analysis, where the corresponding oxidation peaks of the material are observed, due to the presence of rGO, which contributes to the stability of the catalyst. However, for the subsequent analysis, there is a ±5 displacement of the signals in the energy band, revealing a higher concentration of Pd^{2+} and, therefore, a greater oxidation of Pd^0.

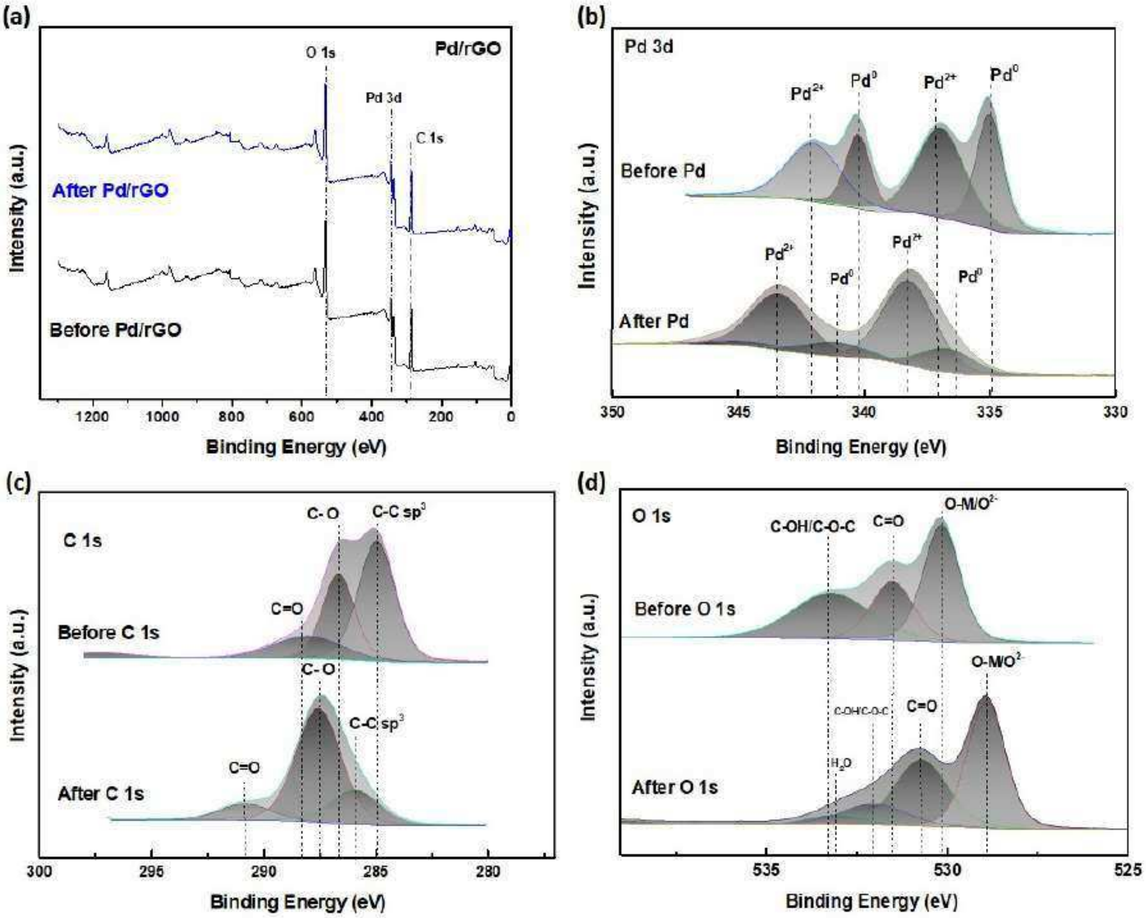

Figure 2. Comparison of high-resolution XPS of Pd/rGO before and after evaluation of DUμFC performance. (**a**) General spectra of Pd/rGO; (**b**) spectra in the Pd 3d; (**c**) spectra in the C 1 s region; and (**d**) spectra in the O 1 s region.

The comparison of the spectra of C 1 s is presented in Figure 2c, which indicates the oxidation degree with three components corresponding to C atoms in different functional groups: the non-oxygenated ring C-C at 284.3 eV, the C atom at the C-O bond at 286.3 eV and the carbonyl C=O at 288.1 eV [29], for both samples. The spectrum showed the same functional groups but with reduced intensities and displaced peak positions in the oxygen-containing groups. Therefore, this can be attributed to the composition of rGO, where the C-O ratio presents a higher proportion due to the elimination of oxygen-containing functional groups caused by the presence of the Pd^0 state before and after the evaluation of the microfluidic cell's performance.

Finally, Figure 2d presents the comparison of the spectra of O 1 s, which indicates the presence of bonds with Pd and rGO, respectively: when analyzing the oxygen-containing functional groups, an increase in sp^2 networks in the basal plane of rGO was observed, as well as the presence of H_2O post-evaluation of the microfluidic device. These changes in chemical functionalities decrease the stability of rGO in an aqueous solution, increasing the tendency of rGO agglomeration with each other [30]. However, rGO could be well dispersed in a high pH solution since the carboxylic groups at the edge of rGO can be deprotonated to provide repulsive charges by containing the interaction with Pd^0 and Pd^{2+} observed in this type of material.

Through the XPS analysis performed, it was possible to conclude the elemental composition, the oxidation states present in the synthesis of Pd/rGO and the concentration ratio, which is involved in the physicochemical techniques outlined in this work.

3.2. Effect of Electrolyte Flow Rate on Cell Performance

Microfluidic fuel cell tests were performed by varying the flow rate in the system. In Figure 3, it can be observed that 150 μL min^{-1} was the flow rate value for which a current density limit and stable maximum power density were obtained, since, when increasing the flow rate to 200 μL min^{-1}, although maximum power density (P_{max}) is maintained, current density (j_{lim}) decreases. This is probably due to the urea oxidation reaction kinetics, where for flows of less than 150 μL min^{-1}, the current limit decreased, since the urea reaching the surface of Pd is quickly consumed before more fuel arrives to be oxidized, primarily due to reduced concentration polarization because of improved mass transfer. In addition, the microfuel cell throughput of flow-through cases remains relatively constant beyond 50 μL min^{-1}, indicating that cell throughput is limited by reaction kinetics [31].

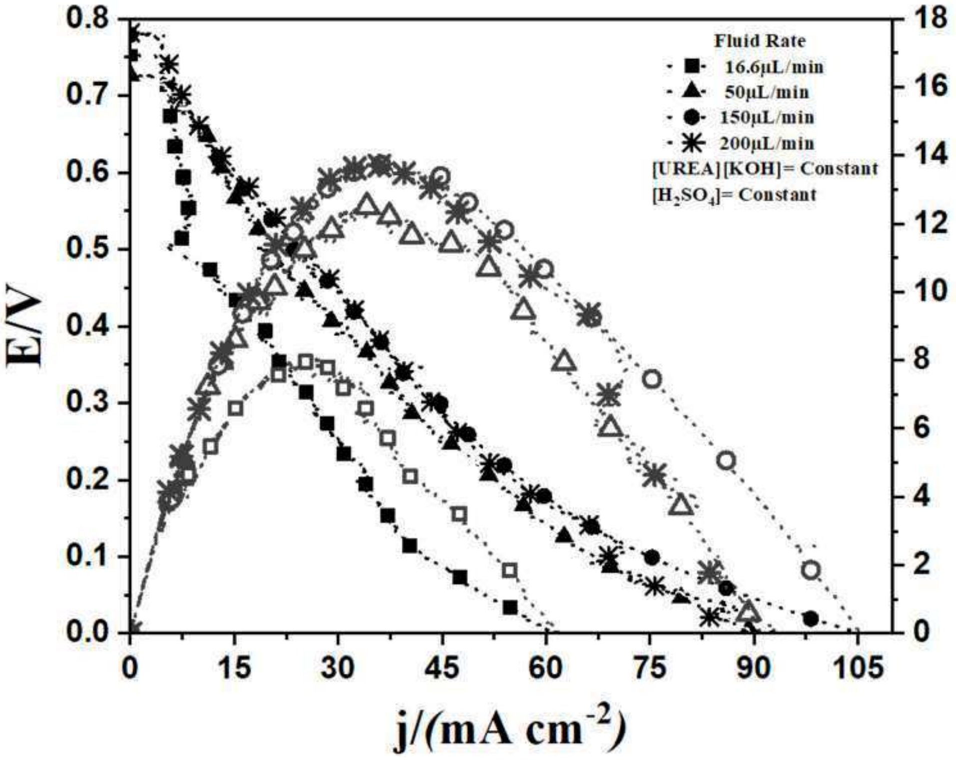

Figure 3. DUμFC performance under different flow rates, using 5 M urea in 1 M KOH and 1 M H_2SO_4 as the anolyte and catholyte, respectively, and applying 10 mV s^{-1} as the polarization curve.

3.3. Effect of Fuel and Anolyte/Catholyte Concentration on DUμFC Performance

DUμFC performance as a function of the variation of anolyte, catholyte and fuel concentration is presented in Figure 4a. All tests were carried out at 50 μL min^{-1} flow rate, which showed the best performance, as seen in Figure 3. Figure 4a shows the effect generated by the increase in fuel concentration on the limit of j_{lim}, where this parameter presents a linear increase from [Urea] = 0.1 M to 1 M, reaching values from 17.2 to 43 mA cm^{-2}. For [Urea] > 1 M and up to 5 M, j_{lim} presented no significant change, until around 42 mA cm^{-2}; this is because at [Urea] = 1 M, the saturation had been reached in the Pd nanoparticles and, due to the pH conditions given by the anolyte, is not possible to improve the urea oxidation kinetics. On the other hand, P_{max} presented a linear increase with respect to [Urea], as, due to the increase in fuel, the [Ox]/[Red] ratio is modified, improving the voltage of the cell and favoring the P_{max} reached, since $P = j_{cell} \cdot E_{cell}$, thus achieving a P_{max} = 7.52 mW cm^{-2} at [Urea] = 5 M. Additionally, it is possible to appreciate an increase in the limit current value and P_{max} when the fuel concentration raises up to a value of j_{lim} = 34.72 mA cm^{-2} and P_{max} = 7.14 mW cm^{-2}, respectively. This behavior is to be expected, since there is a greater number of active species exposed to the respective oxidation, and the OCV increases as the fuel concentration increases, which is also to be expected, achieving a maximum value of E = 0.71 V at [Urea] = 5 M at the limit current.

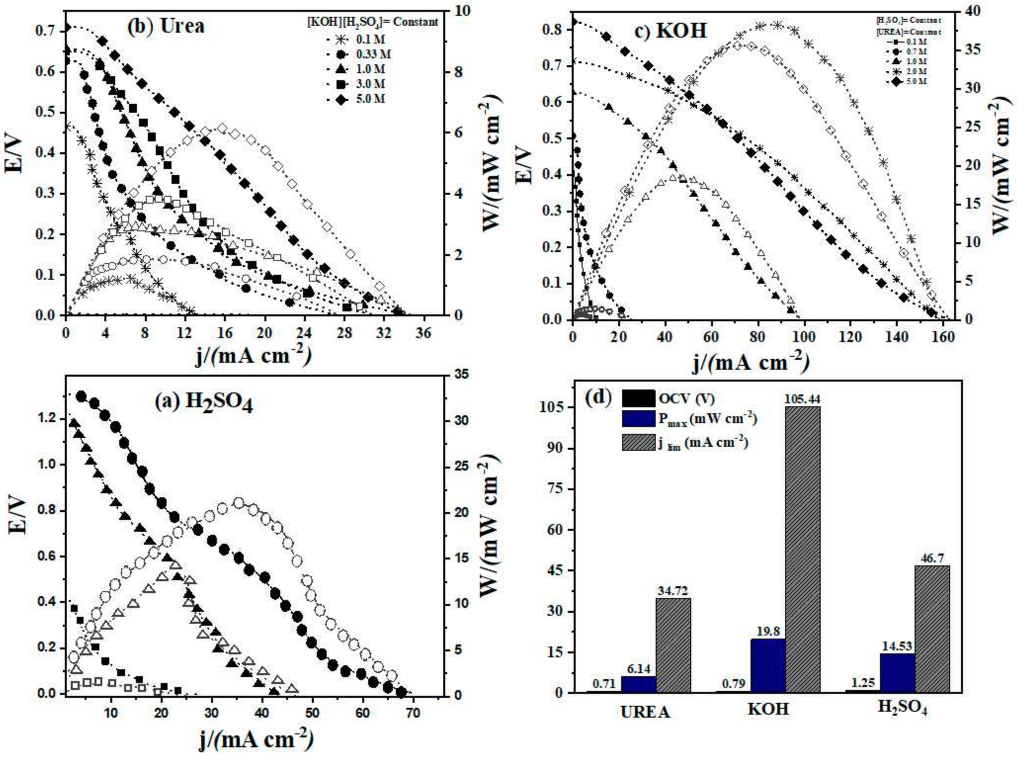

Figure 4. DUμFC performance under different conditions: (**a**) [Urea] variation at a constant anolyte and catholyte concentration; (**b**) [KOH] variation at a constant fuel and catholyte concentration; (**c**) [H_2SO_4] variation and constant anolyte concentration; (**d**) current density limit (j_{lim}), OCV and maximum density (P_{max}) under different conditions.

Figure 4b shows the DUμFC performance as a function of the variation of [KOH], keeping the urea and H_2SO_4 concentration constant. It is possible to observe that the increase in the potassium hydroxide concentration substantially favors the limit current. It is evident that the concentration of the electrolyte has a significant impact on the urea oxidation, since, according to the literature, 6 OH^- groups are necessary to attack the partially positive groups in the urea molecule (C from the C=O group and the two Ns of the NH_2 groups). Once the urea molecule has been attacked by -OH ions, the C-N and N-H bonds can be broken, forming N_2, CO_2 and 5 H_2O [32–34]. Unlike nickel, which is the most widely used electrocatalyst for urea oxidation, palladium presents greater resistance to CO poisoning [35], which is an intermediate by-product of the urea oxidation process. Therefore, with the increase in the KOH concentration, j_{lim} = 198 mA cm^{-2} and P_{max} = 43.68 mW cm^{-2} can be reached.

On the other hand, by increasing [H_2SO_4] to 1 M, it was possible to increase the OCV up to around to 1.3 V (Figure 4c). This is probably due to the fact that, by increasing the acid nature of the cathodic side, extra energy from the neutralization process is provided for both supporting electrolytes [36] and an increase of j_{lim} = 94.86 mA cm^{-2} and P_{max} = 29.64 mW cm^{-2} is reached. Finally, in Figure 4d, the current, power and performance efficiency of the DUμFC on the OCV are compared when varying fuel, analyte and catholic concentrations. It can be seen that the variation of [KOH] has a greater effect on the increase in overall performance of the DUμFC without the fuel saturation that could poison the catalysts or the production of H_2SO_4 that could generate a greater amount of K_2SO_4 at the interface when mixed with KOH [7,37].

3.4. Evaluation of Urine Sample as Fuel

Figure 5 shows the DUµFC performance using human urine (from two healthy voluntary donors) as fuel, reaching OCV, j_{lim} and P_{max} values of 0.45 V, 27 mA cm^{-2} and 1.76 mW cm^{-2}, respectively. Decreases in overall performance may be due to anolyte pH changes, different ionic strengths of the anolyte, adsorbed species on the anode catalyst and different oxidation potentials of organic molecules present in the urine. These results are promising since, despite the decrease in the overall performance of DUµFC under ideal conditions in contrast to real conditions, the generation of energy in urine was possible to achieve, which is a significant contribution of DUµFC since, at present, not all applications using urea from urine as fuel have succeeded in this [6,38].

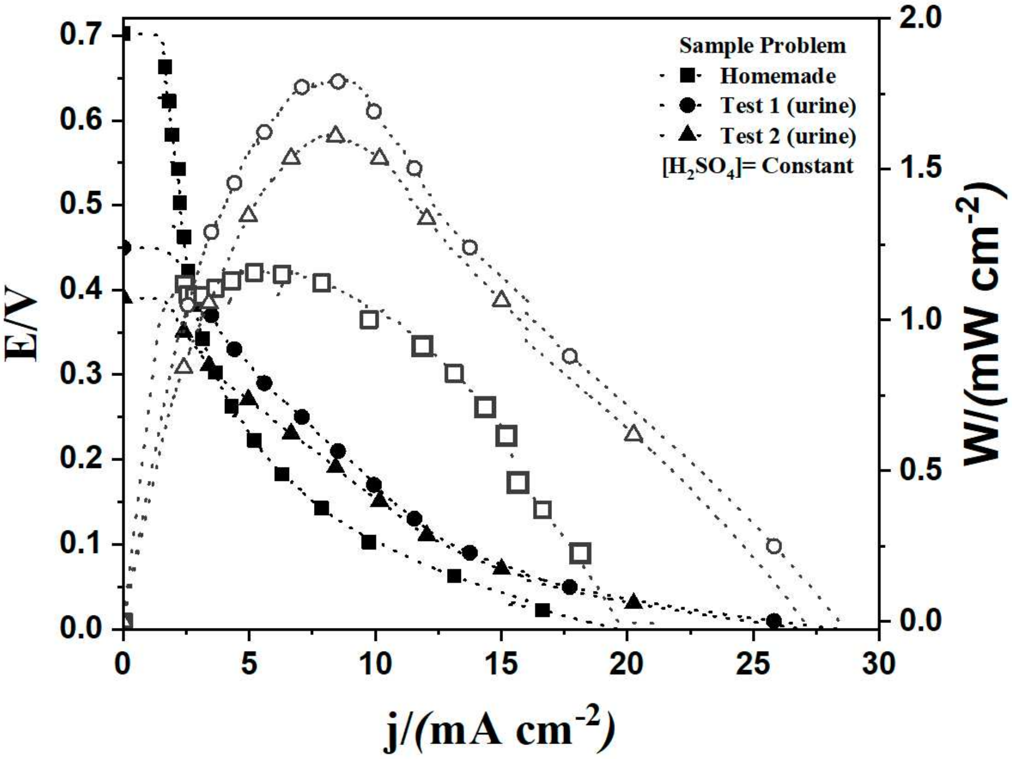

Figure 5. DUµFC performance using urea from urine as fuel.

4. Materials and Methods

4.1. Construction of the DUµFC

For the elaboration of the electrodes, firstly, two catalytic inks were prepared for the anodic compartment, Pd/rGO, 50:50 wt% (home-made), according to Morales-Acosta et al. [39], while for the cathodic chamber, 20% Pt/Vulcan XC-72 (Fuel Cell, Texas, USA) commercial was used. The preparation of both inks was carried out directly in an ultrasonic bath through the aqueous dispersion of 5.0 mg of the catalytic mixture (catalyst/support), 35 µL of Nafion® (5% Electrochem, State Mx, Mexico) and 365 µL of isopropyl alcohol (J.T. Baker CDMX, Mexico). The resulting inks were deposited in the electrode matrix (Toray Paper, Fuel Cell, Texas, USA) by the spray technique, employing an airbrush until the base metal loading was 0.6 mg (see Scheme 1) [40,41]. The microfuel cell µFC design used in this study was derived from the previously published works of the our research group [19,42,43]. Briefly, three-dimensional electrodes of 30 mm × 2 mm × 0.164 mm length, width and thickness were manufactured using Carbon Toray Paper. The µFC was sandwiched by two supporting plates fabricated from polymethyl methacrylate (PMMA) using a micro milling system CNC (computer numerical control), and the top plate had one outlet for the reaction by-products. The bottom plate had an air-breathing window of 20 mm × 2 mm for the take-up of oxygen from the air and two additional inlets for oxidant and fuel electrolytes. The microchannel and gaskets were fabricated of a silicone elastomer film using an Elcometer® Film Applicator (Elcometer, N.L., Mexico) with a final thickness of approximately 600 µm and were traced using a Silhouette® cutting plotter (Silhuette, CDMX, Mexico) (Scheme 1).

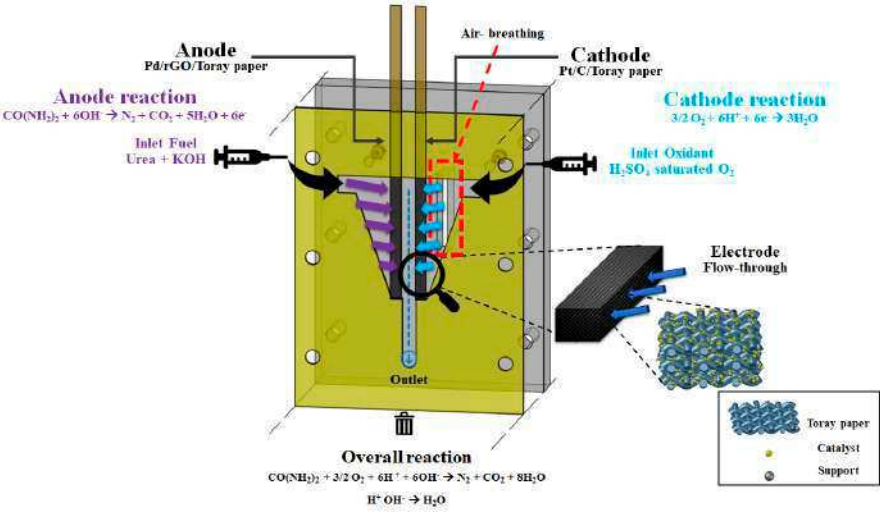

Scheme 1. Schematic illustration of the DUµFC configuration. The operation in flow-through electrolytes with independent inlets and the coupling of the catalysts.

4.2. Direct Urea Microfluidic Fuel Cell Operation

For the evaluation of the device, the analysis of Zhang et al. [20] and the logic analysis of Zou et al. [36] were considered. Based on these analyses as a starting point, it was possible to couple dual acid-base reactions for a DUµFC by neutralizing reactions in the double electrolyte configuration Reaction (4). An anodic reaction of a typical DUFC Reaction (1) and its respective cathodic reaction in an acid medium Reaction (2) was considered. It was possible to obtain an OCV of E = 1.976 V according to the overall reaction Reaction (3), but it was different to that presented in Reaction (4), since it included acid-base neutralization reactions [25]. According to Nernst equation, the voltage generated by the combination of OH^- ions with H^+ ions to form water is equal to E = 0.83 V, under standard conditions [44]. In an direct urea fuel cell/(O_2, H^+), a higher voltage of E = 1.976 V with an additional energy of E = 0.83 V, compared to the direct urea fuel cell/(O_2, OH^-), can be obtained; therefore, it can be interpreted as the energy of the electrochemical neutralization reaction [1] and can be applied to produce energy, favoring the urea energy conversion (Scheme 1).

Anode reaction:

$$\begin{gathered} CO(NH_2)_2 + 6OH^- \rightarrow N_2 + CO_2 + 5H_2O + 6e^- \\ -E^0 = -0.746 \text{ V vs. SHE} \end{gathered} \tag{R1}$$

Cathode reaction in acid medium:

$$\begin{gathered} \tfrac{3}{2}O_2 + 6H^+ + 6e^- \rightarrow 3H_2O \\ E^0 = +1.23 \text{ V vs. SHE} \end{gathered} \tag{R2}$$

Overall reaction for the urea/(O_2, H^+) fuel cell:

$$\begin{gathered} CO(NH_2)_2 + \tfrac{3}{2}O_2 + 6H^+ + 6OH^- \rightarrow N_2 + CO_2 + 8H_2O \\ \Delta E^0 = +1.976 \text{ V vs. SHE} \end{gathered} \tag{R3}$$

$$\begin{gathered} H^+ + OH^- \rightarrow H_2O \\ \Delta E^0 = +0.83 \text{ V} \end{gathered} \tag{R4}$$

Different reaction conditions were used to improve the DUμFC performance by modifying flow rates, fuel concentration, anolytes and catholytes. Both currents, anodic and cathodic, were optimized according to Table 1, and the catholyte stream consisted of saturated O_2.

Table 1. Variations of the parameters for the anodic and cathodic current optimizations of the DUμFC.

Fuel (Urea)/mol L^{-1}	**Anolyte (KOH)/mol L^{-1}**	**Catholyte (H_2SO_4)/mol L^{-1}**
[KOH] = 0.5 M, [H_2SO_4] = 1 M	[$Urea_{Optimal}$]= 5 M, [H_2SO_4] =1 M	[$KOH_{Optimal}$] = 3 M, [$Urea_{Optimal}$] = 5 M
0.1	0.1	0.5
1	0.3	1
3	0.5	1.5
5	0.7	
	1	
	2	
	3	

Oxidant and fuel solutions were fed at a 50 μL min^{-1} flow rate by means two Single-Syringe Infusion Pumps (NE-4000, New Era Pump Systems, Inc, NY USA). Current collectors were cut from a commercial foil (Alumark 50 CDMX, Mexico). In the case of a flow rate effect (1:1), the flow rates were 16.66, 50, 100, 150 and 200 μL min^{-1}. After optimizing system parameters with urea as fuel, urine samples from two voluntary donors were evaluated for the anodic component, while, for the cathode, 1 M H_2SO_4 was used. All solutions were prepared with deionized water DI ($\rho \geq 18$ MΩ cm). Polarization curves were recorded at 10 mV s^{-1} using a BioLogicSAS (Science Instruments, Model VSP, Knoxville, TN, USA). All the evaluations were performed at room temperature with a one-to-one KOH–urine ratio.

5. Conclusions

The performance of a composite based on Pd/rGo, prepared on Carbon Toray Paper using the spray technique, was evaluated. SEM evaluation showed that the mixture of Pd/rGo with Nafion® in the anodic component was dispersed and attached to the paper fibers, generating good electrical contact. XRD analysis confirmed the successful deposition of Pd and rGO on the substrate. XPS was able to verify a possible change in the oxidation states of Pd and C in Pd/rGO, where an oxido-reduction process was executed due to the operation of the electrocatalyst in a DUμFC, resulting in 80% of the oxidized material (Pd^{2+}) available, demonstrating the high stability of the material. Likewise, variables such as Urea, KOH and H_2SO_4 concentration were also assessed, with the aim of optimizing parameters in the system to be able to compare them with a human urine sample. Based on the above, it was possible to observe that the greatest effect in the system under study was generated by the variation of KOH concentration in the fuel, achieving values of P_{max} = 19.8 mW cm^{-2} and j_{lim} =105.44 mA cm^{-2} and, when compared to a real urine sample, these values decreased.

The obtained results have an effect on the performance of the system associated with the different ionic strengths of the anolyte, adsorbed species on the anode catalyst and the different oxidation potentials of organic molecules present in the urine. However, these results are promising since, despite the decrease in the overall DUμFC performance under ideal conditions vs. real conditions, it was possible to generate energy from urine, which is a significant contribution to DUμFCs research, since, at present, not all applications using urea from urine as fuel have successfully achieved this.

Supplementary Materials: The following supporting information can be downloaded at: https://www.mdpi.com/article/10.3390/catal13050788/s1, Figure S1: Rietveld refinement Pd/rGO; Figure S2: Current density limit and maximum power density for (a) urea concentration variation, (b) anolyte concentration variation and (c) catholyte concentration variation; Table S1: Calculation of crystallite size from XRD data using Rietveld refinement; Table S2: Calculation of the microstrain and dislocation density from XRD data using Rietveld refinement; Table S3: Calculation of the crystallographic parameter from XRD data using COD data.

Author Contributions: Conceptualization, R.A.E.-V., M.P.G. and J.C.C.; methodology, R.A.E.-V., M.P.G., J.L.-G. and L.G.A.; software, R.A.E.-V. and F.I.E.-L.; formal analysis, R.A.E.-V., F.I.E.-L., M.P.G., L.G.A. and J.L.-G.; investigation R.A.E.-V., M.P.G. and J.C.C.; resources, J.L.-G. and M.P.G.; visualization, R.A.E.-V., F.I.E.-L. and M.P.G.; writing—original draft preparation, R.A.E.-V., F.I.E.-L., L.G.A., A.M.-L. and J.L.-G.; writing—review and editing R.A.E.-V., M.P.G., L.G.A., A.M.-L. and J.L.-G.; supervision, R.A.E.-V., M.P.G. and L.G.A.; funding acquisition, J.L.-G. and M.P.G. All authors have read and agreed to the published version of the manuscript.

Funding: This research received no external funding.

Data Availability Statement: Not applicable.

Acknowledgments: The authors acknowledge the Mexican Council for Science and Technology (CONACYT) for the financial support through the Project Ciencia de Frontera (Frontier Science) 2019, grant No. 845132; Chairs-CONACYT—Project Number 746; and the National Laboratories 2023-321116 for their technical support.

Conflicts of Interest: The authors declare no conflict of interest. The funders had no role in the design of the study; in the collection, analyses, or interpretation of data; in the writing of the manuscript; or in the decision to publish the results.

References

1. Sayed, E.T.; Eisa, T.; Mohamed, H.O.; Abdelkareem, M.A.; Allagui, A.; Alawadhi, H.; Chae, K.J. Direct Urea Fuel Cells: Challenges and Opportunities. *J. Power Sources* **2019**, *417*, 159–175. [CrossRef]
2. Lan, R.; Tao, S.; Irvine, J.T.S. A Direct Urea Fuel Cell—Power from Fertiliser and Waste. *Energy Environ. Sci.* **2010**, *3*, 438–441. [CrossRef]
3. Wang, J.H.; Zhuang, L.L.; Xu, X.Q.; Deantes-Espinosa, V.M.; Wang, X.X.; Hu, H.Y. Microalgal Attachment and Attached Systems for Biomass Production and Wastewater Treatment. *Renew. Sustain. Energy Rev.* **2018**, *92*, 331–342. [CrossRef]
4. Wang, J.; Li, S.; Guo, S.; Ma, C.; Wang, J.; Sun, J. Analysis of Heat Transfer Properties of Hollow Block Wall Filled by Different Materials in Solar Greenhouse. *Eng. Agric. Environ. Food* **2017**, *10*, 31–38. [CrossRef]
5. Ishii, S.K.L.; Boyer, T.H. Life Cycle Comparison of Centralized Wastewater Treatment and Urine Source Separation with Struvite Precipitation: Focus on Urine Nutrient Management. *Water Res.* **2015**, *79*, 88–103. [CrossRef] [PubMed]
6. Hao, J.; Zhao, S.; Mao, R.; Zhao, X. Nickel Phosphide on Ni Foam as Anode and Peroxymonosulfate as the Chemical Oxidizer for Effective Direct Urea Fuel Cell. *J. Environ. Sci.* **2021**, *110*, 84–91. [CrossRef]
7. Kim, O.H.; Choi, H.J.; Kang, S.Y.; Jang, G.Y.; Karuppannan, M.; Park, J.E.; Sung, Y.E.; Kwon, O.J.; Cho, Y.H. Towards Outstanding Performance of Direct Urea Fuel Cells through Optimization of Anode Catalyst Layer and Operating Conditions. *J. Electroanal. Chem.* **2022**, *921*, 116661. [CrossRef]
8. Ghanem, M.A.; Al-Mayouf, A.M.; Singh, J.P.; Arunachalam, P. Concurrent Deposition and Exfoliation of Nickel Hydroxide Nanoflakes Using Liquid Crystal Template and Their Activity for Urea Electrooxidation in Alkaline Medium. *Electrocatalysis* **2017**, *8*, 16–26. [CrossRef]
9. Ma, Y.; Ma, C.; Wang, Y.; Wang, K. Advanced Nickel-Based Catalysts for Urea Oxidation Reaction: Challenges and Developments. *Catalysts* **2022**, *12*, 337. [CrossRef]
10. Sayed, E.T.; Abdelkareem, M.A.; Bahaa, A.; Eisa, T.; Alawadhi, H.; Al-Asheh, S.; Chae, K.J.; Olabi, A.G. Synthesis and Performance Evaluation of Various Metal Chalcogenides as Active Anodes for Direct Urea Fuel Cells. *Renew. Sustain. Energy Rev.* **2021**, *150*, 111470. [CrossRef]
11. Ranjani, M.; Senthilkumar, N.; Gnana Kumar, G.; Manthiram, A. 3D Flower-like Hierarchical NiCo2O4 Architecture on Carbon Cloth Fibers as an Anode Catalyst for High-Performance, Durable Direct Urea Fuel Cells. *J. Mater. Chem. A* **2018**, *6*, 23019–23027. [CrossRef]
12. Sayed, E.T.; Abdelkareem, M.A.; Alawadhi, H.; Olabi, A.G. Enhancing the Performance of Direct Urea Fuel Cells Using Co Dendrites. *Appl. Surf. Sci.* **2021**, *555*, 149698. [CrossRef]
13. Pierozynski, B. Electrochemical Behaviour of Urea at Pt (111) Single-Crystal Surface in 0.1 M NaOH. *Electrocatalysis* **2013**, *4*, 37–41. [CrossRef]
14. Hassan, K.M.; Khalifa, Z.; Elhaddad, G.M.; Abdel Azzem, M. The Role of Electrolytically Deposited Palladium and Platinum Metal Nanoparticles Dispersed onto Poly(1,8-Diaminonaphthalene) for Enhanced Glucose Electrooxidation in Biofuel Cells. *Electrochim. Acta* **2020**, *355*, 136781. [CrossRef]

15. Zhiani, M.; Abedini, A.; Majidi, S. Comparison of Electro-Catalytic Activity of Fe-Ni-Co/C and Pd/C Nanoparticles for Glucose Electro-Oxidation in Alkaline Half-Cell and Direct Glucose Fuel Cell. *Electrocatalysis* **2018**, *9*, 735–743. [CrossRef]
16. Fashedemi, O.O.; Mwonga, P.V.; Miller, H.A.; Maphanga, R.R.; Vizza, F.; Ozoemena, K.I. Performance of Pd@FeCo Catalyst in Anion Exchange Membrane Alcohol Fuel Cells. *Electrocatalysis* **2021**, *12*, 295–309. [CrossRef]
17. Wang, Y.; Liu, G. Reduced Graphene Oxide Supported Nickel Tungstate Nano-Composite Electrocatalyst for Anodic Urea Oxidation Reaction in Direct Urea Fuel Cell. *Int. J. Hydrogen Energy* **2020**, *45*, 33500–33511. [CrossRef]
18. Lera, I.L.; Khasnabis, S.; Wangatia, L.M.; Olu, F.E.; Ramamurthy, P.C. Insights into the Electrochemical Behavior and Kinetics of NiP@PANI/RGO as a High-Performance Electrode for Alkaline Urea Oxidation. *Electrocatalysis* **2022**, *13*, 283–298. [CrossRef]
19. Gurrola, M.P.; Escalona-Villalpando, R.A.; Arjona, N.; Ledesma-García, J.; Arriaga, L.G. Microfluidic Fuel Cells. In *Encyclopedia of Electrochemistry*; Wiley: Hoboken, NJ, USA, 2021; pp. 1–16. ISBN 9783527610426.
20. Zhang, H.; Wang, Y.; Wu, Z.; Leung, D.Y.C. A Direct Urea Microfluidic Fuel Cell with Flow-through Ni-Supported-Carbon-Nanotube-Coated Sponge as Porous Electrode. *J. Power Sources* **2017**, *363*, 61–69. [CrossRef]
21. Chino, I.; Muneeb, O.; Do, E.; Ho, V.; Haan, J.L. A Paper Microfluidic Fuel Cell Powered by Urea. *J. Power Sources* **2018**, *396*, 710–714. [CrossRef]
22. Ibrahim, O.A.; Navarro-Segarra, M.; Sadeghi, P.; Sabaté, N.; Esquivel, J.P.; Kjeang, E. Microfluidics for Electrochemical Energy Conversion. *Chem. Rev.* **2022**, *7*, 7236–7266. [CrossRef] [PubMed]
23. Wang, Y.; Luo, S.; Kwok, H.Y.H.; Pan, W.; Zhang, Y.; Zhao, X.; Leung, D.Y.C. Microfluidic Fuel Cells with Different Types of Fuels: A Prospective Review. *Renew. Sustain. Energy Rev.* **2021**, *141*, 110806. [CrossRef]
24. Mao, R.; Zhao, X.; Lan, H.; Liu, H.; Qu, J. Efficient Electrochemical Reduction of Bromate by a Pd/RGO/CFP Electrode with Low Applied Potentials. *Appl. Catal. B Environ.* **2014**, *160–161*, 179–187. [CrossRef]
25. Liu, Y.; Liu, L.; Shan, J.; Zhang, J. Electrodeposition of Palladium and Reduced Graphene Oxide Nanocomposites on Foam-Nickel Electrode for Electrocatalytic Hydrodechlorination of 4-Chlorophenol. *J. Hazard. Mater.* **2015**, *290*, 1–8. [CrossRef] [PubMed]
26. Li, J.; Zhou, P.; Li, F.; Ren, R.; Liu, Y.; Niu, J.; Ma, J.; Zhang, X.; Tian, M.; Jin, J.; et al. Ni@Pd/PEI-RGO Stack Structures with Controllable Pd Shell Thickness as Advanced Electrodes for Efficient Hydrogen Evolution. *J. Mater. Chem. A* **2015**, *3*, 11261–11268. [CrossRef]
27. Ge, L.; Zhang, M.; Wang, R.; Li, N.; Zhang, L.; Liu, S.; Jiao, T. Fabrication of CS/GA/RGO/Pd Composite Hydrogels for Highly Efficient Catalytic Reduction of Organic Pollutants. *RSC Adv.* **2020**, *10*, 15091–15097. [CrossRef]
28. Zhang, J.W.; Zhang, B.; Zhang, X. Enhanced Catalytic Activity of Ternary NiCoPd Nanocatalyst Dispersed on Carbon Nanotubes toward Methanol Oxidation Reaction in Alkaline Media. *J. Solid State Electrochem.* **2017**, *21*, 447–453. [CrossRef]
29. Wagner, C.D.; Riggs, W.M.; Davis, L.E.; Moulder, J.F.; Muilenberg, G.E. Handbook of X-Ray Electron Spectroscopy. *Perkin-Elmer Corp.* **1979**, *192*, 72–73.
30. Shin, Y.-E.; Sa, Y.J.; Park, S.; Lee, J.; Shin, K.-H.; Joo, S.H.; Ko, H. An Ice-Templated, PH-Tunable Self-Assembly Route to Hierarchically Porous Graphene Nanoscroll Networks. *Nanoscale* **2014**, *6*, 9734–9741. [CrossRef]
31. Jaleh, B.; Nasrollahzadeh, M.; Eslamipanah, M.; Nasri, A.; Shabanlou, E.; Manwar, N.R.; Zboril, R.; Fornasiero, P.; Gawande, M.B. The Role of Carbon-Based Materials for Fuel Cells Performance. *Carbon N. Y.* **2022**, *198*, 301–352. [CrossRef]
32. Guo, Y.; Liu, X.; Li, Y.; Ma, F.; Zhang, Q.; Wang, Z.; Liu, Y.; Zheng, Z.; Cheng, H.; Huang, B.; et al. Anion-Modulation in CoMoO4 Electrocatalyst for Urea-Assisted Energy-Saving Hydrogen Production. *Int. J. Hydrogen Energy* **2022**, *47*, 33167–33176. [CrossRef]
33. Wang, C.; Du, X.; Zhang, X. Controlled Synthesis of Fe Doped NiCoM (M=O, P, S and Se) as Robust Electrocatalyst for Urea Electrolysis. *J. Alloys Compd.* **2022**, *928*, 167094. [CrossRef]
34. Durrani, S.K.; Naz, S.; Mehmood, M.; Nadeem, M.; Siddique, M. Structural, Impedance and Mössbauer Studies of Magnesium Ferrite Synthesized via Sol–Gel Auto-Combustion Process. *J. Saudi Chem. Soc.* **2017**, *21*, 899–910. [CrossRef]
35. Easa, J.; Yan, C.; Schneider, W.F.; O'Brien, C.P. CO and C3H6 Poisoning of Hydrogen Permeation across Pd77Ag23 Alloy Membranes: A Comparative Study with Pure Palladium. *Chem. Eng. J.* **2022**, *430*, 133080. [CrossRef]
36. Zou, H.; Chen, J.; Fang, Y.; Ding, J.; Peng, W.; Liu, R. A Dual-Electrolyte Based Air-Breathing Regenerative Microfluidic Fuel Cell with 1.76 V Open-Circuit-Voltage and 0.74 V Water-Splitting Voltage. *Nano Energy* **2016**, *27*, 619–626. [CrossRef]
37. Nguyen, P.K.T.; Kim, J.; Yoon, Y.S.; Yoon, H.H.; Hur, J. Mathematical Modeling of a Direct Urea Fuel Cell. *Int. J. Hydrogen Energy* **2023**, *48*, 2314–2327. [CrossRef]
38. Nangan, S.; Ding, Y.; Alhakemy, A.Z.; Liu, Y.; Wen, Z. Hybrid Alkali-Acid Urea-Nitrate Fuel Cell for Degrading Nitrogen-Rich Wastewater. *Appl. Catal. B Environ.* **2021**, *286*, 119892. [CrossRef]
39. Morales-Acosta, D.; Flores-Oyervides, J.D.; Rodríguez-González, J.A.; Sánchez-Padilla, N.M.; Benavides, R.; Fernández-Tavizón, S.; Mercado-Silva, J.A. Comparative Methods for Reduction and Sulfonation of Graphene Oxide for Fuel Cell Electrode Applications. *Int. J. Hydrogen Energy* **2019**, *44*, 12356–12364. [CrossRef]
40. Cruz, J.C.; Baglio, V.; Siracusano, S.; Ornelas, R.; Arriaga, L.G.; Antonucci, V.; Aricò, A.S. Nanosized Pt/IrO2 Electrocatalyst Prepared by Modified Polyol Method for Application as Dual Function Oxygen Electrode in Unitized Regenerative Fuel Cells. *Int. J. Hydrogen Energy* **2012**, *37*, 5508–5517. [CrossRef]
41. Cruz, J.C.; Rivas, S.; Beltran, D.; Meas, Y.; Ornelas, R.; Osorio-Monreal, G.; Ortiz-Frade, L.; Ledesma-García, J.; Arriaga, L.G. Synthesis and Evaluation of ATO as a Support for Pt-IrO2 in a Unitized Regenerative Fuel Cell. *Int. J. Hydrogen Energy* **2012**, *37*, 13522–13528. [CrossRef]

42. Escalona-Villalpando, R.A.; Dector, A.; Dector, D.; Moreno-Zuria, A.; Durón-Torres, S.M.; Galván-Valencia, M.; Arriaga, L.G.; Ledesma-García, J. Glucose Microfluidic Fuel Cell Using Air as Oxidant. *Int. J. Hydrogen Energy* **2016**, *41*, 23394–23400. [CrossRef]
43. Escalona-Villalpando, R.A.; Gurrola, M.P.; Trejo, G.; Guerra-Balcázar, M.; Ledesma-García, A.L. Electrodeposition of Gold on Oxidized and Reduced Graphite Surfaces and Its Influence on Glucose Oxidation. *J. Electroanal. Chem.* **2018**, *816*, 92–98. [CrossRef]
44. Alonso-Vante, N. *Electroquímica y Electrocatálisis: Materiales: Aspectos Fundamentales Y Aplicaciones*; E-libro.net: Miami, FL, USA, 2003; ISBN 1413501001.